Faculty of Science and Engineering

Advanced Analysis of Time-lapse Seismic Data for CO_2 Geosequestration Monitoring

Dmitry Popik

This thesis is presented for the Degree of

Doctor of Philosophy
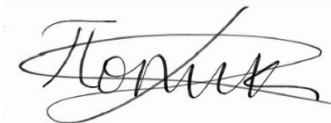
of

Curtin University

May 2019

Declaration

To the best of my knowledge and belief this thesis contains no material previously published by any other person except where due acknowledgment has been made.

This thesis contains no material which has been accepted for the award of any other degree or diploma in any university.

Signature:

Date: 08/05/2019

Abstract

In the last two decades, global concerns about rising greenhouse gas emissions into the atmosphere prompted the development of a number of mitigation technologies. One of the technologies that can substantially reduce CO_2 emissions into the atmosphere is carbon capture and storage, which involves injecting CO_2 into geological formations. When CO_2 is injected into the subsurface it is essential to ascertain that it remains in the desired formation and does not migrate into overlaying strata, into aquifers containing fresh water resources or into the atmosphere. 4D surface seismic has the best potential to image and contour injected CO_2 plumes in space. We demonstrate how an onshore 4D surface seismic monitoring project can be organised to achieve the goals of monitoring based on a case study for Stage 2C of the CO2CRC Otway Project.

The main objective of this research is to develop a methodology to address the challenges of onshore 4D surface seismic. This is a multistage task, hence this thesis covers various aspects of onshore monitoring and verification projects, including development of a 4D acquisition strategy, field acquisition design and CO2 detection feasibility study, as well as processing and imaging of the acquired 4D seismic data for structural and quantitative interpretation.

First, I demonstrate the improvement of repeatability of the field data due to the permanent installation of geophones and the acquisition strategy of monitor surveys that we employed.

I then show how a synthetic feasibility study can be used to verify the detectability of a small-scale injection in the presence of noise. I present a workflow for building an elastic model for 4D forward simulations. I then run wavefield

simulation for the actual field acquisition geometry and the most realistic model of the subsurface and distribution of elastic properties in the gas plume. This workflow can be applied to feasibility studies for monitoring projects of similar size.

Next I use the simulated synthetic data to learn how processing procedures affect time-lapse signal and noise. In particular, a long-window automatic gain control largely preserves the lateral reflectivity of the plume on full-stack images, and hence it can be applied before stacking if the benefit of noise reduction is considerable. Surface-consistent deconvolution should be used instead of spiking trace-by-trace deconvolution because the latter might degrade the quality of well-ties and quantitative interpretation. Time migrations introduce lateral shifts of the faults and the plume even for relatively horizontally-layered geological models. Depth migration resolves these mispositioning issues.

Finally, I present a methodology to produce judicious full-stack 4D images of the small-scale injection with good accuracy of the plume location and definition and seismic amplitude restoration for quantitative interpretation. I start with the analysis of the sources of time-lapse noise. This analysis indicates that the main sources of time-lapse noise are ground roll, source-generated S waves, ambient uncorrelated noise, and instability of the near-surface and excitation parameters. I investigate how different time-lapse attributes respond to different types of time-lapse noise. I find that some attributes are indicative of wavelet mismatch between surveys, while others are good to assessing the degree of suppression of the high-energy time-lapse noise component which is coherent (but not identical) between monitor and baseline traces. These time-lapse attributes complement each other and should be used together to capture the effects of different processing and imaging routines on 4D signal and noise. I demonstrate how to control the quality of the processing and imaging routines from

the perspective of 4D noise and signal using a combination of time-lapse attributes for pre-stack and post-stack configurations. I suggest that time-lapse signal and time-lapse noise should be checked after each routine in the processing workflow. To do so I propose displays of the time-lapse attributes for an insightful look at the data.

Acknowledgements

Contents

Abbreviations

1D	one-dimensional
2D	two-dimensional
3D	three-dimensional
4D	four-dimensional; monitoring using repetitive 3D surveys
AGC	automatic gain control
AVO	amplitude versus offset
B	baseline survey
CCS	carbon capture and storage
CDP	common depth point
CPU	central processing unit
CRC	collaborative research consortium
DAS	distributed acoustic sensing / sensor
FDTD	finite-difference time domain
FDU	field data recording unit
GPS	global positioning system
M[X]	monitor survey from 1 to 5
MPI	message passing interface
NMO	normal moveout
NRMS	normalized root mean square; seismic repeatability measure
PSTM	pre-stack time migration
QC	quality control
QI	quantitative interpretation
RMS	root mean square

RMSDIF	root mean square of a difference
SCD	surface-consistent deconvolution
SDR	signal-to-distortion ratio
SIS	sequential indicator simulation
SNR	signal-to-noise ratio
SOV	surface orbital vibrator
SSTVD	true vertical depth sub-sea
TS	time shifts
TVD	true vertical depth
UTM	universal transverse Mercator
VSP	vertical seismic profile

Chapter 1.

Introduction

In the last two decades, global concerns about rising greenhouse gas emissions in the atmosphere have prompted the development of a number of mitigation technologies. One of the technologies that can substantially reduce carbon dioxide (CO_2) emissions into the atmosphere is carbon capture and storage (CCS), which involves injecting CO_2 into geological formations (Schrag 2007, Pacala and Socolow 2004). In the last 15 years, several pilot (Jenkins et al. 2012, Bergmann et al. 2016, Kharaka et al. 2006, Cook 2014) and production-scale (Chadwick et al. 2010, Hansen et al. 2013, Ringrose et al. 2013) CCS projects, both onshore and offshore, have demonstrated great potential for CO_2 emission abatement. According to the International Energy Agency, CCS has the potential to reduce 14% of emissions by 2050 (IEA 2012).

When CO_2 is injected into the subsurface it is essential to ascertain that it remains in the desired formation and does not migrate into overlaying strata, into aquifers containing fresh water resources or into the atmosphere. Hence every CCS project requires the ability to remotely detect and track small (to the order of 10,000 tonnes) volumes of CO_2 within both the injection interval and the overlaying strata as well as requires quantification of the spatial distribution of the total injected volume of CO_2 (Jenkins et al. 2015).

One technology that has the ability to track the spatial and temporal distribution of CO_2 is time-lapse seismic (also known as seismic monitoring), which involves repeated acquisition of reflection seismic surveys over the reservoir to characterize

changes of subsurface properties (Hannis et al. 2015, Johnston 2013). Time-lapse seismic is a mature technology that is widely used in the petroleum industry to monitor and optimize hydrocarbon production. Changes in the seismic response of the reservoir during production are caused by the changes in elastic properties of the subsurface strata, which are in turn caused by changes in fluid saturation or pressure (Lumley 2001, Landrø 2001).

Different configurations of seismic acquisition techniques are available for monitoring. The most commonly used acquisition setups are repeated vertical seismic profiles (VSPs) and repeated 3D seismic surveys. Time-lapse seismic that acquires repeated 3D surveys using surface seismic sources is commonly referred to as 4D surface seismic. While VSP configurations generally have a higher signal-to-noise ratio (SNR) due to the absence of ground roll and low ambient noise, 4D surface seismic has the best potential to image and contour injected CO_2 plumes in space.

This thesis explores the numerous challenges of monitoring programmes that rely on 4D surface seismic for the monitoring of CO_2 injections for onshore carbon geosequestration projects. This thesis is based on a 4D seismic monitoring case study for Stage 2C of the CCS CO2CRC Otway Project. Even though this is a case study, we expect that many of our findings can be transferred to other onshore monitoring projects after certain modifications.

1.1   Research motivation

Monitoring CO_2 injection with surface seismic is expected to produce images of the injected plume in space and the evolution of the plume in calendar time. The images should be of sufficient quality to satisfy the objectives of a monitoring programme with some confidence. Thus, the time-lapse seismic images should indicate whether the injected plume is contained within a certain geological formation

or not. Ideally, these images should also be indicative of the plume parameters, such as the spatial distribution of the plume's thickness and the saturation of CO_2. From a seismic monitoring point of view, the problem of building reliable, high-quality images of the injection is a question of the restoration of time-lapse seismic signal and the suppression of time-lapse seismic noise.

4D processing is site specific. In particular, the acquisition environment (e.g. onshore or offshore) has the largest impact on the way the processing workflow is built. The majority of successful seismic monitoring projects (including monitoring oil production) are carried out in offshore environments (Calvert 2005a, Helgerud et al. 2011, Hatchell et al. 2017). However, the processing workflows of deep marine seismic monitoring are often not directly transferrable to those on land as the sources of time-lapse noise are generally different. Onshore seismic monitoring is devoid of some of the challenges inherent to offshore monitoring such as source and receiver positioning errors. However, onshore seismic monitoring suffers from other problems, such as high variability of ground properties and high-intensity surface waves, all of which are known to be critical for the Otway site (Shulakova et al. 2014).

From a broader perspective, the main objective of this research is to study and resolve some of the issues caused by onshore time-lapse noise while preserving the time-lapse seismic signal. This is a multistage task; hence, this thesis covers various aspects of onshore monitoring projects for CCS, ranging all the way through from the development of 4D acquisition strategy, to field acquisition and feasibility study, to the processing and imaging of the acquired 4D seismic data for structural and quantitative interpretation.

1.2   Thesis outline

The thesis is structured as follows:

- In Chapter 1 I introduce the subject of CCS and storage monitoring for CCS. I then describe the research motivation.

- Chapter 2 presents an overview of seismic monitoring for CCS projects and the design of the monitoring programme developed for Stage 2C of the Otway Project.

- In Chapter 3 I describe the survey design, including the permanent installation of surface geophones and the acquisition strategy for the baseline and monitor surveys.

- In Chapter 4 I show how synthetic data can be used to verify the detectability of a small-scale CO_2 injection in the presence of noise. This chapter covers the building of the static geological model, flow simulations, preparation of the model for seismic simulations, performing the seismic simulations, modelling the noise, and express (pilot) processing of the synthetic data with added noise. This chapter also describes the compromises we make to afford the seismic simulation of a real scale 4D seismic survey.

- Chapter 5 shows how the processing of 4D synthetics can aid in processing 4D field surface seismic to produce seismic data suitable for quantitative interpretation and better plume definition/location. To this end, I revisit a common processing sequence and further investigate how different processing and imaging routines affect time-lapse signal.

- Chapter 6 addresses the main challenges of onshore 4D seismic processing. I start with a theoretical model of time-lapse noise present in onshore seismic data and approach the ways to suppress it. I then devise a methodology of quality control (QC) of 4D noise and 4D signal

at all the stages of our processing flow. Finally, I justify and produce a workflow that yields time-lapse images that can be used for post-stack quantitative interpretation.

- In Chapter 7 I draw conclusions, discuss the relevance of the findings to other monitoring projects and outline directions for future research.

1.3   Author's contribution

The results presented in this thesis emerged as a result of the collaborative effort of a number of people involved in the surface seismic monitoring programme for Stage 2C of the Otway Project. Thus I use "we" almost everywhere throughout the thesis. For the completeness of presentation I describe all the relevant parts of the experiment irrespective of my involvement in their execution (e.g., I was not involved in rock-physics modelling). My contribution to the dissertation and to the project was as follows:

- I took part in the field acquisition of four monitor vintages. My main roles were the operation of a differential GPS (global positioning system) for the repositioning of vibrator trucks and operation of vibrator trucks (acquisition section of Chapter 3).

- I performed final simulations of the time-lapse synthetic elastic wavefield using SOFI 3D modelling software. Then I processed and imaged the synthetic data, simulated 4D noise and verified the detectability of the injection prior to acquisition of the field monitor data (second part of Chapter 4). I was neither involved in the building of the baseline and monitor models of elastic properties nor in the testing of the parameters for the seismic wavefield modelling.

- I did all the work presented in Chapters 5 and 6; namely, development and application of model-guided approach to the processing of 4D field data with monitoring of 4D signal and noise at each processing and imaging stage.

Chapter 2.

Review of seismic monitoring of CO$_2$ geosequestration

This chapter has two parts. The first part sets up the framework and the context for this research. It reviews the current state of the CCS industry from the perspective of seismic monitoring of CO$_2$ storage. The second part presents how the issues of onshore seismic monitoring for CCS are addressed in the current case study known as Stage 2C of the CO2CRC Otway Project.

This chapter contains text excerpts and a figure from the peer-reviewed and published article I co-authored. The article, "4D surface seismic tracks small supercritical CO$_2$ injection into the subsurface: CO2CRC Otway Project", was published in the International Journal of Greenhouse Gas Control in 2017 (Pevzner, Urosevic, Popik, Shulakova, et al. 2017). Thus, I reuse some of its contents without referencing the actual article. The publisher's consent to reuse the material can be found at the end of the thesis (Appendix A).

2.1 Overview of seismic monitoring for CO$_2$ storage projects worldwide

Time-lapse seismic plays an important role in the monitoring and verification operations of a number of pure CO$_2$ geosequestration projects (Ivandic et al. 2015, White et al. 2014, Couëslan et al. 2014, White 2011, Chadwick et al. 2009) as well as for the projects where CO$_2$ injection is used in the enhanced oil recovery operations (O'Brien et al. 2010, Davis and Benson 2004, Meadows and Cole 2013). Time-lapse seismic is used for both monitoring of the plume evolution and as an assurance

monitoring technique that can demonstrate the absence of significant leakage of the injected CO_2 out of the primary containment (Jenkins et al. 2012). In order to optimize the use of seismic monitoring for these purposes, it is important to understand its limitations in terms of resolution and sensitivity when detecting small quantities of CO_2 in different geological formations. In particular, an important consideration is the potential leakage of supercritical CO_2 (which would turn into gas under near-atmospheric pressure and temperature) into overlaying aquifers, including the shallow aquifers which are an important groundwater resource.

Several field experiments reported different degrees of success in detecting small CO_2 volumes injected into saline aquifers using seismic technology. A strong signal from an injection of as low as 1,600 tonnes of supercritical fluid at a depth of about 1,500 m was observed at the Frio site using time-lapse zero-offset and offset VSP surveys (Daley et al. 2008, Al Hosni et al. 2016). This was done by placing geophones in the well passing through the CO_2 plume both above and below the injection interval. However, 4D surface seismic was not acquired.

To date only a few monitoring programmes for pilot CCS projects have used 4D seismic as the monitoring tool. In the CO2SINK Project (Ketzin, Germany), 4D surface seismic was successfully employed to monitor ~22,000 tonnes of CO_2 in gas form at a shallow depth of 630 m (Lüth et al. 2011, Bergmann et al. 2016). At the same time, no clear time-lapse signal was observed using 4D VSP from approximately 70,000 tonnes of supercritical CO_2 plume in the Decatur experiment (Couëslan et al. 2014).

Overall, while 4D seismic has been effective in tracking large CO_2 plumes (such as Sleipner and Snøhvit offshore Norway), detection and quantification of CO_2 leakage from the target formations is an important topic of current research (Chadwick

et al. 2014). This is particularly topical for onshore 4D seismic monitoring, which faces additional challenges due to temporal variations of near-surface conditions, prominent surface waves, coupling of sources and receivers to the ground, and ambient noise caused by wind, rain and human activity (Lumley 2001, Pevzner, Shulakova, et al. 2010, Johnston 2013).

2.2 Seismic monitoring for Stage 2C of CO2CRC Otway Project

Over the last decade, the CO2CRC Otway Project has contributed to the development of time-lapse seismic monitoring approaches applied to CO_2 geosequestration. The CO_2 storage site of the Otway Project is located onshore, 240 km to the west of Melbourne in the Australian state of Victoria (Figure 2-1). Below, we first summarize the key findings from the previous stages of the project as they play an important role as a precursor for the monitoring concept of Stage 2C. We then describe the monitoring strategy for Stage 2C. A comprehensive description of the Otway Project can be found in Cook (2014).

Figure 2-1: Map of Australia with the location of the Otway site indicated by the red dot.

2.2.1 Stage 2C: background

During Stage 1 of the project (2007-2010), seismic monitoring was used to conduct assurance monitoring and attempt to detect 66,000 tonnes of a supercritical CO_2/CH_4 mixture injected into the depleted Naylor gas reservoir at a depth of 2400 meters through a purpose-drilled CRC-1 well (Jenkins et al. 2012, Cook 2014). 4D seismic was employed using a surface geophone array (~900 receivers), 4D VSP and time-lapse offset VSP. The surface geophone array produced 30-40 % normalized root mean square (NRMS) repeatability. Ambient noise and seasonal variations in the near surface were the main adverse factors affecting the time-lapse data quality (e.g., Pevzner, Shulakova, et al. (2011)). Offset VSP data exhibited comparable level of time-lapse noise to surface 4D (Pevzner, Urosevic, et al. 2010). 4D VSP achieved NRMS values close to 10% (Pevzner, Caspari, Gurevich, et al. 2015, Pevzner, Caspari, Urosevic, et al. 2015). Note that NRMS values of offset VSP are given for unstacked traces, while NRMS values for the 4D surface seismic and 4D VSP are given for the final migrated stacks. This is why NRMS of the offset VSP indicates worse repeatability than the NRMS of the 4D VSP. Please also note that the formula for NRMS and its meaning are introduced in Chapter 6.3 together with other repeatability measures.

Stage 2 consists of 3 sub-stages called 2A, 2B and 2C. During Stage 2A, a CRC-2 well was drilled to serve as an injector for a new small-scale CO_2 injection scheduled for Stages 2B and 2C. CRC-2 was also used to improve the characterisation of the Otway site. During Stage 2B a small amount (140 tonnes) of pure CO_2 was injected into a saline aquifer at a depth of about 1500 m. This injection was done to measure residual saturation of CO_2.

The plan for Stage 2C was to inject about 15,000 tonnes of supercritical CO_2 mixture into the different depth interval (compared to Stage 2B) of the same saline aquifer and test various seismic monitoring techniques to detect and monitor the injection. Preparation for Stage 2C commenced in 2009 – 2010 with comprehensive seismic forward modelling of the time-lapse response from flow simulations. The elastic properties of rocks before the injection and at regular intervals during and after the injection were used as input into time-lapse seismic forward modelling, which was employed to predict the time-lapse seismic for various surface and downhole seismic acquisition geometries. Several modelling workflows were developed (Caspari et al. 2015, Pevzner, Caspari, Gurevich, et al. 2015, Glubokovskikh et al. 2016) in order to take into account principal factors that could affect the level of the signal, such as properties of the injection interval and technical parameters of the seismic survey (geometry, frequency content, etc.). Comparison of the predicted time-lapse seismic signal against the time-lapse noise (estimated from previous monitoring seismic studies in the area (Cook 2014)) showed that detection and tracking of 15,000 tonnes of CO_2 is likely but may be challenging (Pevzner, Caspari, Gurevich, et al. 2015, Glubokovskikh et al. 2016). To increase the likelihood of successful detection it was then decided to perform seismic acquisition using a permanent array of geophones buried into the ground, which was expected to reduce the ambient noise and variability of geophone coupling. In order to examine the potential noise reduction from burying the geophones and establish the ambient noise profile, a small (29 geophones at depths of 1 – 11 m) buried receiver array was deployed on site in 2012 (Shulakova et al. 2014). It showed that deploying the geophones at 3 m or deeper can reduce the noise floor by 20 – 30 dB. During the same experiment, initial tests of distributed acoustic sensor (DAS) technology were carried out using both horizontally (in a 1 m deep

trench) and vertically (in CRC-2) deployed fibre optic cables (Daley et al. 2013). It has also become apparent that permanent receiver installation allows the use of the same buried geophone array for passive seismic monitoring and, potentially, pairing it with continuous seismic sources.

Based on the results of these studies, in early 2015 a buried array of high-sensitivity geophones was designed and installed at the CO2CRC Otway site. This array is being used to monitor the Stage 2C injection through a series of 3D seismic surveys.

2.2.2   Stage 2C: operations

The CO2CRC Otway Stage 2C program includes the following activities:

- Design and installation of the buried receiver array,

- Acquisition of the baseline seismic data,

- Injection of 15,000 tonnes of supercritical CO_2 / CH_4 gas mixture into the saline aquifer (Paaratte Formation) located at 1.5 km depth,

- Acquisition of two monitor seismic surveys during the injection and one survey at the completion of the injection to detect the plume and observe its evolution, and

- Acquisition of two additional post-injection surveys (one and two years after commencement of the injection). This data is to be used in conjunction with fluid flow simulations to demonstrate plume stabilization.

All but the last item were completed by the time of writing this thesis.

In order to both evaluate seismic detectability limits and attempt to prove the stabilization of the plume, it was crucial to improve the quality of the 4D seismic

image. Other factors that influence the monitoring programme design, effectiveness and completeness include land access limitations and survey cost optimization.

The CO2CRC Otway site is located in an active cattle farming area in rural Victoria. To minimize the ground impact, light and environmentally friendly 26,000 lbs Inova vibrator trucks are employed. To minimize the impact on farmland, seismic field operations can take place only in a time window from November to April, when the ground is dry and hard. Furthermore, experience from previous seismic operations in the area shows that the use of surface geophones connected by seismic cables on the ground during seismic acquisition causes significant disruption to farming activities. This can be avoided by using a permanently buried geophone array. Furthermore, the use of the permanent array substantially reduces the mobilization period, leading to a shorter time required for the survey.

Based on these considerations, the core monitoring program consists of the 4D surface seismic acquired using the buried receiver array concurrently with 4D VSP. These two methods provide superior image quality in combination with minimal operational disruptions to the landowners. In addition, zero-offset VSP, offset VSP and surface orbital vibrators are used to evaluate the capabilities of less expensive monitoring techniques.

2.2.3 Stage 2C: monitoring tools

Buried receiver array design and deployment

The crucial feature of this monitoring project is a buried permanent geophone array employed to record surface seismic data (Pevzner, Tertyshnikov, et al. 2015). The buried array helps to significantly improve SNR, avoid geophone redeployment, preserve receiver coupling between the surveys and reduce impact on landowners

(Pevzner, Tertyshnikov, et al. 2015). The details of the permanent installation of high sensitivity geophones are given in the next chapter.

In addition to the permanently installed geophones, in order to evaluate the performance of the DAS technique (Yavuz et al. 2016), fiberoptic cables were deployed in every receiver line trench. A total of ~38 km of optical fibre was connected to two DAS interrogators manufactured by Silixa. The buried receiver array was installed at the Otway site in February 2015.

Acquisition of the baseline and monitor surface seismic and 3D VSP surveys

The deployment of the receiver array was immediately followed in March 2015 by the baseline data acquisition. The injection commenced in December 2015, and three monitor surveys were acquired in January – April 2016 after injection of 5,000, 10,000 and 15,000 tonnes (here and below these surveys are referred to as M1, M2 and M3, respectively). One more monitor survey was acquired in January 2017 (one year after the start of injection). 4D surface seismic acquisition strategy and setup are described in detail in the next chapter.

Concurrent with surface seismic data acquisition, 3D VSP data was also acquired. This was done using a 10-level 3C geophone string with 15 m spacing between the shuttles deployed in the CRC-1 well at a depth interval of 760 – 895 m. In addition, a fibreoptic cable deployed in CRC-2 well was used as a DAS (together with the 2D DAS array). Due to technical issues with the downhole equipment, the M1 3D VSP survey acquired with 3C geophones recorded only ~30% of the total source effort. The other two monitor surveys have complete 3D VSP source coverage.

Survey layout for 4D surface seismic and 4D VSP is shown in Figure 3-5.

Zero-offset and offset VSP

In addition to 3D VSP, zero offset and four offset source positions were used to acquire VSP data with 3C geophones in CRC-1 and DAS in CRC-2 wells (Figure 3-5). The run of VSP tool in CRC-1 well provided receiver coverage of the borehole from 630 to 1800 m with 15 m spacing. For every receiver station, three to four sweeps were recorded, excluding noisy records. The total acquisition duration for zero-offset and offset VSP was two days for the baseline survey and one day per survey for the three monitor surveys (excluding the time to rig down the tool).

Continuous monitoring

Apart from the relatively conventional seismic monitoring setup, Stage 2C involves a field trial of novel continuous seismic monitoring techniques. Active seismic monitoring was performed using a combination of two permanently deployed surface orbital vibrators (SOVs) designed by the Lawrence Berkeley National Laboratory team, and DAS / geophone arrays. SOVs are stationary sources of seismic energy capable of producing sweep signals at regular time intervals. SOVs can operate over several years and hence provide an opportunity for continuous monitoring over the life of a project. Two SOVs capable of producing sweeps up to 80 Hz are installed in the vicinity of Naylor-1 and CRC-2 wells; the location of the vibrators was chosen based on the plume illumination analysis. SOVs were in operation for 120 days covering the time frame from September 2015 to June 2016 with some gaps. Preliminary results of the continuous monitoring are promising (Dou et al. 2016, Freifeld et al. 2016).

The following chapters focus on the analysis of the synthetic and field 4D surface seismic data with the buried geophone array. Even though VSP, DAS and continuous monitoring can assist in processing of surface seismic data (e.g. we can use VSP to get a better insight into anisotropy or 4D VSP to estimate surface-consistent

amplitude scalers for the sources), analysis of VSP, DAS and continuous monitoring data is outside the scope of this thesis.

Chapter 3.

Acquisition of 4D surface seismic for Stage 2C of the Otway Project

This chapter prefaces the chapter on the feasibility study because the feasibility study uses real-scale model and actual field geometry. Thus, we describe the actual field geometry and survey dimensions here.

This chapter is split into two parts. The first part describes the permanently buried geophone setup for the 4D seismic acquired for Stage 2C. It shows how the geophones are installed and how we benefited from this installation. The second part describes the acquisition strategy for the 4D surface seismic experiment of Stage 2C.

This chapter contains text excerpts and figures from a peer-reviewed and published article I co-authored. The article, "4D surface seismic tracks small supercritical CO_2 injection into the subsurface: CO2CRC Otway Project", was published in the International Journal of Greenhouse Gas Control in 2017 (Pevzner, Urosevic, Popik, Shulakova, et al. 2017). I reuse some of the contents of the article without referencing the actual sources. The publisher's consent to reuse the material can be found at the end of the thesis (Appendix A).

3.1   Installation of the permanent geophone array

Key parameters of the buried receiver array are (Pevzner, Tertyshnikov, et al. 2015):

- Eleven receiver lines, instrumented with seismic sensors. Distance between the lines is about 100 m, receiver spacing along the line is 15 m. The line lengths

vary from line to line and hence the number of active geophones per line varies from 60 to 95, with a total of 908 geophones deployed.

- High-sensitivity vertical component 5 Hz geophones in marsh-line casings are deployed in PVC cased wells at the depth of 4 m. Each geophone is connected to an individual field data recording unit (Figure 3-1). Three-component geophones are not used in this experiment.

- The field data recording units (FDUs) and all the cables are deployed in 0.8 m deep trenches (Figure 3-2).
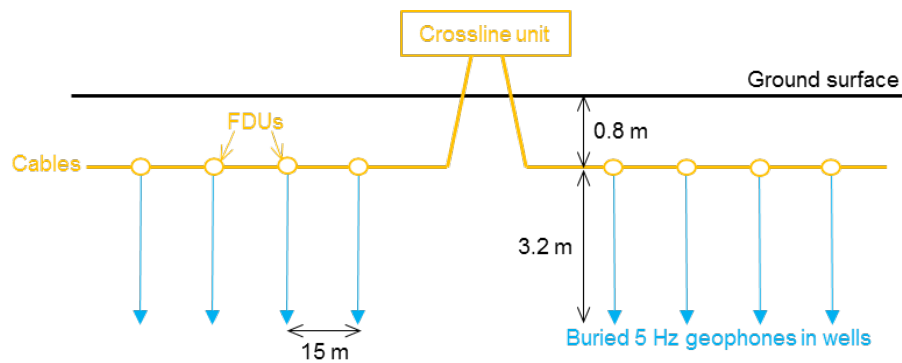
Figure 3-1: Scheme of a receiver line showing installation of cables and geophones. Not to scale.
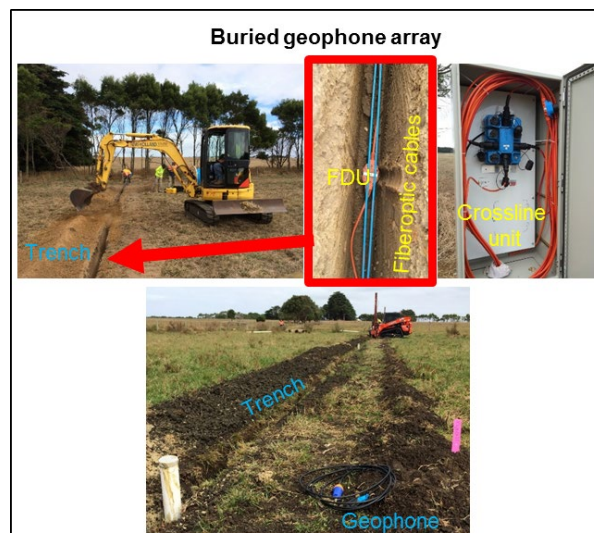
Figure 3-2: Photos of deployment of the recording equipment (both geophones and fibre-optic cables).

The recording system is built on the Sercel 428 XL platform. This telemetric system was purposefully chosen to avoid any issue with electric interference (we do not use wired geophone groups). Each receiver line contains one cross-line unit located roughly in the middle of the line to distribute power to the individual field recording units and transmit the data to a central recording facility located in the vicinity of the CRC-2 well. Cross-line units themselves are connected by both power and data cables to the recording facility; the cables are housed in the backbone trench. The central recording facility is designed such that the whole system is reliable and can be controlled remotely to allow unmanned operation for passive seismic experiments with seismic records having GPS time stamps.

The main objective of the installation of the geophone array below the surface was to substantially reduce the noise level. Thus, it is important to compare noise levels between the surface and buried geophones. To this end, six surface geophones were deployed on the surface above some of the buried geophones.

Figure 3-3 shows the comparison of a single common receiver gather obtained using surface and buried geophones and the source line oriented in a north-south direction. It is clear that the ambient noise level is significantly lower in the buried geophone data. The character of the source-generated wavefield is somewhat different for the buried and surface geophones. The change in the character of reflections (signal) may be caused by the presence of receiver ghost in the buried geophone data (White et al. 2015, Hamarbatan and Margrave 1998). In this study we do not try to deghost the data and use the ghosted wavelet as it is because 1C recording alone does not provide sufficient information to deghost land data.
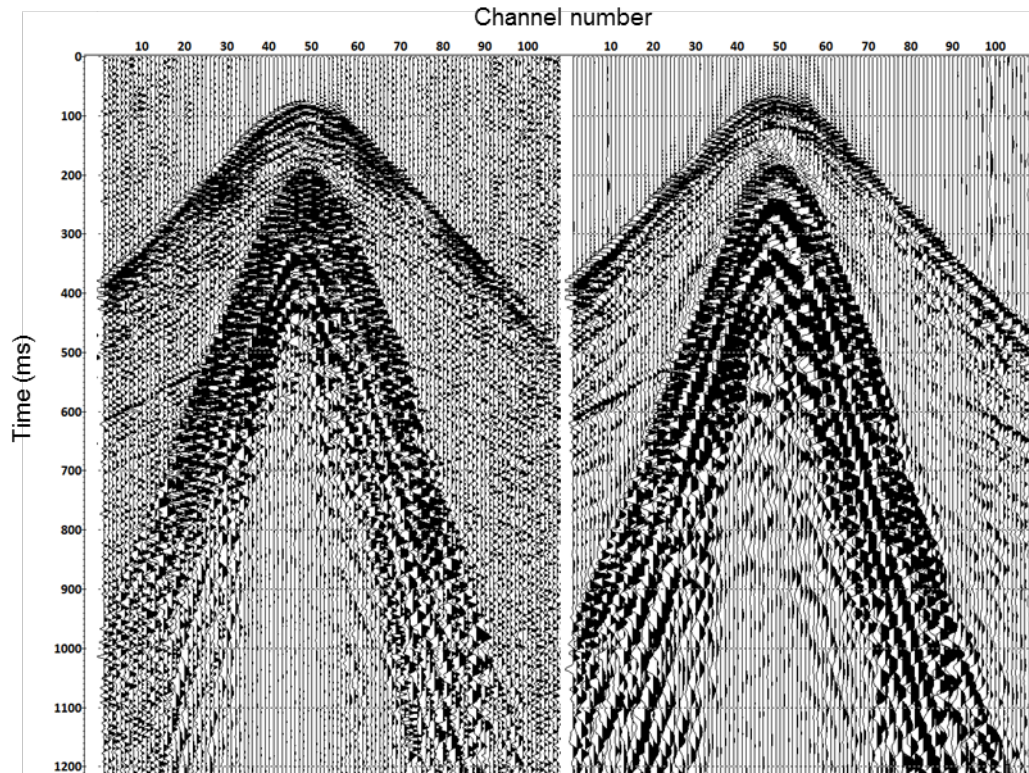
Figure 3-3: Common receiver gathers for surface (left) and buried (right) geophones (reproduced after Pevzner, Urosevic, Popik, Shulakova, et al. (2017)).

The ambient noise level obtained from uncorrelated geophone data as a function of frequency is presented in Figure 3-4. Within the sweep frequency range (from 6 to 150 Hz), the noise is reduced by 10–50 dB, with most of the useful frequency range having the noise floor decreased by over 20–30 dB. Very low frequencies do not show much of a change in the ambient noise level because they are mainly contaminated by surface waves, which do not decay at 4 m depth, while the main cause of the noise at higher frequencies is wind. Interestingly, we observe the noise spikes in the spectra at 90 Hz and 180 Hz. The latter is presumably a harmonic of the former. We speculate that the nature of these spikes is some interference coming from a SOV located nearby.

The effect of the geophone burial on the level of seismic signal is shown in Shulakova et al. (2014).
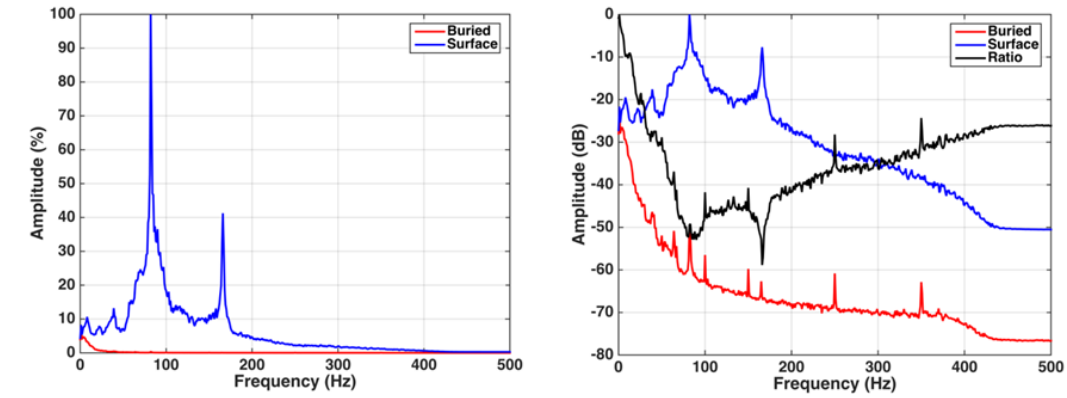
Figure 3-4: Comparison of ambient noise level on buried and surface geophone data in linear (left) and logarithmic (right) scales. The black curve in the right panel shows the logarithm of the spectral ratio between noise levels on buried and surface geophones. Sweep bandwidth is 6 – 150 Hz. Reproduced after Pevzner, Urosevic, Popik, Shulakova, et al. (2017).

3.2   Acquisition of the 4D surface seismic survey

The seismic monitoring field experiment for Stage 2C was designed around the injection of ~ 15,000 tonnes of supercritical CO_2-reach fluid into the sandstone saline aquifer with the operations taking place in the Australian state of Victoria (Cook 2014). From the standpoint of seismic processing and imaging, geology of the target overburden (Dance 2013) has sedimentary layering close to horizontal. Two major faults are present in vicinity of the target area, and one more in the shallow subsurface.

Near-surface is expected to be the major cause of non-repeatability of the seismic data (Shulakova et al. 2014). To maximize SNR we deployed a permanent receiver array of about 900 geophones (5 Hz) at a depth of 4 meters (Pevzner, Tertyshnikov, et al. 2015). Buried receivers made it possible to improve repeatability, significantly reduce the level of ambient noise, preserve receiver coupling for all the vintages, and spare the costs of redeploying receivers. By the start of the baseline survey in March 2015, the geophones had been installed along 11 lines as shown in Figure 3-5.
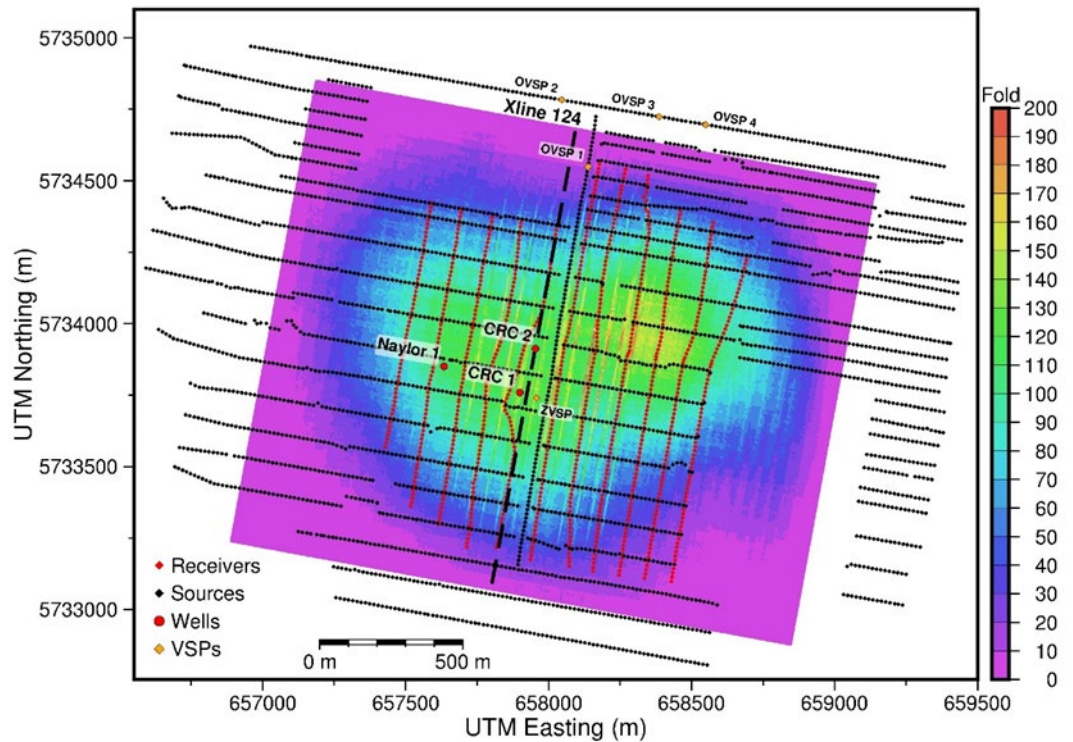
Figure 3-5: CO2CRC Otway Project Stage 2C acquisition geometry and fold of CDP coverage. Geodetic projection is UTM (zone 54). Reproduced after Pevzner, Urosevic, Popik, Shulakova, et al. (2017).
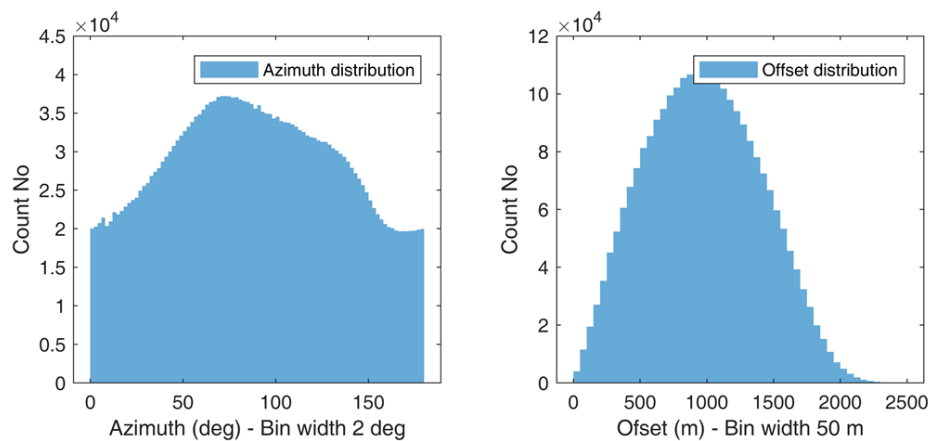
Figure 3-6 Azimuth (left) and offset(right) distributions for the traces in the survey.

Baseline data were acquired using two 26,000 lbs vibrator trucks. About 3000 source points were grouped into 27 lines, with source line spacing varying from 50 m to 100 m. Denser source coverage on the north-east side was used to partially compensate for the presence of large inaccessible areas. The source spacing along the

line was 15 m. Previous experiments (Pevzner, Shulakova, et al. 2010) suggested that repeatability of final images correlates with the level of uncorrelated noise within each individual vintage. As CDP stacking is the strongest attenuator of uncorrelated noise, the survey design aims to boost CDP fold for the target area. The CDP fold map for bin size of 7.5 by 7.5 m is shown in Figure 3-5. The average fold around the area of interest is around 130 with the maximum fold values reaching 200 for certain CDP bins. Figure 3-6 shows distributions of the azimuths (left) and offsets (right) in our data.

The shooting was done in flip-flop mode with a single sweep per shot location to speed-up the acquisition. We conducted multiple sweep tests during the baseline in 2015 and compared several shorter sweeps vs one long. One long was marginally better and it also had less operational issues. Thus, the decision was made to go with a single sweep. The linear sweep of 24 s with 0.5 s cosine tapers on both sides spanned the frequency range from 6 to 150 Hz and was followed by the listening period of 5 s. Table 3-1 summarizes the relevant acquisition parameters for the surface monitoring programme for Stage 2C. The acquisition duration for the baseline survey was ten days.

Table 3-1: Seismic acquisition parameters.

General Survey Parameters		Source Parameters	
Survey	Otway 4D	Source type	INOVA vibrator UNIVIB (26000 lbs, 70 % peak force)
Location	Otway Basin, Victoria, Australia	Number of vibrators	2
Total number of source lines	27	Stacking fold	1
Total number of source points	~3000	Sweep frequency	6-150 Hz
Total number of receiver lines	11	Tapers	0.5 s
Total number of receiver points	908	Sweep length	24 s

Total number of swaths	1	Listening time	5 s
Bin size	7.5 m inline by 7.5 m crossline	Source Geometry	
Bin grid azimuth	10.46o	Source line spacing	From 50 m (eastern part) to 100 m (western part)
Total number of inlines	219	Source point spacing	15 m
Total number of crosslines	266	Sweep technique	Flip-flop
Maximum stacking fold	200	Receiver Parameters	
Offset range	0 m – 2500 m	Receiver type	5 Hz high-sensitivity geophone
Receiver line orientation	South-North	Recording pattern	Orthogonal cross-spread pattern
Source line orientation	West-East (1st-26th lines), South-North (27th line)	Receiver line spacing	100 m
Differential GPS	NavCom SF-3040	Receiver point spacing	15 m
Recording Parameters		Receiver depth	4 m
Instrument type	Sercel 428 XL	Cable depth	0.8 m
Record length	29 s		
Sample Interval	1 ms		
Tape format	SEG-D, floating point		

Injection started in December 2015 and progressed in 3 increments each of 5,000 tonnes with a monitor survey acquired after every injection increment (roughly in January, February and March of 2016). The fourth monitor survey was acquired about one year after the start of the injection (January 2017). The surveys were scheduled for the summer months as winter rains cause troubles with vibrator access to the source points.

Excitation and recording parameters were kept virtually constant during the whole campaign. The baseline shot locations were revisited for each monitor survey using differential GPS to ensure good repeatability of the field data. Coordinates recorded during the baseline survey were used in processing of all the surveys due to the very good precision of repositioning of the vibrator trucks. As we use a single sweep per shot point per vintage the coupling change may occur only between the

sweeps for the same shot point but different vintages. However, the coupling depends on the time of the year and the time between the surveys. Time of year can induce quite noticeable time-lapse noise due to changes of the ground water level (e.g. surveys B and M3 have the best repeatability and have been acquired during the same month of the adjacent years). Different sources of TL noise have different magnitude - changes in the near-surface throughout the year can have larger impact than shaken ground. The acquisition duration was around a week for each of the monitor surveys. It was important to minimize the duration of the monitor surveys as all the injection and seismic operations had to be completed within the dry season and with minimal time spent on the farmers' properties with vibrator trucks.

During the acquisition of the monitor surveys about 0.5 % of the source points acquired in the baseline survey were skipped due to recently emerged surface obstacles or soft ground conditions. We also experienced issues with the permanent receiver array during M4 (we experienced some deterioration of electronic components due to the water ingress into the field acquisition equipment), which led to some of the channels not recording the data. After winnowing all 5 datasets to have exactly the same traces we ended up with 2976 shot gathers containing 2,689,167 traces.

In this thesis we refer to the baseline and monitor surveys as B, M1, M2, M3, and M4, respectively. One more survey (M5) is planned for the beginning of 2018.

3.3 Conclusions

The buried geophone array considerably drops the level of ambient noise at a wide frequency range. Apart from that, the permanent geophone setup reduces the invasiveness of acquisition on farming, reduces the time of mobilization and demobilization and potentially reduces costs of the monitor surveys.

The monitoring field experiment for Stage 2C allowed quick acquisition of 3D surveys with high repeatability of shot and receiver positions. High fold of coverage promises good repeatability and high quality of the final plume images. At this stage the field monitor data can be input into a processing and imaging workflow.

In the following chapter we show how a monitoring seismic feasibility study helps to verify detectability of a small-scale CO_2 injection.

Chapter 4.

Study of the detectability of the injection using seismic forward modelling

Essentially, the time-lapse seismic response to the CO_2 injection is controlled by the magnitude of elastic changes induced by the pore fluid substitution and size of the plume. Stage 2C of the Otway Project was designed to examine the capabilities of surface seismic to detect a small-scale CO_2 leakage, and thus, the signal was expected to be relatively low, especially in the earlier stages of the injection. Hence, prior to the field experiment, we had to ensure the detectability of the small-scale injection using the proposed monitoring system given the acquisition and geological conditions. Also design of the processing sequence requires special care, given the subtle time-lapse response, since an inappropriate approach to noise suppression and imaging may compromise the effort done at the acquisition stage.

From this perspective it is extremely handy to have a relatively realistic 4D synthetic seismic dataset to validate the monitoring design and train processing workflows on it. For the feasibility study of Stage 2C we build a full-earth geological model of the Otway site. We then simulate two 3D surveys with actual field geometry (described in this chapter) for the baseline model and for a monitor model after a flow simulation.

This chapter describes the feasibility study and shows how we verify detectability of a small 15,000-tonne CO_2-rich injection for Stage 2C. It covers model building, generation of the synthetics and addition of seismic noise, which are followed by express processing of the noisy synthetic data.

It is important to note that the study of the rock-physics response to the injection as well as of the time-lapse AVO response and simple signal detectability had been done prior to my involvement in this project. Thus, I do not include this information directly into the thesis. I do not repeat this kind of study myself as it would be redundant and useless for the purposes of both the project and the thesis. The results of these modelling studies are available in the two papers (Caspari et al. 2015, Pevzner, Caspari, Gurevich, et al. 2015) which are referenced throughout the thesis. These papers are easily accessible from the SEG digital library or from the authors. I reference these papers here as they may give a broader and deeper understanding of the project as a whole.

This chapter contains text excerpts and figures from the peer-reviewed and published article I co-authored. The article, "Seismic monitoring of CO2 geosequestration: CO2CRC Otway case study using full 4D FDTD approach", was published in the International Journal of Greenhouse Gas Control in 2016 (Glubokovskikh et al. 2016). Thus, I reuse some of its content without referencing the actual article. The publisher's consent to reuse the material can be found at the end of the thesis (Appendix A).

4.1 Background of the feasibility study

The predicted time-lapse signal for the project is relatively low (Caspari et al. 2015) compared with published examples of successful detection of sequestered CO_2 using surface 4D seismic; for example, the Sleipner CO_2 storage (Arts et al. 2004, Chadwick et al. 2010) and Weyburn-Midale field project (White 2009, 2011). However, even in favourable conditions processing workflows control the uncertainty of quantitative characterisation of the CO_2 plume (Jenkins, Chadwick, and Hovorka 2015).

Analysis of synthetic seismic datasets provides a reliable means to optimize a workflow for time-lapse processing. Validity of the obtained results is determined by the adequacy of (1) the seismic property model, (2) the seismic simulation approach, including modelling of wave propagation and actual seismic acquisition geometry, and (3) simulation of both 4D signal and noise components. An exhaustive literature review indicated that other 4D seismic feasibility studies suffer from the same lack of rigor in implementation of points (1) to (3). Often, authors neglect the effect of the overburden on the time-lapse signal of the target interval: Arts et al. (2010) tested seismic inversion algorithms using 1D convolutional and 2D elastic modelling for a simplified model of the Sleipner field; Sodagar and Lawton (2014) used 2D acoustic modelling at the Devonian Redwater Reef. Even if a detailed full-earth seismic model were built, computational cost of 3D elastic simulations might be prohibitive, as for the most recent published studies at the Ketzin CO_2 geosequestration site (Huang et al. 2015) and at an offshore seismic monitoring of an oilfield in the Gulf of Mexico.

At the same time, the amount of the geological and geophysical information for the Otway site makes it feasible to build a very detailed full-earth seismic model, and thus to ensure realistic seismic imaging conditions of the CO_2 plume. Caspari et al. (2015) established a model of the elastic properties changes due to the presence of CO_2-rich gas in the target formation. Spatial distribution of the elastic properties of the injection is according to reservoir simulations of Ennis-King et al. (2011). Using this monitor model combined with field data analysis, Pevzner, Caspari, Gurevich, et al. (2015) developed a workflow to analyse time-lapse noise and signal. Given these and the relatively small sizes of the monitor medium (3 km × 4.5 km × 1.5 km), we performed 4D elastic simulations in the detailed full-earth model of the Otway site for the actual field acquisition spread.

4.2 Elastic model for the Otway Stage 2C experiment

An adequate seismic model of the geologic medium plays a key role for the generation of realistic synthetic seismic datasets. Usually, one concentrates on the seismic model of the target zone and its changes related to CO_2 injection. In this study we aim to create a realistic seismic model of the whole subsurface to obtain realistic seismic imaging conditions for the target zone. Correct simulation of wave propagation through the overburden formation is crucial for Stage 2C because of the relatively small magnitude of the predicted time-lapse signal.

In the following subsections we give a brief description of the Otway site along with the geological and geophysical datasets used for building the seismic model. Then we present the modelling workflow itself for both the baseline and monitor models and finally assess the quality of the results.

4.2.1 Geocharacterisation of the Otway site

Geological characterisation of the Otway Project site is presented in great detail for Stage 1 in Dance (2013), and for Stage 2 in Lawrence et al. (2012) and Dance et al. (2012). Structurally, the Otway Basin forms part of the Southern Rift System that originated during the continental separation of Australia and Antarctica. A north–south geological cross-section is presented in Figure 4-1, including the structure and stratigraphy for the Otway Project site. Large offset faulting is most prominent in the Shipwreck and Sherbrook Group sequences associated with Cenomanian to Maastrichtian extensional basin development (Krassay et al. 2004). The Paaratte Formation and overlying stratigraphy exhibit relatively low angle structural dips (less than 6 degrees), and much of the faulting terminates below the Tertiary. The major faults are the Buttress complex to the north, the Naylor South Fault, and its associated smaller relay splay fault, intersected at CRC-1 at approximately 1400 m. CRC-2 is

located about 200 m to the north of CRC-1, and does not penetrate any seismically resolved faults.

The Otway Basin belongs to an area known for numerous small methane and CO_2 rich fields. The major gas-bearing reservoir is the Late Cretaceous Waarre Formation, sealed with the regionally extensive thick Belfast Mudstone (Figure 4-1), which was the target object during Stage 1 of the Otway Project.
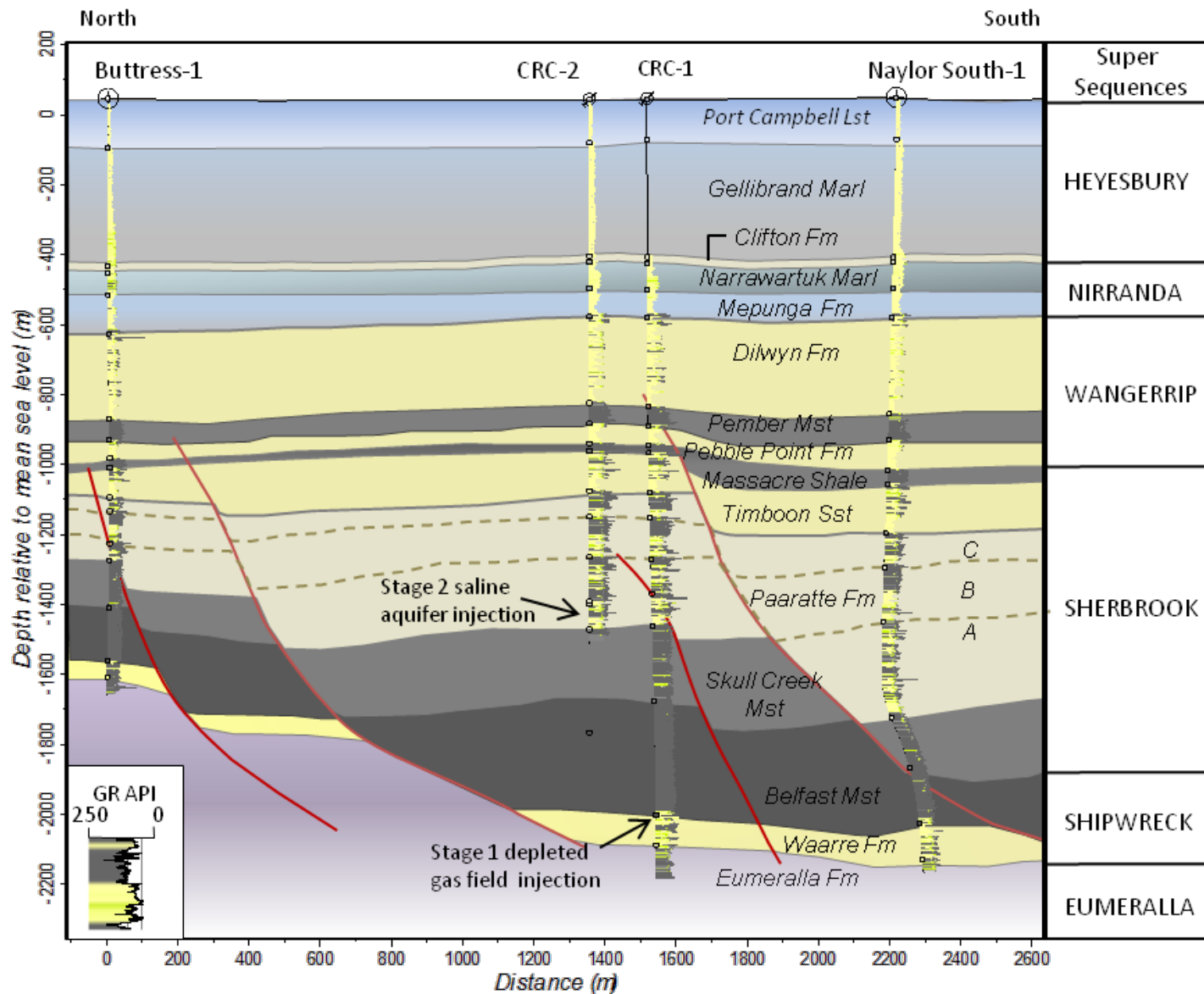
Figure 4-1: Geological cross-section through the site from north to south including structure, stratigraphy, and wells with gamma ray logs displayed (yellow: sand, grey: shale). The CO$_2$ source gas is from the Buttress-1 well. CRC-1 is the Stage 1 injection well, targeting the Waarre Formation. CRC-2 is the Stage 2 injection well targeting unit A of the heterogeneous Paaratte Formation. Horizontal to vertical scale is 1:1 (i.e. no vertical exaggeration). Reproduced after Glubokovskikh et al. (2016).

Formations that comprise the immediate overburden to the Belfast Mudstone are: Skull Creek Mudstone, a dark grey to black, carbonaceous mudstone with minor interbedded siltstones and sandstones becoming more frequent towards the top. Overlying the Skull Creek Mudstone is the Paaratte Formation, Campanian to Maastrichtian in age. This is the target aquifer for the Stage 2 injection. The entire sequence is up to 400 m thick in the study area and comprises laminated fine-grained to coarse sandstones interbedded with siltstones and mudstones deposited in a deltaic to shallow marine depositional environment. The Formation has been informally subdivided into units A, B and C on the basis of a paleontological study by Partridge (2001) and correlated flooding surfaces (Dance et al. 2012). The sandstones exhibit moderate to good porosity of 20–35 % and an average permeability of ~ 1500 mD. The sandstones are frequently overprinted with diagenetic dolomite cemented zones, 0.5–4 m thick, with less than 10 % porosity. Unit A (injection interval for Stage 2C) is overlaid by a thin continuous mudstone layer that is predicted to prevent migration of CO_2 into the upper layers. Timboon Sandstone overlies the Paaratte Formation and consists of predominately poorly consolidated, fine-grained, micaceous sandstone deposited by fluvial processes in an upper delta plain. Above the Timboon are the formations of the Wangerrip Group, including Massacre Shale and Pember Mudstone. These are characterised to provide secondary seals to the site in the unlikely event that CO_2 should breach the primary targets. The rest of the overburden plays an insignificant role for the geosequestration operations.

4.2.2   Static geological modelling

Major formations are mapped across the regional 3D seismic data (Nirranda-Heytesbury survey in 2000) to produce the structural and stratigraphic model. Supplementing the regional data are CO2CRC's Stage 1 baseline and monitoring 3D

seismic surveys, ZVSP, walk-away VSP and 3D VSP data, which provide greater detail directly over the study area. Well data of petroleum wells are sourced from existing non-proprietary petroleum databases and combined with the Otway Project's extensive data acquired during drilling of CRC-1 and CRC-2. This includes high resolution petrophysical well logs, over 220 m of core, fluid samples, and pressure tests, and the data from several years of production, injection, and monitoring. A series of detailed geocellular models is created at the reservoir scale (Dance et al. 2012) for the purposes of numerical modelling of the various Stage 2C injection scenarios (Ennis-King et al. 2011). A model representing the base scenario is then expanded to encompass an area of interest beyond the buried receiver array and entire sedimentary sequence to the surface; hence referred to as a "full-earth" static model.

A common practice for static modelling is to populate properties guided by depositional facies (rock type) distributions. This method also enables facies prediction in areas away from well control by using analogue data and sedimentary deposition principals. The workflow for the Otway full-earth model is to first correlate packages of genetically similar rock types within each of the stratigraphic zones already mapped. A discrete facies log is created for each well and the sub-zones are populated with facies via standard variogram-based Sequential Indicator Simulation (SIS). In this case well data is honoured at its location, but between wells the reservoir bodies are interpolated using SIS. This is guided by the major anisotropy axis (azimuth/dip) of the 3D variograms, and the magnitude of continuity, or range, along that direction for each facies component in the model (Doyen 2007). Porosity and density are then modelled using facies as a constraint. This method makes the minimum assumptions about the data. Essentially, the method takes the porosity and density measurements at the well (from the petrophysical analysis) and calculates

statistical parameters, assuming that the data are normally distributed. Away from the well locations the overall property distribution is created randomly, but with the final overall result matching statistical properties as calculated at the well locations.

4.2.3   Rock physical modelling

Once we have the static model we need to convert petrophysical parameters into continuous 3D distributions of seismic properties: bulk density ρ, compressional velocity V_p, and shear velocity V_s. A traditional rock physical modelling workflow has two steps:

- rock physical diagnostics – determination of a suitable model that relates geological parameters of a particular rock type to its seismic properties (Dvorkin et al. 2013);

- interpolation of seismic properties within the structural framework. We use structure-oriented interpolation techniques, that is, layer boundaries are honoured during interpolation.

To estimate the seismic properties for a given porosity and lithology within a specific stratigraphic unit one can use either a deterministic or geostatistical approach (Avseth et al. 2005). The former approach is preferable when the studied area lacks geophysical information or correlation between the seismic properties and porosity is poor. The geophysical dataset of the Otway site contains extensive measurements of ρ, V_p and V_s in several wells that are in good agreement with the porosity data. In addition, the studied area is sufficiently small to assume small variability of the rock physics relations. Thus, we utilize a geostatistical approach for the model building.

We calculate the seismic properties within each cell of the geocellular model by a collocated approach to co-kriging (Xu et al. 1992). Uncertainty of the method

decreases as the correlation coefficient between primary and secondary variables increases. The highest correlation for a given rock type with the porosity φ of the static model is obtained for ρ. In turn, ρ is well-correlated with the compressional velocity V_p. The final workflow is summarized as follows:

- find values of ρ for each rock type and porosity within a particular geological zone; $\square$

- find a volume distribution of V_p using collocated co-kriging with ρ as a guiding variable;

- collocated co-kriging of V_s using V_p, found at the previous stage, as a guiding variable.

Due to the limited information about velocities in the uppermost interval (Port Campbell carbonates), we use linear predictors $V_p(\rho)$ and $V_s(\rho)$ using density information from CRC-2 and velocities from CRC-1 below 150 m TVDSS.

Note that independent geostatistical modelling of seismic properties gives inevitably inconsistent combinations of these properties within a particular cell, leading to intensive scattering artefacts in the synthetic data. The proposed workflow reduces these effects.

At this point we have a geo-cellular model populated with ρ, V_p and V_s and with cell sizes varying from 0.5 m to 5 m along the vertical axis and from 20 to 50 m in the horizontal plane. As shown in greater detail later in the text, we use finite-difference time domain modelling to produce a real-scale 4D time-lapse seismic response from the injection. As we use wave equation seismic modelling, we need to have our model on a reasonably fine computational grid with the velocities smoothed. To generate a computational grid we resample the properties from the geo-cellular

model onto a regular Cartesian grid with a voxel size of 2.5 m × 2.5 m × 2 m. Test computations show that the resampling should be combined with an interpolation of the properties laterally and vertically, otherwise strong artificial scattering was observed in the output of the seismic modelling. We omit the details of the used interpolation, noting only that the final value in the computational grid results from weighted averaging over the volume consisting of two vertical model layers, each containing 10 adjacent geocells. Depending on the resolution of the static model in the particular interval, the averaging is performed over the volumes 20 m × 20 m × 1 m to 50 m × 50 m × 10 m.

To assess the quality of the resampled model we address two criteria:

- similarity between the model properties and the initial data;

- preservation of the geologic structure after inter-well interpolation.

In Figure 4-2 we compare the final property distribution at the well location of CRC-1 and CRC-2 with the original well logs. The parameters of the model became smoother as a result of the resampling. However, we did try to capture thin layers of high AI contrast in our model. For example, very stiff dolomitised sandstones (see spikes in Figure 4-2) may affect the seismic response from the injection reservoir. So we took special care to preserve sufficiently thick inclusions in the seismic model for numerical simulations (see spatially coherent purple lenses in Figure 4-7).

The shallow part of the model is characterised by noticeable discrepancy between the measured and modelled values. This fact leads to a more homogeneous synthetic seismic image of the uppermost interval compared to the real field image.

The geology of the area is conformal and flat, and thus, faults and thin, stiff interlayers of cemented sandstones in the target interval primarily define seismic imaging conditions for the survey. In Figure 4-3 and Figure 4-4 we can distinguish

both the stiff interlayers (purple colour) and intensive sub-vertical faulting across the whole model. In Figure 4-5 we see the Naylor South Fault, which is critically important for CO_2 propagation within the Lower Paaratte formation.
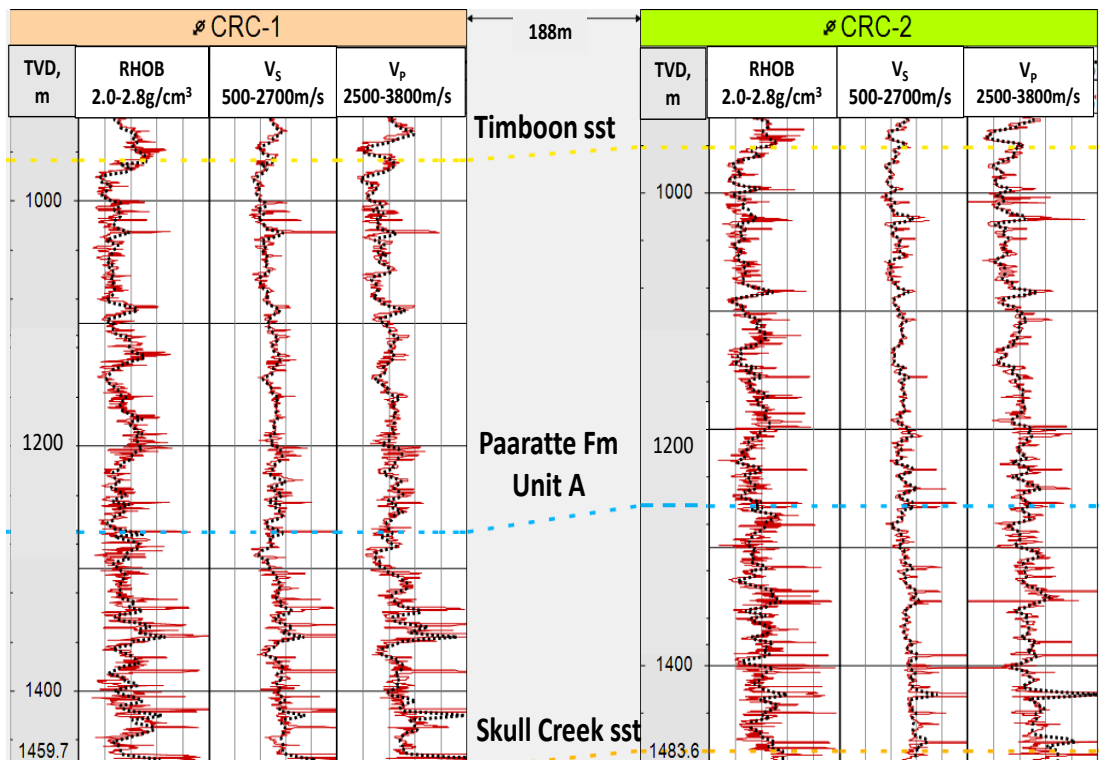
Figure 4-2: Modelled seismic properties (red solid lines) along with measured well-logs (black dashed lines) extracted along the CRC-1 and CRC-2 boreholes. Reproduced after Glubokovskikh et al. (2016).
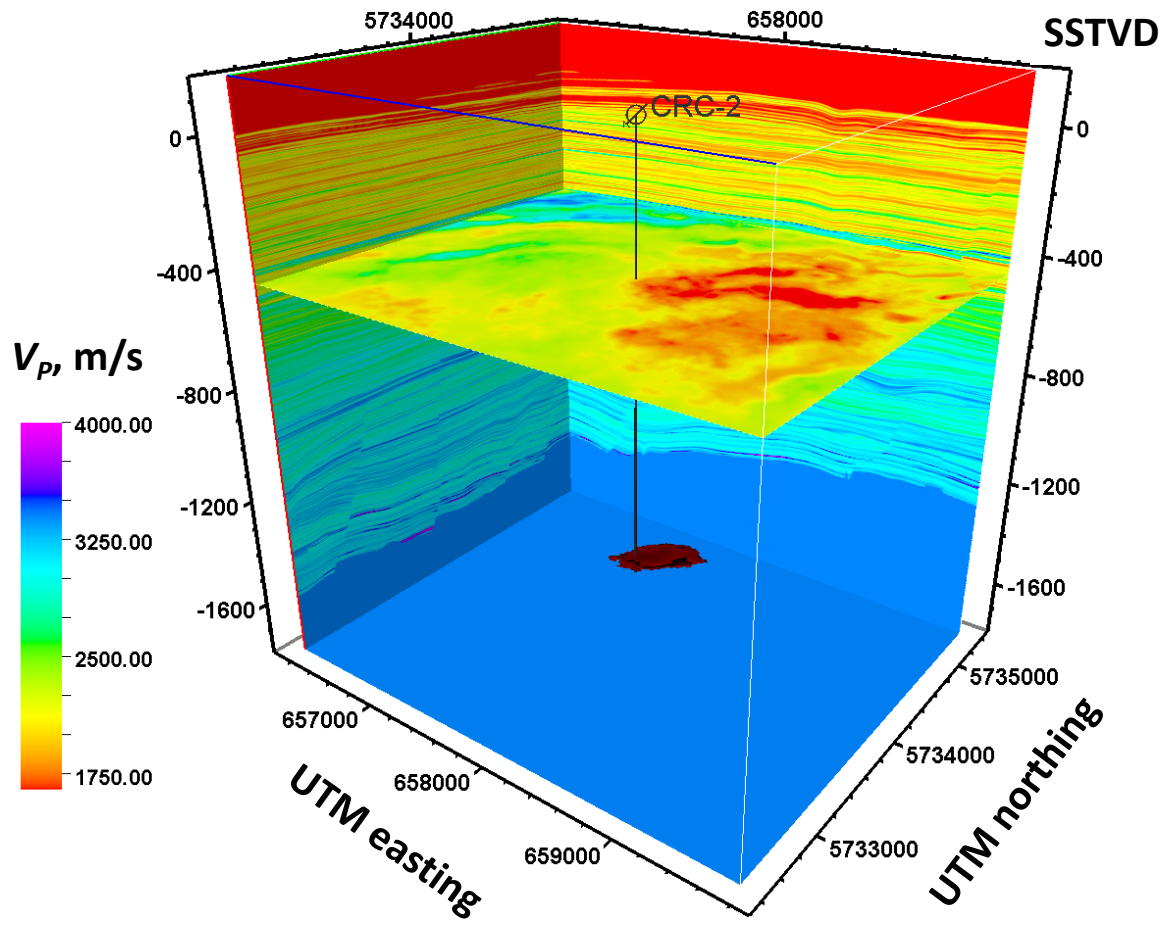
Figure 4-3: Orthogonal sections of the generated V_p model along with CRC-2 well-path and CO_2 plume model (red at the CRC-2 bottom). Reproduced after Glubokovskikh et al. (2016).
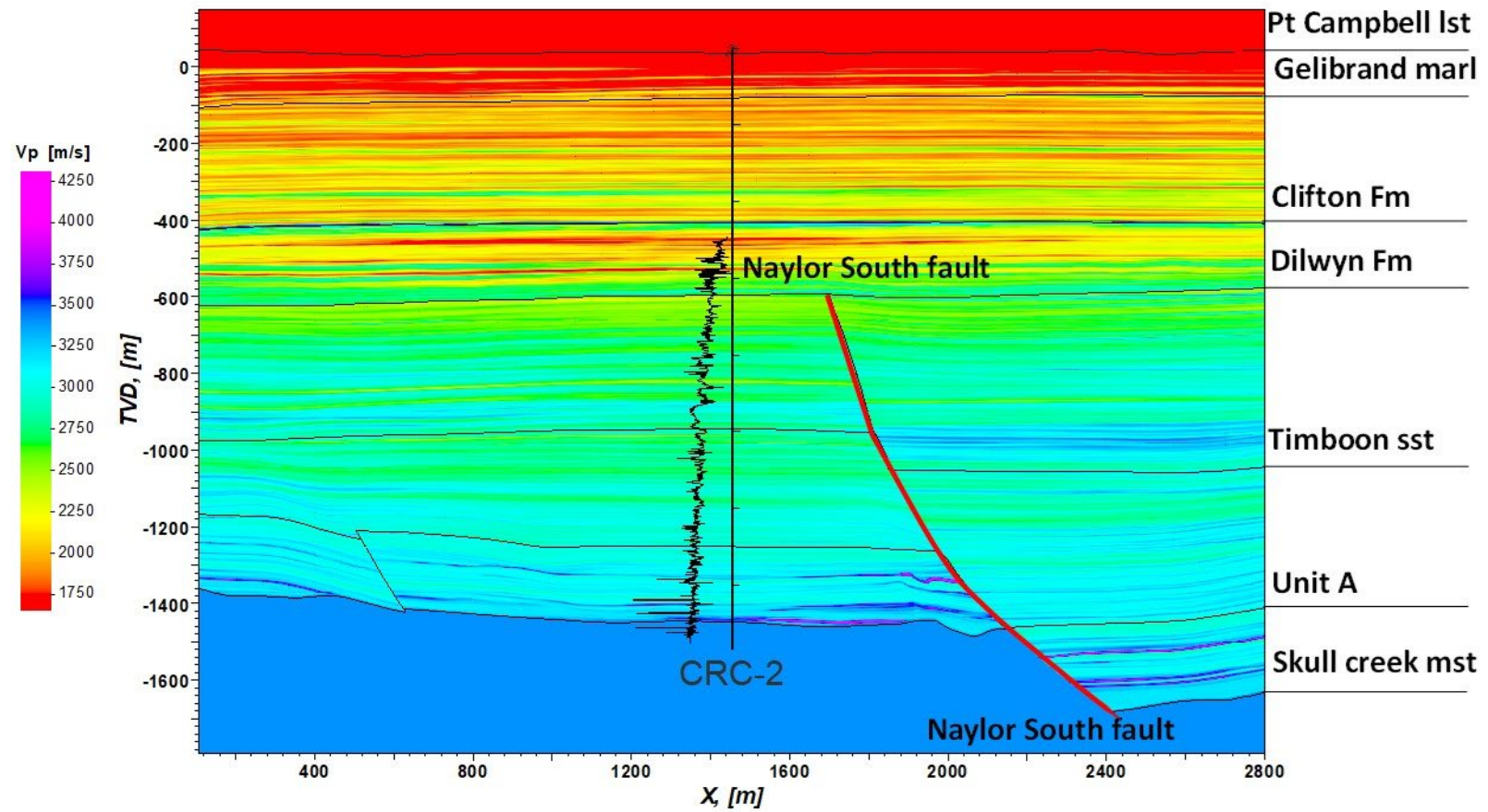
Figure 4-4: Vertical section of the V_p model through UTM Easting = 658000 m along with CRC-2 well-path and P-wave log. Reproduced after Glubokovskikh et al. (2016).
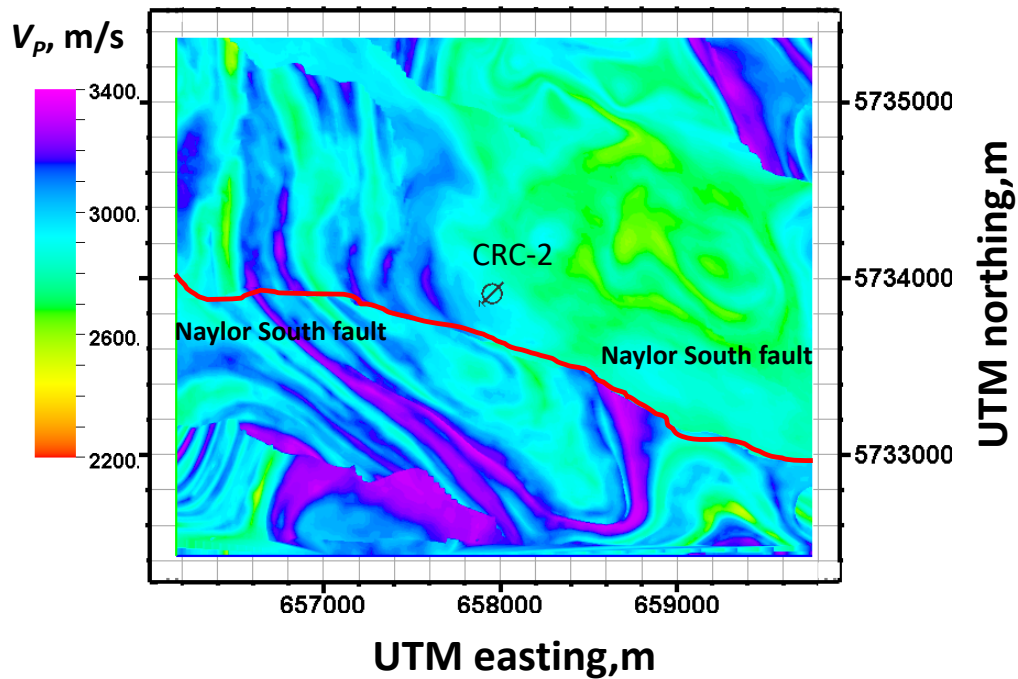
Figure 4-5: Horizontal section of the V_p model at TVDSS = 1050 m along with CRC-2 well. Curved red line denotes intersection of the Naylor South fault with this section. Reproduced after Glubokovskikh et al. (2016).

4.2.4   Monitor model

The baseline model contains velocity distributions corresponding to brine saturated rocks within the injection interval. To calculate changes of the seismic properties due to brine displacement in the pore space by the injected CO_2 we need an appropriate fluid substitution scheme. Essentially, fluid substitution consists of two steps: estimation of a bulk modulus K_{fl}^{ef} of the pore filling fluid mixture and an effective stiffness of the rock corresponding to different pore-filling fluids. Caspari et al. (2015) studied this problem in great detail for the conditions of Stage 2C using the results of reservoir modelling by Ennis-King et al. (2011). The stiffness reduction caused by the presence of CO2 in reservoir rocks was predicted by Caspari et al. [2015] from well logs and core data. Figure 4-6 shows the mean value of the acoustic

impedance variation (ΔAI) computed for the storage reservoir along the injection well, CRC-2, based on the well logs. A sharp drop (from left to right) of ΔAI at small saturations is followed by a gentle linear decline as saturation increases. Also, note that the variance (error bars) of ΔAI around the mean value (caused by the porosity and lithology variations) is relatively small. These two observations justify the assumed homogeneity of the plume. The plume thickness is estimated from the reservoir simulations.
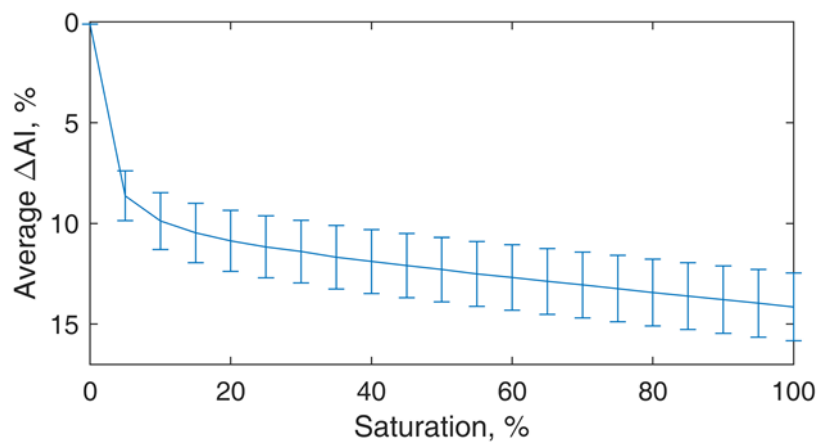
Figure 4-6: Average relative TL change of acoustic impedance ΔAI along the CRC-2 well and its standard deviation (error bar) versus CO2 saturation computed by taking into account spatial variability of rock properties, as predicted from well logs (Caspari et al. 2015). Note a sharp drop of the average impedance at around saturation of 5%.

We build the monitor model for the end of injection of 15,000 tonnes CO_2 at a rate of 110 tonnes per day. In Figure 4-7 we present a vertical section of the V_p model of the Lower Paaratte formation along with the modelled CO_2/CH_4 saturation after 135 days of injection. We limit the saturation colour scale because a magnitude of changes of the seismic properties is nearly constant for the gas saturation above 10 %.

Within the reservoir simulations interval we embed the monitor and baseline seismic models, built by Caspari et al. (2015) using a geostatistical approach. This is

done to allow for comparison with the previous seismic modelling studies. Below we give a brief description of the utilized fluid-substitution approach.
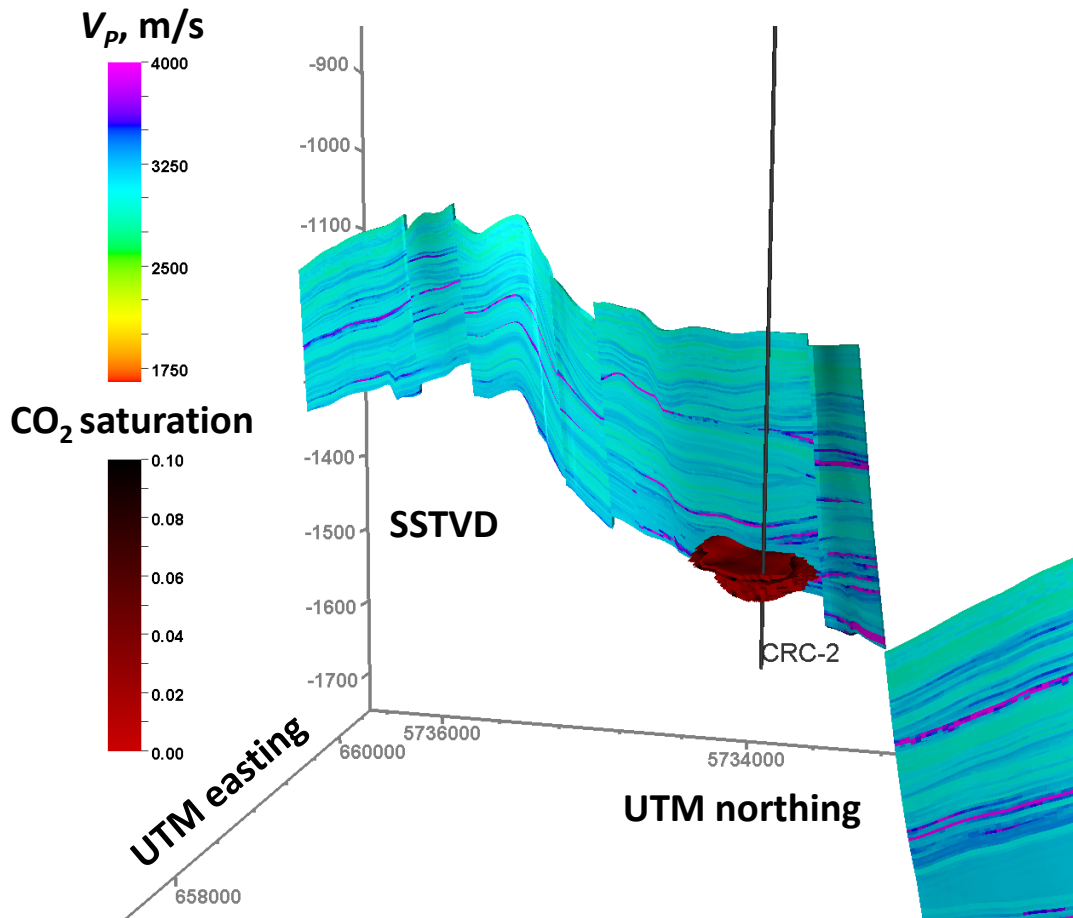
Figure 4-7: Vertical section of the V_P model of the Lower Paaratte formation along with CRC-2 well-path and modelled distribution of the CO_2 saturation. Reproduced after Glubokovskikh et al. (2016).

The distribution of CO_2/CH_4 and brine in the pore space and the frequency of the seismic wave control a proper choice for the effective fluid bulk modulus K_{fl}^{ef} (see Johnson (2001)). Previous analyses ascertained that the fluid phases are in equilibrium within the cell size (0.5 m) of the reservoir modelling grid (not resampled). Therefore, application of Wood's mixing rule to each grid cell is justified (Mavko et al. 2009):

$$K_{fl}^{ef} = \left(\frac{1}{K_{br}} + \frac{1}{K_{gas}} \right) \qquad \text{4-1}$$

44

where K_{br} and K_{gas} are the bulk moduli of brine and Buttress gas, respectively. The in-situ brine bulk modulus is calculated using the empirical formulae of Batzle and Wang (1992). We use the constitutive equation of the GERG-2004 model (Kunz et al. 2007) to find the bulk modulus of the free gas from the predicted gas composition and pressure values at each cell by the flow simulation.

Instead of the conventional Gassmann-Wood relation we calculate the effective stiffness of the rock for a given K_{fl}^{ef} using a scheme developed by Dvorkin et al. (2007) for shaley sediments. We use this model because their scheme takes into account only effective porosity which accounts only for the pore volume accessible to injected fluids. This is more realistic for our case as we expect to have shaley sediments for which effective porosity can be considerably smaller than total porosity.

So far a vertical cell size of the final seismic monitor model is determined by the resolution of the flow simulations ~ 0.5 m. At that scale the described fluid-substitution approach is justified. However, we use finite-difference time domain (FDTD) modelling code that allows fixed grid cell sizes without local grid refinement. We have to resample our model onto 2 m vertical sequence to make the seismic simulation computationally affordable. By changing the vertical cell dimension from 0.5 m to 2 m we decreased the computation time by about 20 times. The resampling smears the fine structure of the monitor model, leading to some lack of rigor in the physical grounding of the workflow. The interpolation significantly affects the time-lapse response of the part of the plume with thickness < 2 m, changing the contrast in seismic impedance at the boundaries of the gas-saturated cell and time delay between the top and bottom reflections.

4.3   Seismic forward modelling

In this study we assume that elastic isotropic medium is an adequate representation of the subsurface at the Otway site. Previous studies indicate the presence of mild (less than 10 %) azimuthal anisotropy (Pevzner, Gurevich, et al. 2011), which we disregard in the model. However, large scale apparent azimuthal anisotropy can manifest in our model due to lateral variability of the velocity and a couple of large faults embedded into the model. Similarly, we do not include any explicit polar anisotropy in our model. However, deviation of the far-offset moveout from the 2nd order NMO may naturally occur due to the horizontal layering of the model which causes apparent polar anisotropy. We also do not include seismic attenuation at this stage due to the difficulties in its implementation in FDTD simulation algorithms.

After several tests of available seismic modelling software, we concluded that an open-source FDTD modelling software Elastic SOFI3D (Bohlen et al. 2015) fits the purposes of the study. This software works in the parallel message passing interface (MPI) environment (Bohlen 2002); i.e., it allows for domain decomposition, and hence sufficiently increases the time-efficiency of computations. The input model for computations is a regular rectangular grid, thus the geocellular models need to be resampled onto this grid.

Two major conditions should be satisfied to provide stability of FDTD calculations. The first one is a maximum size dh of the grid, required for adequate spatial sampling of a wave field up to a maximum frequency component of the signal amplitude spectrum f_{max}:

$$dh \leq \frac{V_{min}}{n f_{max}} \qquad \text{4-2}$$

where n is a coefficient defined by the type of the finite difference scheme. We use the 4th order scheme with Holberg coefficients, which leads to $n = 8.32$ (Bohlen et al. 2015). The second condition arises due to the temporal discretization, known as Courant instability criterion:

$$dt \leq \frac{dh}{\sqrt{3}kV_{max}} \qquad\qquad 4\text{-}3$$

where $k = 1.185$ for the Holberg 4th order FDTD (Bohlen et al. 2015).

According to equations 4-2 and 4-3, the computational cost of 3D seismic modelling is inversely proportional to dh^4 (three spatial dimensions and time). This limits the maximum frequency of the simulations and range of seismic velocities in a model to keep the simulation times feasible. Thus, we replace the shallowest weathered sediments ($\sim$ 10 m) with the properties of the uppermost limestone formation. Since the structure and properties of the shallowest sediments control the propagation of surface waves, the ground roll in the synthetic records does not capture the corresponding features of the real Otway records. Therefore, we exclude all effects of the surface acquisition system (ground roll, air wave, surface-related multiples, and static shifts) by introducing a homogeneous layer from 50 m below the source-receiver plane to 120 m above. The properties of the layer correspond to Pt Campbell porous limestones: V_p = 1650 m/s, V_s = 700 m/s and ρ = 1.9 g/cm³. By introducing this homogeneous layer below the source-receiver plane, our modelling neglects the major cause of non-repeatability in land 4D seismic – near-surface. Because of this limitation we cannot directly use this synthetic dataset to investigate the effect of the variations in the near-surface on seismic repeatability.

The highest frequency component of the vibrator source is $\sim$ 150 Hz, yielding dh < 0.56 m. Such a level of detail significantly exceeds the expected resolution of

the real seismic sections as well as characteristic thickness of geological units in the section. We use a Ricker wavelet with a central frequency of 35 Hz ($f_{max} \sim 70$ Hz) leading to $dh \sim 1.2$ m. Even this value for dh would result in an unfeasible computational cost. Therefore we restrict the shear wave velocity to values above 1500 m/s, which is a good approximation since a velocity below 1500 m/s rarely occurs across the studied area. We ran several test simulations, which justified the use of the following parameters for the computations: 2.5 m × 2.5 m × 2 m grid size and $dt =$ 0.15 ms. To eliminate reflections from the model boundaries we surround the model with a highly attenuative perfectly matched layer from all the six sides (Bohlen et al. 2015).

We emphasize that the top side of the model has an absorbing boundary 120 m above the source-receiver plane which implies that our dataset does not have ground-roll, source or receiver ghosts due to the burial of the geophones and surface-related multiples.

The acquisition layout for the synthetic datasets approximates the real monitoring survey up to the grid size – receivers and shot points are located in the centre of the upper grid face. Finally, we perform simulations of 3003 shots twice (the baseline and monitor) for ~ 1.67 billion of the grid points and 16,667 time steps, using computational power of the Pawsey Supercomputing Centre.

4.4   Synthetic data processing – initial workflow

The usual goals of seismic data processing include the improvement of signal/noise ratio and some changes in the representation of signal aimed to improve the spatial/temporal resolution and correct the geometry of the events. Time-lapse processing aims to reduce the inevitable discrepancy between 3D datasets which are not related to temporal changes in seismic properties of the target object (Nguyen et

al. 2015). Having a synthetic 4D seismic dataset with realistic geological model and the same acquisition geometry as in the field seismic data can allow us to establish the optimal time-lapse processing flow through the careful evaluation of the effect of each routine on both time-lapse signal and noise.

In this study we present a simple processing flow developed for the synthetic dataset (yet based on the processing of the field baseline data acquired in March 2015). We also conduct a basic assessment of the detectability of the time-lapse signal using a simple noise model, leaving more sophisticated analysis for the future. A sample synthetic common shot gather is shown in Figure 4-8. We can observe a fairly complex wavefield for a synthetic dataset. As a comparison we show a raw correlated seismic gather of the field data for the same shot position (Figure 4-9). We can clearly see the correlation between some of the events of the field and synthetic datasets. The most obvious differences between these two datasets are in the presence of ambient noise and ground roll on the field data and higher frequency content of the field data.
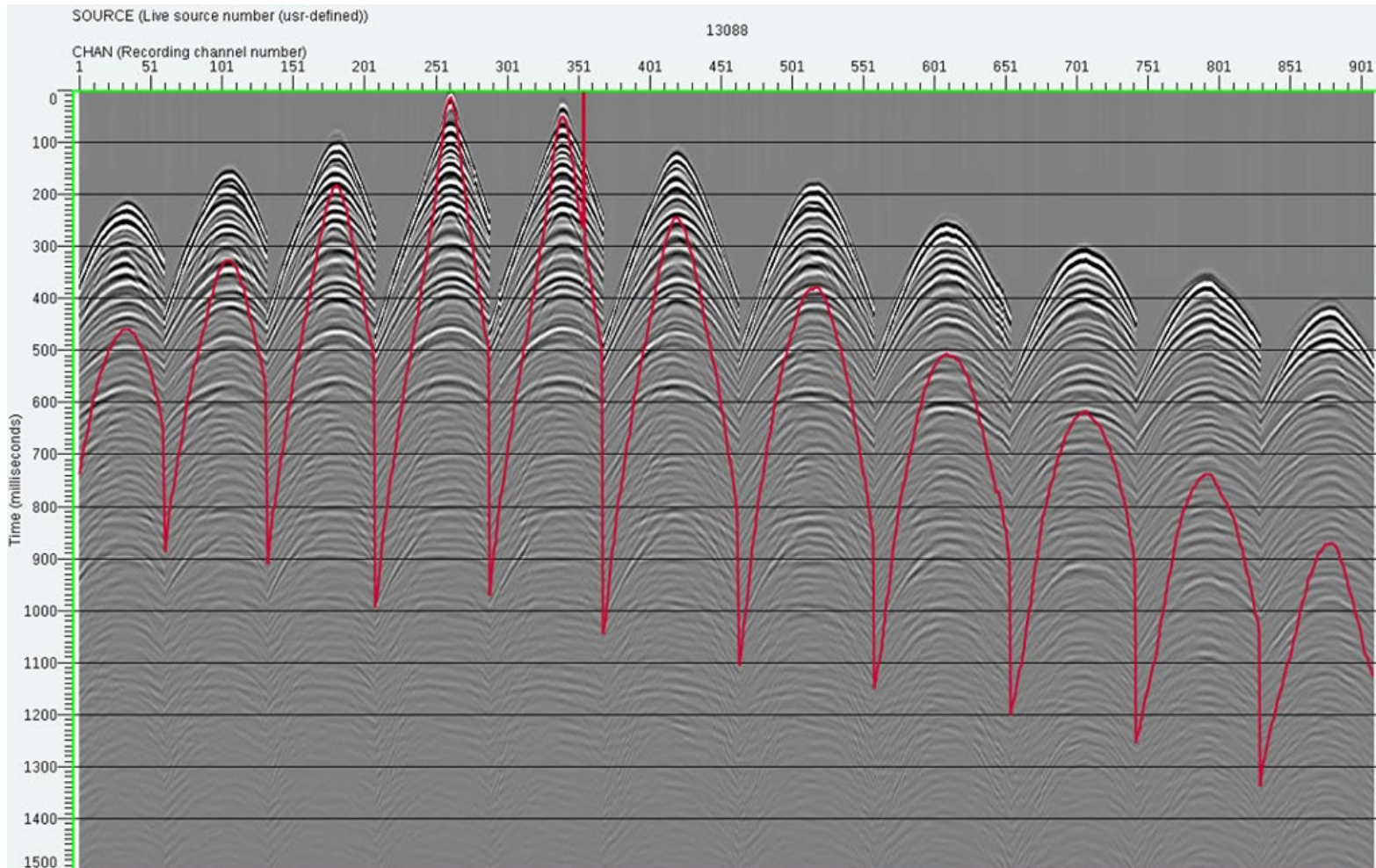
Figure 4-8. A sample common shot gather from the finite-difference simulation. The red line is the border between the areas with (below) and without (above)ground roll for the field data.
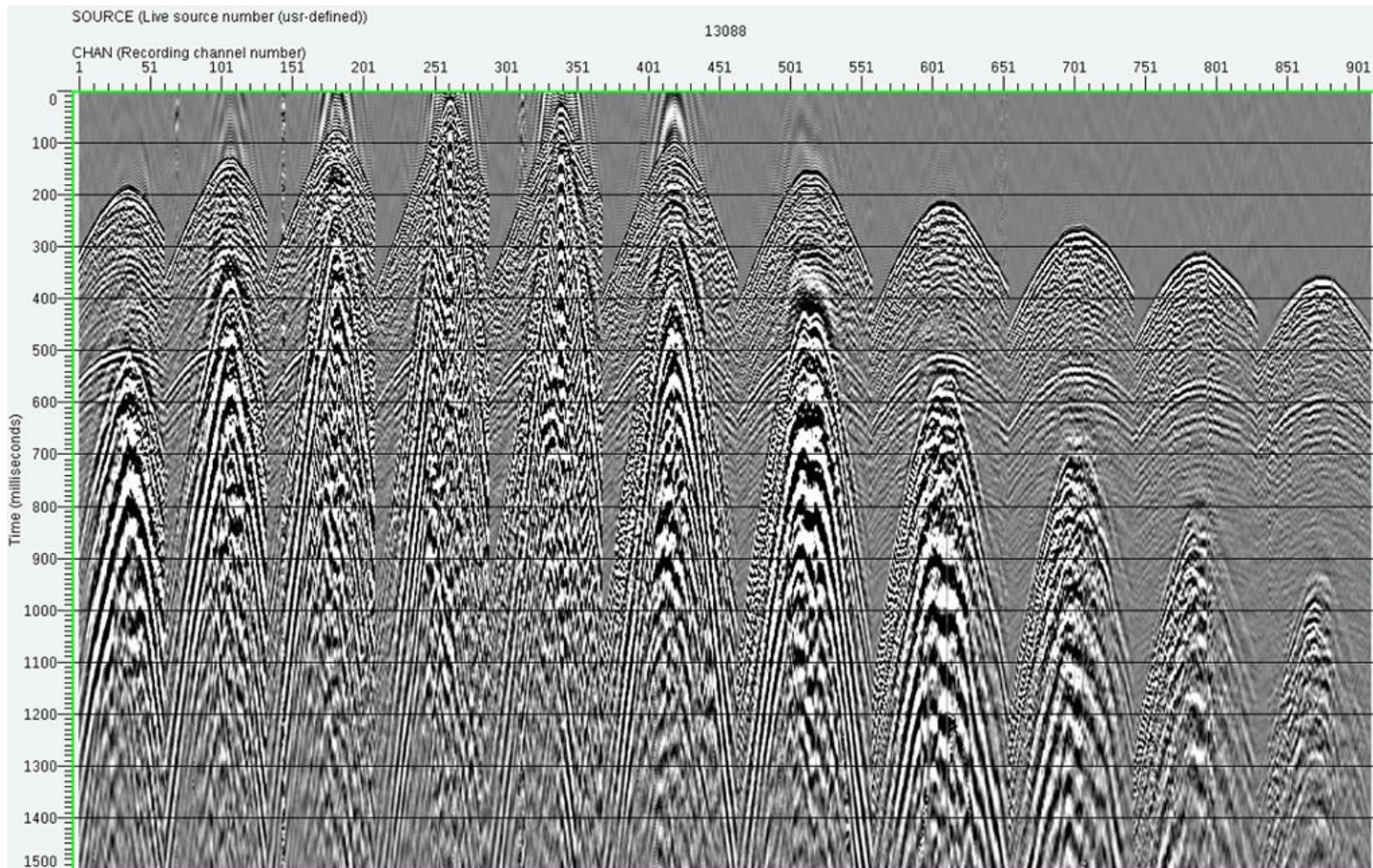
Figure 4-9. A sample correlated common shot gather from the field acquisition.

4.4.1   Data processing flow

We use a processing workflow (Table 4-1) similar to the one built for the field baseline seismic data as a starting point in the analysis of the synthetic data. This flow is applied to the baseline and monitor synthetic datasets.

The datasets exhibit prominent converted waves that may obscure the time-lapse signal. To suppress these presumably hyperbolic events we use Radon filtering.

The first iteration of velocity analysis yields velocities for the normal moveout (NMO) corrections, which we apply before the Radon filtering and remove after. Then we mute the signal in the $\tau - p$ domain with the parabolic Radon filter and subtract thereby the modelled noise from the initial data. Automatic gain control (AGC) and NMO with low velocities were applied before and removed after the filtering. We perform a second iteration of the velocity analysis on the Radon-filtered data. Then we apply amplitude corrections for spherical divergence and NMO corrections using velocities obtained upon suppression of the converted waves, and stack the data.

Comparing Figure 4-10 (without Radon filtering) and Figure 4-11 (with Radon filtering) we note steep slant stripes that are more prominent on the former figure. Radon filtering doesn't much affect the time-lapse signal on the difference between the baseline and monitor stacks (right panels of Figure 4-10 and Figure 4-11).

At the post-processing stage we pad the data in 3D with empty traces, apply a FK filter to suppress the above mentioned slanted stripes, and migrate the stacks with smoothed velocities yielded by the second iteration of velocity analysis (Figure 4-12).

Table 4-1: Preliminary processing workflow for the data simulated as part of Stage 2C of the Otway Project. Reproduced after Glubokovskikh et al. (2016).

Data Input	Seg-Y data input
Binning	Binning grid is chosen to be the same as for the field data with the bin size 7.5 m x 7.5 m
Interactive Velocity Analysis	First iteration. VA Grid – 150 m x 150 m
Preparation for Radon filtering	New headers are calculated to resort the data into the domain for radon application
Radon Filtering	Parabolic Radon filter applied in modelled noise subtraction mode to remove converted waves
Interactive Velocity Analysis	Second iteration. VA Grid – 150 m x 150 m
Bandpass Filtering	Ormsby, zero-phase, 6-10-100-150
True Amplitude Recovery	Basis for spherical divergence correction $1/(time*vel^2)$
NMO and CDP Stacking	NMO stretch muting threshold – 30 % Stacking method – mean Exponent for stack normalization – 0.5
Interval Velocity Calculation	
3D Framework Padding	Inlines 1 – 219, crosslines 1 – 266
FK Filtering	Applied to Inline gathers
Migration	Post-stack phase shift time migration
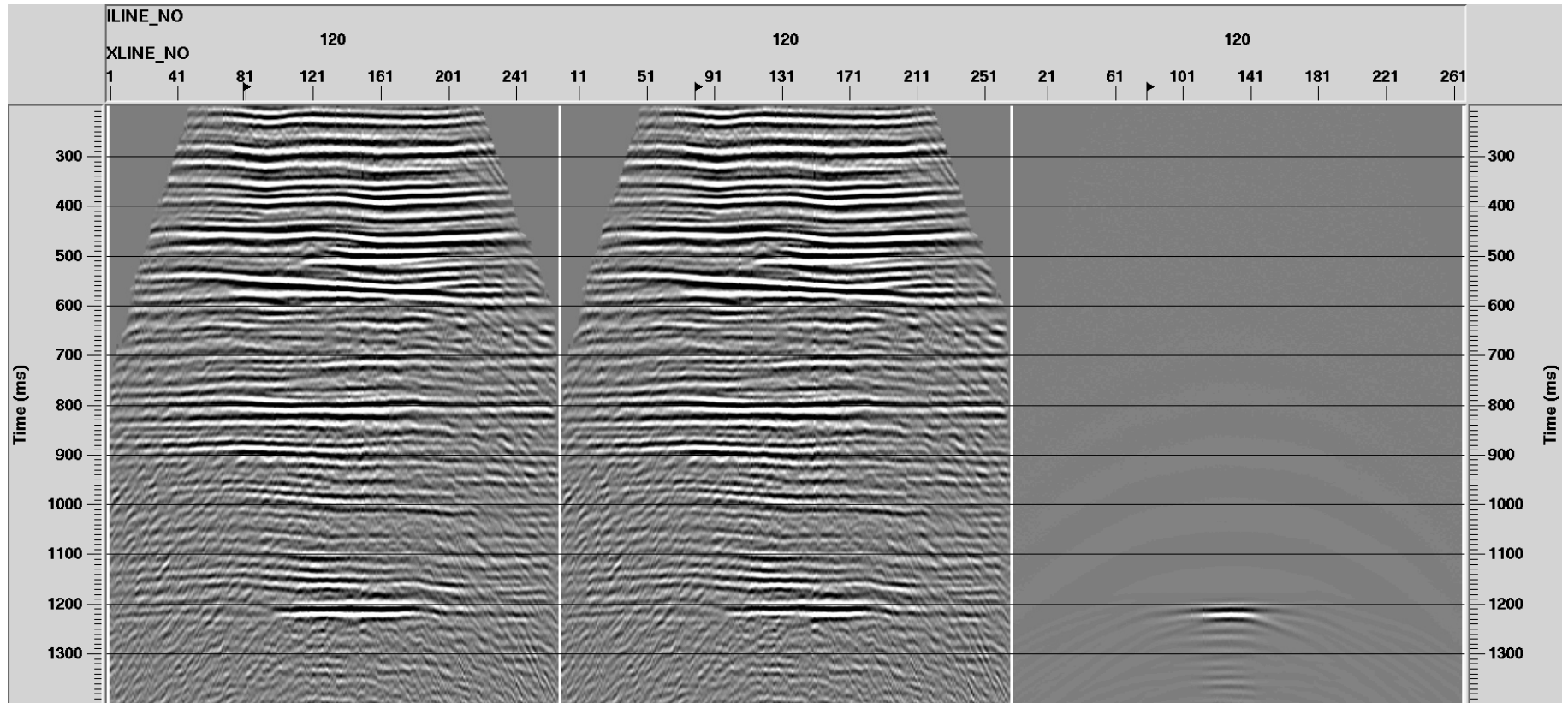
Figure 4-10: Seismic stacks without Radon filter. Sections cross over the CO2 plume along Inline 120. Left panel – M, middle panel – B, right panel – M-B. Scaling – entire screen. Reproduced after Glubokovskikh et al. (2016).
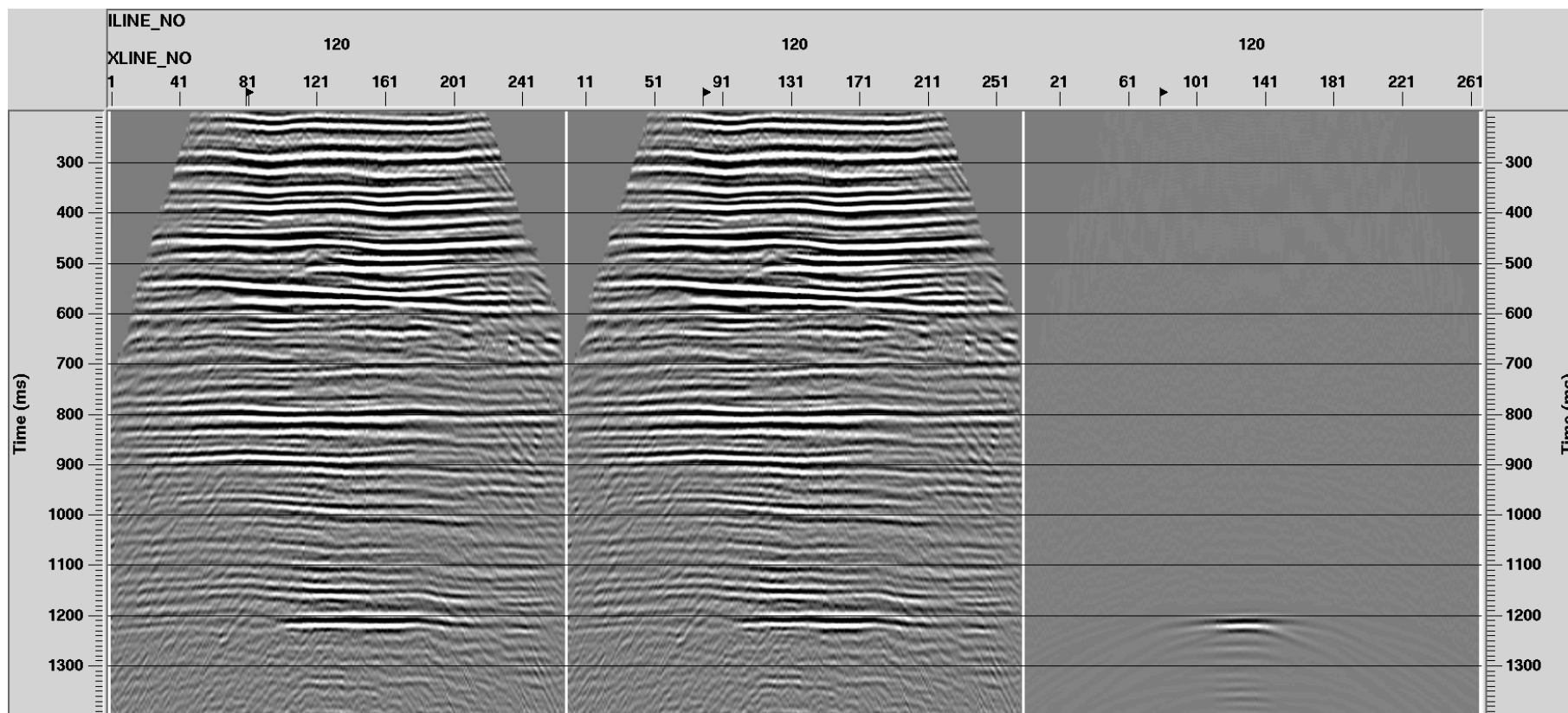
Figure 4-11: Seismic stacks with Radon filter. Sections cross over the CO_2 plume along Inline 120. Left panel – M, middle panel – B, right panel – M-B. Scaling – entire screen. Reproduced after Glubokovskikh et al. (2016).
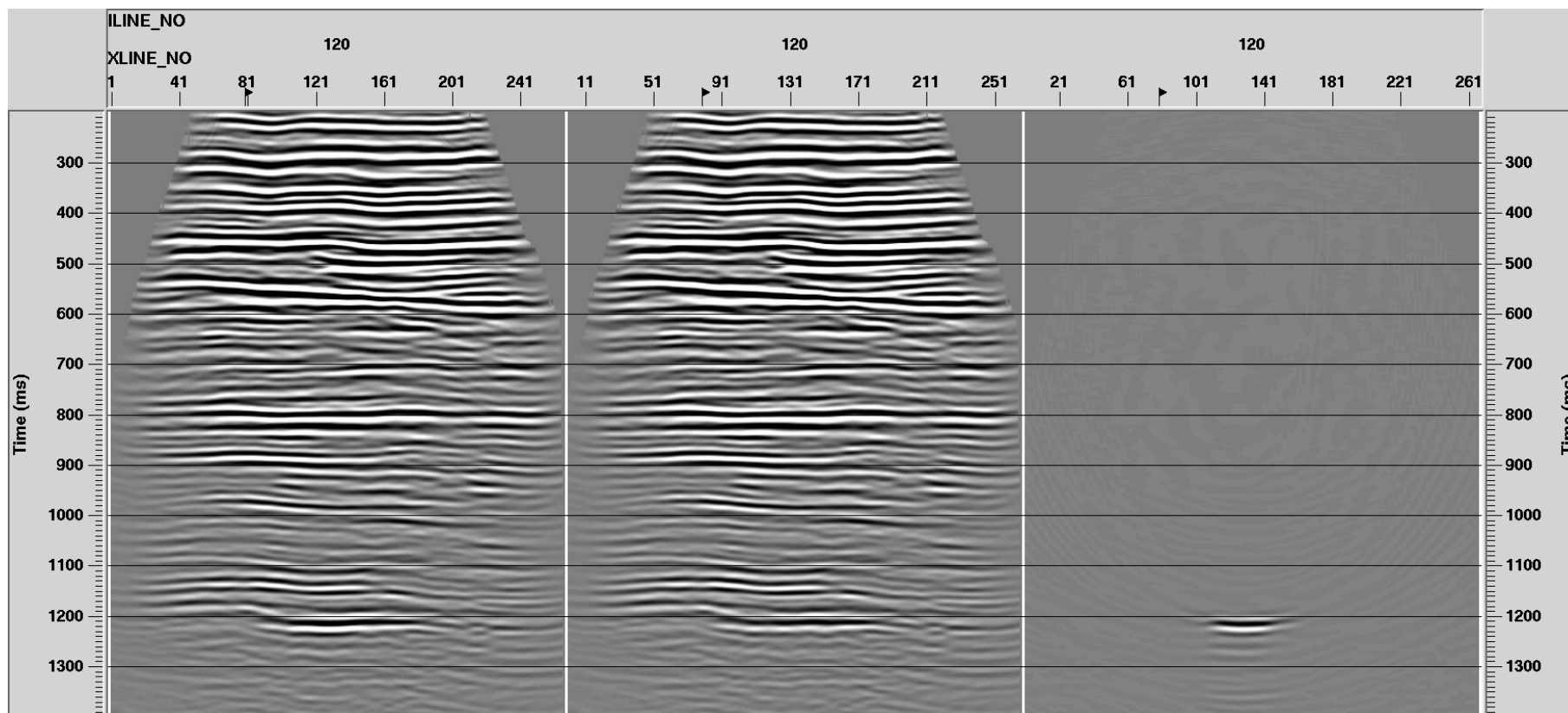
Figure 4-12: Seismic stacks with Radon filter and phase-shift post-stack time migration. Sections cross over the CO₂ plume along Inline 120. Left panel – M, middle panel – B, right panel – M-B. Scaling – entire screen. Reproduced after Glubokovskikh et al. (2016).

4.4.2   Plume detectability: adding noise to the synthetics

We add two different realizations of bandlimited random noise to the baseline and monitor synthetic datasets to get a first insight into the influence of noise on the time-lapse signal. The intensity of the synthetic noise corresponded to the intensity of the noise in the field data.

We estimate the SNR as the alpha-trimmed RMS calculated in the offset-time windows for each field seismogram: the offset range of 600–800 m and time range of 60 ms are indicated by green boxes in Figure 4-13. Obtained values of the SNR are visualised as a histogram (red line in Figure 4-15). Then we topped up the synthetic data with the bandlimited noise to reach the amount of noise calculated in the previous step (Figure 4-14). Distributions of the real and synthetic SNR differ noticeably in shape, though they have the same mean and RMS values.

We repeated the same processing sequence for the noisy synthetic data. Figure 4-16 and Figure 4-17 illustrate the results of the same processing stages as shown in Figure 4-11 and Figure 4-12, with the only difference being the pre-stack addition of bandlimited random noise. The time-lapse response of the modelled plume remains stronger than the level of the time-lapse noise, indicating that we shall still be able to detect the 4D signal from a small injection of CO_2.
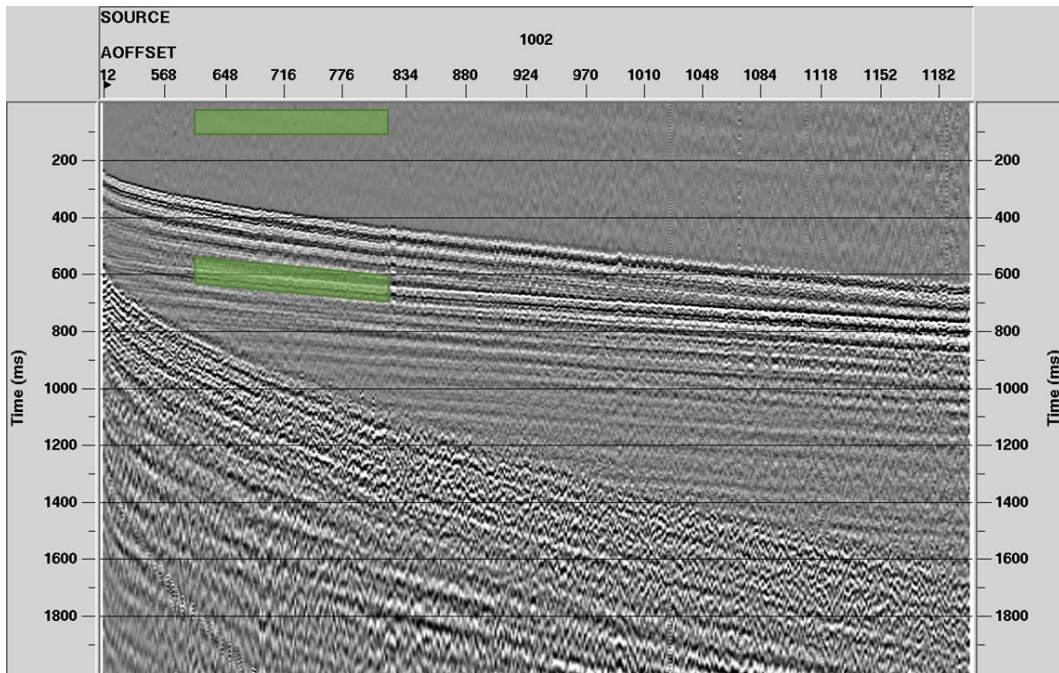
Figure 4-13: Seismic shot gather from the field B data with traces sorted via absolute value of offset. Green overlay shows windows for estimation of noise (top) and signal (bottom) levels. Reproduced after Glubokovskikh et al. (2016).
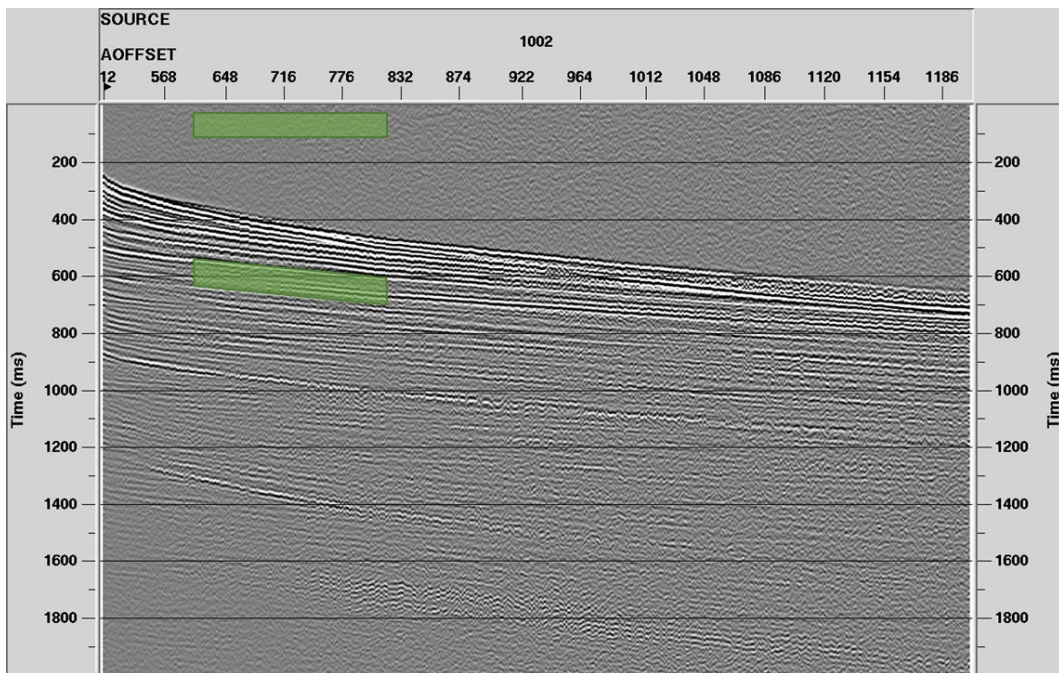
Figure 4-14: Seismic shot gather from modelling B data with traces sorted via absolute value of offset. Bandlimited noise has been added. Green overlay shows windows for estimation of noise (top) and signal (bottom) levels. Reproduced after Glubokovskikh et al. (2016).
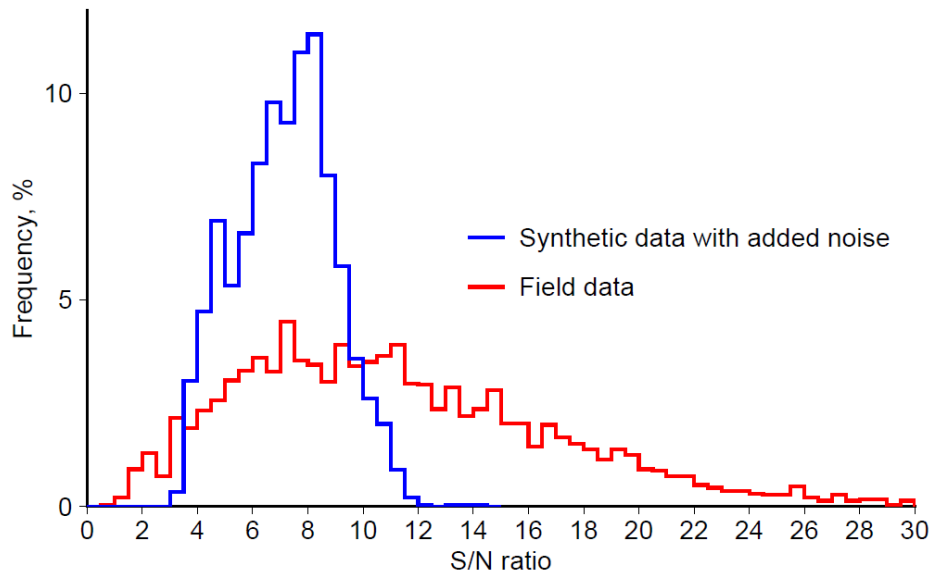
Figure 4-15: Histograms showing distribution of the SNR in the field and synthetic data. S/N values were calculated in the windows displayed in Figure 4-13 and Figure 4-14 for each shot gather. Bin size – 0.5. Reproduced after Glubokovskikh et al. (2016).

In Figure 4-18 we present a time slice of RMS amplitudes calculated between migrated noisy cubes (24 ms window centred at 1210 ms) and compare the spatial distribution of the plume thickness (superposed contours) with the time-lapse signal. The intensity of the signal is correlated with the thickness within the injection interval. Preliminary analysis shows that we can reliably recover the location of the continuous and relatively thick (> 2 m) part of the plume. We note that the distribution of the plume RMS amplitudes does not match the actual plume thickness very well. We use a phase shift post-stack time migration to produce the plume images shown in this chapter (Table 4-1). As we shall see further, this mismatch of thickness and RMS happens due to the limitations of time migrations.
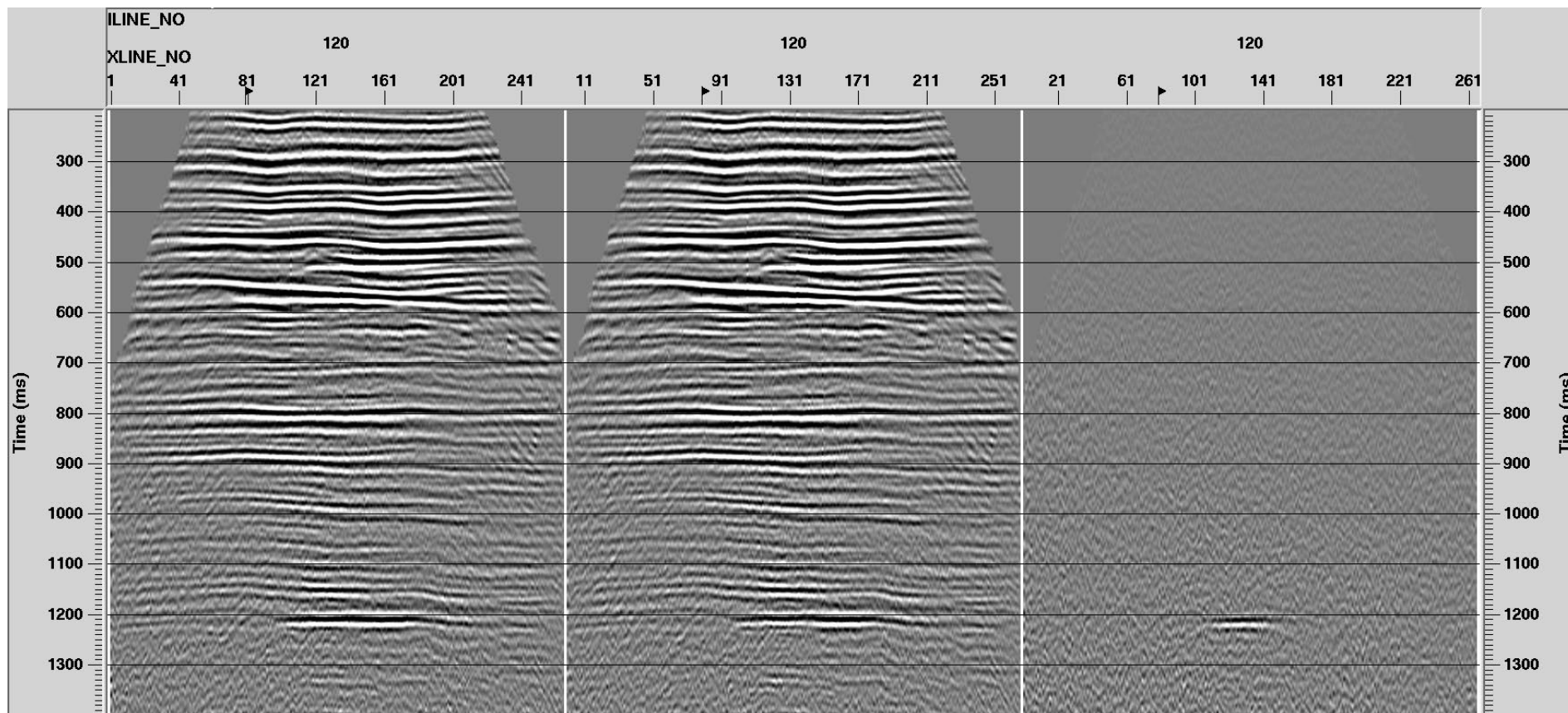
Figure 4-16: Noisy seismic stacks with Radon filter. Sections cross over the CO_2 plume along Inline 120. Left panel – M, middle panel – B, right panel – M-B. Scaling – entire screen. Reproduced after Glubokovskikh et al. (2016).
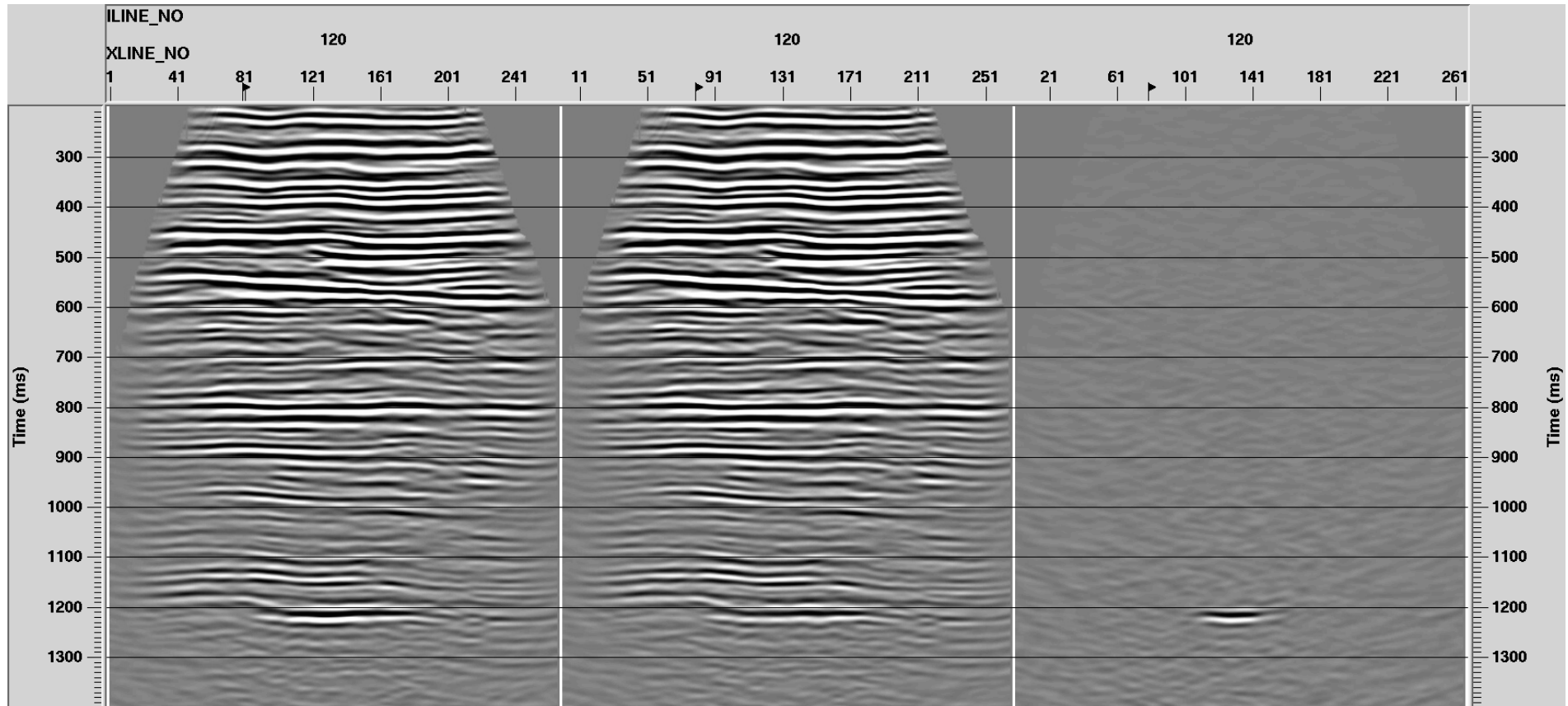
Figure 4-17: Noisy seismic stacks with Radon filter and phase-shift post-stack time migration. Sections cross over the CO$_2$ plume along Inline 120. Left panel – M, middle panel – B, right panel – M-B. Scaling – entire screen. Reproduced after Glubokovskikh et al. (2016).
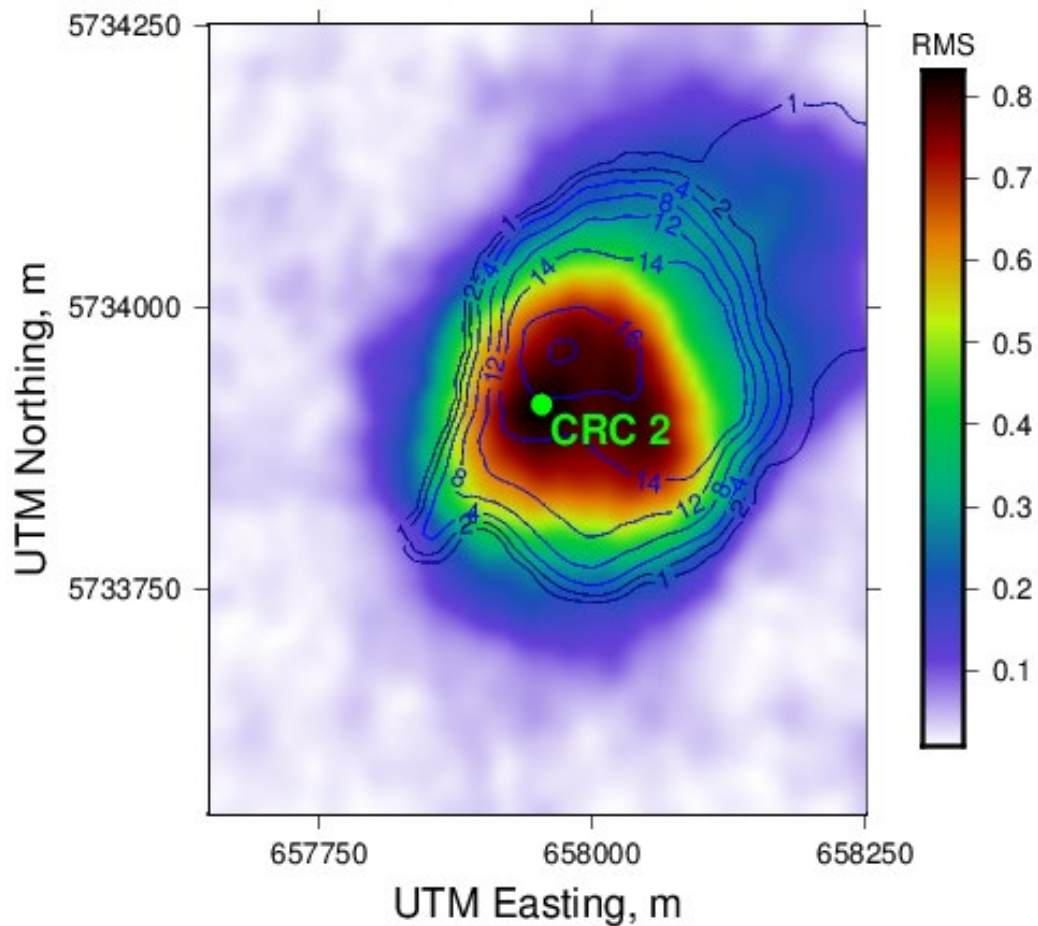
Figure 4-18: Map of RMS amplitudes calculated from the difference between noise-contaminated migrated seismic cubes. RMS amplitude is calculated in 24 ms window centred at 1210 ms. Blue contours represent plume thickness obtained in the reservoir simulation. Modified after Glubokovskikh et al. (2016).

4.5   Conclusions

This chapter presented a thorough synthetic study of the Stage 2C monitoring programme. Unlike previous seismic feasibility studies, we kept simplifying assumptions to a minimum when building the Otway seismic model, aiming to put the CO_2 plume into adequate seismic imaging conditions. Such an "uncompromising" approach became feasible due to the following advantages of Stage 2C of the Otway Project:

- An abundance of geophysical and geological information about the site;
- access to modern, high-performance computing facilities;

62

- the relatively small size of the site.

In order to populate the geological inter-well space, we developed a geostatistical workflow that preserved subtle geological features that would have been lost if a deterministic interpolation were employed instead. Test of the seismic simulations showed that realisations of ρ, V_P, and V_S must be consistent with one another in geostatistical simulations, otherwise seismograms get contaminated by unrealistic intense artificial scattering. Inadequate resampling of the geocellular model to the computational grid may be another source of strong artificial scattering.

The small size of the area was the key to successful seismic simulation. It allowed us to build a detailed model with a grid size suitable for sampling of the thin plume and for adequate propagation of the waves of seismic frequency range. On the other hand, available supercomputing resources allowed us to simulate an elastic 4D dataset for the detailed model consuming ~ 5 million of CPU hours. We believe that rapid development of supercomputing technologies (both algorithms and hardware) will reduce the significance of the first point above and enable routine use of the proposed workflow.

Pevzner, Shulakova, et al. (2010) has shown that ambient noise is one of the major contributors to the repeatability of the time-lapse seismic data for the site. We use this as a justification to simulate the time-lapse noise by adding the random band-limited noise to the synthetic seismograms. However, analysis of the synthetics suggests that anticipated intensity of the time-lapse signal is rather high if only this type of non-coherent noise is present.

As we show later, correlated noise is a big issue in processing of our field data because this noise is often of high energy and not exactly repeatable between baseline and monitor surveys. In our synthetic data sheared waves, converted waves and inter-

bed multiples represent correlated noise but these types of noise are perfectly repeatable between the baseline and monitor modelling scenarios (at least for the part of the model above the simulated injection) and can be eliminated via direct subtraction between monitor and baseline surveys. As our modelling does not feature neither vintage-dependent ground roll nor any anthropogenic noises (such as vehicles) we leave the issues of correlated noise for Section 6.2.

The seismic image of the plume is in the correct location but extends further in the west/south west direction compared to the contour overlay of the plume's thickness. We speculate that this could be the result of the limitations of the imaging technique used; CDP summation followed by post-stack time migration can smear sharp edges of the 3D objects. However, we may conclude that the resolution of the seismic data and the recovered velocity model provide data quality that allows us to locate the parts of the CO_2 plume with thickness over 5 m.

In the following chapter we show how we use the simulated synthetics to optimise the processing workflow for our field data.

Chapter 5.

Optimization of the processing flow using synthetic data

In this chapter we illustrate the use of the 4D synthetics to tune in the workflow for 4D field surface seismic data to produce images suitable for quantitative interpretation and better plume definition/location. We revisit the processing sequence and further investigate how different processing routines affect time-lapse signal. The workflow is optimised so as to preserve the time-lapse signal as far as possible while minimising processing-induced noise. We also analyse the effects of imaging on the lateral positioning of the time-lapse image of the plume.

To avoid unnecessary complications, we use the noise-free data throughout this chapter, leaving the discussion of time-lapse noise and repeatability to Chapter 6.

5.1   Effect of processing procedures on 4D signal

Once we have verified the detectability of the plume in the presence of noise and built an initial processing workflow for the field data, we investigate how commonly used processing algorithms affect the final appearance of the plume. The post-stack migrated images produced by the express processing workflow for synthetics (see Section 4.4) are shown in Figure 5-1 and Figure 5-2. Figure 5-1 shows essentially the same data as shown in Figure 4-12 along crossline 124, while Figure 5-2 shows an RMS amplitude map of the monitor and baseline difference computed for the target interval using the same noise-free dataset. Figure 5-2 differs from Figure 4-12 only by the absence of random noise and a different colour palette. This section illustrates ground roll removal, AGC and deconvolution affect the plume images.
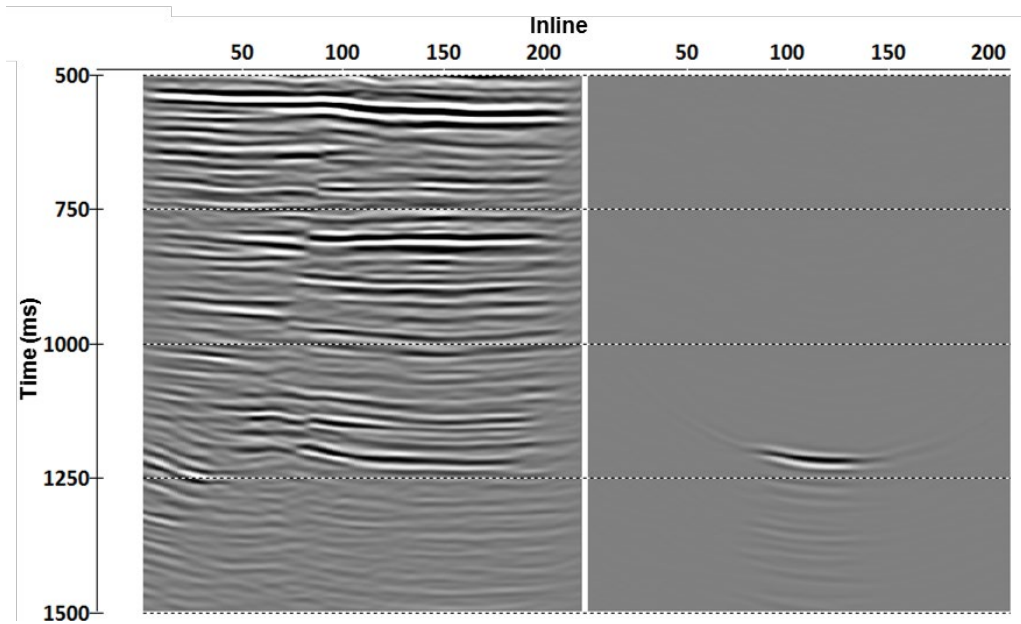
Figure 5-1: Crossline 124 through the final image produced by the express-processing workflow for noise-free data. B – left panel, M-B – right panel.
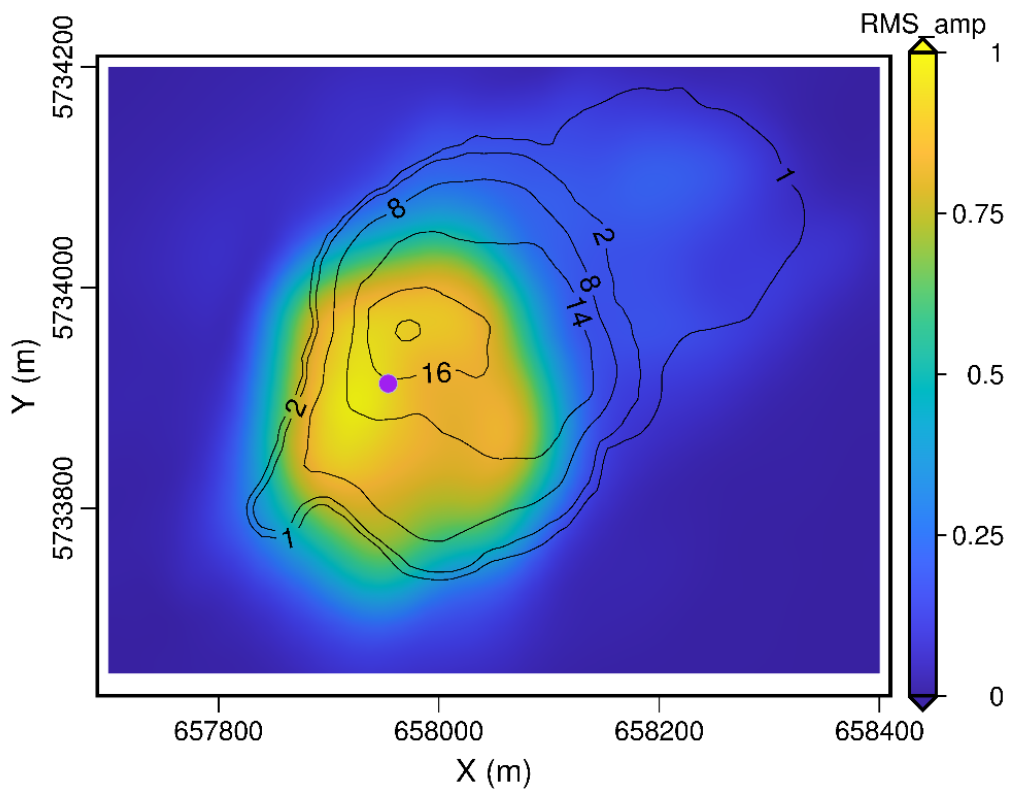
Figure 5-2: Map of RMS amplitudes calculated from the difference between noise-free final seismic images (M-B). RMS amplitude is calculated in 44 ms window centred at 1210 ms. Black contours – plume thickness from reservoir simulation.

5.1.1 Ground roll removal

As it will be shown in the next chapter, ground roll is an intense time-lapse noise at the Otway site, and therefore its removal is an essential component of the processing of field data. To analyse the importance of ground roll removal, it is important to check whether there is a significant time-lapse target signal inside and/or outside of the area covered with ground roll. We did not simulate ground roll due to: (1) the lack of detailed knowledge of the near-surface velocity field and (2) low velocities of the ground roll that would make computations prohibitively time-consuming (cell size becomes too small). Thus we estimate the first arrival times of ground roll from the baseline field survey (see the red line in Figure 4-8) and use these times to separate the synthetic data into two parts: far-offset part after bottom mute (Figure 5-3 and Figure 5-4) and near-offset part after top mute (Figure 5-5 and Figure 5-6). We stack and migrate both of these datasets and observe the plume image for both muting scenarios.

We clearly observe 4D signal for both near- and far-offset stacks although the RMS amplitudes of the near stack are about 3 times higher than for the far-offset stack as can be seen from the comparison of Figure 5-4 and Figure 5-6. As expected, we observe a general drop of RMS amplitudes for both mutes compared to the initial image shown in Figure 5-2.

We conclude that we might expect detectable 4D signal on both near- and far-offsets of the field data. In addition, we see that most of the 4D signal will be covered by ground roll. This emphasizes the importance of careful ground roll suppression such that the reflections obscured by ground roll are preserved.
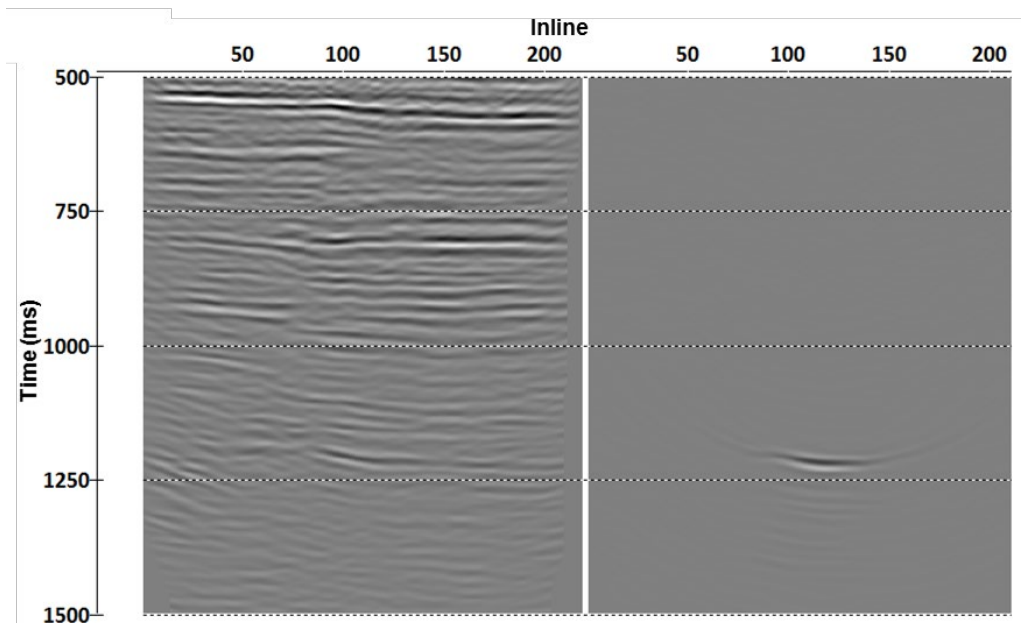
Figure 5-3: Crossline 124 through the migrated image of far offsets (bottom mute applied before stacking). B – left panel, M-B – right panel.
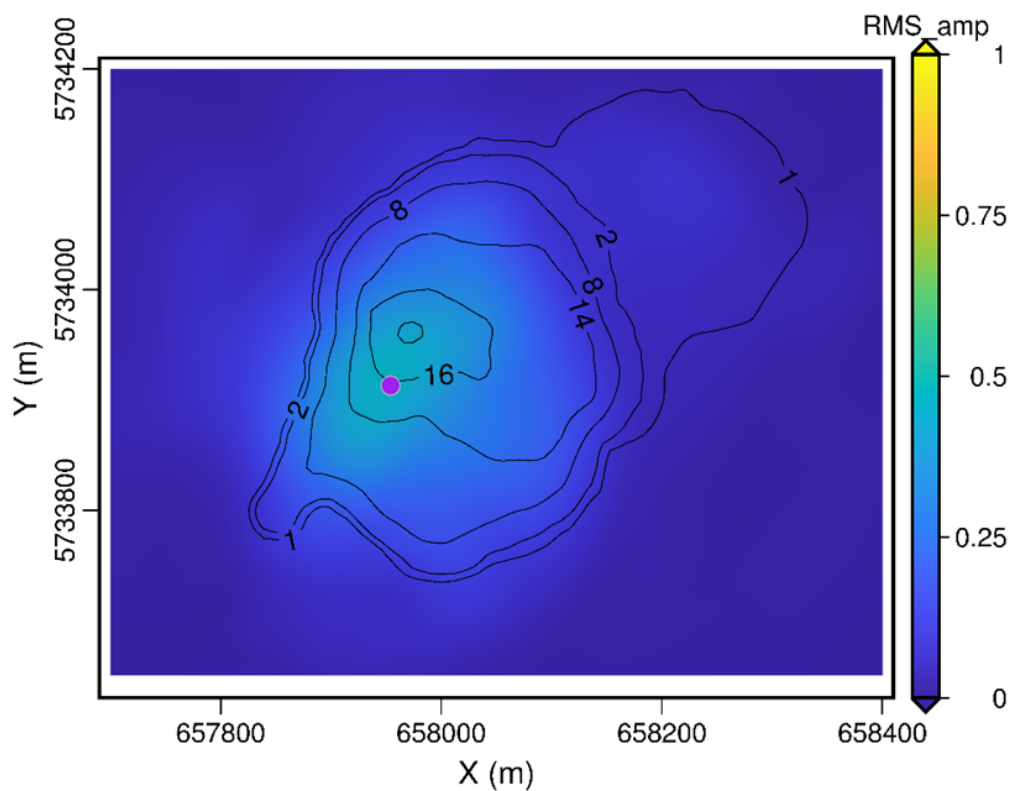
Figure 5-4: Map of RMS amplitudes for M-B for far offsets (bottom mute applied before stacking). RMS amplitude is calculated in 44 ms window centered at 1210 ms. Black contours – plume thickness.
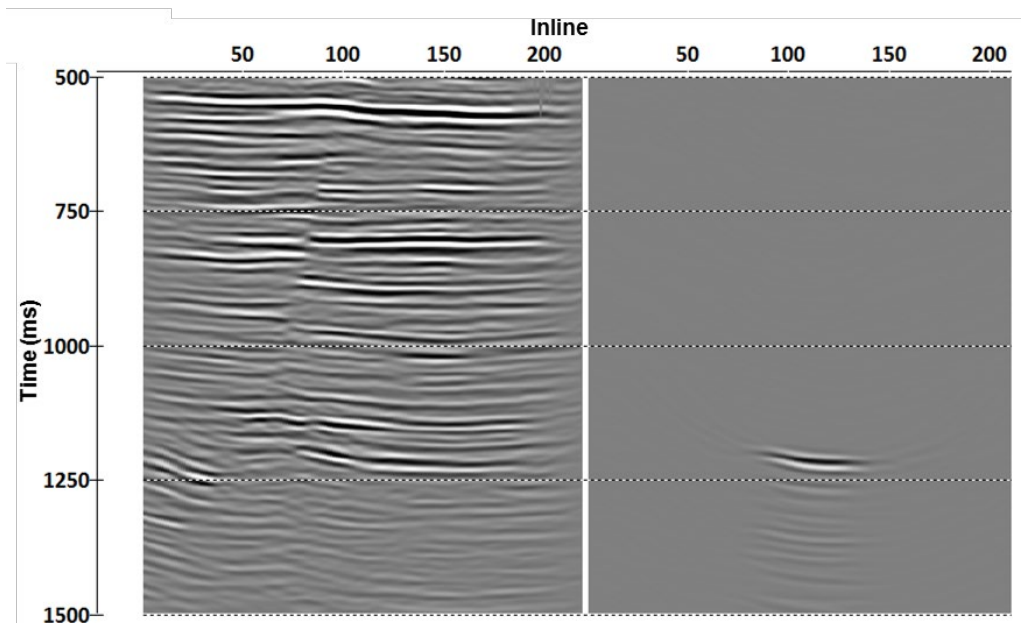
Figure 5-5: Crossline 124 through the migrated image of near offsets (top mute applied before stacking). B – left panel, M-B – right panel.
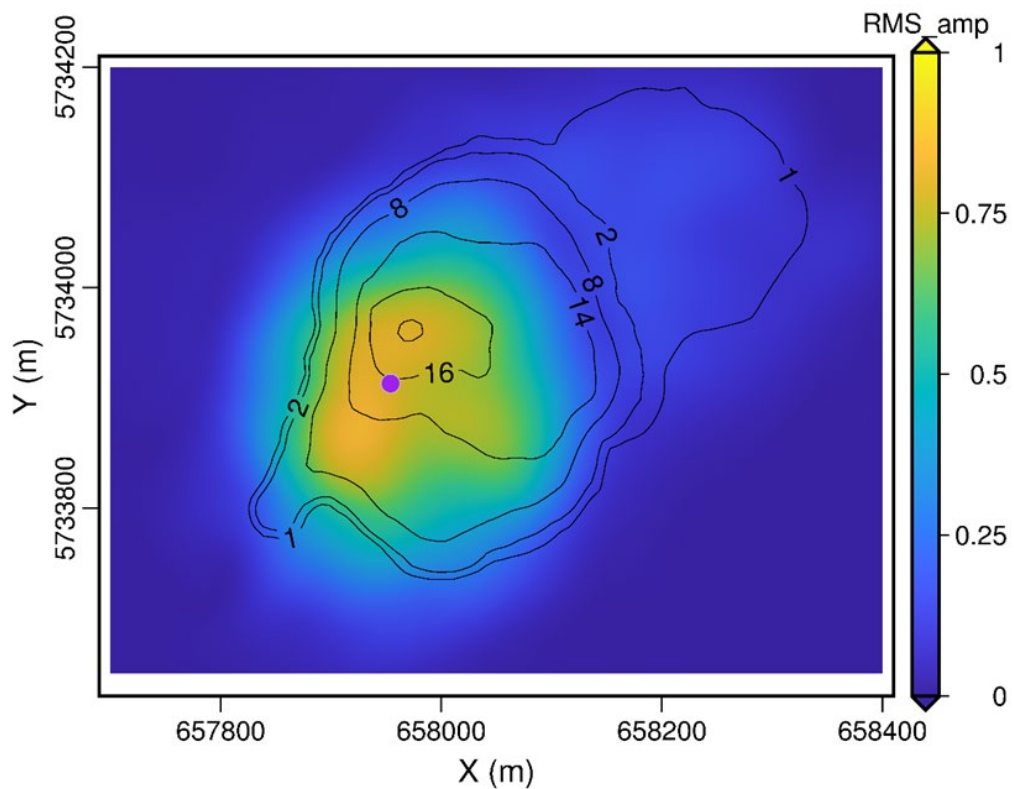
Figure 5-6: Map of RMS amplitudes for M-B for near offsets (top mute applied before stacking). RMS amplitude is calculated in 44 ms window centered at 1210 ms. Black contours – plume thickness.

We have a limited range of offsets (due to the way the survey was designed) and AVO was not considered as something we could rely upon. As such no modelling is presented in the thesis, however the field gathers do show some AVO effect as shown in Chapter 6. The detailed AVO modelling for this project, which shows the time-lapse signal at various offsets, can be found in Caspari et al. (2015).

5.1.2   Automatic gain control

AGC is frequently assumed to be incompatible with true-amplitude processing. However, it may be necessary to apply AGC to the actual field 4D data to improve the SNR. Application of AGC in a long window (say 500 ms) reduces amplitude distortion along a trace for the reflections that are close in time, but trace-to-trace amplitude relations (and thus AVO-effect) are still compromised. If a post-stack image is the required output, we expect that a long-window AGC before stacking should preserve zero-offset reflectivity and suppress residual noise.

We check this hypothesis by applying AGC in 500 ms window to the synthetic traces before stacking (Figure 5-7 and Figure 5-8). Comparison of Figure 5-2 and Figure 5-8 shows that the general relationship between the plume thickness and RMS amplitudes is similar for both figures, though AGC introduces some changes into the distribution of RMS amplitudes in space. Figure 5-9 shows a crossplot of the data from Figure 5-2 (noAGC stack – x axis) and Figure 5-8 (AGC stack – y axis). We can see that the general trend in the data is preserved – the cloud of blue points quite well follows the $y = x$ relationship (red line). That is, the high amplitudes of AGC data correspond to the high amplitudes of non AGC data and the low amplitudes of AGC data correspond to the low amplitudes of non AGC data. However, AGC introduced a slight deviation of the RMS amplitudes (blue dots) from y=x curve (red line) both in

trend and scatter. A dense cloud of the points in the low RMS value range corresponds to the 4D noise while the main trend of the higher RMS – to the 4D signal.

We suggest that the field data processing benefits from the AGC if the desired outcome is full-offset stacked images suitable for structural and quantitative interpretation (QI) purposes. To minimise data-driven character of AGC yet to preserve its noise suppression benefits, for safety, AGC scalers can be computed not for each sample but for a window shift of say 100 ms and then interpolated in between. For additional safety the AGC scalers same (say derived from the Baseline survey) can be applied to all the vintages to eliminate the dependence of these scalers on the time-lapse noise and signal. Of course, if noise can be removed successfully on all offsets (which is often impossible for land data) then AGC is not required.
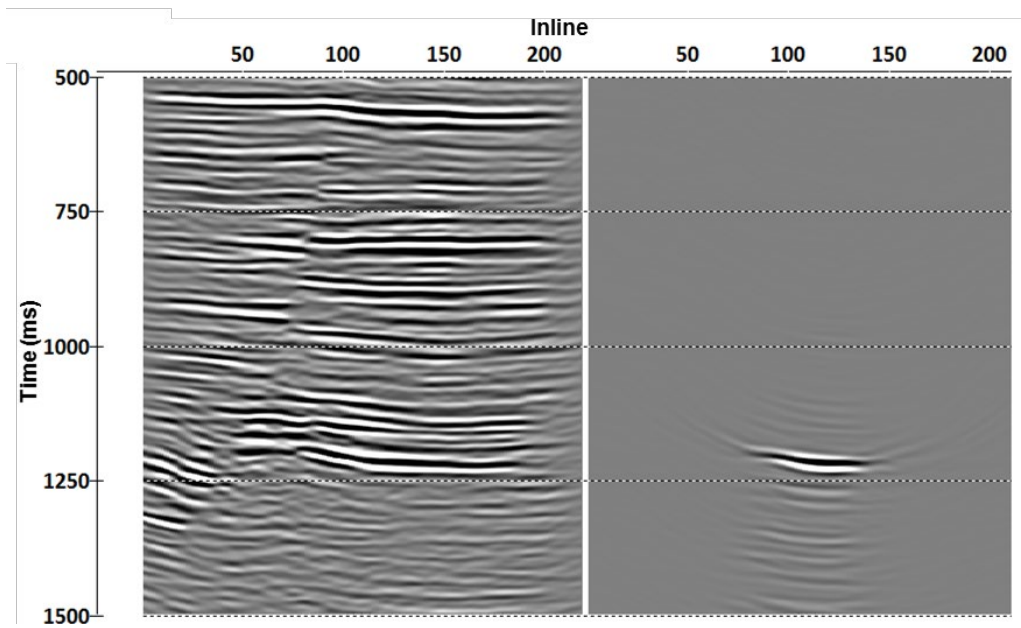
Figure 5-7: Crossline 124 through the migrated image with 500 ms AGC applied before stacking. B – left panel, M-B – right panel.
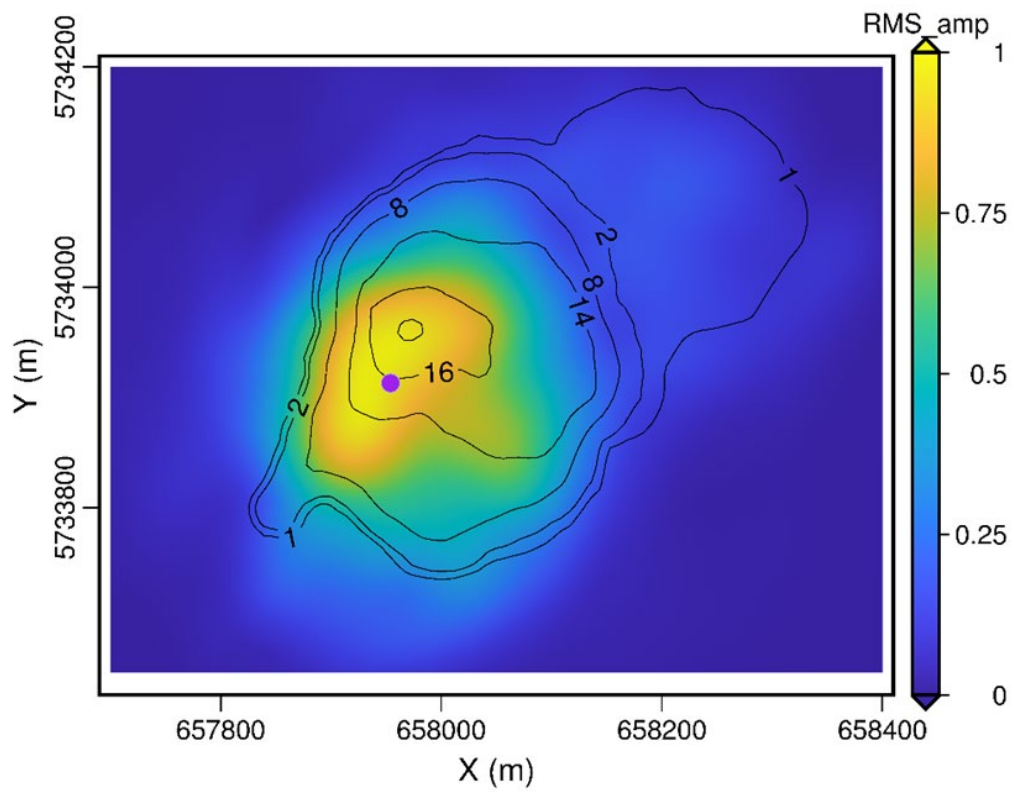
Figure 5-8: Map of RMS amplitudes for M-B (AGC in 500 ms window applied before stacking). RMS amplitude is calculated in 44 ms window centered at 1210 ms. Black contours – plume thickness.
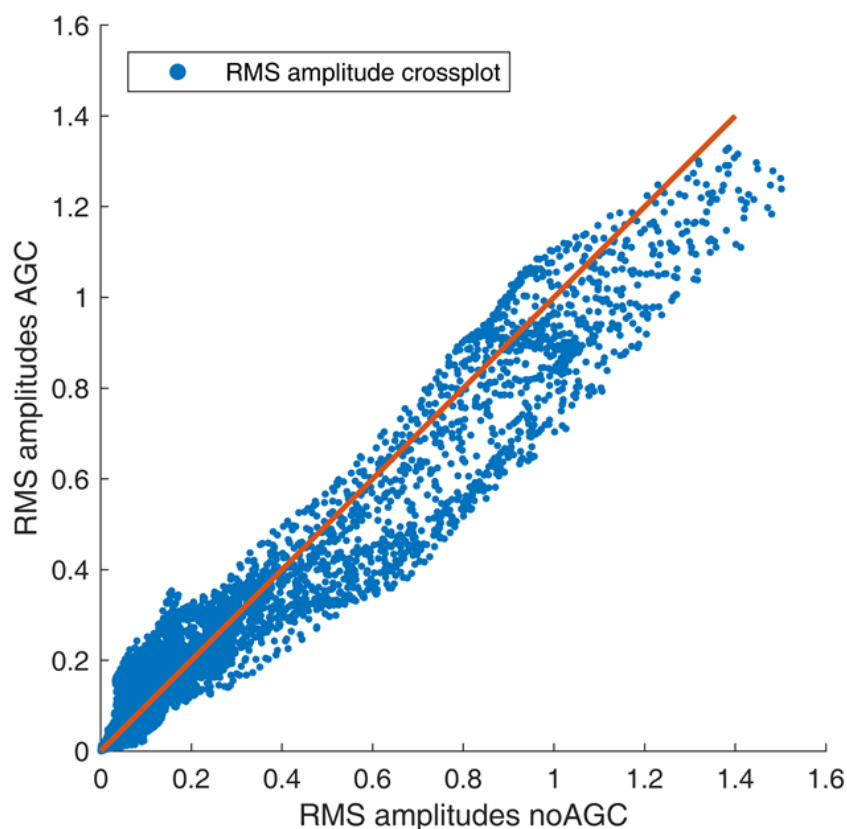
Figure 5-9. Crossplot of the RMS amplitudes of the plume computed from the data shown in Figure 5-2 (noAGC stack – x axis) and Figure 5-8 (AGC stack – y axis). The red line follows equation $y = x$.

5.1.3   Deconvolution and post-stack migration

We shall now optimize deconvolution and imaging. These two procedures are core components of any processing workflow and control the quality of the seismic image: its vertical and lateral resolution and consistency of the amplitudes. While the importance of these procedures is well known, it is not obvious how one can quantify their impact in terms of signal and noise. A straightforward approach examines the similarity of a synthetic seismic response computed using well logs at a well location and the actual seismic trace. Essentially, we use the quality of well-ties for acoustic inversion as a quality measure of the performance of deconvolution and migration.

Deconvolution affects the quality of well-ties and seismic inversions because it changes the shape of the wavelet. In onshore field seismic data, a source signature is normally not known so we apply statistical spiking deconvolution, which aims to collapse the actual wavelet to a spike. After a number of tests, we chose to apply zero-phase spiking deconvolution filters with 120 ms length and 0.1 % noise level. The filters are computed and applied independently for each trace. The true model used to produce synthetic data has no lateral variations near the acquisition plane, and hence we could not test surface-consistent deconvolution and instead focus on spiking deconvolution. Even though we test spiking deconvolution on the synthetics due to inability to test surface-consistent deconvolution, we do not use spiking deconvolution when processing the field data and use surface-consistent deconvolution instead as demonstrated in Chapter 6.

There are many approaches to implementing post-stack time migration (Bancroft 2007). Most of them are controlled by the migration aperture and initial velocity model. Apart from these two parameters, implementation of migration algorithms in a given processing software package requires more parameters that are specific to a given migration implementation. We compare two industry standard approaches: Kirchhoff and finite-difference time migrations, both with and without the deconvolution.

Figure 5-10 shows maximum correlation coefficients estimated between a processed trace and a synthetic trace obtained from the well-tie. The synthetic trace in this case is produced by convolution of the extracted wavelet with the reflectivity computed from the true model of elastic properties at a virtual well location. The left column is for the well-tie in the injection interval from 1100–1230 ms while the right column is for the entire trace well-tie. The top row shows the correlation coefficients

for CRC-2 well and the bottom row the correlation coefficients for the location 15 inlines to the north and 15 crosslines to the east from CRC-2 location. The colours indicate which migration has been used and whether deconvolution has been applied or not. We clearly see that the quality of the well-tie decreases after the application of deconvolution.

One reason for this behaviour is that deconvolution attempts to flatten the data spectrum by boosting the energy of the signal as well as of the noise. Even though we use "noise-free" data throughout this chapter and we do not expect much boosting of the ambient noise after deconvolution, still spiking deconvolution introduces a small amount of random noise into the estimation of the deconvolution operator to stabilize the solution of the deconvolution. As the wavelet is bandlimited, the SNR (after addition of this white noise) at the lower and higher frequencies of the wavelet spectrum is lower than the SNR around the central frequency. The SNR at the edges reduces after the application of the spiking deconvolution and the data get contaminated by the boosted noise. Another reason for the reduced quality of the well-tie is the complexity of the wavefield which contains reverberations of the p-waves as well as converted waves. However, the well-tie is done using a simple p-wave convolutional model which does not account for any of these effects.

The choice of the migration algorithm shows virtually no effect on the well correlation in the interval of interest (left column). However, for the entire trace, the finite-difference migration does a better job in amplitude restoration compared to Kirchhoff, although there is potential to improve the result by further adjusting aperture and scaling parameters in the Kirchhoff migration.
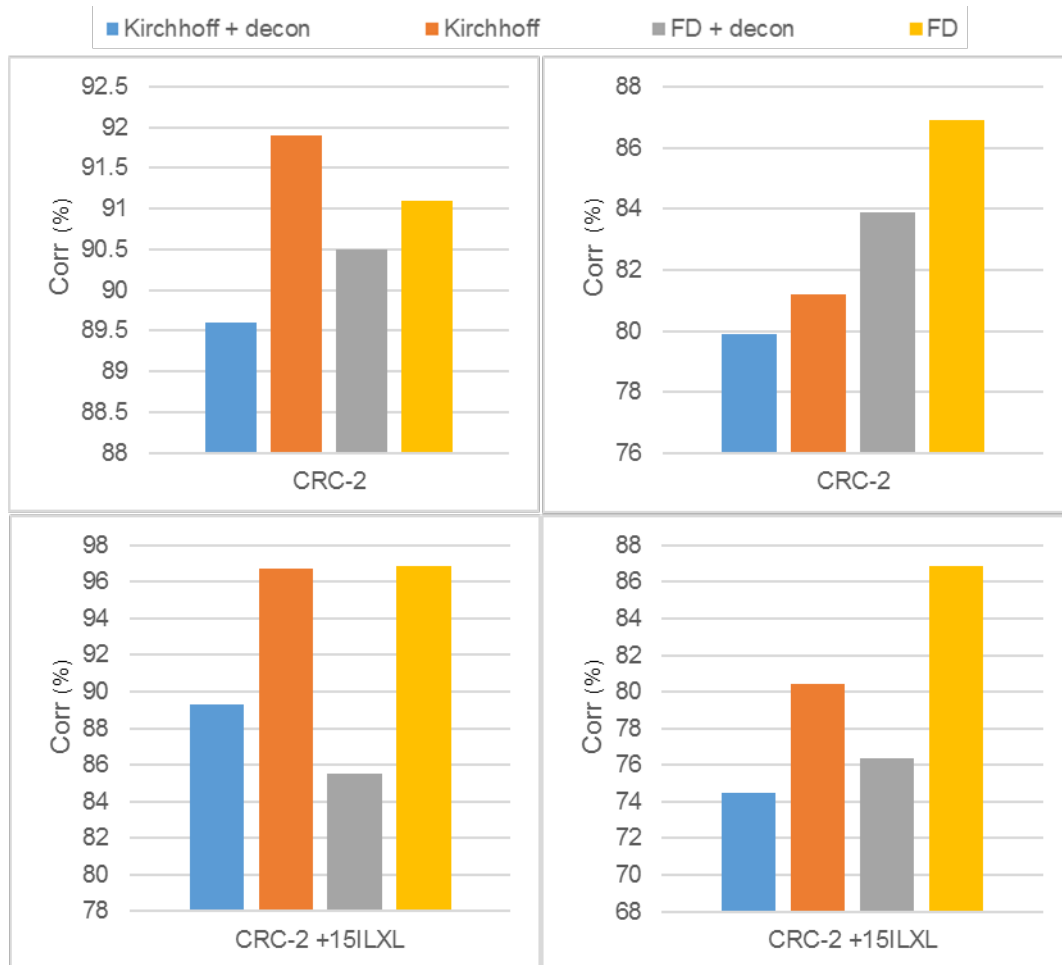
Figure 5-10: Correlation coefficient obtained after seismic-to-well ties for synthetic B dataset for 4 different versions of the workflow (see legend at the top). Top row – well-tie for CRC-2 well, bottom row – 15 inlines to the north and 15 crosslines to the east from CRC-2. Left column – well-tie for 1100 – 1230 ms window, right column – for the entire trace.

While the correlation may not be affected severely by the deconvolution (as little as 0.5% for some processing graphs), trace-based deconvolution distorts the extracted optimal wavelets and they vary significantly between the wells, thus compromising acoustic inversion. To see this effect, we compare the influence of deconvolution on amplitudes by running acoustic inversion of the baseline synthetics after the well-tie. The left panel of Figure 5-11 shows acoustic impedance of the baseline model AI_{MB} along an inline cutting through CRC-2 well. The middle and

right panels show relative errors of restoration of actual acoustic impedance achieved by acoustic inversion for the cases without and with deconvolution, respectively. Relative error RE is computed as:

$$RE = \left| \frac{AI_{SB} - AI_{MB}}{AI_{MB}} \right| \times 100 \qquad\qquad 5\text{-}1$$

where AI_{SB} is the acoustic impedance produced by the inversion. An abundance of purple colour in the right panel clearly shows that spiking deconvolution degrades the performance of the inversion.

We conclude that the choice of the post-stack time migration algorithm does not introduce much error, as confirmed by the quality of well-tie. On the contrary, the trace-based spiking deconvolution might degrade the quality of the well-tie even for the noise-free synthetic data, and thus should be avoided.
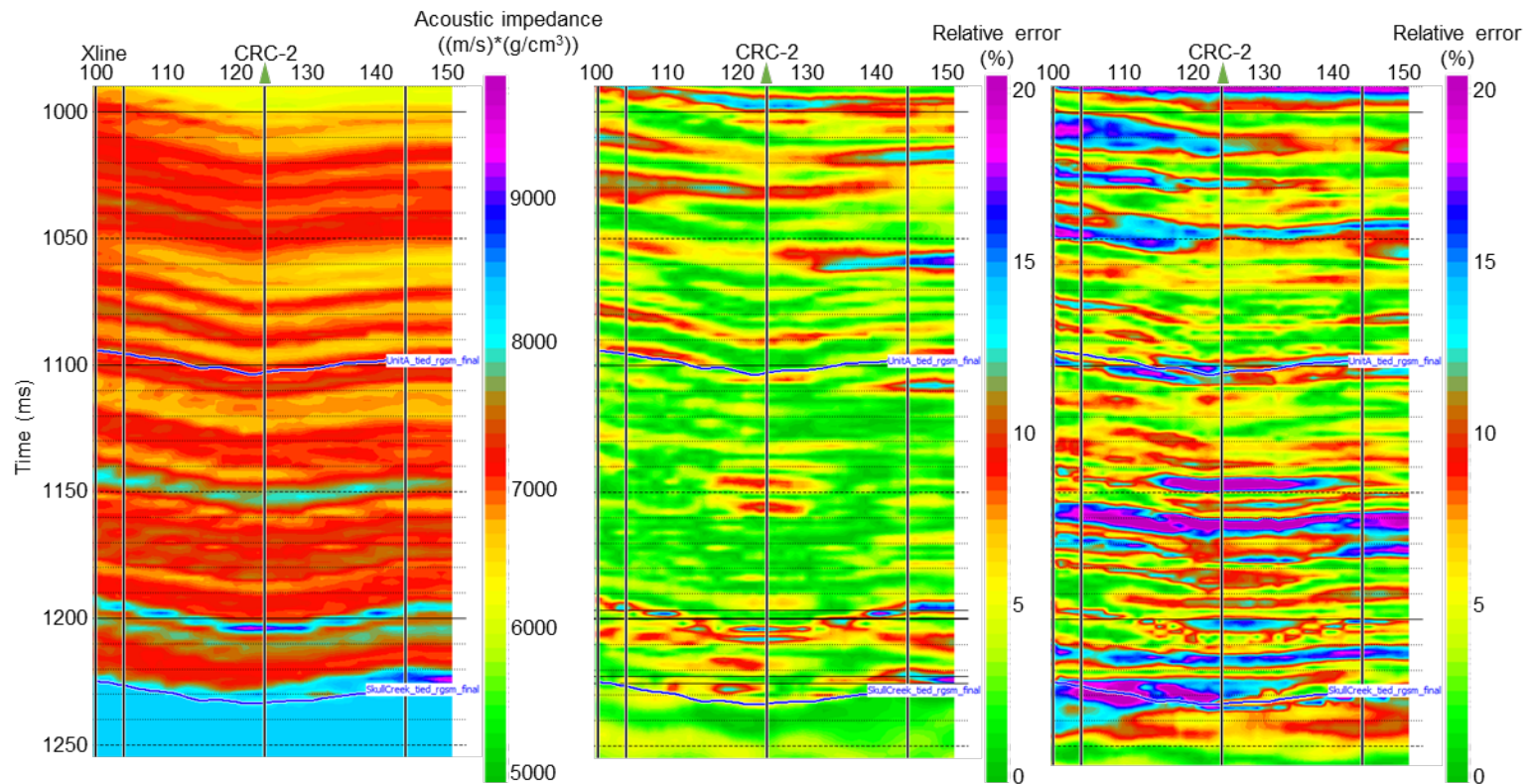
Figure 5-11: Actual acoustic impedance of the B model (left panel) along an Inline. Magnitude of the relative error of acoustic inversion for the data without deconvolution (middle panel) and with deconvolution (right panel). Green tringle at the top marks the location of CRC-2 well.

5.2 Effect of imaging on structural reconstruction and plume positioning

So far we have discussed preservation of the relative seismic amplitudes for the 3D and 4D synthetic data. We have shown that location of the plume image as a whole can be shifted with regards to the actual location (Figure 5-6). Predictably, the same thing happens to the faults as shown in Figure 5-12. Blue lines in Figure 5-12 indicate faults picked on the velocity model (left panel) and then projected onto the seismic image (right panel). We clearly see that imaged faults are laterally misplaced a few tens of meters compared to the actual faults (CDP spacing is 7.5 m).

The dataset shown in Figure 5-6 is post-stack migration in time with the velocities obtained after two iterations of velocity analysis, which is different from the actual (model) velocity field shown in the left panel of Figure 5-12. We speculate that the mispositioning can occur due to:

- the use of post-stack migration instead of the pre-stack migration;

- the errors in the velocity field;

- the flawed performance of the time migration in the presence of the lateral velocity variations in the model. This is because time migration uses a 1D velocity function to build a migration operator which is not valid for the areas with lateral velocity changes.

We now troubleshoot the mispositioning issues in an attempt to move the faults and the plume into their actual model locations.

We start the troubleshooting by running pre-stack Kirchhoff time migration with the same picked velocity field (right panel of Figure 5-13). The right panels of Figure 5-14 and Figure 5-15 show the images of structures and plume after pre-stack

migration. We observe no improvement in the plume and fault positioning, although the definition of the faults slightly improved (compare to Figure 5-12).

It is interesting to note a velocity pulldown in the time domain velocity model (black arrows in Figure 5-12). This non-geologically looking pulldown in the velocity model is introduced during depth-to-time conversion due to the discontinuity of the depth velocity field across the major fault. The left panel of Figure 5-18 shows the same velocity section in depth (actually this depth section was used to produce the time section in Figure 5-12). We see that this depth section has no such velocity pulldown (black arrows). It indicates that time domain migrations (they assume laterally non-varying velocities) may have problems imaging our model in the areas of complex geology such as nearby faults.
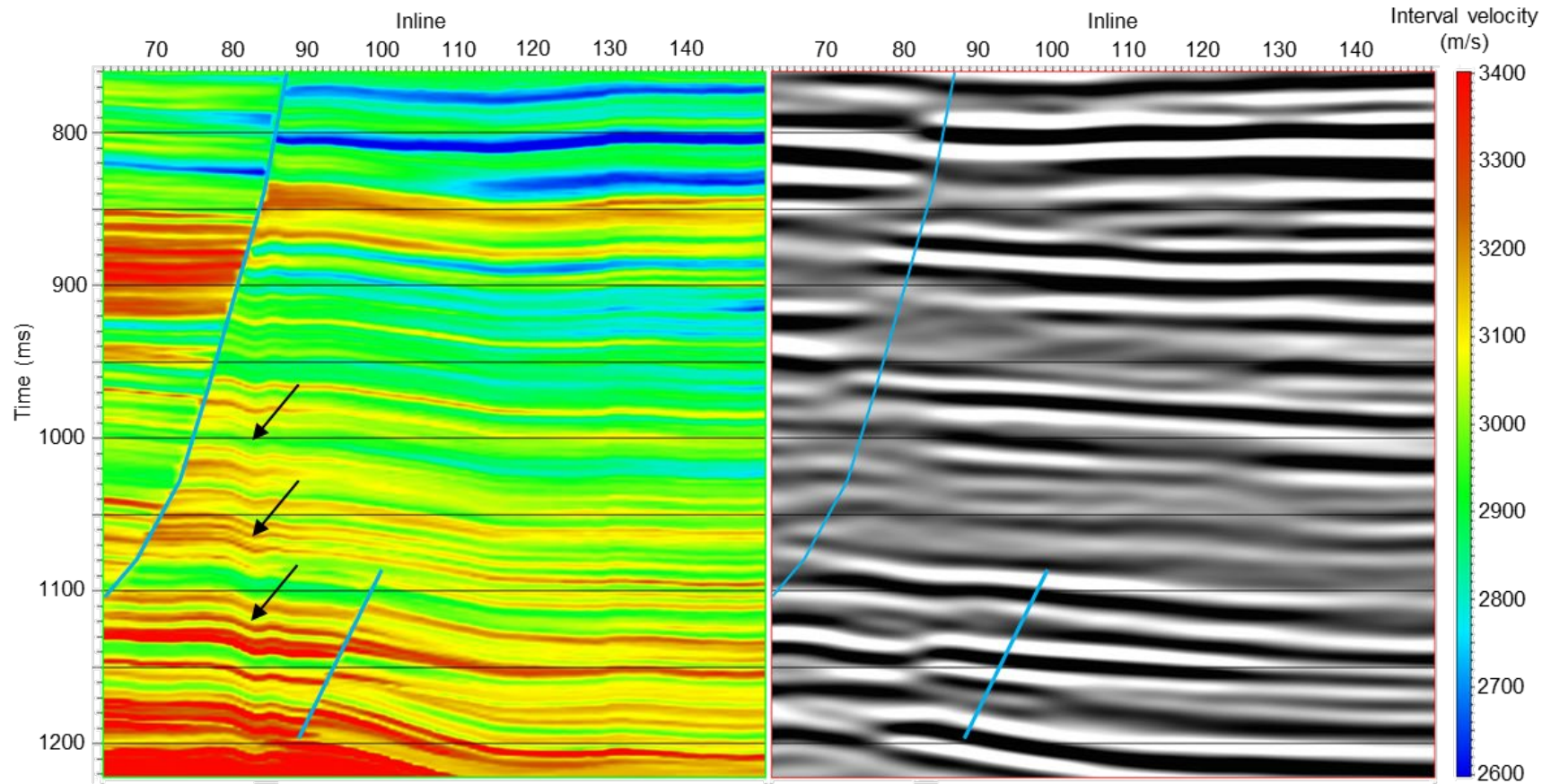
Figure 5-12: Slice along crossline 124 through the B model of interval velocities in time domain (left panel). Result of application of post-stack finite-difference time migration (right panel). Light-blue lines show faults picked on the model section and projected onto the seismic section. Black arrows indicate an area with the interval velocity pull-down artefacts. Note that this artefact is not present in the original depth interval velocity model (see black arrows in Figure 5-18).
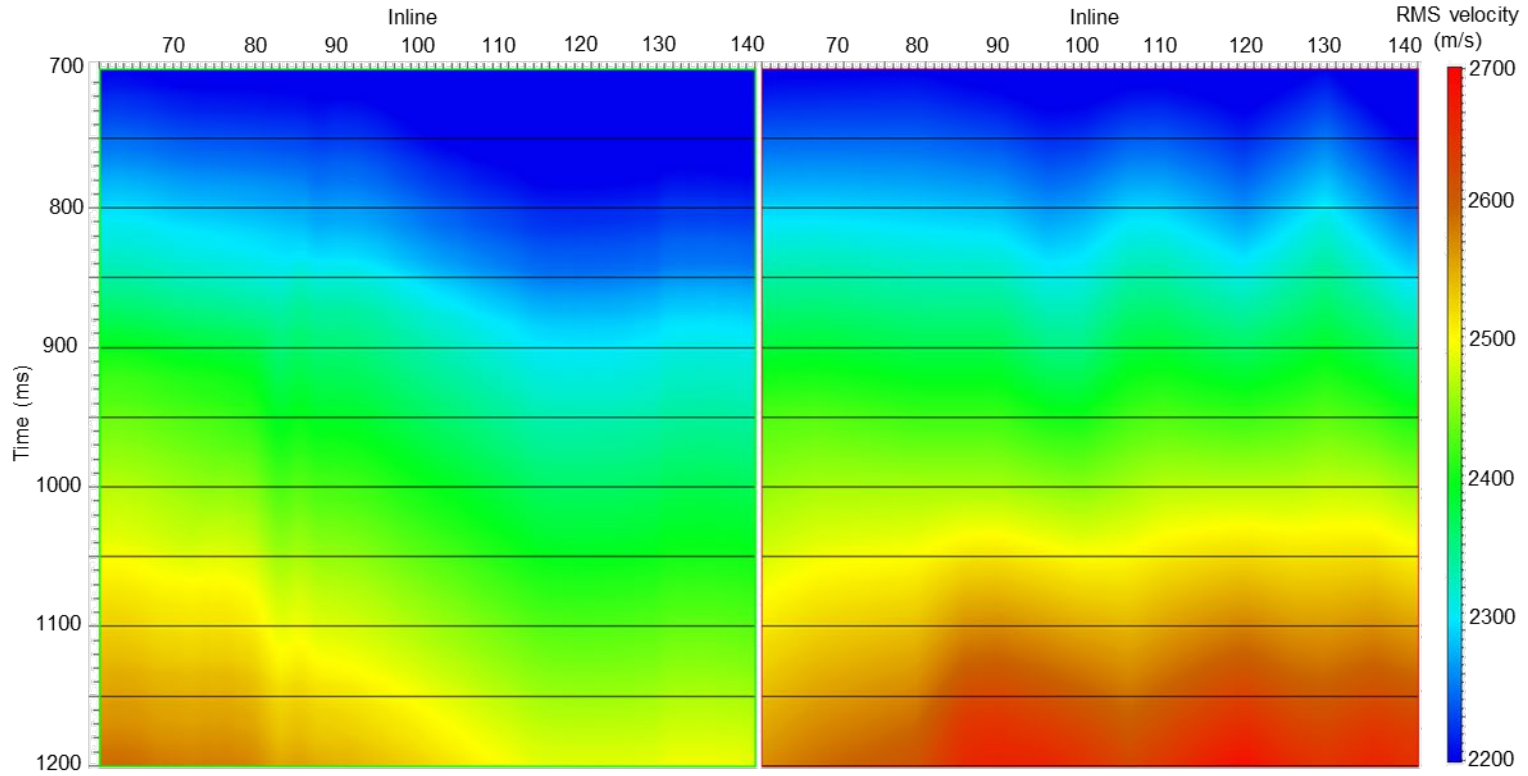
Figure 5-13: RMS velocity slice along crossline 124. RMS velocities computed from actual baseline model (left) and interpreted after two iterations of velocity analysis (right). The last reflector in our model is at about 1500 m depth, which corresponds to the time of about 1200 ms.
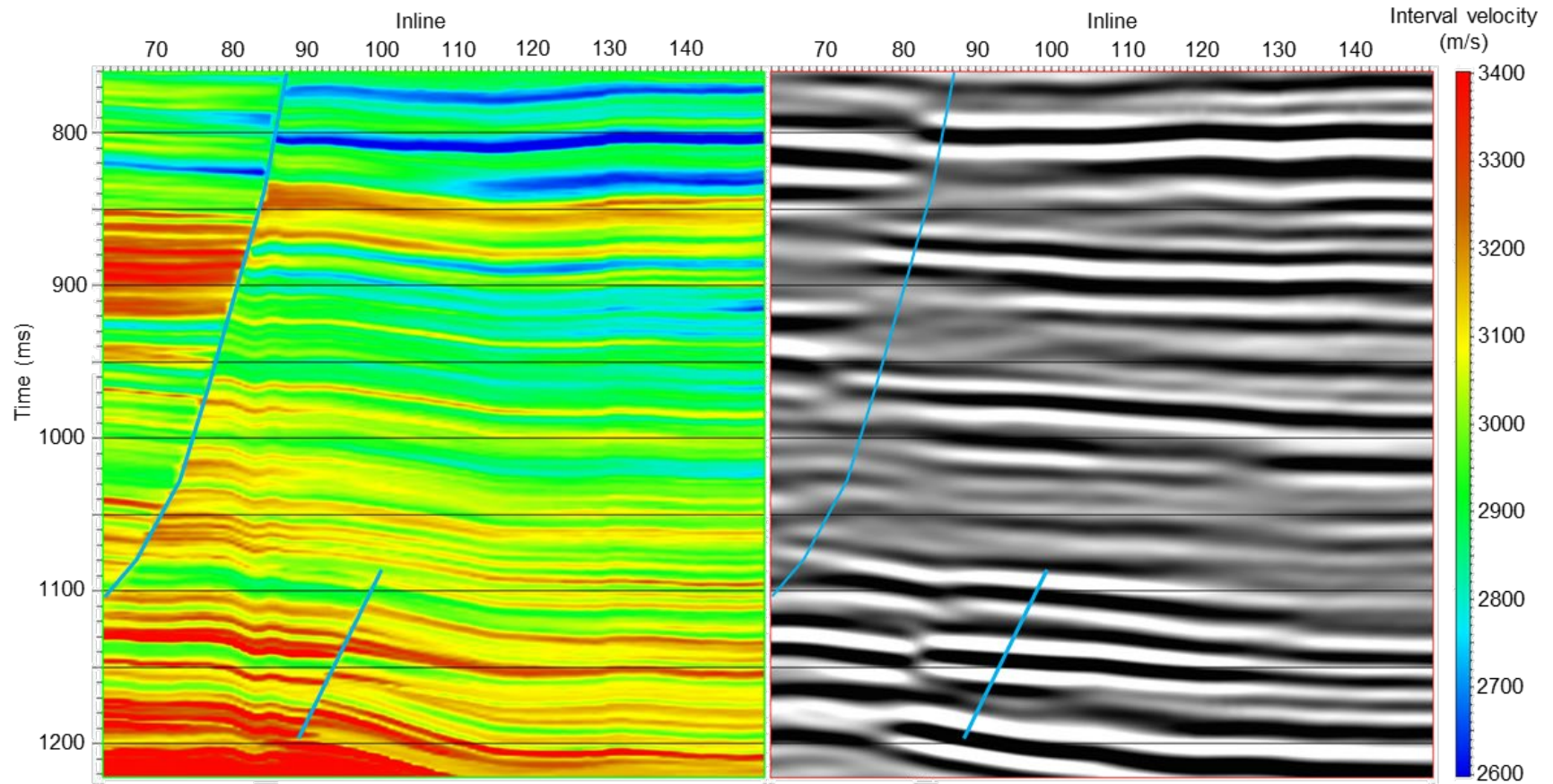
Figure 5-14: Slice along crossline 124 through the B model of interval velocities in time domain (left panel). Result of application of pre-stack Kirchhoff time migration with picked RMS velocity (right panel). Light-blue lines show faults picked on the model and projected onto the seismic.
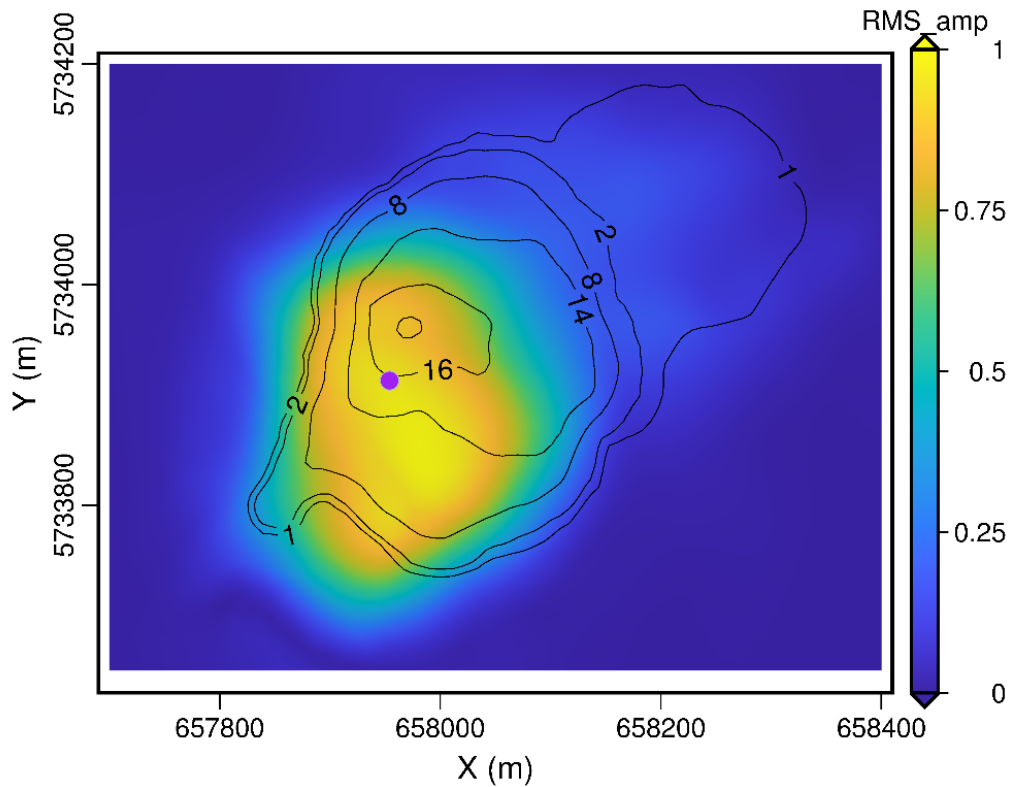
Figure 5-15: Map of RMS amplitudes calculated from the difference between images after pre-stack Kirchhoff time migration with picked RMS velocity (M-B). RMS amplitude is calculated in 44 ms window centred at 1210 ms. Black contours – plume thickness from reservoir simulation.

We next run the same pre-stack Kirchhoff time migration but using RMS velocities directly computed from the actual baseline velocity model (left panel of Figure 5-13). In this case the positioning issue is not resolved (Figure 5-16) but on top of that, the plume image is even noisier (Figure 5-17).

The next step is to try depth imaging, as it should account for the lateral variation of the velocity present in our model. Note that the depth migrations used the true baseline velocity that was used in the seismic forward modelling.
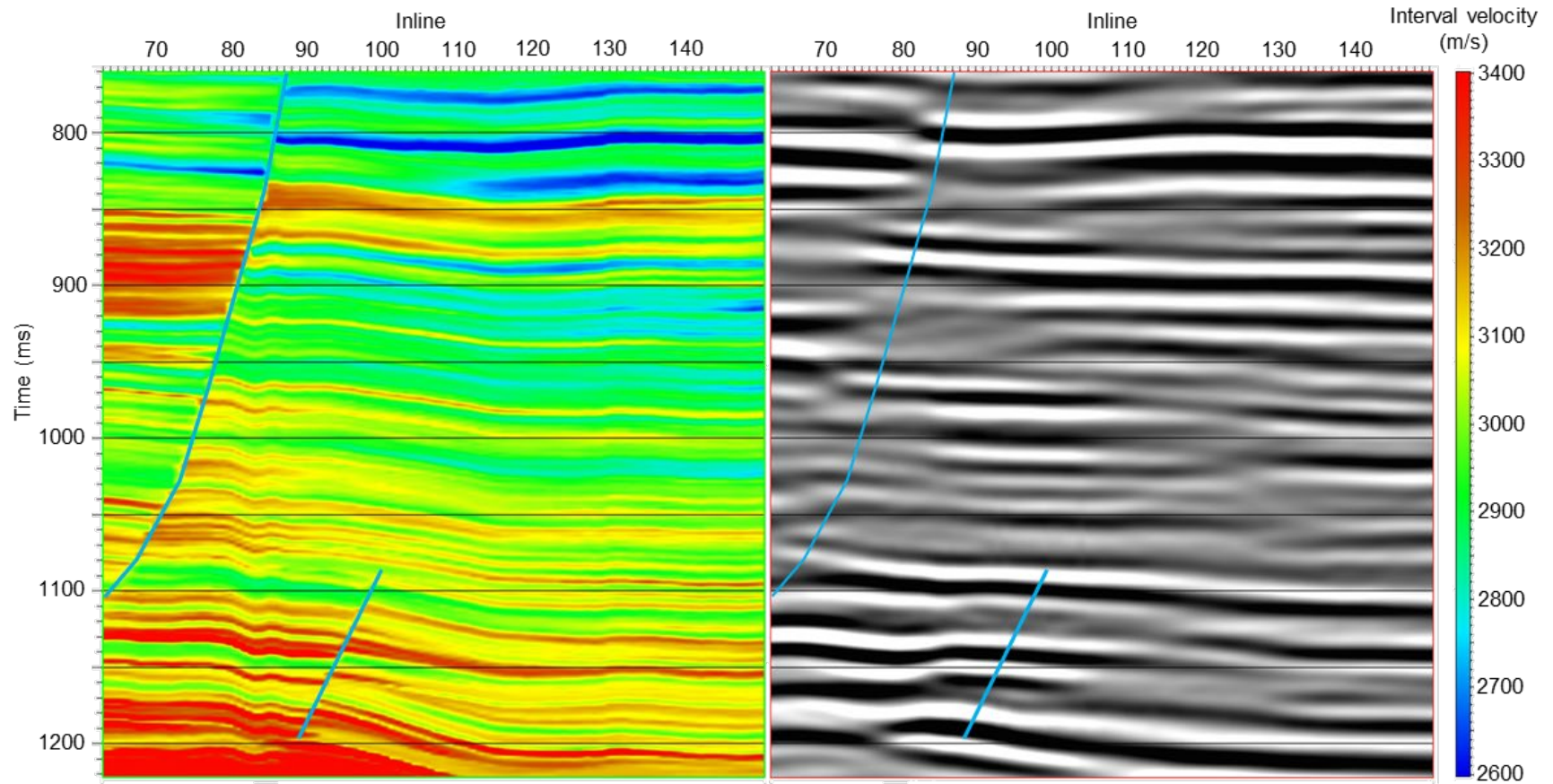
Figure 5-16: Slice along crossline 124 through the B model of interval velocities in time domain (left panel). Result of application of pre-stack Kirchhoff time migration with actual RMS velocity (right panel). Light-blue lines show faults picked on the model and projected onto the seismic.
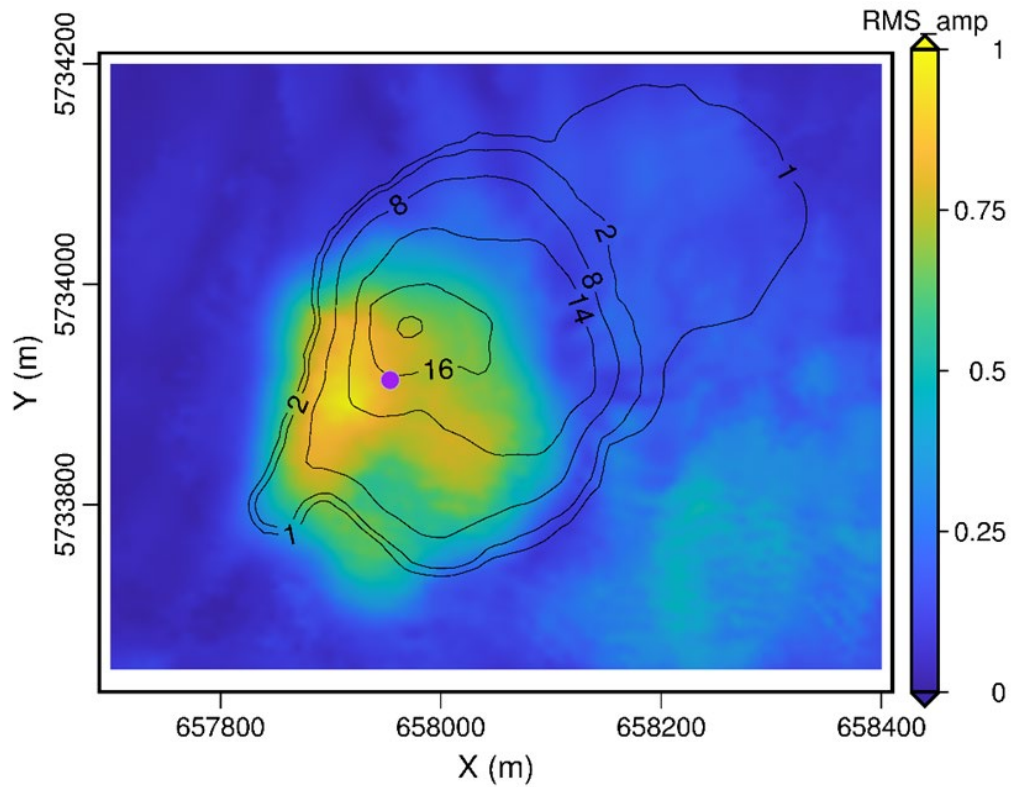
Figure 5-17: Map of RMS amplitudes calculated from the difference between images after pre-stack Kirchhoff time migration with actual RMS velocity (M-B). RMS amplitude is calculated in 44 ms window centred at 1210 ms. Black contours – plume thickness from reservoir simulation.

We start with the post-stack depth migration, which extrapolates the stacked wavefield downward using the exploding reflector model and produces the depth image of the subsurface using zero time imaging condition at each depth step (Jin et al. 1999). The right panels of Figure 5-18 and Figure 5-19 indicate improvement in the positioning of the faults and the plume. However, the continuity of the deeper reflectors is degraded compared to the results of the time migrations.
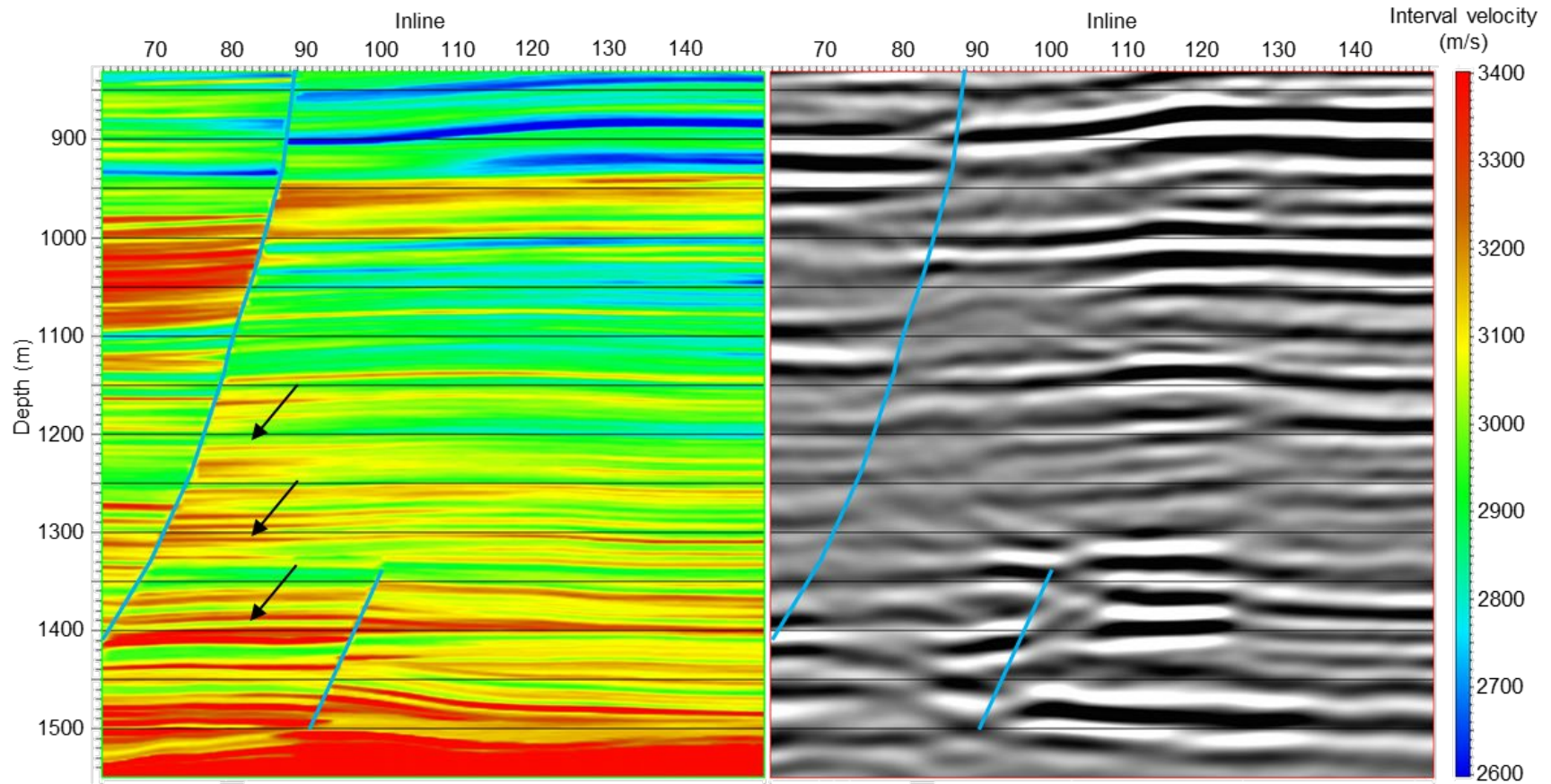
Figure 5-18: Slice along crossline 124 through the B model of interval velocities in depth domain (left panel). Result of application of post-stack depth migration with actual interval velocities in depth (right panel). Light-blue lines show faults picked on the model and projected onto the seismic. Black arrows indicate an area where the interval velocity model in time has a pull-down artefact (for comparison see the black arrows Figure 5-12).
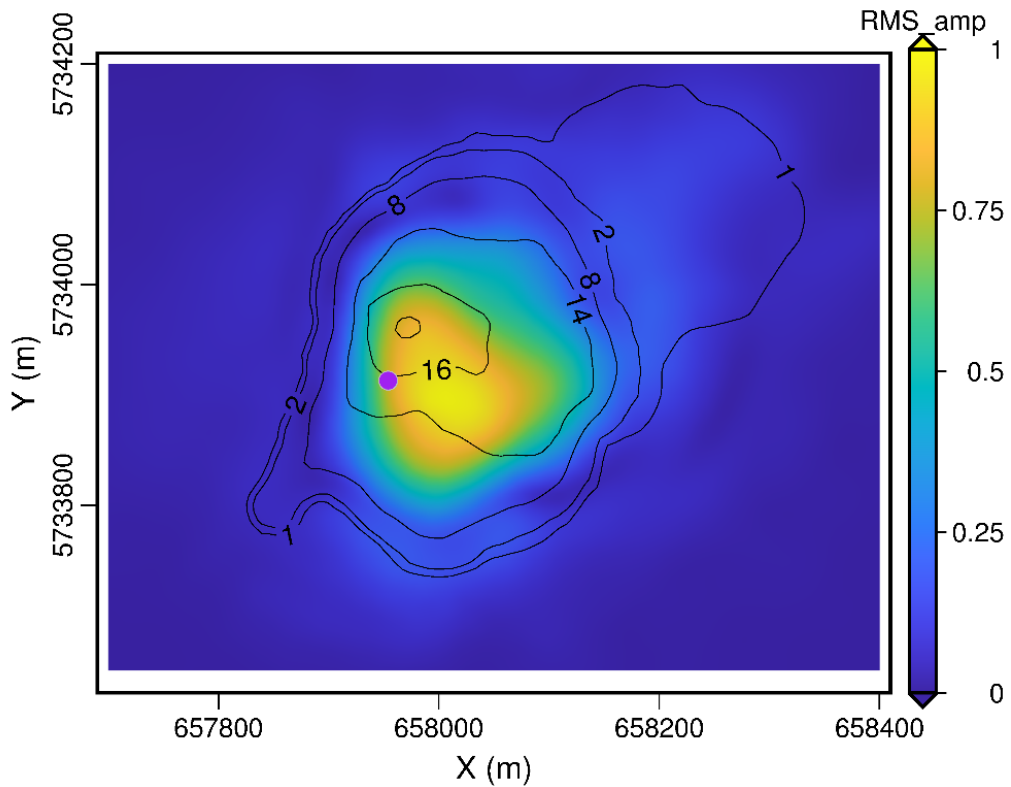
Figure 5-19: Map of RMS amplitudes calculated from the difference between images after post-stack depth migration with actual interval velocities in depth (M-B). RMS amplitude is calculated in 58 m window centred at 1493 m. Black contours – plume thickness from reservoir simulation.

Finally, we apply reverse time migration (RTM). RTM computes contribution to the image domain from each shot independently (migrates each shot separately). This algorithm performs forward and backward wavefield simulations for each shot through a given velocity model and applies an imaging condition at each depth step (Baysal et al. 1983).

We use the same velocity model for the imaging of B and M datasets. The depth imaging of the plume is more concerned with the depth interval velocities above the plume. Our B and M velocity models differ only at the injection area with the CO_2 saturation. As the plume is quite thin (thinner than 20 m), we are not able to separate between the reflections and diffractions from the top and bottom of the plume. Thus, the moveout of the reflections of plume-containing horizon as well as the shape of the

diffractions from the plume edges are the same for both the top and the bottom of the plume. Also CO_2 being buoyant inside the brine-filled aquifer is not going to move deeper than the depth of the injection interval. Thus, we do not require the use of different velocity models for imaging of B and M datasets. The use of separate velocity model for the migration of the monitor survey may be required only for the imaging of the reflectors below the plume, which is not the objective of this discussion.

The right panels of Figure 5-20 and Figure 5-21 show the images stacked after RTM. The faults and the plume are now imaged into their proper locations with minimal lateral shift. RTM is very time-consuming and hence we have only produced an image for the subset of imaging space with inlines ranging from 60 to 150 and crosslines ranging from 110 to 200. This explains the white area in Figure 5-21.

Inability of the time migration to handle the correct positioning of the injection and the faults is quite surprising given the near-horizontal layering throughout the model. As this is a flat geology PSDM is not normally considered required for imaging. We now briefly speculate about the reasons for the mispositioning.

Firstly, we note that the lateral mispositioning of the time images is not drastic and is in the order of a few tens of meters. Secondly, we refer to the Figure 4-4 and note two things. One is Naylor South Fault with a lateral velocity variation across the fault boundary. This velocity variation is within the migration aperture and can influence inaccurate imaging of the plume location. The other thing we note from the Figure 4-4 is that the layering is not strictly horizontal. As the velocity model was built to be conformant with the layering, we observe a slow lateral velocity variation (for example, see the red and yellow velocity layers inside the Dilwyn Formation between 400 and 600 m). We speculate that these subtle but pervasive lateral velocity changes are in charge of the failure in the accurate imaging using time migration.
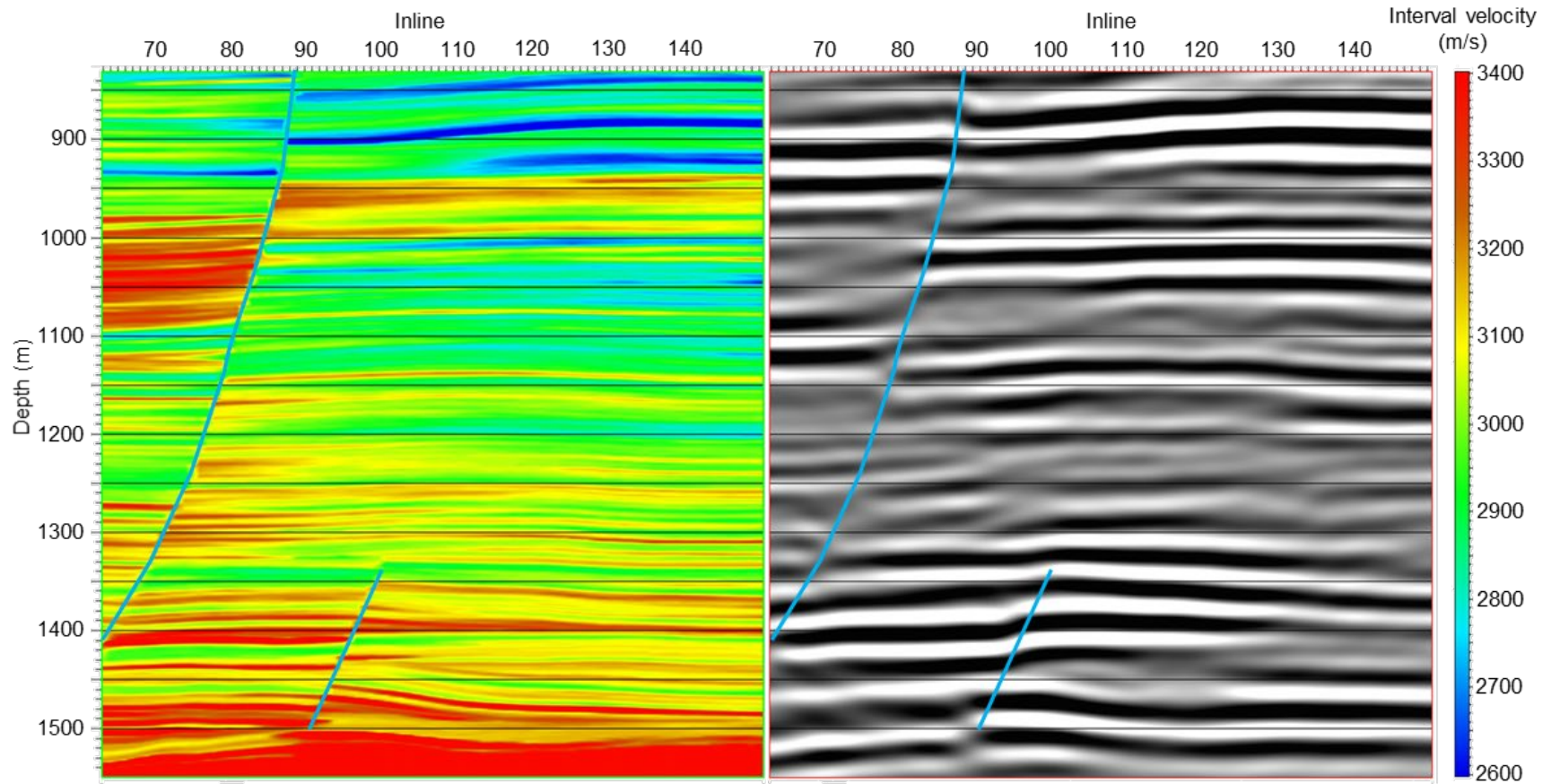
Figure 5-20: Slice along crossline 124 through the B model of interval velocities in depth domain (left panel). Result of application of RTM with actual interval velocities in depth (right panel). Light-blue lines show faults picked on the model and projected onto the seismic.
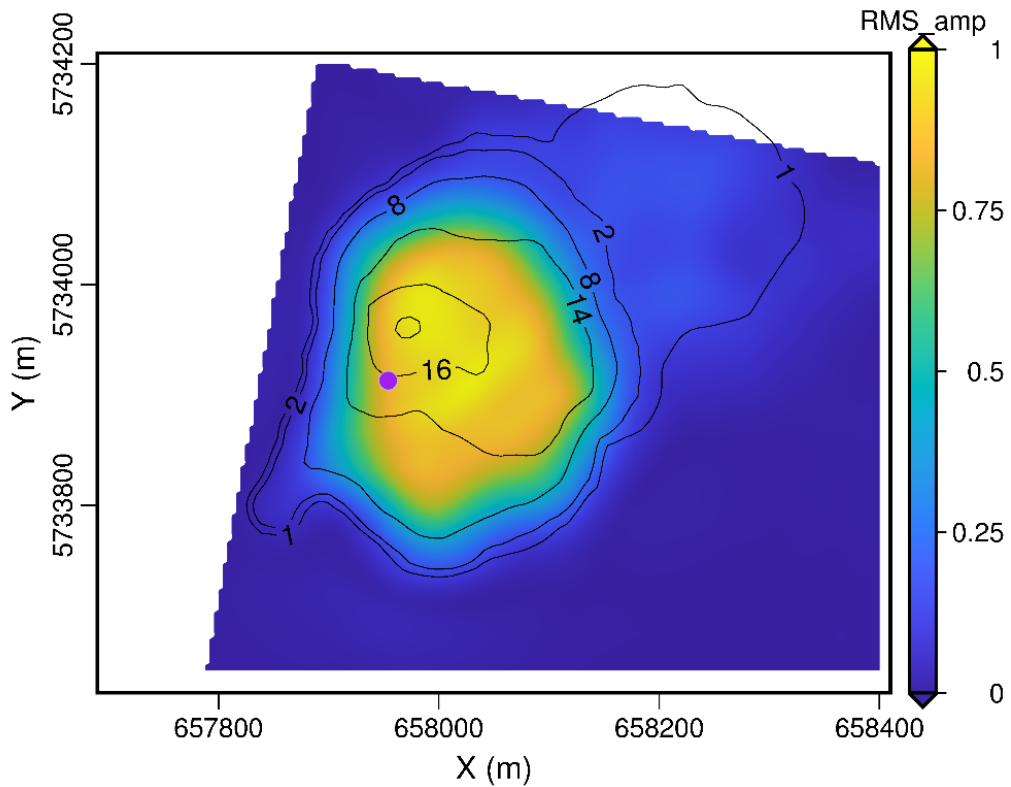
Figure 5-21: Map of RMS amplitudes calculated from the difference between images after RTM with actual interval velocities in depth (M-B). RMS amplitude is calculated in 58 m window centred at 1493 m. Black contours – plume thickness from reservoir simulation.

To summarise, we see that neither pre-stack nor post-stack time imaging can handle the relatively mild lateral velocity variation in the subsurface model built for Stage 2C. In addition, neither the use of picked velocities nor the use of the initial model velocities can resolve the positioning error. Even subtle lateral velocity variations can cause errors in the time imaging. Depth migration is required to fix the imaging errors. With the synthetic data we are in a favourable position as we have the actual velocity model in depth, which is never known exactly for any field data. Thus, building of the depth velocity model is important if one wants to ensure proper positioning of the time-lapse signal in space.

5.3   Conclusions

We now summarize the main findings from processing of the synthetic data that we could use in building a time-lapse processing workflow for the field data:

1. Reflections obscured by the ground roll actually contain a lot of the time-lapse signal. It follows that the ground-roll removal for our field data must be carefully designed to avoid losing the 4D signal.

2. Application of long-window AGC in the time-lapse processing workflow is acceptable for a zero-offset acoustic inversion of a full-offset stack in case when relatively strong residual noise is present in the data (e.g. near-mid offsets contain residual ground-roll).

3. Spiking deconvolution might degrade the quality of well-ties and QI even for the noise-free data. Care should be taken when applying spiking deconvolution.

4. The choice of the post-stack migration algorithm is not crucial if we focus on the target interval.

5. Both pre-stack and post-stack time migrations introduce errors in lateral positioning of the plume even for the near horizontal geology of the current model. These errors occur for the true velocity model and for the velocity model derived from the synthetic data. For the elastic model built for Stage 2C, pre-stack depth migration is required to ensure proper positioning of the faults and plume.

6. Unlike the common believe, depth imaging might be a must even for the imaging in the areas with a presumably simple geology.

Chapter 6.

Processing strategy and results for field data

In the previous chapters we have covered data acquisition and modelling and also analysed the effect of commonly used processing routines on synthetic 4D signal. We, thus, prepared the background for the processing of the actual 4D field data.

In this chapter we address the challenges of onshore 4D seismic processing. We start with a theoretical model of time-lapse noise present in onshore seismic data and approach ways to suppress it. We then devise a methodology of QC check of 4D noise and 4D signal at all the stages of our processing flow. We capitalize on the findings from the processing of synthetics to make decisions on the application of certain processing procedures to processing the field data. Finally, we justify and produce a workflow that yields time-lapse images that can be used for post-stack quantitative interpretation.

As this chapter is fairly large it is helpful to provide an outline:

- We start by giving a background setting of the challenges which rise before the time-lapse processing for onshore surveys – 4D noise in our case;

- Then we provide a theoretical and experimental basis which allows us identify the various sources which contribute to this noise using the examples of our data;

- This analysis then allows us devise a comprehensive set of metrics and their displays that we use to measure the initial level of 4D noise and

4D SNR. We then use these metrics to validate the processing choices throughout our processing workflow from the standpoint of the preservation of integrity of 4D signal and suppression of 4D noise. We also discuss requirements which data need to satisfy in order to be used in QI workflows;

- Next we build our processing flow – step by step – while keeping track of the noise and signal measures at each step. As the possibility of workflow testing and ramification is virtually unbounded (and we did quite a lot of testing), we show here only the final (that is, the best out of what we have tested) processing sequence virtually without any branching. Notably, we use the same plots of repeatability measures (as applicable) for different processing steps to make the results before and after a processing step comparable:

  - We start with the raw correlated data;

  - Followed by denoise – ground roll removal;

  - Followed by removal of the bad traces;

  - Followed by surface-consistent deconvolution;

  - Followed by pre-stack time migration and a brief look at the pre-stack manifestation of the plume;

  - Followed by a study of the applicability of AGC to the data preparation for structural interpretation and post-stack QI;

- We then summarise the findings and justify the choice of the processing steps that we use. We compare these steps to those simpler steps that we had used when building fast-track images of the plume;

- Then we show the final results of our 4D processing workflow applied to all the surface seismic monitoring data available to date;

- Finally, we draw the conclusions from our findings.

6.1   Background

The major problems of onshore monitoring arise due to the presence of highly heterogeneous near-surface. Elastic properties of near-surface sediments largely depend on precipitation levels and weather conditions, thus, the properties change significantly with the season. From the seismic perspective, the near-surface changes affect the source signature and receivers' response to the ground movement between surveys.

Apart from that, the near-surface gives rise to poorly repeatable ground roll and source-generated S-wave. High energy and complex wavefield patterns make ground roll the strongest contributor to the time-lapse noise in onshore seismic monitoring (Shulakova et al. 2014, Bakulin et al. 2016). Source generated S-waves have a frequency content similar to P-waves and low effective velocities, which make the S-wave suppression challenging.

The main advantage of onshore monitoring over offshore monitoring is repeatable acquisition geometries between surveys (Calvert 2005a, Misaghi et al. 2007, Cantillo et al. 2010). In onshore monitoring, the positioning of sources and receivers is not an issue because baseline source and receiver locations can be conveniently revisited with high precision for each monitor survey using differential GPS.

We start with the development of a mathematical formulation of time-lapse signal estimation from noisy seismic monitoring data. We show that a rather simple

model of seismic trace containing additive and multiplicative sources of non-repeatability provides sufficient insight into the problem.

6.2   Sources of time-lapse noise

We analyse the repeatability of the data following Cantillo (2011). This approach was developed for offshore monitoring, so we extend it to the onshore data. We assume that baseline (v_1) and monitor (v_2) traces may be modelled as:

$$\begin{cases} v_1 = W_1 \cdot e_1 + n_1 \\ v_2 = W_2 \cdot e_2 + n_2 \end{cases}$$

6-1

e_i are a series of reflection coefficients distributed within the subsurface. W_i model effects of wave propagation and radiation (Margrave 1998). The terms n_i denote all seismic events except the primary reflections, which include coherent noise like ground roll and random events like ambient noise. In our case we expect the noise terms n_1 and n_2 to be somewhat different ($n_1 \neq n_2$).

The quantity $W_i = N \cdot w_i$ represents source signature w_i affected by propagation through heterogeneous Earth, such as: geometrical spreading of the source energy, scattering, and inelastic attenuation (O'Doherty and Anstey 1971). Here N is the term that describes non-stationarity. We expect N to be the same for baseline and monitor surveys. The seismic wavelets w_1 and w_2 vary between surveys due to the effects of coupling and stability of instrumentation.

In the marine case, w_2 can be accurately approximated as a time-shifted version of w_1, because the recording and excitation parameters of the instrumentation and water layer are relatively stable. For the onshore case, seasonal near-surface

variations complicate the model, because now different frequency components may be affected differently, so their amplitudes and relative time shift may be changed independently. The simplest way to model such a process analytically involves convolution of the baseline wavelet with a linear stationary filter Δw.

$$w_2 = w_1 * \Delta w \qquad\qquad 6\text{-}2$$

The filter accounts for all changes in the excitation and recording parameters that affect the far-field (at the reflector's depth) signature of the wavelet for a given seismic trace (Figure 6-1). As a result, the initial and final wavelets are not mere scaled and shifted copies of each other, but may look very different.

We expect the major contributions to Δw from variation of the effective source and receiver coupling between the surveys.
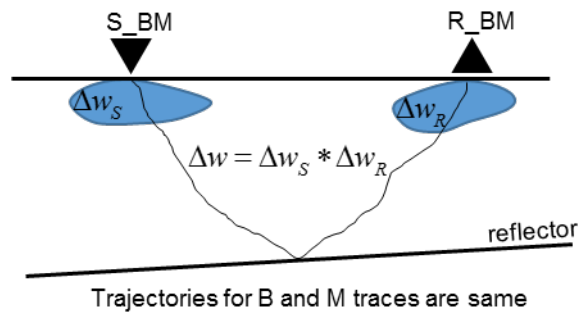
Figure 6-1: Scheme explaining the meaning of Δw, which accounts for the linear stationary variation of the trace wavelet between the vintages. Monitor and baseline locations of sources coincide. Monitor and baseline locations of receivers coincide. Blue shapes indicate variation of coupling. Δw_S is the variation of the wavelet on source side, Δw_R is the variation of the wavelet on receiver side. Legend: S – source, R – receiver, B – baseline, M – monitor. Not to scale.

For the sake of simplicity, we assume a common convolutional model of a seismic trace, which disregards non-stationarity and turns equation 6-1 into:

$$\begin{cases} v_1 = w_1 * e_1 + n_1 \\ v_2 = w_2 * e_2 + n_2 \end{cases}$$

6-3

From Cantillo (2011), reflectivity of the subsurface for a monitor survey can be approximated as:

$$e_2 \approx e_1 + \frac{\partial e}{\partial P}\Delta P + \frac{\partial e}{\partial G}\Delta G$$

6-4

$\frac{\partial e}{\partial P}\Delta P$ denotes changes of subsurface reflectivity due to production or injection – the 4D signal. This variation vanishes if no 4D signal is present. The other differential $\frac{\partial e}{\partial G}\Delta G$ accounts for discrepancy between seismic wave propagation trajectories in baseline and monitor surveys.

To identify noise sources in our data we use equations 6-2 and 6-4 to make substitutions into the expression of v_2 in equation 6-3. Then the difference between monitor and baseline traces away from 4D signal ($\Delta P = 0$) reduces to the following expression for 4D noise:

$$v_2 - v_1 = (\Delta w - \delta_0)*w_1*e_1 + \frac{\partial e}{\partial G}\Delta G*w_1*\Delta w + (n_2 - n_1)$$

6-5

where δ_0 is Dirac delta-function that is defined by $\delta_0 * w_1 = w_1$.

The first term accounts for difference in instrumentation performance – source signature and receiver response to the ground movement – and it has nothing to do with wave propagation through deeper parts of the subsurface (see Figure 6-1). This term vanishes when wavelets are matched to each other.

Intensity of the second type of time-lapse noise is controlled by $\frac{\partial e}{\partial G}\Delta G$. The differential ΔG equals to absolute displacement of sources ΔS and receivers ΔR between surveys (left panel of Figure 6-2). This term has a dominant effect in marine

acquisition where repetition of the baseline configuration of sources and receivers might be off by tens or hundreds of meters (Landro 1999, Cantillo et al. 2010). The partial derivative $\frac{\partial e}{\partial G}$ quantifies heterogeneity of the overburden (right panel of Figure 6-2). For land seismic, $\frac{\partial e}{\partial G}$ is usually large but ΔG is small, because repetition of the baseline source and receiver locations can often be done with a precision of less than 0.5 m. Increase of ΔG for onshore seismic may compromise land monitoring completely as shown by Jervis et al. (2012).
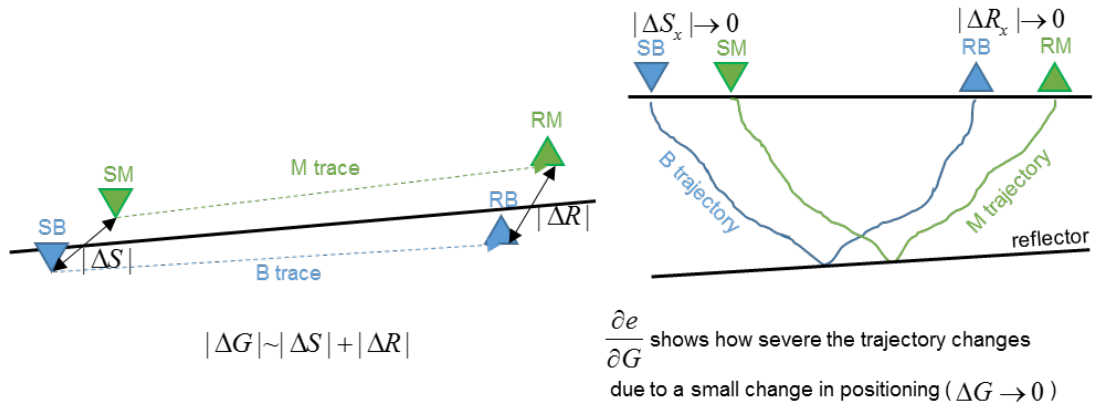
Figure 6-2: Diagrams explaining the meaning of ΔG (left panel) and $\frac{\partial e}{\partial G}$ (right panel). The left panel shows the map view and the right panel shows vertical intersection along the black line from the left panel. ΔG is the precision of the repetition of baseline geometry. $\frac{\partial e}{\partial G}$ quantifies changes of seismic wave travel path through overburden induced by ΔG. Legend: S – source, R – receiver, B – baseline (light-blue), M – monitor (light-green), $|\Delta S|$ – error in repeating the source location SB, $|\Delta R|$ – error in repeating the receiver location RB, $|\Delta S_x| \to 0$ – projection of $|\Delta S|$ onto the black line in the left panel, $|\Delta R_x| \to 0$ – projection of $|\Delta R|$ onto the black line in the left panel. Not to scale. Distances $|\Delta S|$ and $|\Delta R|$ are much smaller than trace offsets.

The third term in equation 6-5 ($n_2 - n_1$) accounts for any energy present in seismic data that has nothing to do with signal – primary P-wave reflections. Below we consider some specific noise types that contribute to the magnitude of the third term at the Otway site.

We start with non-repeatable ambient noise (Figure 6-3), which is usually uncorrelated in the CDP domain and can be significantly suppressed by stacking. However, Pevzner, Shulakova, et al. (2010) have shown clear correlation between repeatability of the final seismic images and SNR in individual monitoring vintages. They measured noise-to-signal ratio (NS) on the final 2D seismic images under an assumption of zero mean, spatially uncorrelated and additive noise from Hatton et al. (1986):

$$NS(v_i[j], v_i[j+1]) = \sqrt{\frac{1 - max(xcor(v_i[j], v_i[1+j]))}{max(xcor(v_i[j], v_i[1+j]))}} \qquad 6\text{-}6$$

In this equation $xcor()$ is the normalized cross-correlation function between two traces that takes on values in the range from -1 to 1; j – trace number inside a vintage and i – identification number of the monitoring vintage. In accordance with their study, we expect non-correlated ambient noise to degrade repeatability of our pre-stack traces and final images.

Air blast can be seen in some records, even though we use a buried receiver array (highlighted by red arrows in Figure 6-4). Interestingly, air blast appears stronger in the difference seismic compared to the baseline. Air blast has relatively amplified high frequencies and low velocities, occupies limited location on shot gathers and has relatively low energy. Thus, we do not expect it to require specific attention in our processing flow.

The third wave type consists of direct arrivals and diving waves that occur as the first breaks in the data (red arrows in Figure 6-5). These waves do not interfere with reflections of interest, especially after NMO or migration muting is applied.

Source-generated S-waves and converted P-to-S and S-to-P waves contaminate reflections at near- and mid-offset range (red arrows in Figure 6-6). Having relatively low velocity, they onset not long before ground roll and often get aliased, which complicates their suppression. We expect converted waves to be repeatable such that they could be suppressed by simple vintage subtraction. The repeatability of source-generated S-waves is still questionable. However, source-generated S waves and converted waves might get attacked by the routines that we use to remove ground roll.

Finally, ground roll causes the most severe time-lapse noise (green arrows in Figure 6-6) due to its huge amplitude and occurrence in the target time interval. Time-lapse variability of the near-surface is the key factor causing the non-repeatability of surface waves (Shulakova et al. 2014). Suppression of the ground roll in individual seismic vintages is crucial for rendering less noise into final images and for better satisfaction of the assumptions underlying surface-consistent deconvolution, cross-equalization and migration.

As we have discussed the potential sources of noise, we next establish an approach to track 4D noise and signal through the processing workflow.
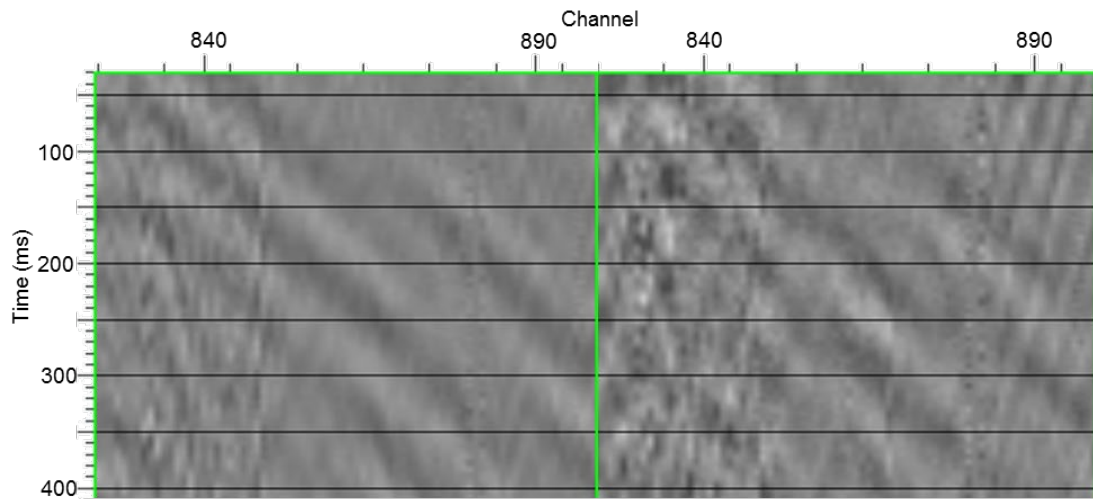
Figure 6-3: Part of a shot record with ambient noise that is not related to our active seismic source. Left panel – B, right panel – M3-B.
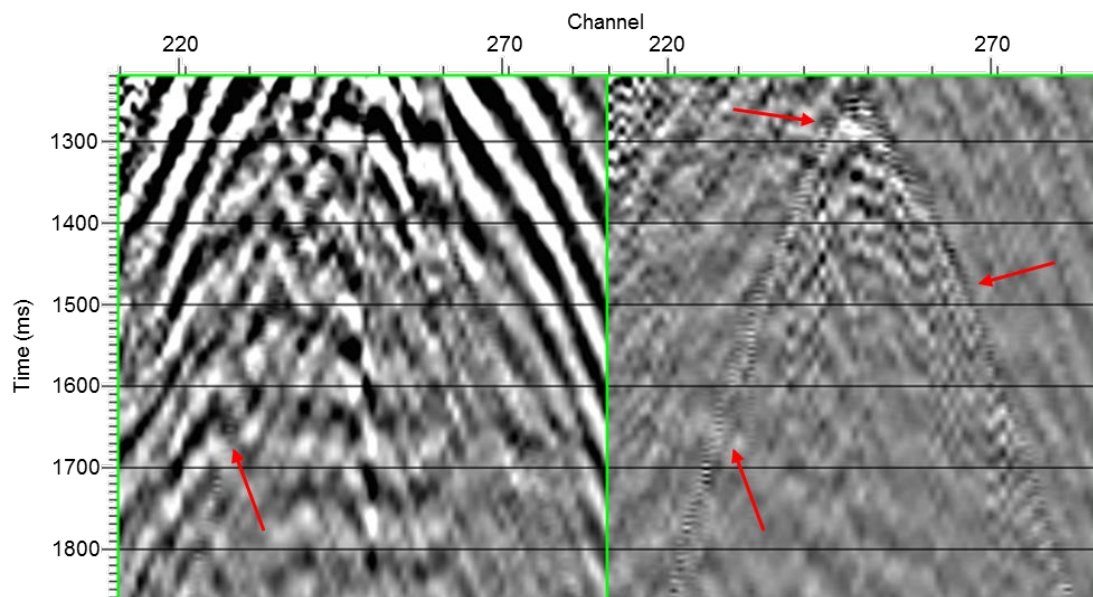
Figure 6-4: Part of a shot record with air blast (indicated by red arrows). Left panel – B, right panel – M3-B.
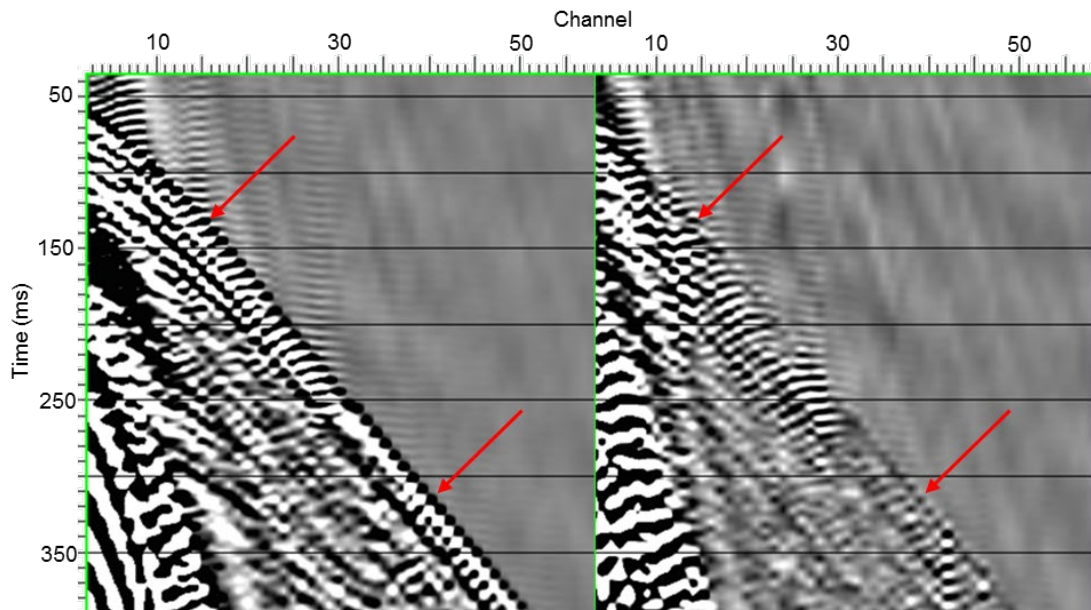
Figure 6-5: Part of a shot record with direct and refracted waves (indicated by red arrows). Left panel – B, right panel – M3-B.
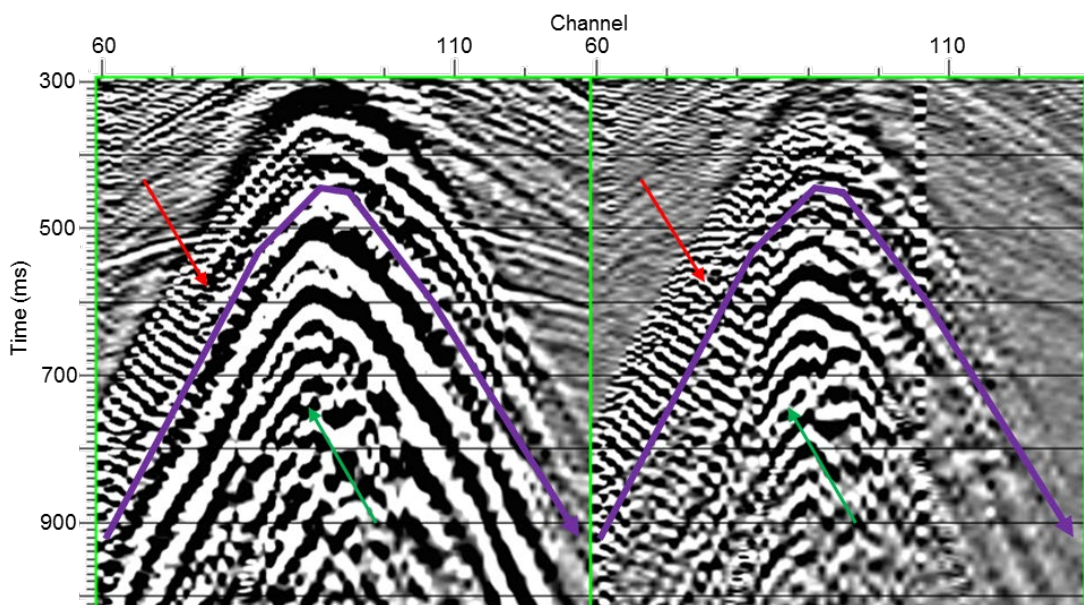
Figure 6-6: Part of a shot record with ground roll (green arrows) and presumably source-induced S-waves (red arrows). Left panel – B, right panel – M3-B. Purple line roughly separates S-waves / converted waves and ground roll.

6.3 Tracking repeatability through processing

In essence, seismic repeatability should measure how similar seismic vintages are. Since complicated alterations of the seismic data at each processing stage may not

be quantified by one simple measure, it is better to compute a number of time-lapse metrics that validate the applicability of the processing procedures that we use. Then, problematic sources, receivers, offsets and processing procedures can be identified through analysis of trace gathers for common shot/receiver/offset/image point domains. It is not obvious in advance which repeatability measure is best suited for QC of a processing sequence for a given dataset. Hence, we test and propose a set of measures that complement each other.

A common estimate of traces repeatability is NRMS metrics. This measure has been introduced in Kragh and Christie (2002) as:

$$NRMS(v_1, v_2) = \frac{2 \cdot RMS(v_2 - v_1)}{RMS(v_2) + RMS(v_1)} \qquad \text{6-7}$$

NRMS is very sensitive to subtle time shifts between the traces of magnitude less than the sampling rate (Calvert 2005b). However, this metric does not distinguish some essentially different cases; e.g., two identical traces shifted by one sample and traces completely different by the appearance (Cantillo 2012).

Predictability (Kragh and Christie 2002) is another metric which is commonly used to estimate the quality of time-lapse seismic. This metric is based on cross- and autocorrelations of traces. In his paper Cantillo (2012) demonstrates that predictability does not have enough resolution and stagnates around $0.9 - 1$ for the traces with generally good but still different level of repeatability.

Instead of predictability we use another cross-correlation-based measure known as Signal-to-Distortion Ratio (SDR) that was introduced in Cantillo (2011). The author derived expression for the SDR under the assumption that monitor and baseline wavelets differ only by a time shift τ ($w_2 = w_1 * \delta(t - \tau)$). This is a valid approximation for offshore environments but may be ambiguous for land data.

However, we use SDR as an additional QC parameter of our processing flow and compute SDR as follows:

$$SDR = \frac{max(\ xcor(v_1,v_2\ ))^2}{1-max(\ xcor(v_1,v_2\ ))^2} \qquad 6\text{-}8$$

In this equation, *xcor()* is the same cross-correlation function as in equation 6-6 . We limit the range of time shifts for which we estimate values of cross-correlation down to a few samples as we do not expect large time shifts between the corresponding traces and to avoid cycle skipping.

The time shifts attribute (TS), estimated as the time at which $max(\ xcor(v_1,v_2\ ))$ occurs, is another parameter that we track. As mentioned above, these time shifts affect estimates of NRMS. TS may also be an independent measure of seismic repeatability, which is very sensitive to velocity variations in the near-surface.

The fourth metric that we use is RMS amplitudes of the difference between corresponding traces in monitor and baseline vintages (RMSDIF). This is a simple way to see how much actual 4D noise will propagate into the final image.

We compute NRMS, SDR, TS and RMSDIF before and after stacking outside of the area of anticipated 4D signal after different stages of the processing flow for each pair of vintages.

Figure 6-7 illustrates the use of the developed suite of repeatability measures and demonstrates the importance of using a few repeatability measures rather than one. This figure shows two pairs of traces windowed according to their offset values (window is taken between the red lines in Figure 6-12). Each panel of Figure 6-7 shows a baseline trace (blue), corresponding monitor trace (orange) and their difference M-B (black). Interestingly, both panels show trace pairs with the same value of NRMS

equal to 0.5. The top panel shows mid-offset traces, while the bottom panel shows near-offset traces.

Even though NRMS is the same for the both trace pairs, we clearly see that these trace pairs are very different and we would like to differentiate between these two cases using additional repeatability measures. We note that the top pair has SDR of 3.2, TS of 0 ms and RMSDIF of about 2000; while the bottom panel has SDR of 36, TS of 0.5 ms and RMSDIF of about 42000. We also note that the vertical scale of the top panel is 10 times larger than the vertical scale of the bottom panel. The bottom panel contains ground roll that onsets at about 800 ms, bringing very strong 4D noise.

We see that sources of 4D noise in both panels are of a different nature and manifest themselves in different ways even though both panels have the same NRMS values. It is clear that by looking only at NRMS values it is impossible to find the difference between two such cases. Using combinations of time-lapse attributes (as shown in Figure 6-16 and Figure 6-18) we might better track how the quality of the data changes after each processing stage compared to the use of only one parameter.
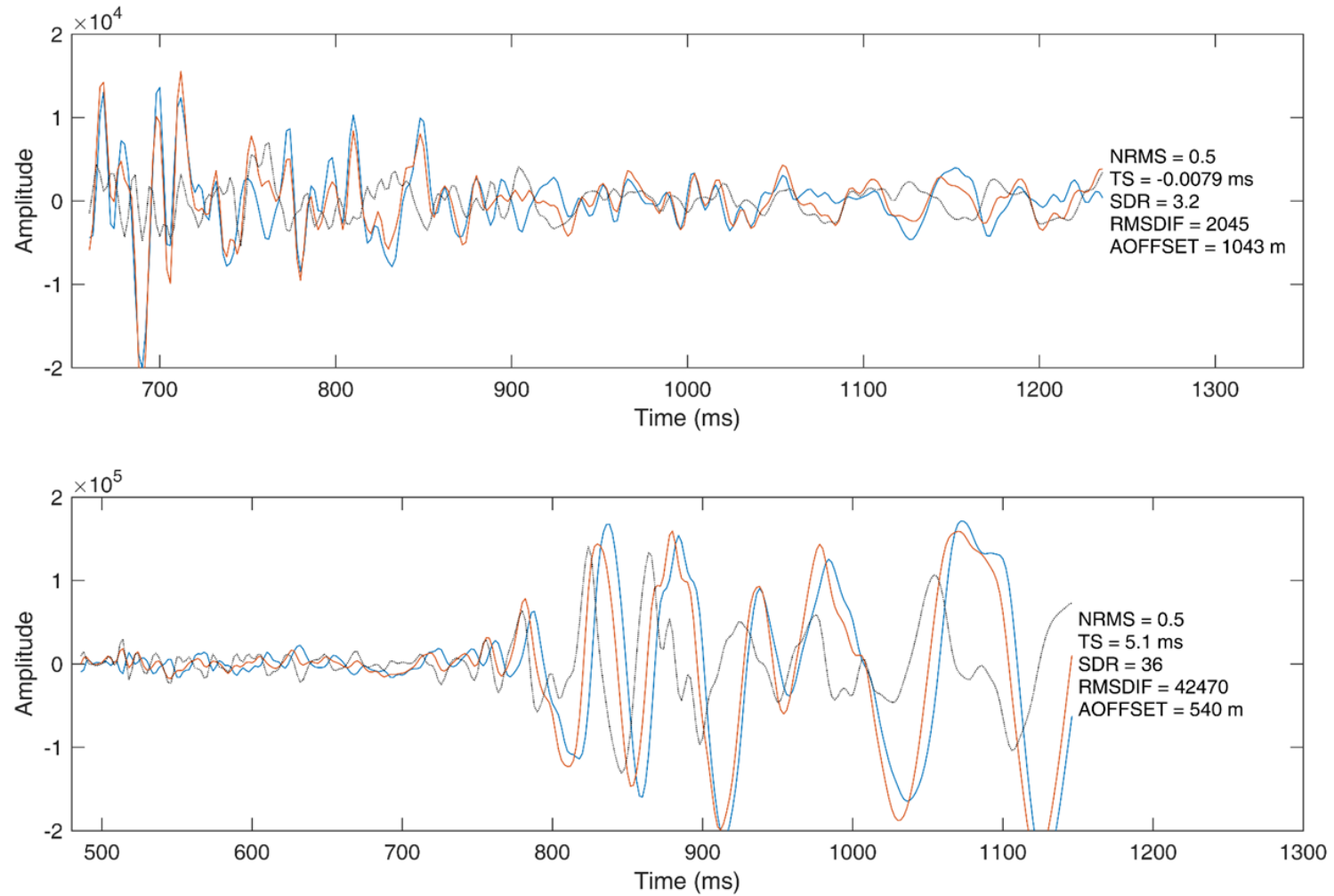
Figure 6-7: Windowed trace pairs with the same NRMS of 0.5 and the corresponding time-lapse metrics. Top panel – trace pair with poor SDR, bottom panel – trace pair with high SDR. Baseline traces – blue line, monitor traces – orange lines, difference M-B – black lines. Repeatability attributes and absolute value of traces' offset are given on the right of each panel.

Apart from computing a single value of a 4D metric per trace, we also assess the effectiveness of processing procedures by computing NRMS in a 60 ms running window for a subset of traces (as shown in Figure 6-11). This gives us a trace of NRMS for a pair of traces from two vintages so that we can see how NRMS changes along a trace.

Tracking 4D signal down the processing workflow is harder than tracking 4D noise as we have parts of the record where only noise is present, while the signal is always contaminated by the noise. We estimate 4D signal on the CDP-stacked images by computing RMS amplitudes of the differenced volumes in a window centred at the horizon that represents the top of the injection interval. We then estimate a mode value of the obtained map of RMS (noise level) and divide the map by this value. We thus get the following quantity $\frac{s+n}{n}$, which approaches an estimate of 4D SNR for the CDPs that contain 4D signal – $s \gg n$.

6.3.1 Reflections on the data preparation for time-lapse QI

We only slightly touch the subject of QI in this work, however, we feel that there need be some discussion on the quality of the data prepared for 3D or 4D QI. In this subsection we outline some major considerations which we shall take into account.

Preparation of the data for quantitative interpretation can depend upon the anticipated QI technique to be applied. If we talk about the industry standard approach to QI (full-offset/angle stacks/gathers attributes and inversions) then we shall concentrate on the primary reflections. Reflected amplitudes should be prepared for the inversion and rock-physics workflows. Whether it is a 3D or a 4D seismic, the main steps of the data preparation for 3D or 4D QI are similar. However, the employed techniques can be somehow different as the definitions of time-lapse signal and noise

are somewhat different from those for 3D seismic case as described above. The main steps to produce the data suitable for 3D and/or 4D QI are:

- Firstly, primary (non-multiple) reflections should be cleared for all available offsets via the removal (up to a point of a desired signal-to-noise ratio) of all the other events present on a seismic record (multiples, non-correlated noise, conversions, source-generated noise) - basically denoise should be applied. However, during this denoise original relative frequency-dependent amplitudes and phases of reflections should be preserved (vertically and horizontally at least for the target interval and the background vicinity). Also artefacts associated with the denoise application, like imprints of the impulse responses of filters, signal leakage and introduction of the additional energy into the signal, should be avoided.

- Secondly, the effects of all the linear filters associated with the wave propagation (at least we normally treat them as linear) should be deconvolved from the reflections, in particular, effective source and receiver signatures. We hope to obtain a zero-phase wavelet with a widened amplitude spectrum after this step.

- Thirdly, the frequency-dependent amplitudes and phases of the reflections should be somehow compensated for the geometric spreading effect, attenuation (inelastic and maybe scattering). These compensations may happen before, during and/or after migration.

- Fourthly, the frequency-dependent amplitudes and phases of the reflections should be repositioned to their "true" subsurface locations using static corrections and migrations.

- Finally, for 4D case cross-equalization may need to be applied somewhere in the processing sequence to minimize time-lapse seismic noise.

After all this we can expect to obtain seismic reflection images (3D) or difference reflection images (4D) which would have their amplitude and phase variations correspond only to the variations of the incidence angles of the waves and elastic properties of the medium (including tuning effect) for 3D and the time-lapse variations of the elastic properties for 4D. These elastic properties (or their changes) will, in turn, relate to the rock-physics properties (or their changes) of the underlying geology.

6.4 Processing workflow for time-lapse field data

We use only three (B, M3, M4) out of five seismic vintages for most of this study for the sake of compactness of presentation. To justify the choice of B vintage we refer to the pre-injection feasibility studies done prior to the field operations for Stage 2C. The rock physics model (Caspari et al. 2015) predicts rapid decrease of the reservoir stiffness once CO_2 saturation reaches several percent. Numerical modelling by Glubokovskikh et al. (2016) suggests correlation between the plume thickness and the RMS amplitudes of the plume reflection. Thus, the time-lapse signal depends on the spatial configuration of the CO_2 plume (thickness and location) rather than on saturation. We conclude that B should be used in this study to capture most of the plume signal.

We now require two monitor vintages: one with the best repeatability of acquisition to benchmark the repeatability we can achieve, and the other one with the worst repeatability of acquisition. The blue curves in Figure 6-8 are histograms of the cross-correlation maxima for all the monitor vintages against the baseline vintage. The other three vintage pairs are quite similar to each other. For each trace, we choose the

minimum value of cross-correlation coefficient among all the four vintage pairs. The orange curve in Figure 6-8 is a cumulative histogram of such values. We see that M1, M2 and M3 are much more similar to B compared to M4 (dash-dotted blue line) and M4 contributes most of the values to the orange curve.
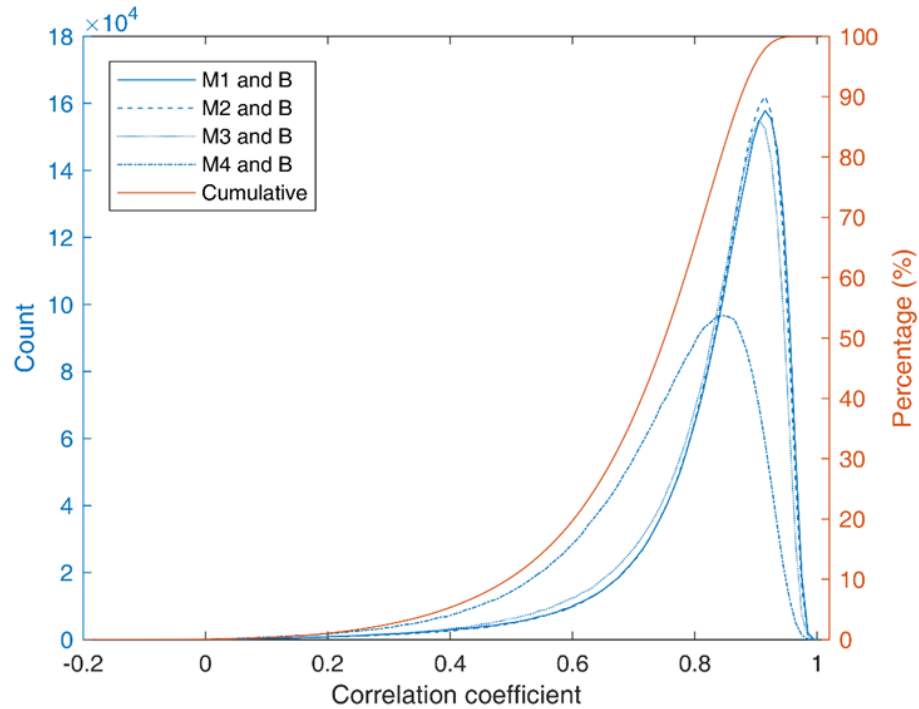
Figure 6-8: Histograms of the maxima of cross-correlation functions for all the vintage pairs shown in the figure legend (blue curves) and a cumulative histogram of the minima among the maxima of cross-correlations for each trace (orange curve).

Figure 6-8 and our initial studies suggest that out of all the surveys acquired for Stage 2C, M3 has the best initial repeatability and M4 the worst. The near-surface effects are the most similar for B and M3, because both vintages were acquired in March of consecutive years hence ground water level and weather conditions were similar. On top of that, M3 was acquired after the end of injection so we expect the 4D signal to be of the maximum possible energy. On the other hand, M4 was acquired in January so we expect larger variation of the near surface compared to B and M3. Another issue with M4 is the reduction of push down pressure of the vibrator trucks.

111

Even though the sweep parameters were identical to those used in previous surveys, the shape of the wavelet was changed and repeatability deteriorated (Pevzner, Urosevic, Popik, Tertyshnikov, et al. 2017).

In the following we use B, M3 and M4 to illustrate the repeatability evolution through processing and substantiate the final workflow for all data sets.

6.4.1   Repeatability of the raw data

We use theoretical pilot sweep to correlate the vibrator records. To prepare the data for time-lapse analysis we apply geometry and bin the data into 7.5 by 7.5 m bins with the maximum CDP fold reaching 200 (Figure 6-9). We process all the vintages on a flat datum of 30 m (legacy value), where we shift receivers and sources by application of elevation statics with the velocity of 1800 m/s. We refer to such datasets as the raw data.
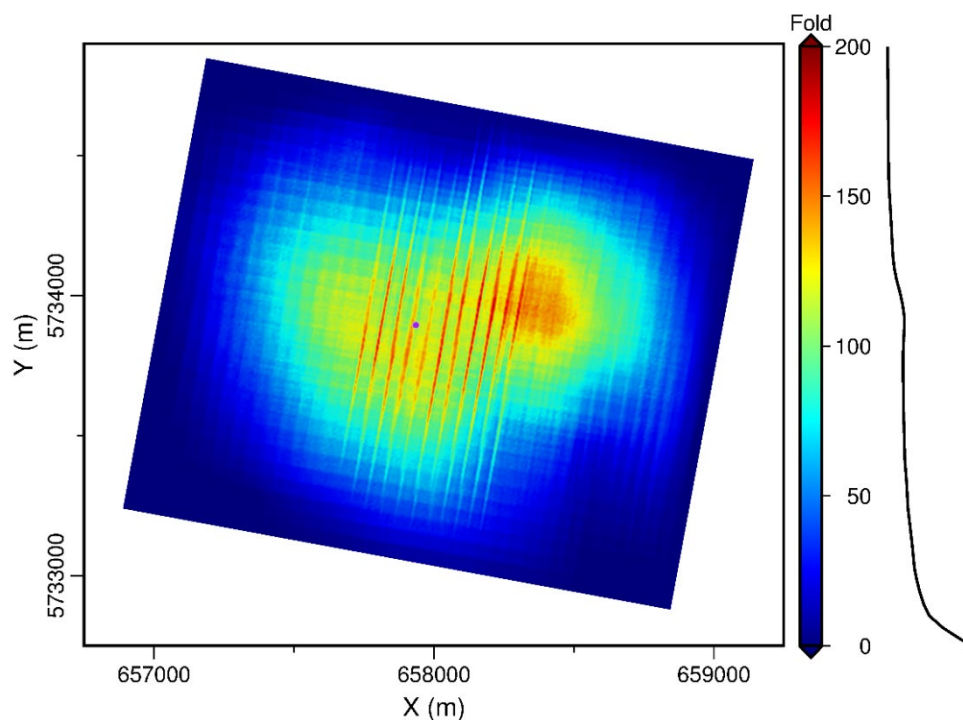
Figure 6-9: CDP fold map and its histogram (black curve on the right). The data are binned with 7.5 by 7.5 m step with the maximum CDP fold reaching 200. The CDP

fold above the target area does not drop below 100. Anomalous near-vertical red stripes of high fold are due to one source line aligned with the receiver lines.

Figure 6-10 shows common-shot gathers for two receiver lines and source position 11040 (red bars in Figure 6-13). The left panel shows the baseline record, while the other two panels show the differences M3-B and M4-B. The colour scale is the same for the panels. We see that the (M3, B) pair is more similar, since ground roll, converted waves and reflections are less pronounced in the difference seismogram. However, the ground roll is still strong at small offsets, which means that we should suppress ground roll individually in each vintage to reduce 4D noise. As expected, the pair (M4, B) is less repeatable and we see strong energy remaining after the subtraction for all the components of the wavefield.
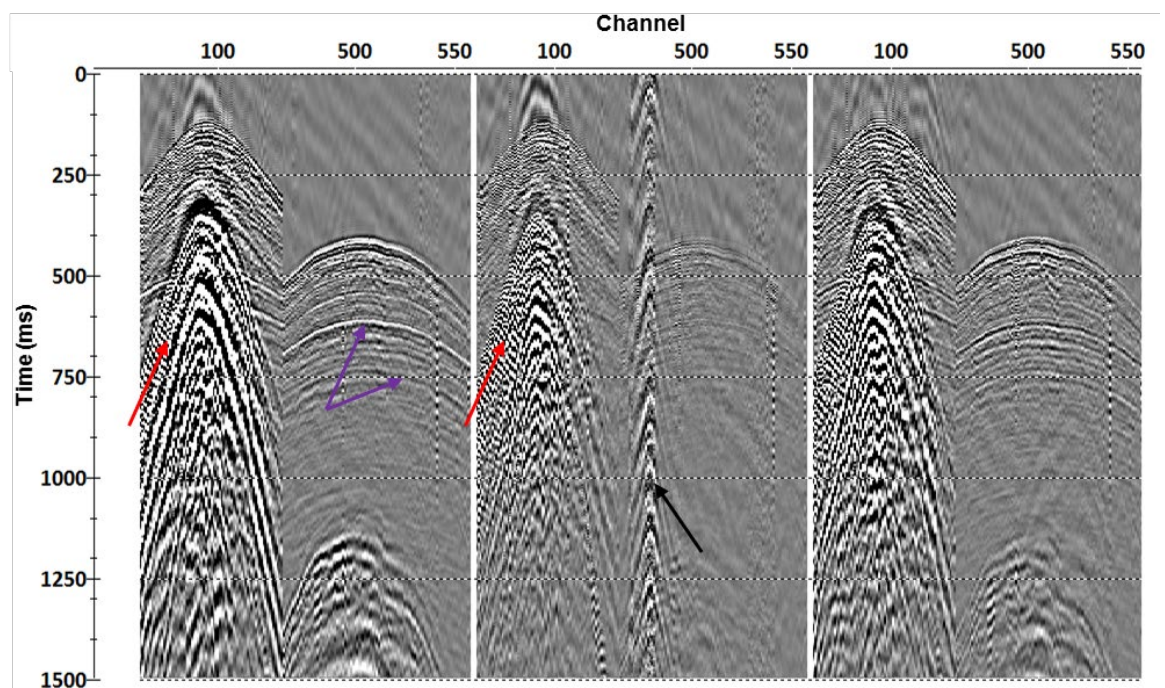
Figure 6-10: Raw seismic gathers recorded onto two receiver lines of a single shot. Left panel – B, middle panel – M3-B, right panel – M4-B. Red arrows indicate strong residual source-generated noise, purple arrows indicate a strong and a weak reflection, and the black arrow indicates a strong noise event present only on one vintage.

A rather comprehensive study of the repeatability of seismic records and stacks representative of the Otway Site has been done during the previous stages of Otway Project (Pevzner, Shulakova, et al. 2010, Shulakova et al. 2014). Thus, we do not focus on the analysis of the raw wavefield but rather deal with repeatability estimates for the sake of tracking it through the processing workflow. We start by computing NRMS in a 60 ms running window (Figure 6-11) for the traces shown in Figure 6-10. The dark blue colour corresponds to relatively good repeatability according to NRMS while yellow indicates relatively poor repeatability. We clearly observe a deterioration of repeatability for the (B, M4) pair compared to (B, M3). We note that repeatability largely depends upon the energy of the events present in the window of estimation rather than represents the amount of time-lapse noise. That is, two windows with considerably different levels of differential energy (different levels of 4D noise) can yield the same repeatability values. In particular, if a strong event is present in both vintages (e.g., ground roll), it will yield the best repeatability measure even if the actual 4D noise is strong (red arrows in Figure 6-10 and Figure 6-11). Another notable thing is that weak repeatable reflections and strong repeatable reflections from the same shot exhibit different values of repeatability, possibly due to ambient noise (purple arrows in Figure 6-10 and Figure 6-11).

Thus, we conclude that the ambient noise level noticeably influences repeatability. Finally, we note that repeatability metrics respond well to the strong spurious events present only on one of the vintages (black arrow in Figure 6-10 and Figure 6-11). These observations support the idea mentioned above of complementing repeatability measures by estimating RMSDIF and tracking this quantity through processing.
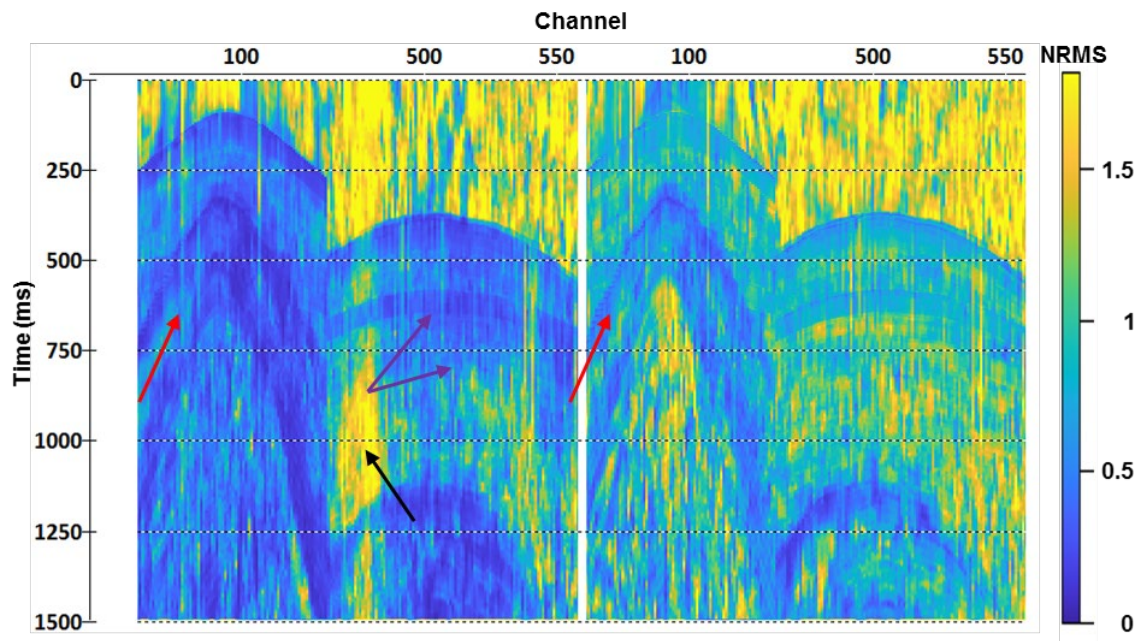
Figure 6-11: NRMS computed in 60 ms window for the data from Figure 6-10. Left panel – M3 vs B (corresponds to the middle panel of Figure 6-10), right panel – M4 vs B (corresponds to the right panel of Figure 6-10). Arrows indicate the same events as in Figure 6-10.

Commonly used approaches to measuring repeatability of pre-stack data focus on repeatability estimations of either direct arrivals or reflections. Direct arrivals can be useful when geophones are buried deep enough (e.g., 30 m) to discern ground roll and direct waves for the events that propagate through the near surface sub-vertically (Bakulin et al. 2014, 2015). As the geophones in our study are buried only 4 m deep, we use the energy of reflections above the injection interval. We base our choice of window for estimation of 4D metrics on the study done for the Ketzin geosequestration project. Bergmann et al. (2014) used relatively large windows (about 500 ms) centred on the interval with reflections of interest, although they note that there are multiple choices yielding similar estimates of the TS and NRMS. We estimate repeatability of the surveys in an offset-dependent window shown in Figure 6-12. This figure shows a selection of a few shots from different shot points in the survey area with the traces

sorted by the absolute value of offset. We estimate all the 4D metrics in the window between the two red lines. This window spans the data where we do not expect 4D signal from the injection and incorporates most of the reflections at all the offsets as can be seen in Figure 6-12. The blue line approximates the top mute for 30 % NMO stretch that we apply before stacking. Even though the data above the blue line does not contribute to the final image, we still use it for estimation of more meaningful time-lapse QC parameters.
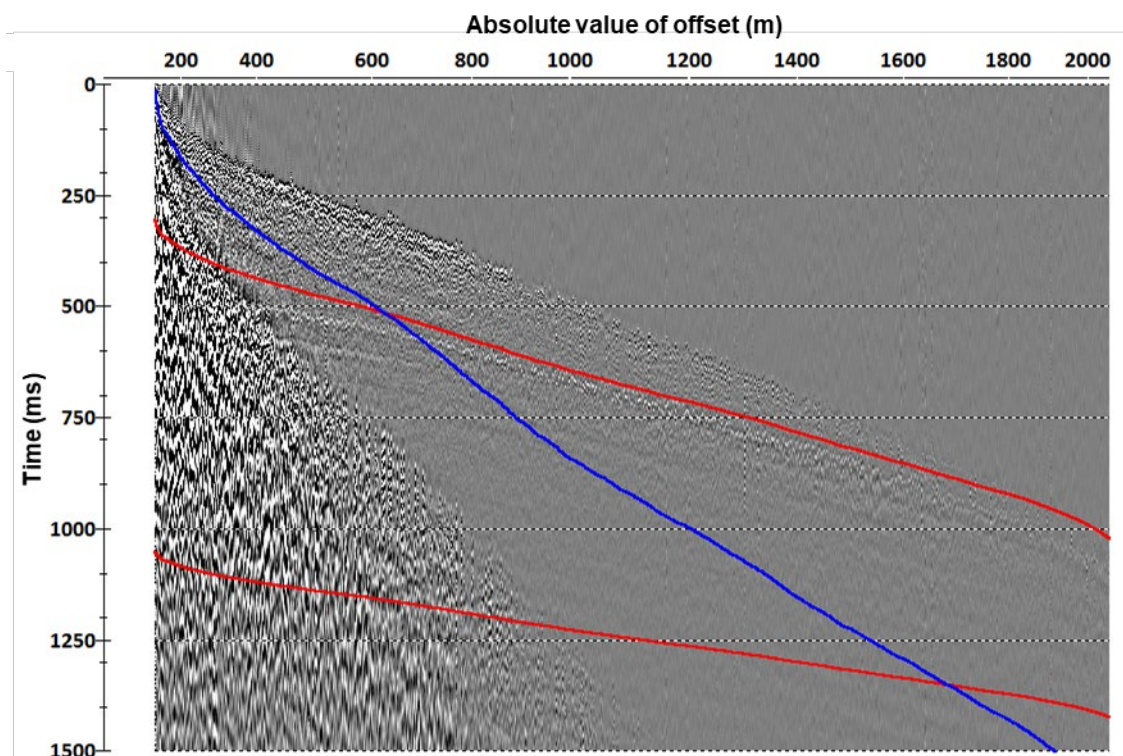
Figure 6-12: A group of traces sorted by offset. The red lines specify the time window for repeatability estimates on pre-stack data. Data above the blue line will be muted after application of NMO with 30 % stretch muting.

The initial estimates of NRMS for the raw data of (B, M3) and (B, M4) are shown in the top and bottom of Figure 6-13, respectively. We clearly observe an overall drop in repeatability for the second pair of vintages as histograms on the right suggest increase of NRMS of about 0.15 and increase of the variance of the

distribution. Circular features in Figure 6-13 are offset-dependent and appear due to the presence of ground roll in the windows for NRMS estimation.

We average NRMS for some of the domains commonly used in processing. We observe variability of NRMS with respect to the source and receiver locations for both vintage pairs (Figure 6-14). The overall repeatability for (B, M4) is generally worse than for (B, M3). The poorly repeatable shot and receiver locations are mostly the same for both vintage pairs. This indicates that these locations feature the strongest variability of the near-surface (the largest $\frac{\partial e}{\partial G}$ in equation 6-5) because repeatability of the acquisition geometry was very accurate and precise (see Section 3.2). Surface-consistent deconvolution and/or pre-stack cross-equalization are important steps in the workflow that should suppress such time-lapse noise.

We observe that for the raw data the variance of the source distribution is larger than the variance for the receiver distribution. The sources span a larger area than the receivers and, as can be seen in the north-eastern corner of the top-left panel of Figure 6-14, enter the area of high NRMS value.
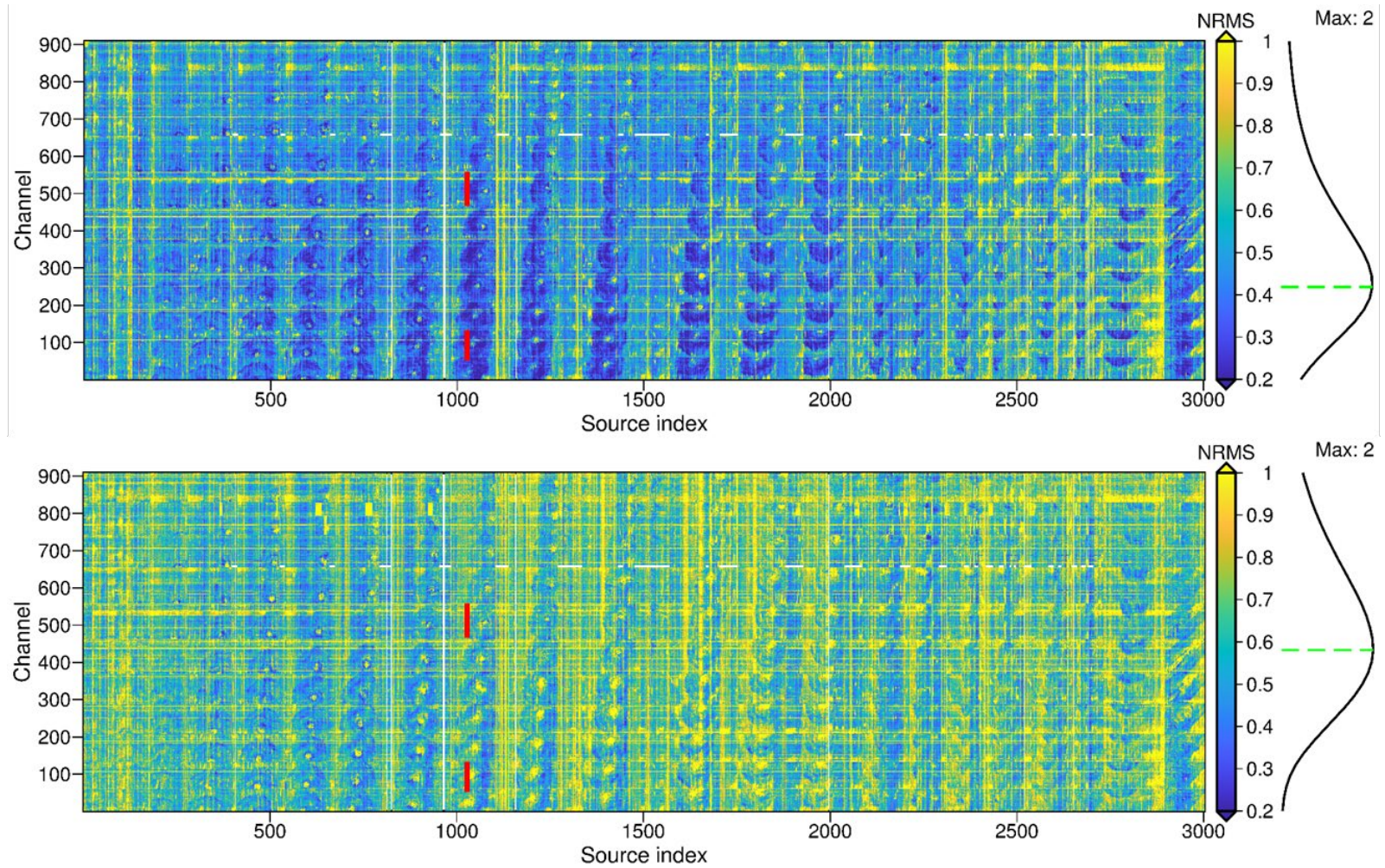
Figure 6-13: NRMS for the raw traces computed in the window shown in Figure 6-12. Top panel – M3 vs B, bottom panel – M4 vs B. The red bars show locations of the gathers shown in Figure 6-10.
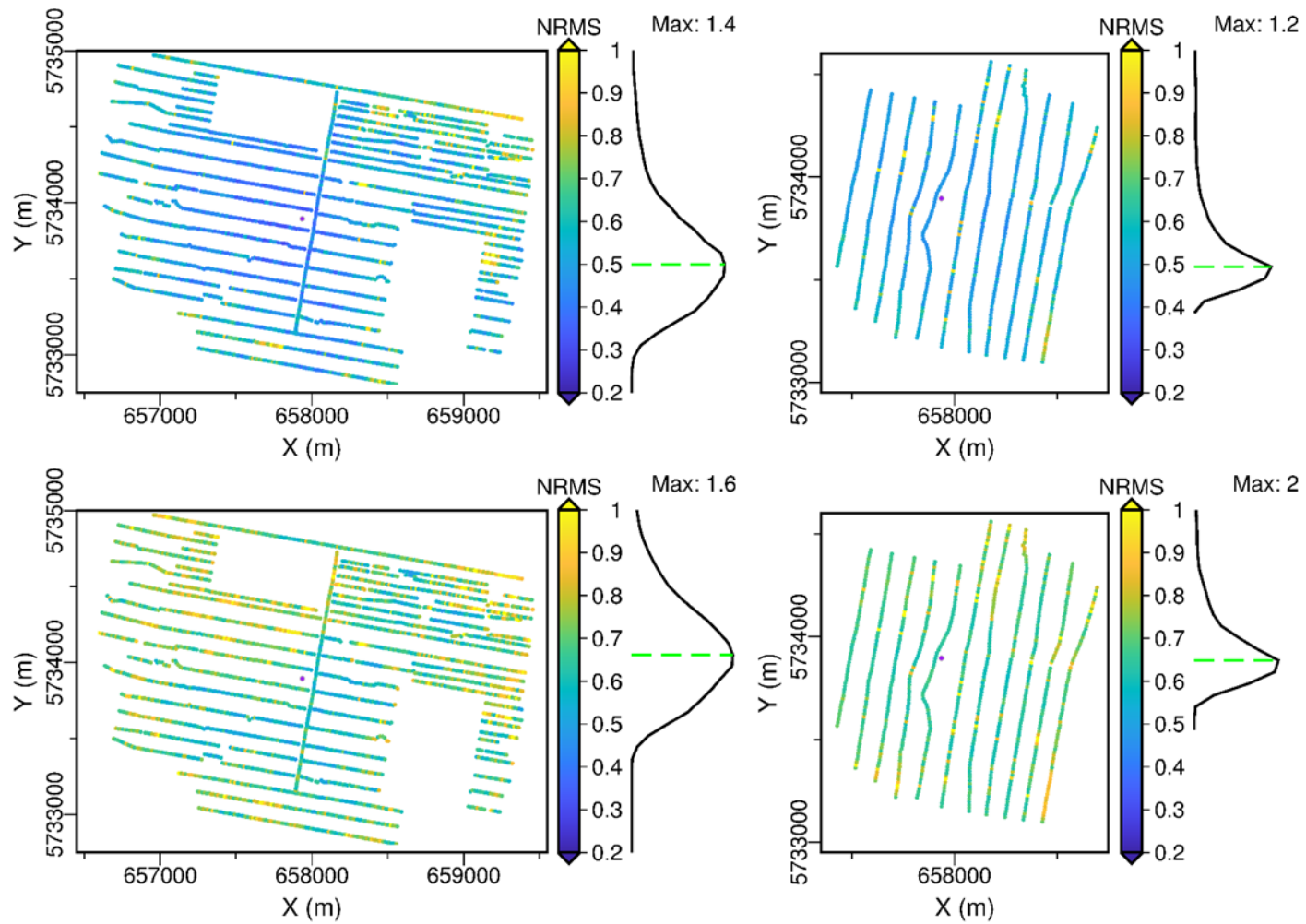
Figure 6-14: Averaged NRMS in source (left) and receiver (right) domains computed from the data of Figure 6-13. Top row– M3 vs B, bottom row – M4 vs B. The purple dot indicates the injector well CRC-2.

119

Figure 6-15 shows a 2D histogram representing the distribution of NRMS with the absolute value of offset. Again, we see poorer repeatability of (B, M4) compared with (B, M3) but the panels look very similar. In the both histograms, the trend changes abruptly at offset ~900 m. At this offset, the window for NRMS computation leaves the interval of intense coherent noise – ground roll and converted/secondary waves. Interestingly, we note that NRMS is higher for the area without ground roll compared to the area with ground roll contamination (red oval). This, together with the observations from the right panel of Figure 6-15, confirms that events of high energy (ground roll direct waves and converted/secondary waves) can yield low NRMS values while bringing a considerable amount of 4D noise.
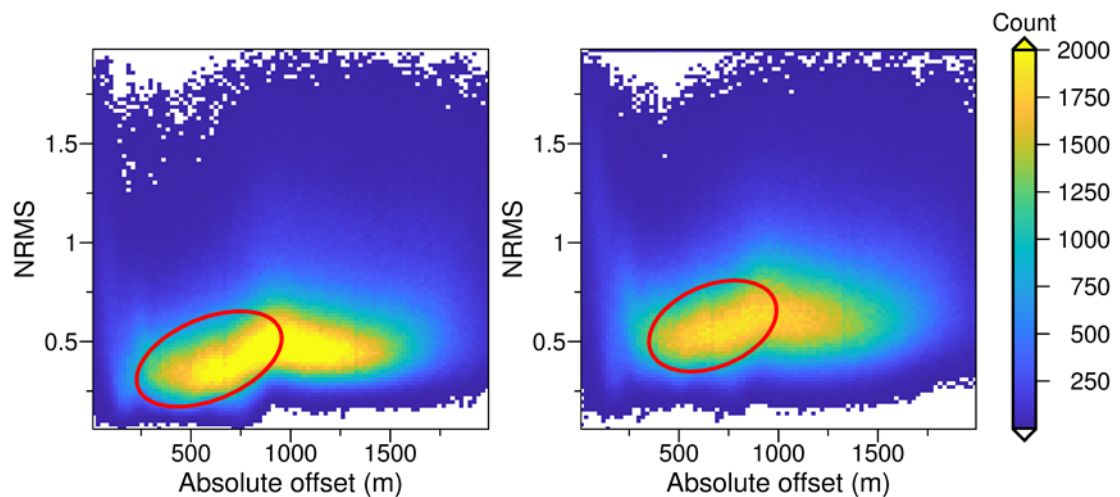
Figure 6-15: 2D histograms showing the dependence of NRMS on absolute value of offset computed from the data of Figure 6-13. Left panel – B vs M3, right panel – B vs M4. The red oval indicates the area with low NRMS values due to the presence of ground roll.

As we demonstrated, NRMS may be an ambiguous measure to represent 4D noise and track it through the processing workflow. Thus, we complement NRMS by using three more attributes: TS, SDR and RMSDIF. We compute all these attributes trace by trace for each vintage pair in the window shown in Figure 6-12. Figure 6-16

shows the 2D histograms of the crossplots of these attributes for the raw vintage pairs (B, M3) (top row) and (B, M4) (bottom row).

We use this kind of plots throughout the chapter to track the 4D noise through processing stages, so it is important to understand how to interpret them. The top row is always for (B, M3) and the bottom row is always for (B, M4). The left column shows 2D histograms for TS vs NRMS crossplots. The closer the 2D histogram values cluster to the zero NRMS and zero of TS the lower the 4D noise is. The middle column shows 2D histograms for SDR vs NRMS crossplots. In this case lower values of NRMS and higher values of SDR indicate low 4D noise. Finally, the right column shows 2D histograms for RMSDIF vs NRMS crossplots. In this case, clustering of 2D histogram values closer to the zero NRMS and zero of RMSDIF indicates low 4D noise. Thus, we can build these plots for the data areas without 4D signal after different processing steps and see how these processing steps affect 4D noise.

Figure 6-16 clearly shows better repeatability for (B, M3) compared to (B, M4) as confirmed by smaller TS, higher SDR and lower NRMS for the former vintage pair. The red oval in the top panel of Figure 6-16 highlights the data with small NRMS and large SDR which is not present in the top panel of the same figure. The purple oval in Figure 6-16 depicts the values of a very poor repeatability that are present in M4 and absent in M3. The RMSDIF does not show as much difference between the two cases. A green oval indicates a typical feature of the RMSDIF vs NRMS plot. In accordance with our observations from Figure 6-10 and Figure 6-15, the green oval in the low NRMS range corresponds to the ground roll, which gives rise to the high energy in the difference seismic, while the NRMS values still indicate good repeatability.
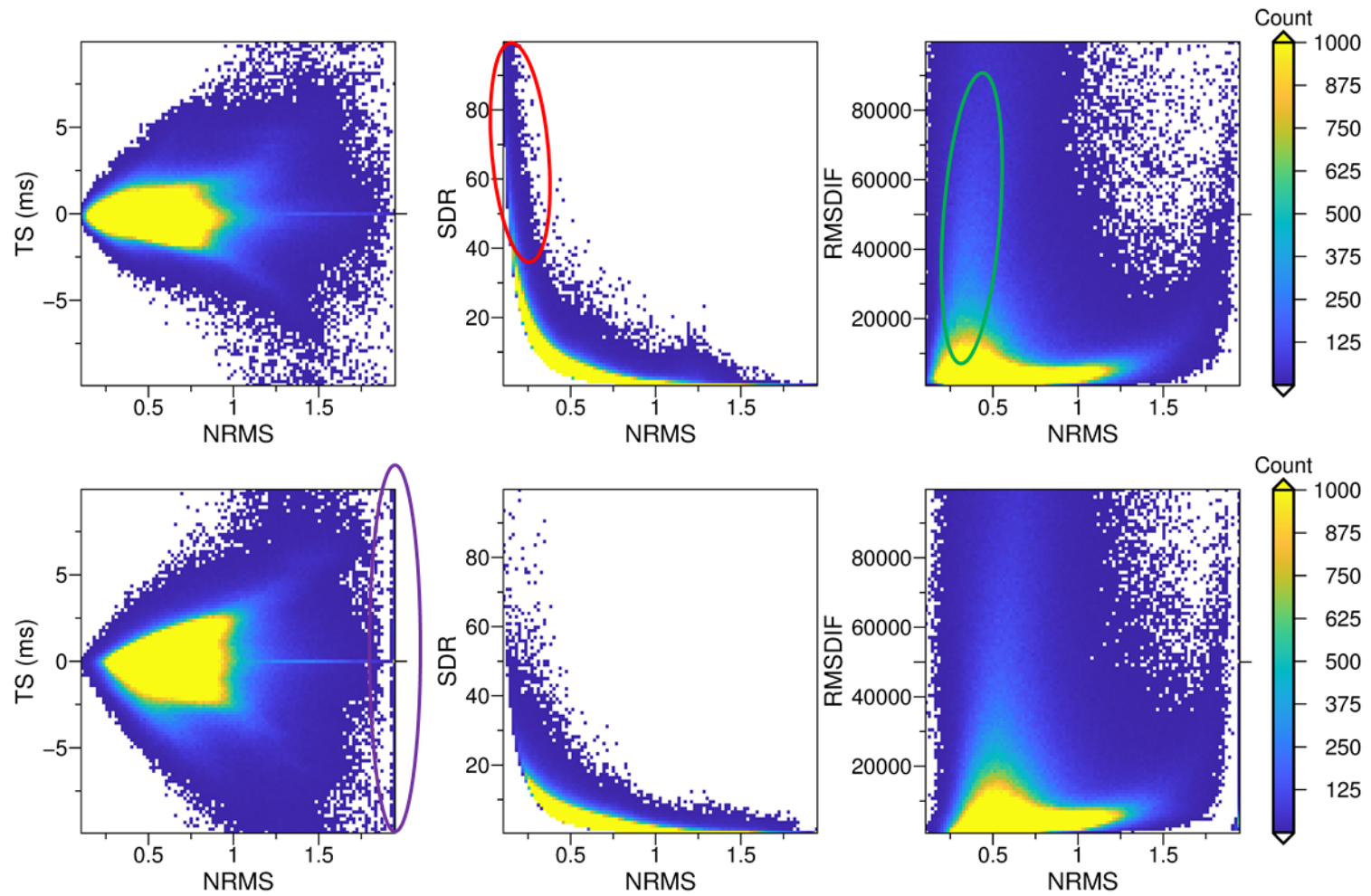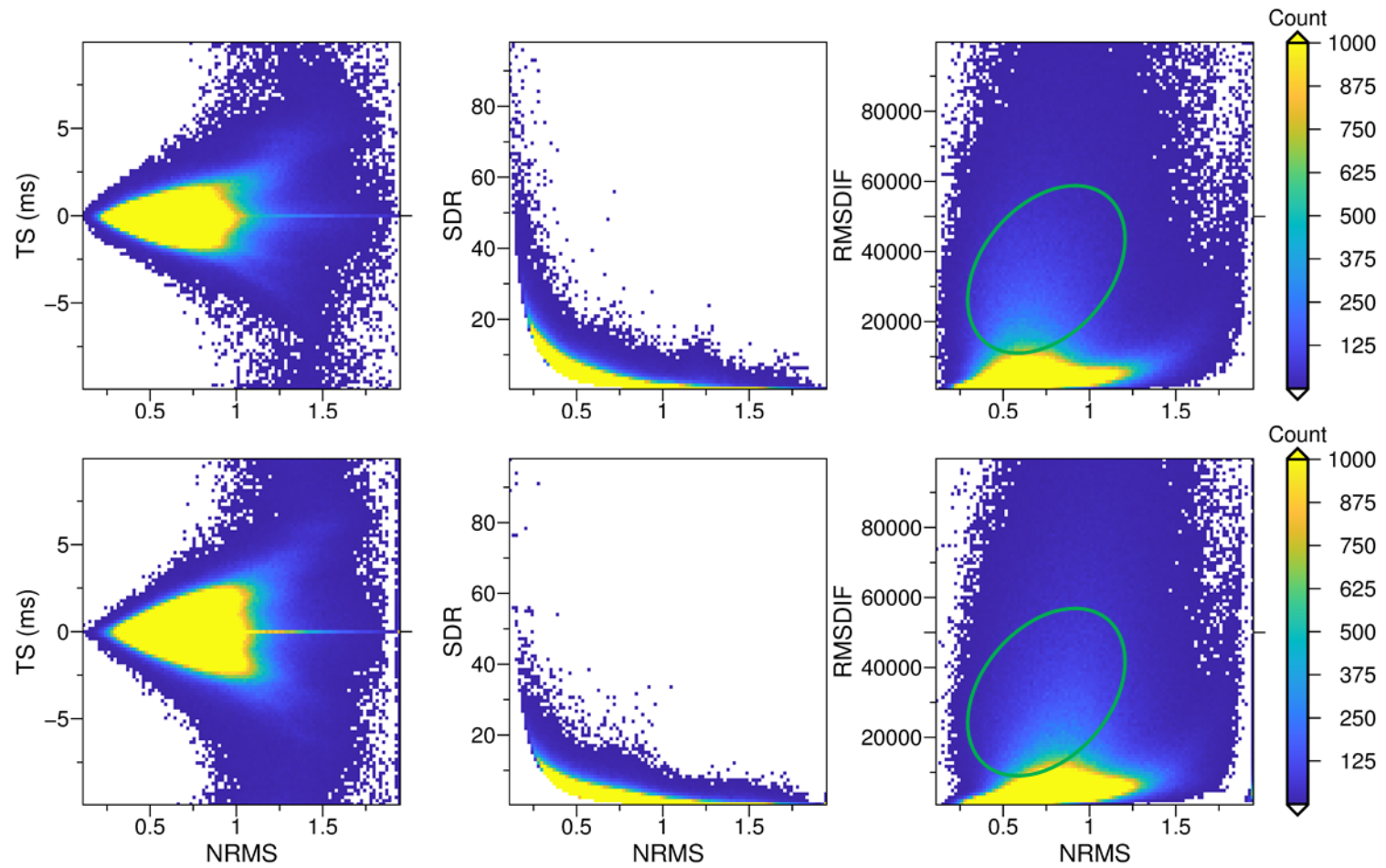
Figure 6-16: 2D histograms of repeatability measures for the raw data. Plots of TS vs NRMS (left), SDR vs NRMS (middle), RMSDIF vs NRMS (right). Top row– M3 vs B, bottom row – M4 vs B. Ovals are referred to in the text.

We can now check how the data at a given processing stage look after stacking. We compensate for geometrical spreading, apply a mild bandpass filter and residual static corrections, followed by NMO with 30 % stretch mute and stacking. Figure 6-17 shows maps of CDPs coloured by NRMS values computed in a 400–900 ms window for (B, M3) and (B, M4) pairs. The window is chosen above the plume level and spans from 400 to 900 ms for each trace (the plume is at about 1210 ms). We note that both panels exhibit similar internal patterns of NRMS distribution in space throughout the area except for the large area surrounded by the red oval in the right panel. NRMS of (B, M4) increases significantly relative to the (B, M3).

Figure 6-18 shows the corresponding 2D histograms of all the time-lapse attributes. Again, distribution of TS is wider for the (B, M4) pair as the large histogram values at the level of zero time shift inside the purple oval are due to the time shifts running beyond the threshold during computation of time shifts and being zeroed. There are many more such values for (B, M4) compared to (B, M3). The residual amplitude of noise is also higher for (B, M4) as shown in the green oval.

As we cannot identify plume on the brute stack data, we apply an FXY filter to the stacked volume and run finite-difference 3D time migration. Only then we can observe the time-lapse signal as shown in Figure 6-19.
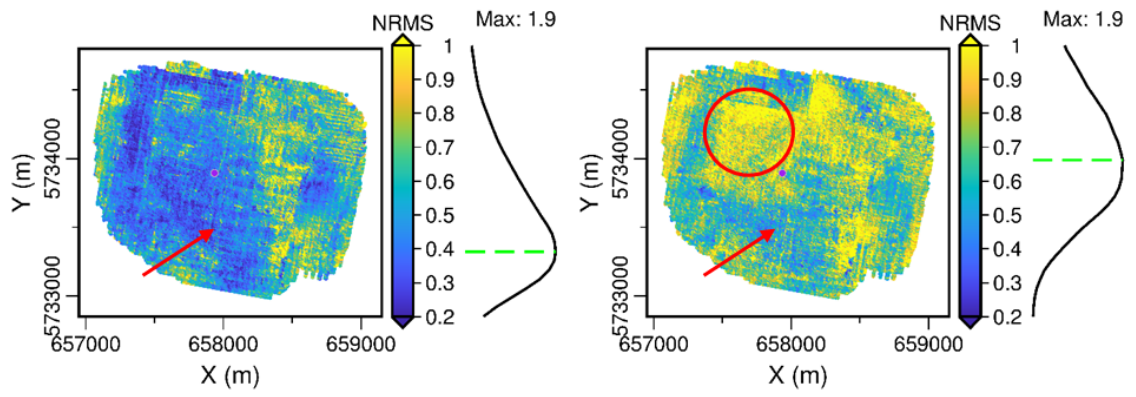
Figure 6-17: NRMS for CDPs with stacking fold above 4. NRMS is computed in a window from 400 to 900 ms on the raw stacked data. Left panel – B vs M3, right panel – B vs M4. The purple dot indicates the injector well CRC-2.
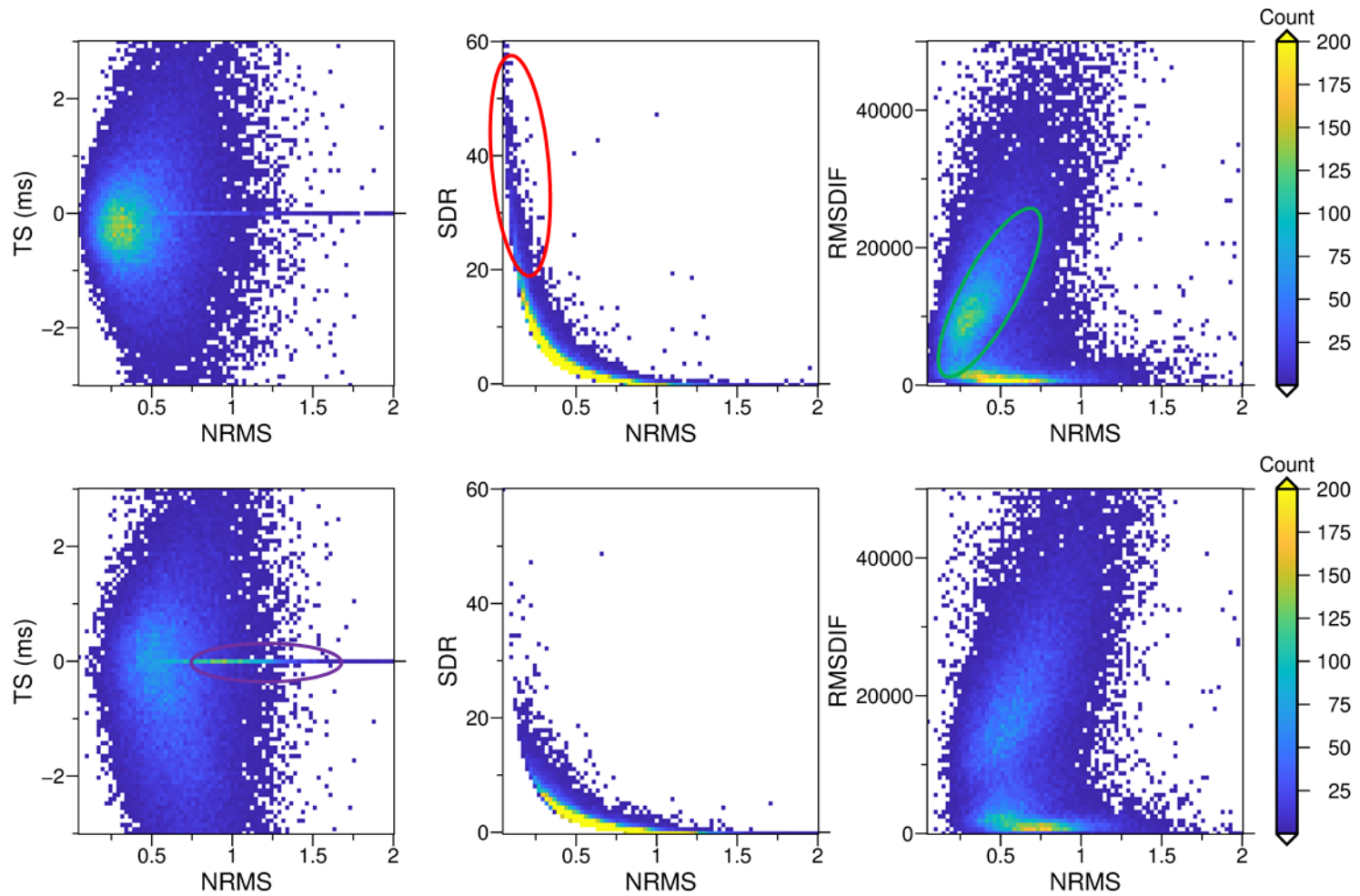
Figure 6-18: 2D histograms of repeatability measures for the raw data after stacking. Plots of TS vs NRMS (left), SDR vs NRMS (middle), RMSDIF vs NRMS (right). Top row– M3 vs B, bottom row – M4 vs B. Ovals are referred to in the text.
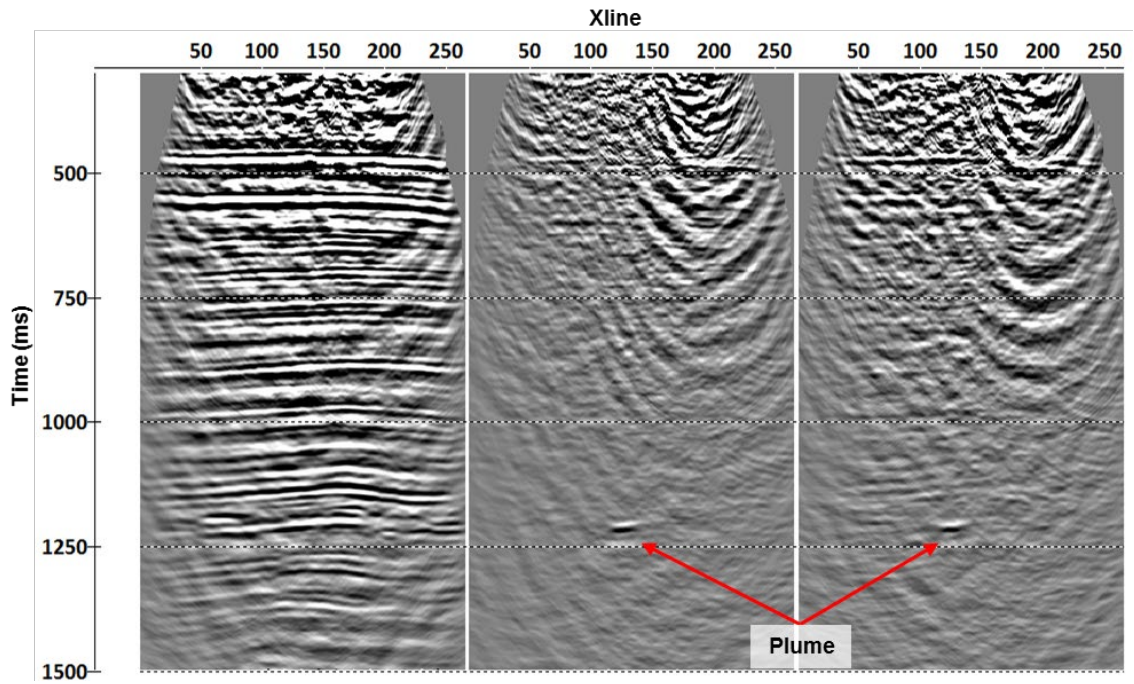
Figure 6-19: Section of the migrated brute stack through Inline 110. FXY deconvolution is applied after stacking. Left panel – B, middle panel – M3-B, right panel – M4-B.

Most of the previous plots represent 4D noise in the data. Now we show how we QC 4D SNR of our data. Once we have the difference seismic images, we compute the RMSDIF attribute in 24ms window centred at the injection interval of 1210ms, which contains most of the reflected energy from the plume. We then divide these amplitudes by the mode (most common) value of the same RMSDIF amplitude slice, which we consider as a representation of noise level (as our signal is localised in space and most of the slice contains noise amplitudes). We thereby obtain a measure of 4D SNR for the CDPs containing the signal. We note that the window chosen for computation of the RMS amplitudes strongly affects values of 4D SNR. Thus, we keep the window strictly the same for entire processing flow. Figure 6-20 shows a close-up of plume images expressed as 4D SNR for (B, M3) and (B, M4) vintage pairs. As expected, SNR and plume definition is better for the (B, M3) pair compared to (B, M4).

126

Below, we present some findings on the processing stages that the final workflow needs to account for.

Ground roll and source-generated shear waves render intense time-lapse noise into difference cubes. They carry strong energy that can seem repeatable according to the values of repeatability measures such as NRMS (Figure 6-15), while actually rendering severe noise into differences between the vintages (mid and right panels of Figure 6-10, right panels of Figure 6-16). We do not expect any reflection-matching cross-equalization to reduce 4D noise associated with these events for the following reasons:

- ground roll does not manifest itself as a seismic wavelet (neither phase nor amplitude) and being a surface wave has a different nature compared to body waves. Though not tested by us, we speculate that one can derive a ground roll noise model from one of the vintages (or average ground roll noise models among all of the vintages) and carefully adaptively subtract (localized matching) this model from each vintage.

- source-generated S-waves have the same frequency spectrum as P-waves at the source location (Gaiser 2016, 104) but the recorded time wavelets at the receiver location may differ significantly from the P-wave wavelets in their amplitude spectrum due to the differences in the apparent attenuation (both intrinsic and scattering-induced). We can recall that even P-wave wavelets are not stationary throughout the recorded data.

Thus, we remove ground roll from individual vintages in our workflow.

The Stage 2C data feature areas of pertinent anomalously high NRMS values in the source and receiver domains (Figure 6-14). These are due to the variation of the reflected signals caused by changes in the near-surface ($\frac{\partial e}{\partial G}$ in equation 6-5) and time-lapse change in the wavelet due to variation in coupling and excitation/recording parameters (Δw in equation 6-5). Surface-consistent deconvolution (SCD) is likely to partially compensate for Δw. The wavelet Δw occurs at each source and receiver (trace) location due to variation in the effective source and receiver signatures between a pair of vintage surveys. This wavelet has two components: a global component for all shots and/or receivers (global mismatch between two surveys) as well as a local (short, mid or long wavelength) component. SCD done independently on vintage surveys will not compensate for the global component of Δw but can compensate for the local component because it brings the amplitude spectra of different sources and receivers to the same shape common to a given survey.

Even mere location of the 4D signal is hard prior to migration because the injected plume is small and manifests in unmigrated seismic records as a diffractor rather than a specular reflector. Thus, we QC the effect of processing procedures on 4D signal based on the plume occurrence in the imaged cubes.
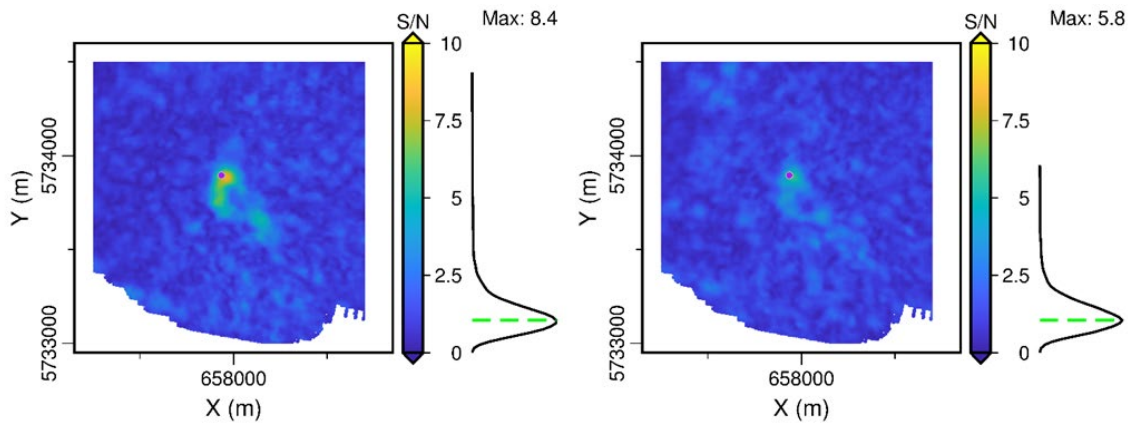
Figure 6-20: Plume images in the stacked and migrated raw data. SNR map is obtained by computing RMS amplitude in 24 ms window centred at 1210 ms and normalizing the values by the mode value. Left panel – M3-B, right panel – M4-B. The purple dot indicates the injector well CRC-2.

6.4.2 Ground roll suppression

To assess the influence of ground roll on the plume image, we first separate the data covered and not covered by ground roll. We estimated the first arrival times of ground roll from the baseline field survey and use these times to separate the B and M3 data into two parts: a far-offset part after bottom mute (left panels of Figure 6-21 and Figure 6-22) and a near-offset part after top mute (right panels of Figure 6-21 and Figure 6-22). We stacked and migrated both of these datasets and observed the plume on both images.

Both panels of Figure 6-22 are normalized by the same amplitude value so the strength of the plume reflection could be compared between far (left panel) and near (right panel) offsets. Amplitudes of the plume reflection are of similar strength on both panels of Figure 6-21 and Figure 6-22 while the noise level is much stronger for the near-offset case due to the presence of ground roll. This indicates significant potential gain in the 4D signal after ground roll removal.
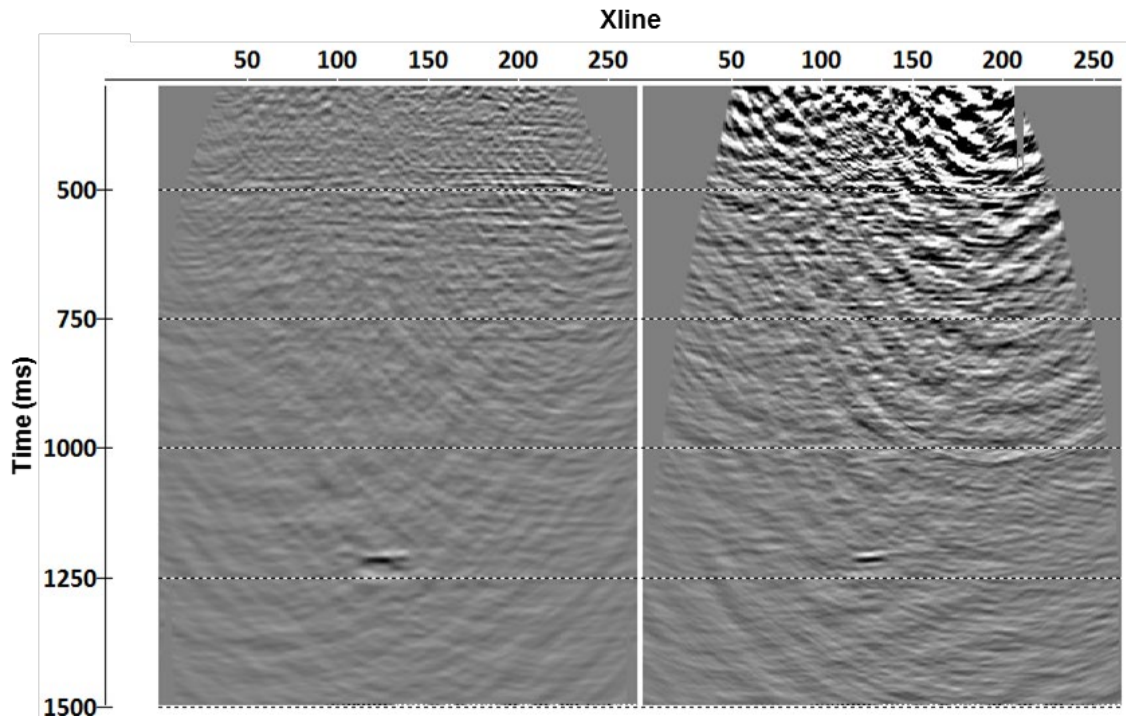
Figure 6-21: Sections of the migrated brute stack through Inline 110 for the difference between M3 and B. FXY deconvolution is applied after stacking. Left panel – bottom mute case to remove ground roll. Right panel – top mute case to retain the data covered with ground-roll.
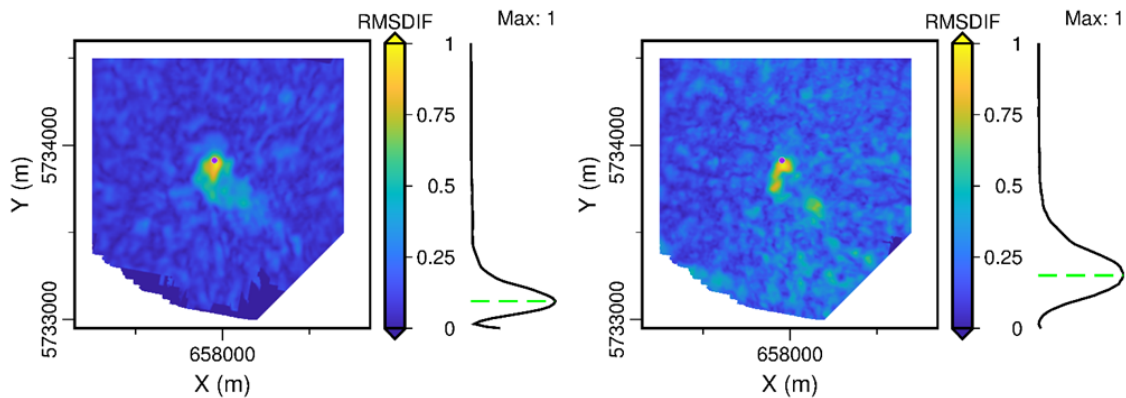
Figure 6-22: Plume images in the stacked and migrated raw data (M3, B). Left panel – bottom mute case to remove ground roll. Right panel – top mute case to retain ground-roll covered data. Both images are normalized by the same value of amplitude to allow for comparison between the plumes. The purple dot indicates the injector well CRC-2.

We apply ground roll removal based on singular value decomposition (Cary and Zhang 2009). At the first stage the routine uses singular value decomposition of the data in a localized space-time window to estimate ground roll. At the second stage the modelled noise is adaptively subtracted from the input data. Unlike Radon and FK filtering, this technique can efficiently deal with spatially aliased data and irregular trace sampling. As this technique is data-dependent we must be careful to avoid removing the plume from the data covered by ground roll at near offsets. To ensure careful preservation of the signal, we stack the removed noise in the CDP domain (as if processing the signal), migrate it and observe no coherent signal in the difference seismic that may be attributed to the plume. We apply this routine independently to each vintage keeping its settings the same. This means that the routine is still data-driven but the way it adapts to the data is fixed the same for all the vintages.

Figure 6-23 shows the same traces as Figure 6-10 after application of ground roll removal. We observe general reduction of the energy of ground roll on time-lapse differences compared to the raw data (Figure 6-10). Still there remains quite a high level of noise, which is now less correlated between the adjacent traces. As can be seen from Figure 6-23, the level of noise in the baseline data (left panel) is higher than the level of noise in the differences (particularly M3-B), which indicates that the remaining ground roll energy is likely to be repeatable.
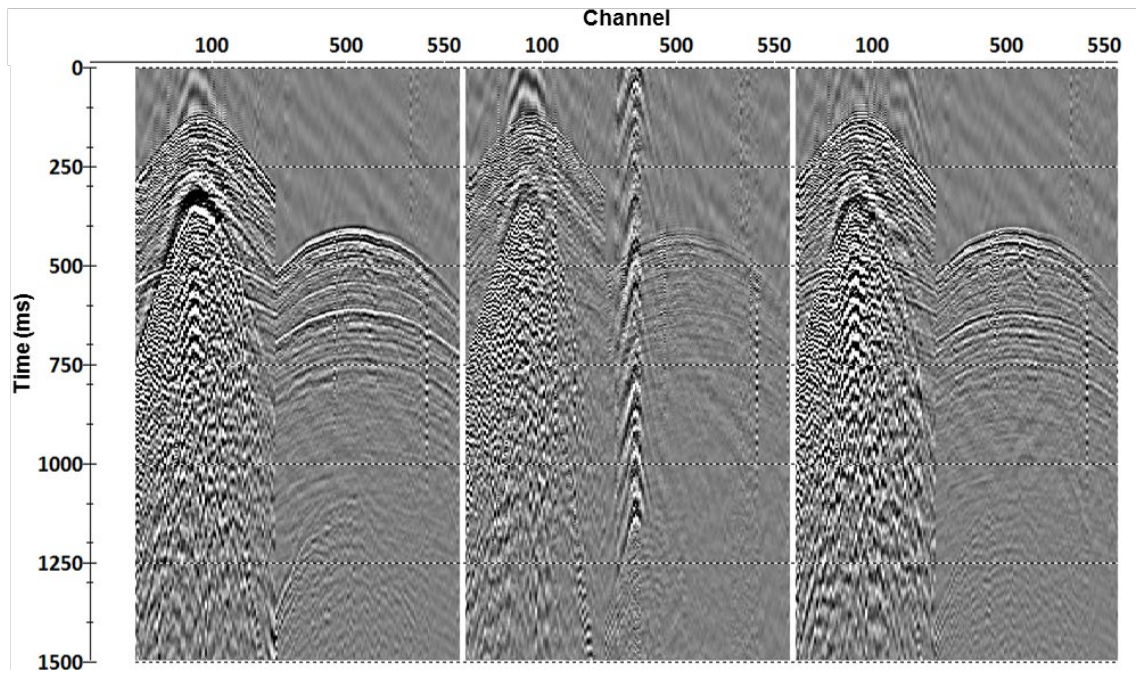
Figure 6-23: Seismic gathers after ground roll removal for two receiver lines of a single shot. Left panel – B, middle panel – M3-B, right panel – M4-B.

We repeat the same sequence of data QC as we have done for the raw data to check how repeatability of the samples has changed due to suppression of surface waves. Figure 6-24 shows NRMS computed in a running 60 ms window. We observe a general increase of NRMS even though the energy of 4D noise has been reduced (compare the middle panels of Figure 6-10 and Figure 6-23).
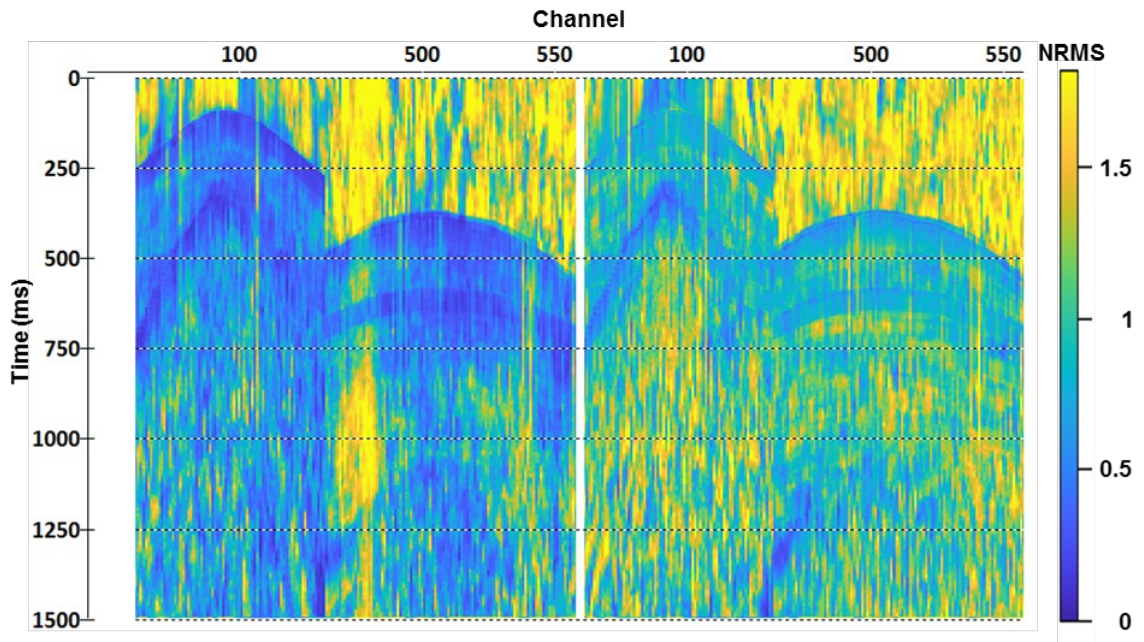
Figure 6-24: NRMS computed in 60 ms window for the data from the previous figure. Left panel – M3 vs B (corresponds to the middle panel of Figure 6-23), right panel – M4 vs B (corresponds to the right panel of Figure 6-23).

Figure 6-25 shows the estimates of NRMS for the datasets in the windows from Figure 6-12 after ground roll suppression. We note an increase in mode value of NRMS from 0.42 to 0.5 for (B, M3) and from 0.58 to 0.66 for (B, M3). We also note that circular areas of low NRMS values from Figure 6-13 have now disappeared because most of the ground roll has been removed. As shown in Figure 6-26, mode NRMS for source and receiver domains for both vintage pairs exceed those for the raw data (Figure 6-15).

Removal of ground roll has noticeably increased NRMS for the traces with small offsets (compare Figure 6-27 with Figure 6-15). NRMS is smaller before ground roll removal due to the similarity of ground roll between the vintages (due to its low frequency – small numerator in equation 6-7) and strong energy of the ground roll compared to the reflections (large denominator in equation 6-7). Once the ground roll is suppressed in individual vintages its coherency between the vintages weakens

(increase of the numerator in equation 6-7) and energy drops (decrease of denominator in equation 6-7), hence the NRMS increases. This suggests that ground roll is now more distorted between the different vintages; however, the energy of the remaining ground roll in differences has decreased as can be seen if we compare the data inside the green ovals in the right panels of Figure 6-28 and Figure 6-16. Deterioration of NRMS values due to ground roll removal affected (B, M3) stronger than (B, M4) probably because ground roll has been more similar for B and M3 (acquired during similar time of the year).

Based on the analysis of SDR vs NRMS crossplots we see that higher SDR values in Figure 6-16 were sourced by the traces covered by ground roll, as such high SDR values are no longer present in the data after ground roll has been suppressed (SDR vs NRMS plot in Figure 6-28). SDR, being a cross-correlation based metric, decreased due to the same reason as the numerator of NRMS increased – residual ground roll is more distorted between the vintages. TS is not indicative of the effect of the ground roll removal on 4D time-lapse noise.

We note that measures of TS, NRMS and SDR are meaningful when they are computed for windows dominated by primary reflections that are stronger than any of the noise contributors embedded in ($n_2 - n_1$), such as ambient noise and ground roll. It means that these measures should be more meaningful when computed for the stacked data as reflections get emphasized after stacking.

We conclude that removal of ground roll is quite efficient in removing 4D noise even though some of the repeatability measures (NRMS, SDR) indicate "worsening" of repeatability (see the next paragraph). Also, surface-consistent deconvolution benefits from the suppressed ground-roll, because its theoretical model does not properly account for ground roll. Finally, we note that the approach used to suppress

ground roll may affect the behaviour of the metrics, e.g. in the ideal case when ground roll is removed to an extent such that the near-offset reflections are revealed and preserved – the time-lapse noise measures will become indicative of the actual wavelet mismatch between the vintages ($n_2 - n_1$ is small).
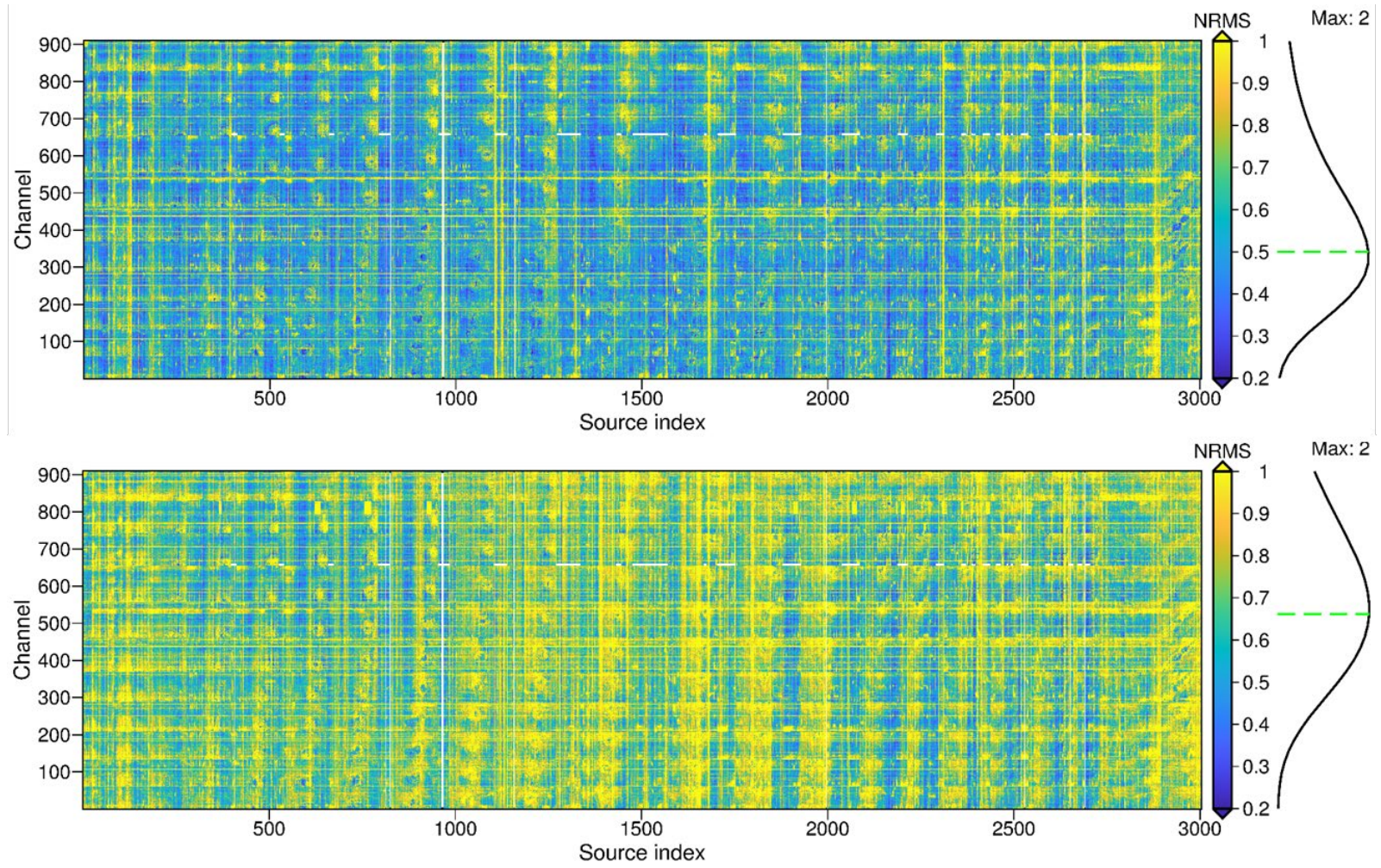
Figure 6-25: NRMS for the traces after ground roll removal. Top panel – M3 vs B, bottom panel – M4 vs B.
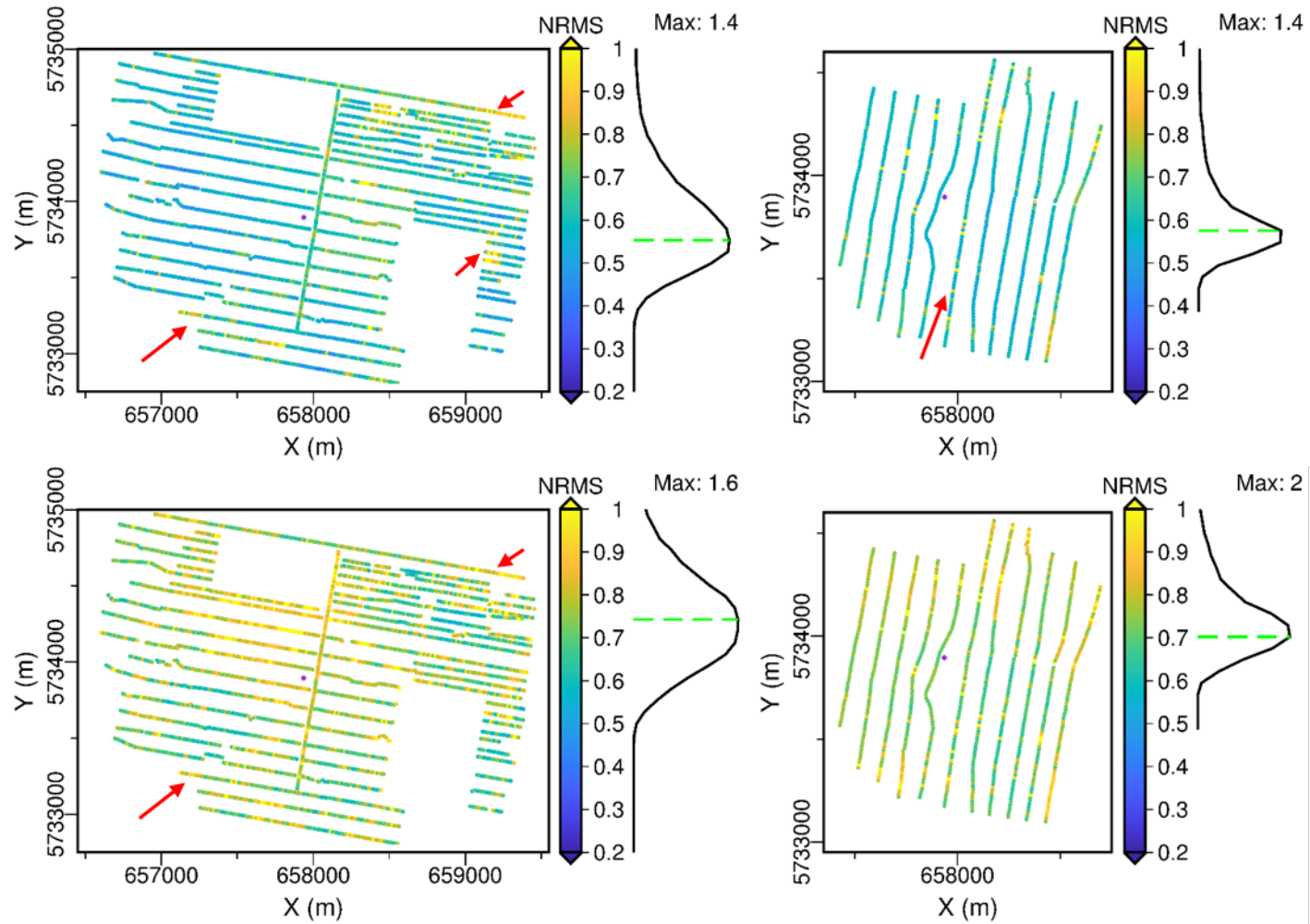
Figure 6-26: NRMS mean in source (left) and receiver (right) domains computed for the traces after removal of ground roll. Top row– M3 vs B, bottom row – M4 vs B. The purple dot indicates the injector well CRC-2.
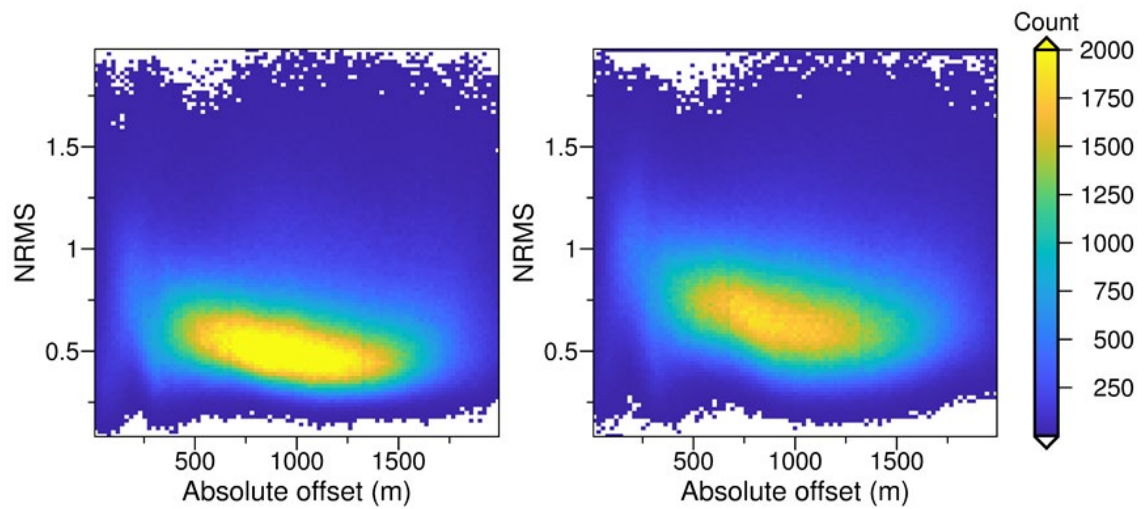
Figure 6-27: 2D histograms showing dependence of NRMS on absolute value of offset for the traces after removal of ground roll. Left panel – B vs M3, right panel – B vs M4.

We now stack the data to check the effect introduced into the 4D noise and plume image due to the removal of ground roll. Stacking and migration are done using the same workflow as has been used for the raw data. Figure 6-29 confirms an increase of NRMS values for both (B, M3) from 0.39 to 0.52 and (B, M4) from 0.67 to 0.72. Interestingly, the overall increase of NRMS due to removal of ground roll is larger for (B, M3) compared to (B, M4). We also note that some features with lower NRMS values (like the one indicated with the red arrows) emerged after the ground roll had been suppressed.

Figure 6-28: 2D histograms of repeatability measures for the pre-stack data after ground roll removal. Plots of TS vs NRMS (left), SDR vs NRMS (middle), RMSDIF vs NRMS (right). Top row– M3 vs B, bottom row – M4 vs B. Ovals are referred to in the text.
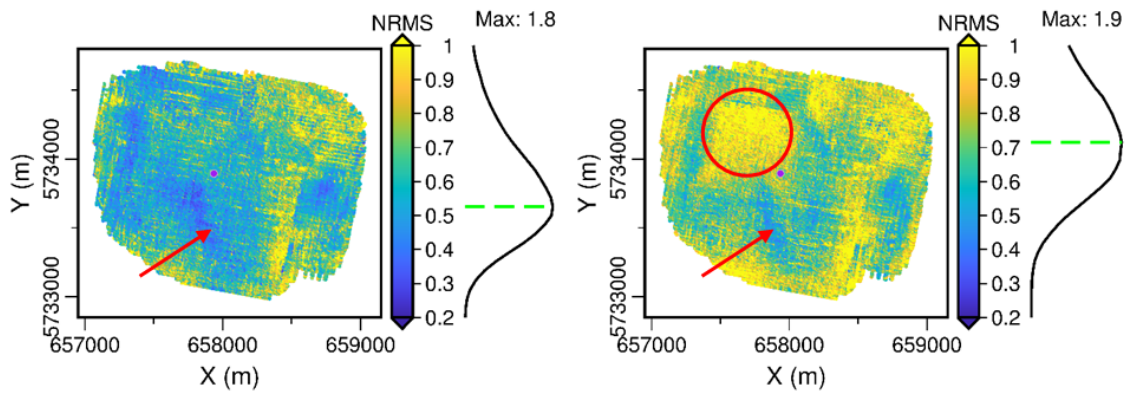
Figure 6-29: NRMS for CDPs with stacking fold above 4. NRMS is computed in a window from 400 to 900 ms on the data stacked after removal of the ground roll. Left panel – B vs M3, right panel – B vs M4. The purple dot indicates the injector well CRC-2.

We now compute all the repeatability metrics for the stacked data in the same manner as we have done for the raw data (compare Figure 6-18 and Figure 6-30). There are a few variations in the crossplots that we can observe. As the left panels indicate, the number of outliers in the estimates of TS is much smaller now as suggested by the drop of histogram values within the purple oval (exact zeros), while the amount of small TS required to cross-equalize the vintage pairs is higher (yellow bins in purple rectangle). The right panels indicate significant decrease in the energy of 4D noise though rather a considerable amount of the noise is still present in the data. Further suppression of ground roll can be attempted to better remove remnants of the noise.

On the contrary, SDR and NRMS indicate a general deterioration of repeatability as average NRMS increases and SDR decreases (the red oval in the middle panel of Figure 6-30 became empty). We shall now look at the 4D signal at the current processing stage to gain a better insight into the benefits of removing the ground roll.
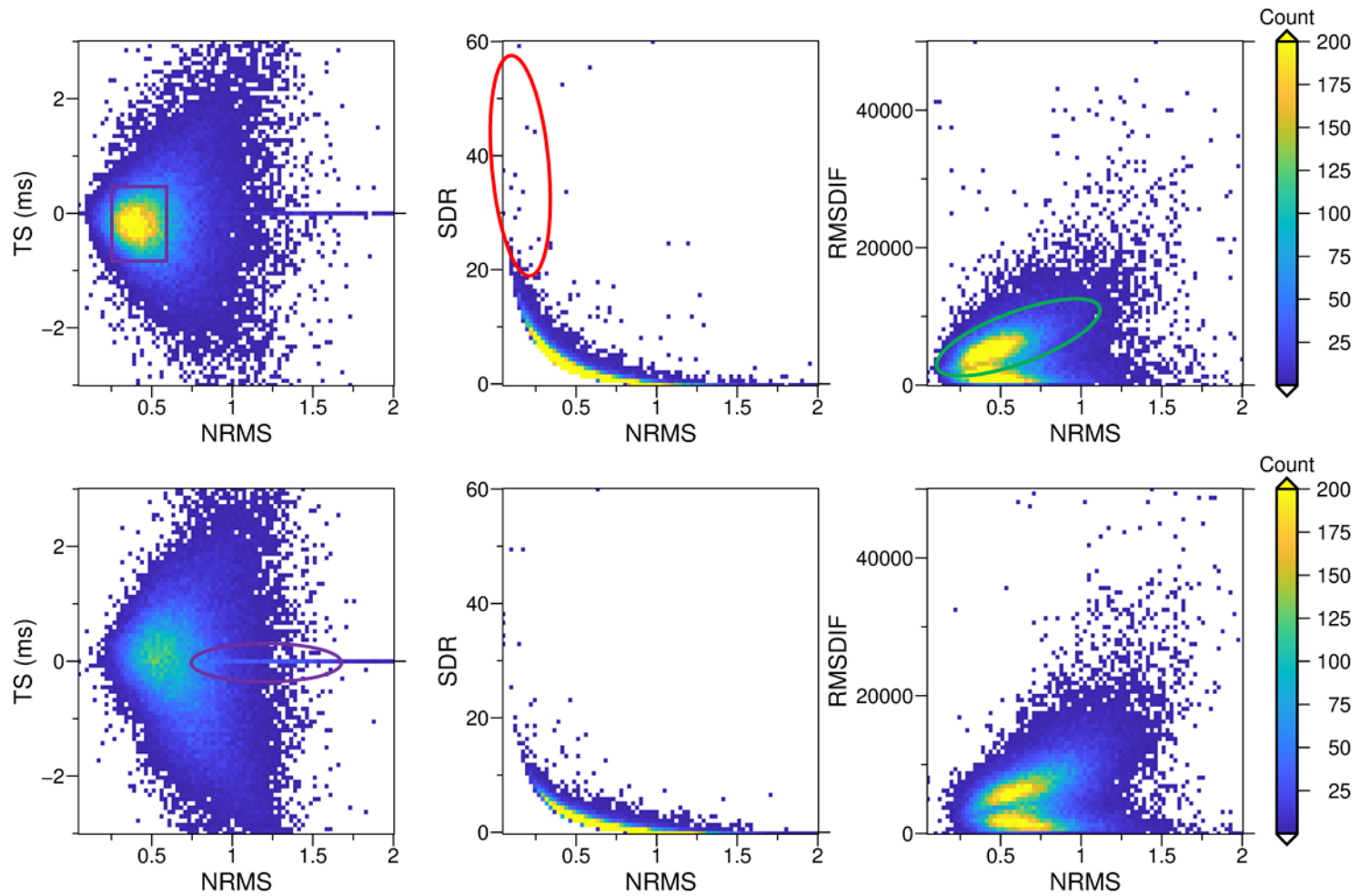
Figure 6-30: 2D histograms of repeatability measures after stacking of the data with ground roll suppressed. Plots of TS vs NRMS (left), SDR vs NRMS (middle), RMSDIF vs NRMS (right). Top row– M3 vs B, bottom row – M4 vs B. Ovals are referred to in the text.

Figure 6-19 and Figure 6-31 show differenced migrated images before and after removal of ground roll, respectively. We note considerable reduction of the 4D noise around the target interval, while the 4D signal itself appears to be quite similar in both figures. Residual reflections in the right panel of Figure 6-31 are significantly stronger compared to the ones in the centre panel which again means that cross-equalisation is particularly important in the processing of M4 vintage.

We now compare the maps of SNR in Figure 6-20 and Figure 6-32. Maximum SNR has increased from 8.4 to 11 for (B, M3) and from 5.8 to 7.7 (B, M4). Definition of the plume boundaries is now much clearer for the both vintage pairs.

So far we have seen that repeatability measures can be controversial. For example, after suppression of ground roll SDR decreased and NRMS increased, which indicates deterioration of repeatability. On the contrary, RMSDIF decreased, indicating improvement of repeatability. Lastly, plume images have improved after ground roll suppression. Thus, we emphasize that it is important to use a combination of attributes rather than rely on a single parameter for workflow QC.

We conclude that ground roll removal allows for better plume delineation and reduction of the amount of 4D noise rendered into final images. We are sure that suppression of ground roll will be even more critical if we pursue pre-stack images suitable for QI.
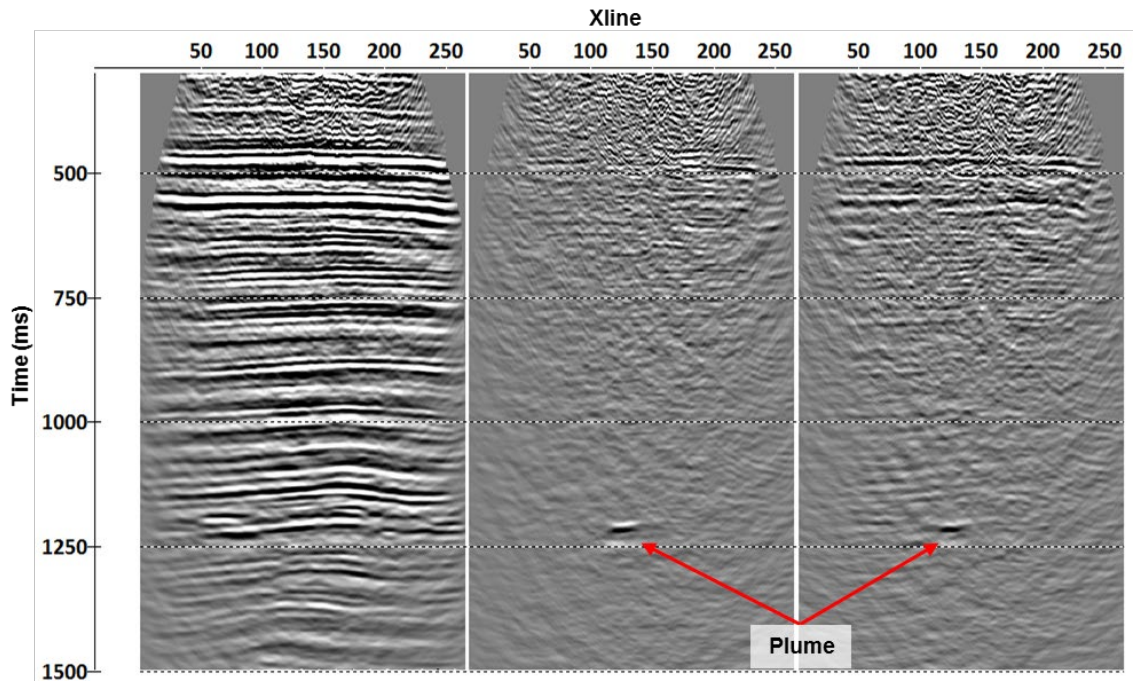
Figure 6-31: Section along Inline 110 through the migrated stack after removal of ground roll. FXY deconvolution is applied after stacking. Left panel – B, middle panel – M3-B, right panel – M4-B.
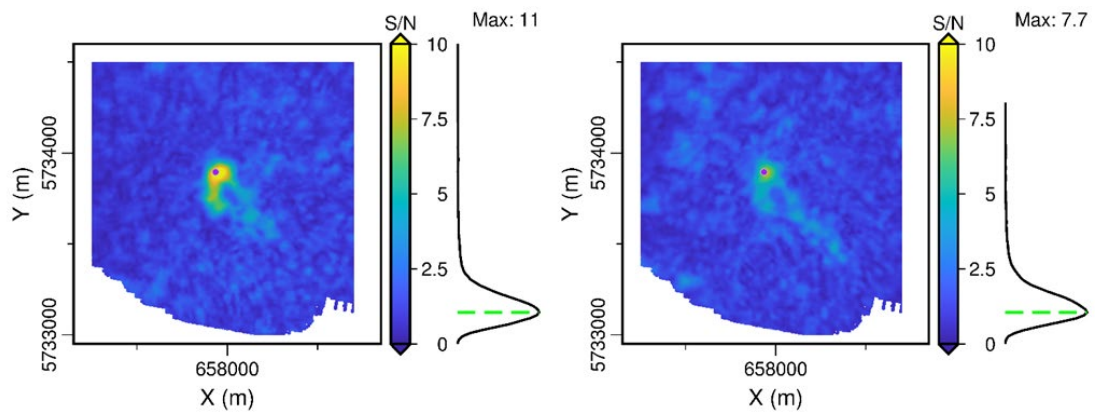
Figure 6-32: Maps of 4D SNR showing plume images on the migrated stack after suppression of ground roll. Left panel – M3-B, right panel – M4-B. The purple dot indicates the injector well CRC-2.

6.4.3   Removing bad traces

We now remove particularly non-repeatable traces from the processing flow for all the surveys, as we expect that their presence effectively reduces 4D SNR. To

run pre-stack imaging of the data, we have to remove traces from all of the other vintages.

To identify the traces to be excluded, we use the orange curve shown in Figure 6-8. We set the threshold to 0.35, which discards about 5 % of the traces (orange curve in Figure 6-8). We expect that some of the traces with intermediate values of cross-correlation can be improved at the stage of surface-consistent deconvolution. We end up with a relatively moderate threshold, which leaves us with 2,560,000 traces for further processing.

The plume images after removal of traces are shown in Figure 6-33. There is virtually no improvement in the plume images for both vintage pairs. We conclude that for our case removal of the non-repeatable traces does not bring value if the desired output is the full-offset stack. However, for surveys with the poorer repeatability of the raw data due to ambient noise (e.g. higher percentage of poorly repeatable traces) removal of non-repeatable traces may be a crucial step in the processing flow. For our dataset, the potential benefit of the bad trace removal is the reduction of noise prior to estimation of the filters for surface-consistent deconvolution.
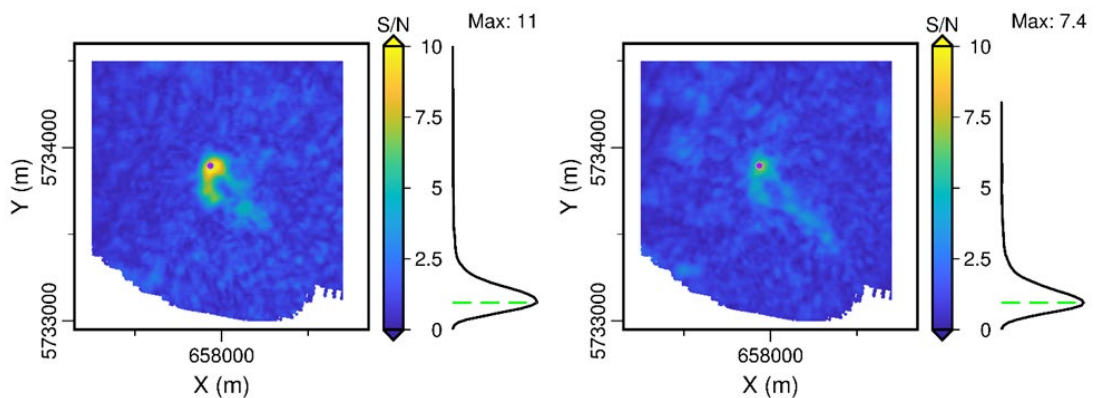
Figure 6-33: Maps of 4D SNR showing plume images on the migrated stack after removal of poorly repeatable traces. Left panel – M3-B, right panel – M4-B.

6.4.4 Surface-consistent deconvolution

At the next stage of our processing flow, we apply SCD to compensate for the effect of wavelet variation with source and receiver position within each individual vintage (Cary and Lorentz 1993). On top of that, we compute individual sets of filters for different vintages as we also expect the deconvolution to minimize the effect of Δw (equation 6-5), which appears due to the variation of coupling of sources and receivers with the time of vintage acquisition and the change of push down pressure of the vibrator trucks during M4. SCD with individual sets of filters is likely to cross-equalize the vintages among each other if the average spectra of these vintages are similar. That is, in such a case SCD with individual filters will be bringing all the vintages to the same average spectrum, thereby eliminating the differences induced by Δw. The average amplitude spectra, which are estimated in the windows used for running SCD, are shown in Figure 6-34. We note that the spectra are very similar to each other, thus we can expect SCD to cross-equalize the monitor and baseline vintages.
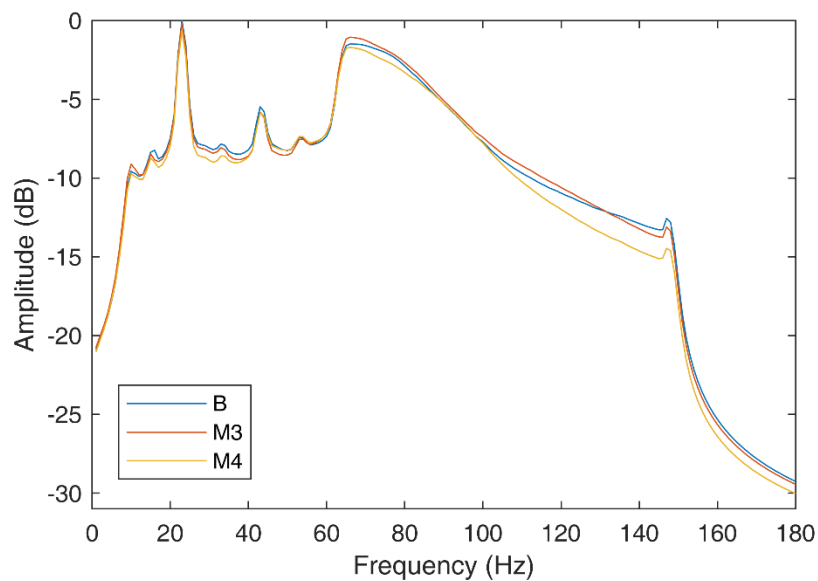
Figure 6-34: Average amplitude spectra for B, M3 and M4 vintages. Spectra are estimated after suppression of ground roll and application of a correction for spherical

divergence. All the spectra are normalized by the maximum value of amplitude spectrum for B vintage before conversion to dB amplitude scale.

After testing of the deconvolution parameters, we settled upon the following: use a single gate for estimation of deconvolution operator for each trace; use spiking deconvolution operator of 110 ms length with 0.1 % of white noise introduced into the main diagonal of the operator; run Gauss-Seidel decomposition of the data starting with offset, followed by source number, receiver number, and CDP (Cary and Lorentz 1993). The deconvolution operators are computed in windows above the target interval to avoid matching the 4D signal. Only source and receiver deconvolution components are applied to the data.

Figure 6-35 displays shot and receiver lines as shown in Figure 6-23 after removal of the bad traces and application of surface-consistent deconvolution. We do not observe significant changes from Figure 6-23 for the displayed gather, apart from the reduction of 4D noise on the right panel that corresponds to M4-B case (red oval). We note that the final filter applied to each trace is a convolution of source and receiver filters and can yield more noticeable quality uplift for traces from other sources (to be seen later).
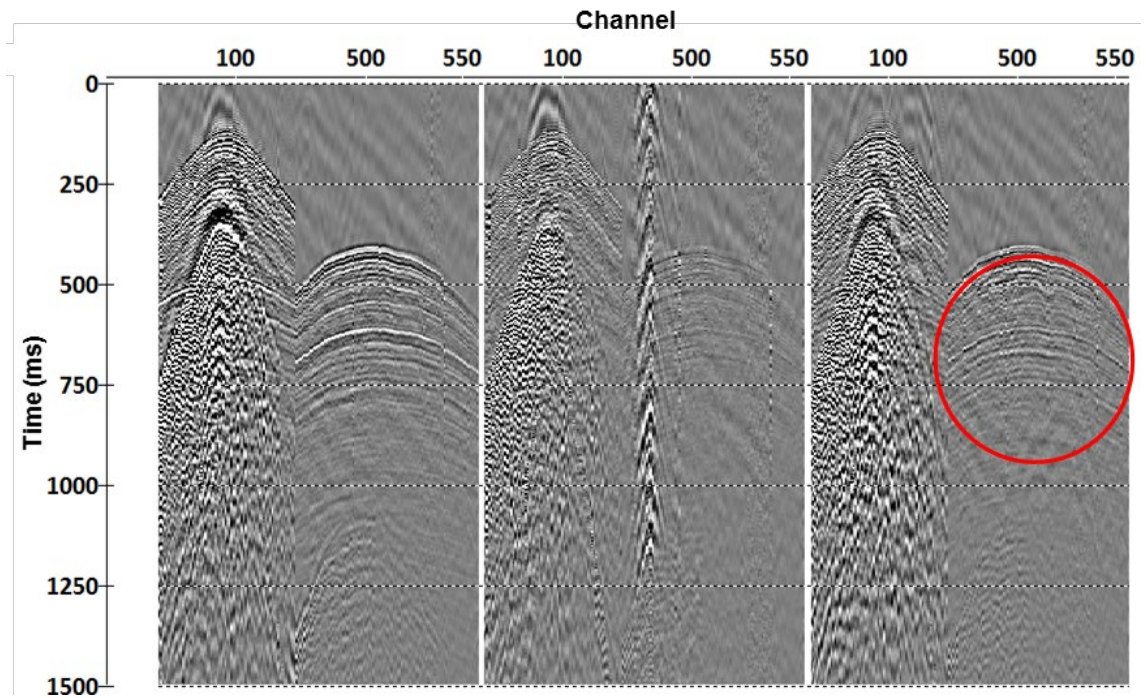
Figure 6-35: Seismic gathers after surface-consistent deconvolution with individual filters for two receiver lines of a single shot. Left panel – B, middle panel – M3-B, right panel – M4-B. The red oval is referred to in the text.

An NRMS estimate in a running window confirms improvement of repeatability for (B, M4) vintage pair by a slight drop of NRMS values as can be seen in the red oval shown in Figure 6-36.
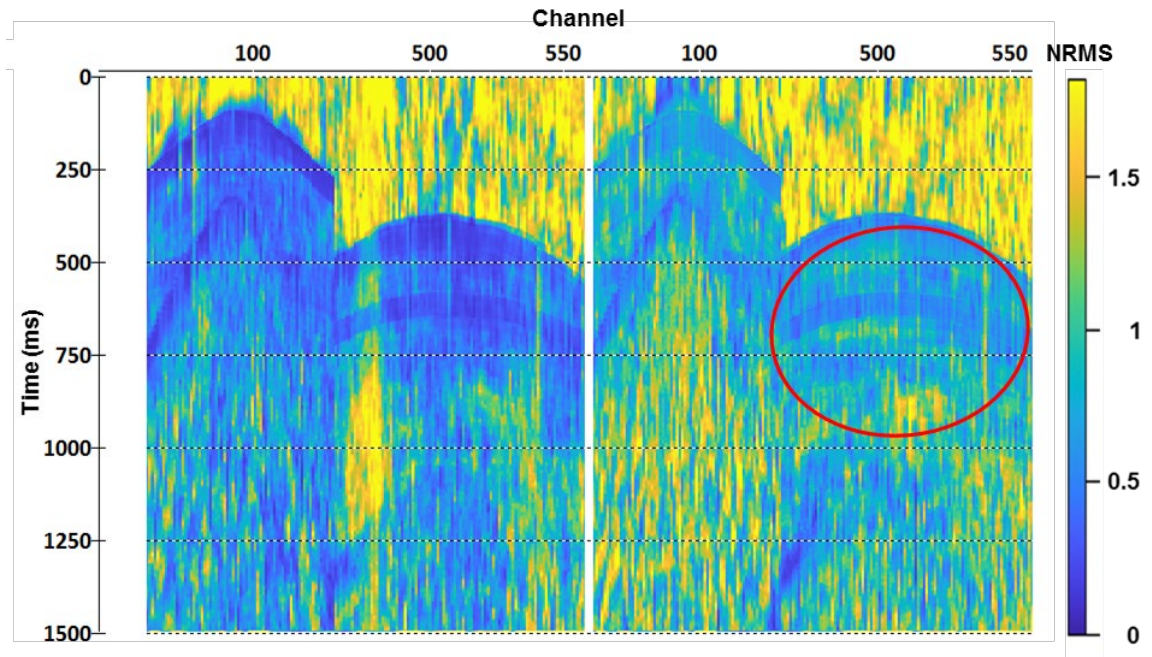
Figure 6-36: NRMS computed in 60 ms window for the data from the previous figure. Left panel – M3 vs B, right panel – M4 vs B. The red oval is referred to in the text.

Figure 6-37 shows the estimates of pre-stack NRMS after application of SCD. Unlike ground-roll removal, SCD causes a slight drop of mode NRMS from 0.5 down to 0.47 for (B, M3) vintage pair and more considerable drop of NRMS from 0.66 to 0.58 for (B, M4) vintage pair, as can be seen from the comparison of histograms in Figure 6-25 and Figure 6-37.

The following figures of NRMS estimates in different processing domains illustrate the combined effect of removal of the bad traces and application of SCD.

NRMS values (presented in Figure 6-37) averaged in source and receiver domains are shown in Figure 6-38. Apart from the general decrease in NRMS values, SCD improved repeatability of some individual sources and receivers with particularly poor repeatability (compare the highlighted areas in Figure 6-26 and Figure 6-38).

After comparison of Figure 6-39 and Figure 6-27 we can see that distribution of NRMS values has become narrower for (B, M4) vintage pair and now better resembles the benchmark, which is (B, M3) vintage pair.

The left cross-plots in Figure 6-40 show further reduction of the TS between the traces, which indicates that SCD quite successfully eliminates differences in phase spectrum (compared to Figure 6-28) between the baseline and monitor surveys. Again, an overall decrease in NRMS is evident in all of the graphs of Figure 6-40.
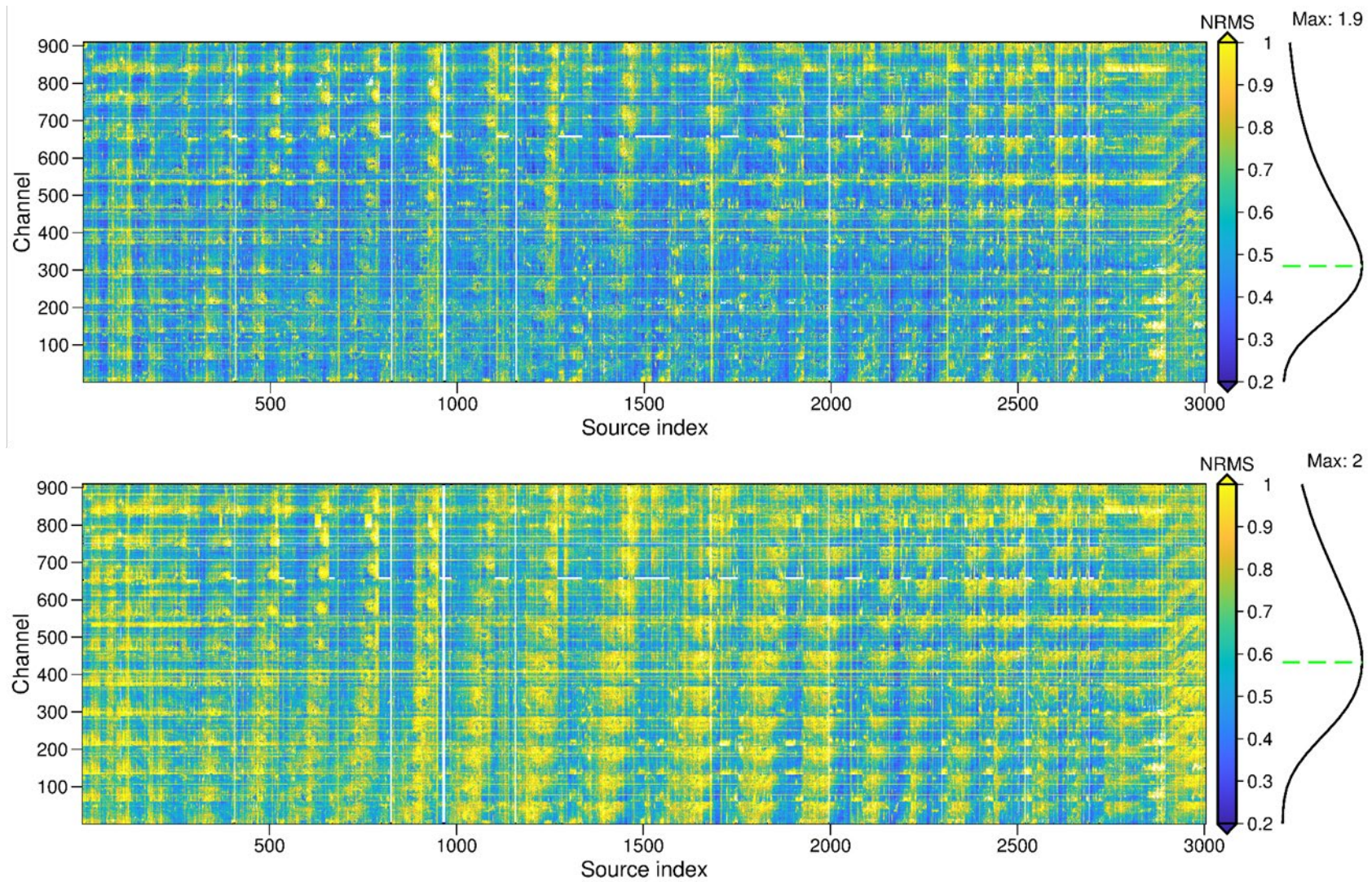
Figure 6-37: NRMS for the traces after application of surface-consistent deconvolution. Top panel – M3 vs B, bottom panel – M4 vs B.
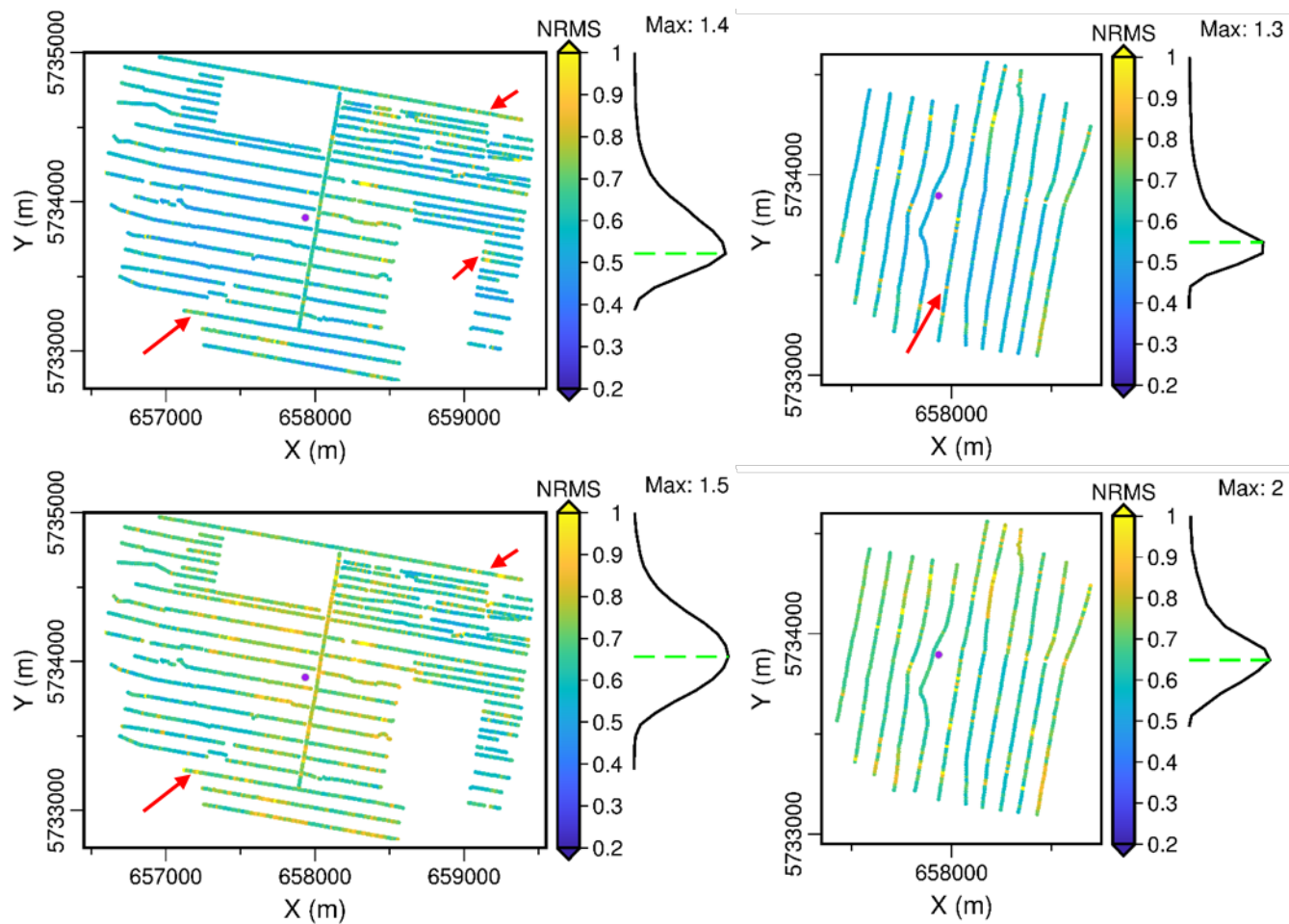
Figure 6-38: NRMS mean in source (left) and receiver (right) domains computed for the traces after application of SCD. Red arrows indicate sources and receivers in which repeatability improved after application of SCD. Top row– M3 vs B, bottom row – M4 vs B.
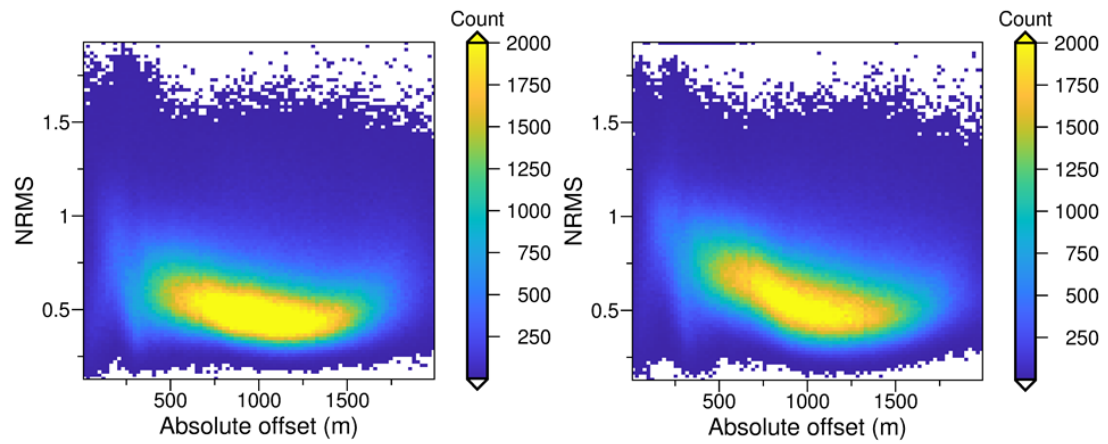
Figure 6-39: 2D histograms showing dependence of NRMS on absolute value of offset for the traces after application of SCD. Left panel – B vs M3, right panel – B vs M4.

Figure 6-41 shows reduction of NRMS caused by SCD in the stacked data: mode value of NRMS reduced from about 0.52 down to 0.5 for (B, M3) and from 0.72 to 0.66 for (B, M4). Stacking and migration are done using the same workflow as has been used for the data after suppression of ground roll.

As the next QC step, we compute all repeatability metrics for the stacked data as we did with the raw data (compare Figure 6-30 and Figure 6-42). We observe virtually no change in the cross-plots except for the small increase of the distribution density of the data points in the left panels in the vicinity of the zero time-shift zone (compare the purple rectangles in Figure 6-30 and Figure 6-42).
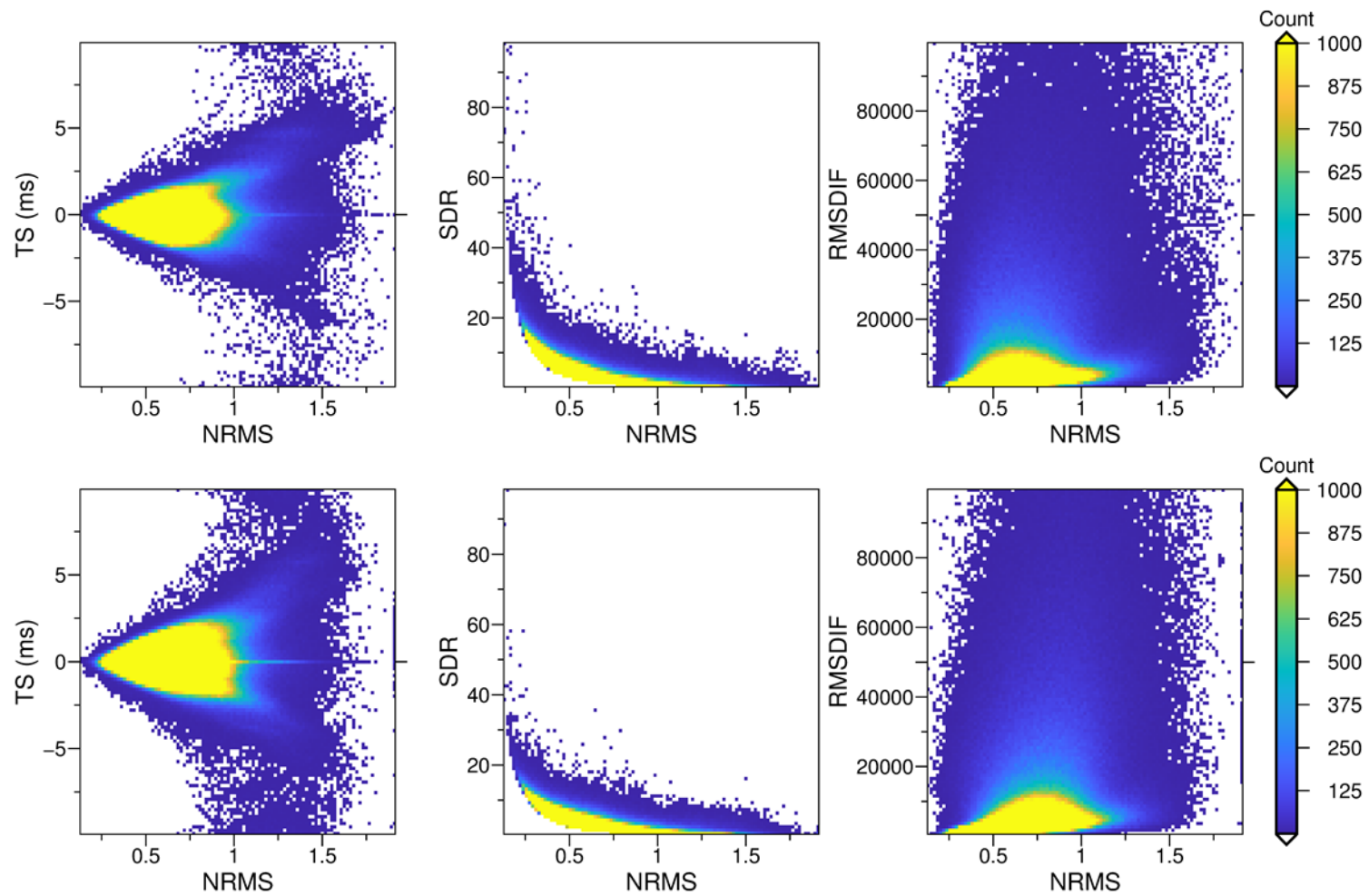
Figure 6-40: 2D histograms of repeatability measures for the pre-stack data after application of SCD. Plots of TS vs NRMS (left), SDR vs NRMS (middle), RMSDIF vs NRMS (right). Top row– M3 vs B, bottom row – M4 vs B.
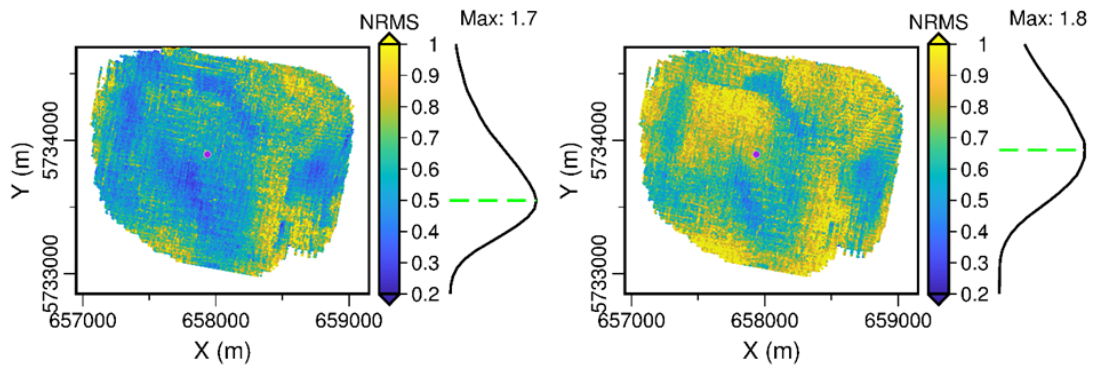
Figure 6-41: NRMS for CDPs with stacking fold above 4. Computed in a window from 400 to 900 ms on the data stacked after application of SCD. Left panel – B vs M3, right panel – B vs M4.

Figure 6-43 shows the post-processed and migrated images after SCD. It shows a reduction of 4D noise at the top of the sections compared with Figure 6-31 (weaker residual reflections pointed out by blue arrows). The improvement is more evident for the (B, M4) vintage pair compared to the (B, M3) vintage pair.

The plume images after application of SCD with individual sets of filters are shown in Figure 6-44 in top view. We observe minor improvement of continuity of the plume for the (B, M3) vintage pair. For the (B, M4) vintage pair SCD notably improves appearance of the plume and increases maximum 4D SNR from 7.4 to 9.2. This demonstrates that SCD with individual filters can do the job of partial cross-equalization of poorly repeatable vintages (explanation given at the end of subsection 6.4.1). We consider SCD with individual filters as a useful routine from a 4D perspective and include it in our processing flow.
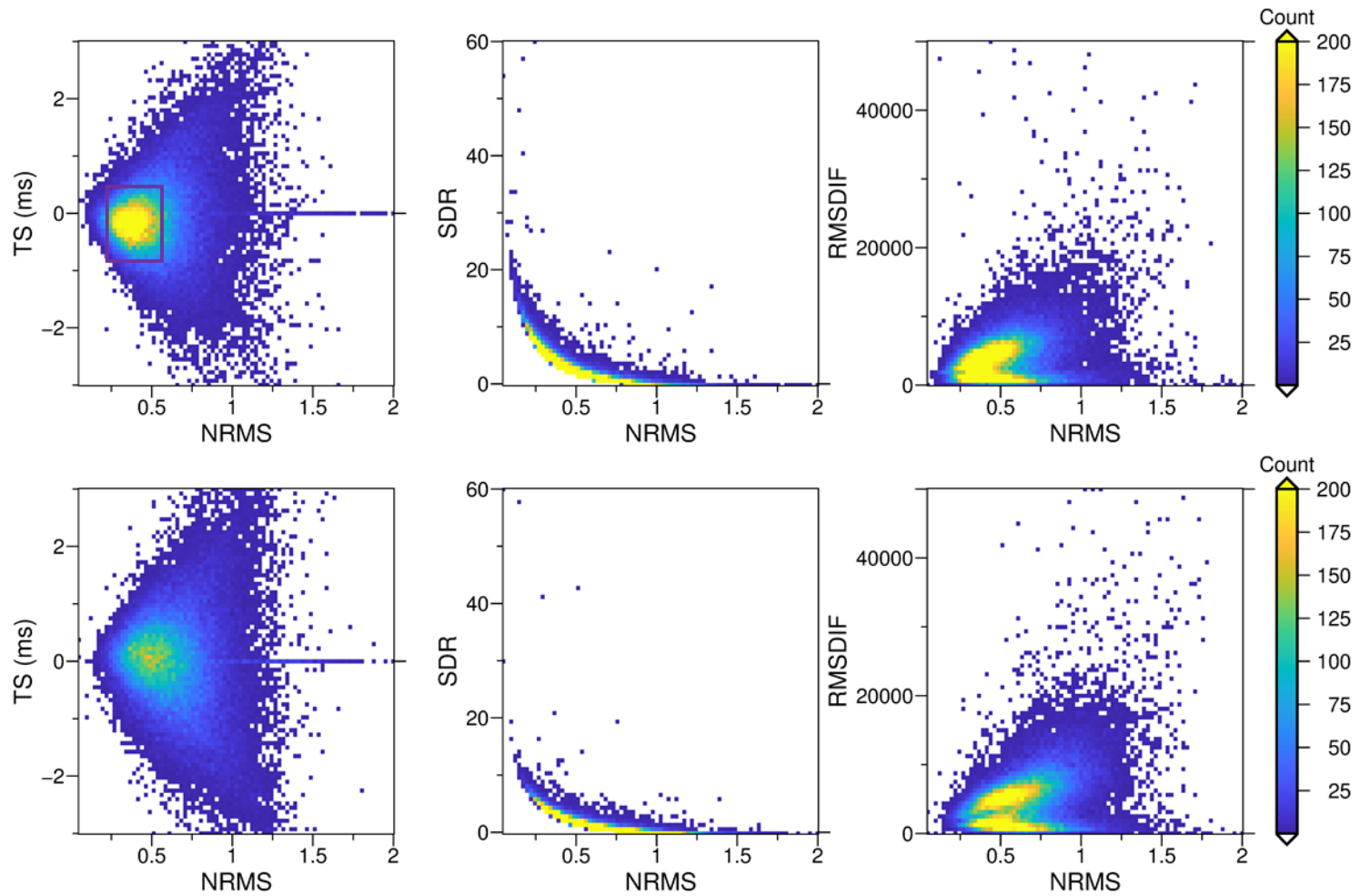
Figure 6-42: 2D histograms of repeatability measures after stacking for the data with surface-consistent deconvolution applied. Plots of TS vs NRMS (left), SDR vs NRMS (middle), RMSDIF vs NRMS (right). Top row– M3 vs B, bottom row – M4 vs B. Purple rectangle is referred to in the text.
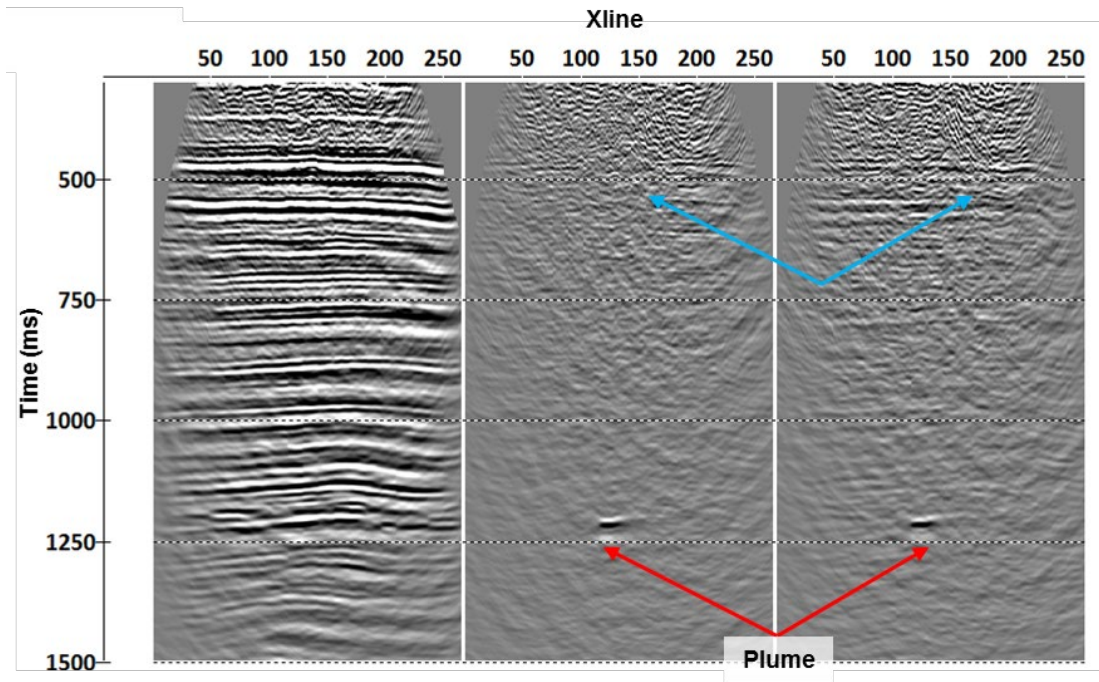
Figure 6-43: Section along Inline 110 through the migrated stack after application of SCD. Left panel – B, middle panel – M3-B, right panel – M4-B. Blue arrows indicate the weakening of the residual reflections due to application of SCD.
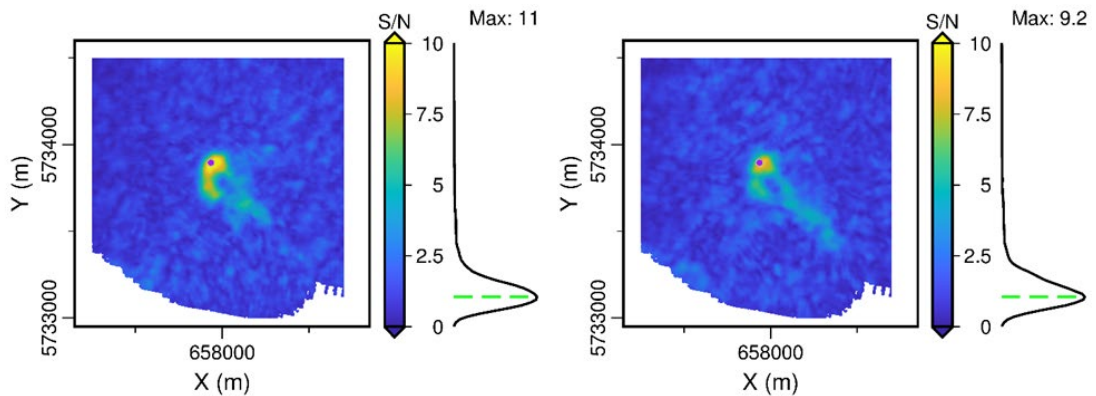
Figure 6-44: Maps of 4D SNR showing plume images on the migrated stack application of SCD. Left panel – M3-B, right panel – M4-B.

6.4.5 Pre-stack time migration

So far, we have built the plume images using post-stack time migration. We now migrate the data using Kirchhoff pre-stack time migration (PSTM) applied to offset bins. We apply PSTM for the following reasons:

- as PSTM images the data before stacking, we migrate intact diffractions (plume and faults in particular) before they get affected by incoherent stacking.

- we also check whether it is feasible to produce images suitable for the time-lapse AVO (migrated gather) analysis.

- PSTM gives opportunity to derive dip-independent velocities (not much applicable to the case of our geology).

We use variable sizes of offset bins as the data have very uneven distribution of traces with offsets, which is quite common for onshore acquisition. Near and far offsets are underpopulated so the offset bin sizes vary from ~120 m at the low offset edge to ~ 20 m in the middle of the offset range to ~40 m at the high offset edge (about 1600 m).

To prepare the data for PSTM, we apply bandpass filter and surface-consistent residual static corrections (estimated on B and applied to all the surveys). Then we resort the data into offset bins. Velocity model and migration aperture have the most significant impact on the migration outcome. The velocities that we have been using for stacking and post-stack migration provide relatively flat seismic reflections in the PSTM common image point gathers, which is a conventional QC criterion. The aperture parametrization was established through extensive testing (see the right column of Table 6-1). The common image gathers are shown in Figure 6-49 and discussed in more detail in section 6.4.6.

Figure 6-45 shows that quality uplift from the SCD propagates into the post-stack domain: mode value of NRMS reduced further from about 0.5 down to 0.32 for (B, M3) and from 0.66 to 0.39 for (B, M4). The distributions of NRMS became much wider now compared to what they had been before PSTM. The change of the width of

the NRMS distribution is primarily due to the histograms' peak values shifting towards smaller NRMS values (which is a good sign) due to the coherent stacking of the diffracted energy which is repeatable between the vintages and gets even more repeatable when focused and due to the effective denoising effect of the migration as most of the remaining noises are stacked incoherently during migration.

The next QC step is to compute all the repeatability metrics for the stacked data (compare Figure 6-42 and Figure 6-46). We observe that PSTM considerably affects all of the plots. These plots support general decrease on NRMS after PSTM (yellow extrema move left). However, they also show that some traces have increased values of NRMS (more points in the right parts of the plots of Figure 6-46). The increase of NRMS for these traces correlates well with the areas of lower fold (see Figure 6-9). A better insight into the effect of PSTM on repeatability can be obtained from the pre-stack analysis of the traces. In particular, we speculate that the effect of acquisition-induced holes in the coverage of various offset bins needs to be studied. In this case 5D interpolation may play an important role in improving repeatability of the 4D images.

Interestingly, we observe a general though subtle (tenths of a millisecond) change in the shape and the trend of the TS vs NRMS plots (again compare Figure 6-42 and Figure 6-46) while the value ranges are preserved. While before PSTM the distribution of the points was symmetric relative to the axis of zero TS (Figure 6-42), after PSTM there is a subtle bias of the maxima of the data points' clouds into the negative (for (B, M3) yellow colour shifted into negative TS) and positive (for (B, M4) yellow colour shifted into positive TS) areas of TS. We speculate that this bias of TS might occur because we use same baseline statics and velocity for the PSTM and/or NMO for all the vintages. Our statics and velocity field do not account for the possible

near-surface velocity variation between the vintages. As a result we have small errors in the shallow part of the velocity model which are expressed as very small TS values in the post-stack images. These errors are likely present in our data before migration but we see them better after PSTM as the migration further reduces ambient component of 4D noise (the third term $(n_2 - n_1)$ in equation 6-5) and the noise introduced by variation of the ray trajectories due to the time-lapse changes in the near-surface ($\dfrac{\partial e}{\partial G}$ in equation 6-5) takes precedence.

To conclude, the increase in SDR values and decrease in RMS amplitudes of the difference complement the overall reduction of NRMS hence justifying the use of PSTM. The improvement of repeatability occurs for the both vintage pairs.
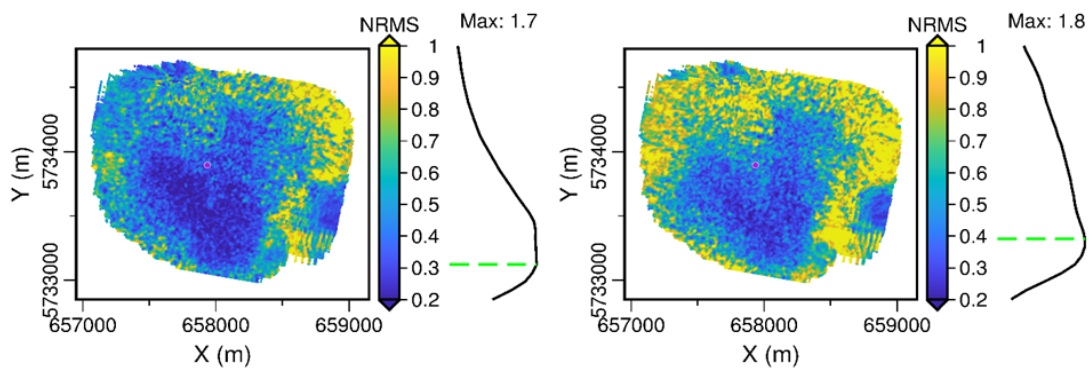
Figure 6-45: NRMS for CDPs computed in a window from 400 to 900 ms on the data stacked after PSTM. Left panel – B vs M3, right panel – B vs M4.
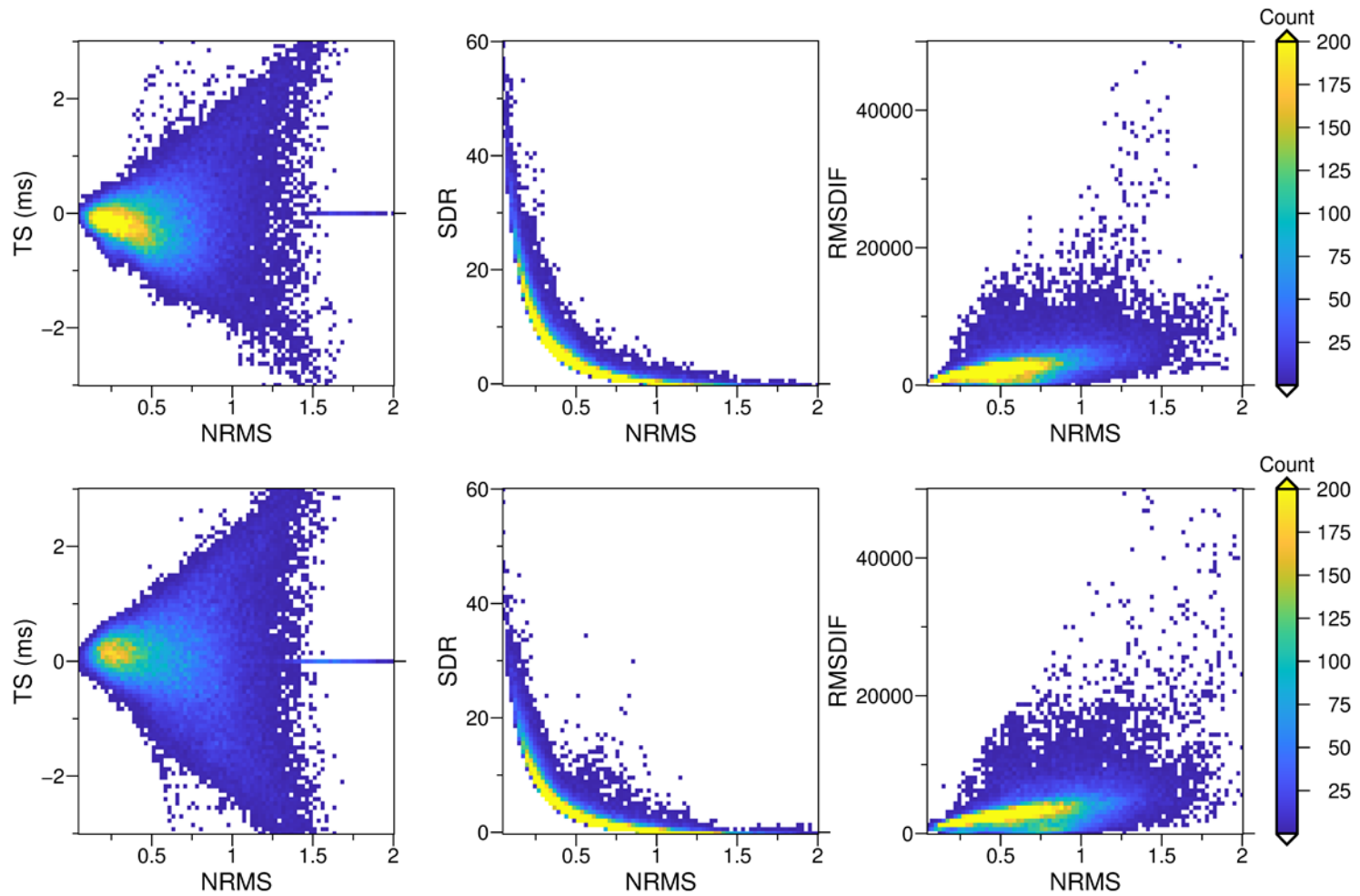
Figure 6-46: 2D histograms of repeatability measures after stacking of the data with PSTM applied. Plots of TS vs NRMS (left), SDR vs NRMS (middle), RMSDIF vs NRMS (right). Top row– M3 vs B, bottom row – M4 vs B.

The plume images after application of PSTM and FXY deconvolution are shown in Figure 6-47. We note that both of the differences have more similar 4D noise patterns than previously (see Figure 6-43). The geological 4D noise (energy of residual reflections) is now reduced compared to Figure 6-43.
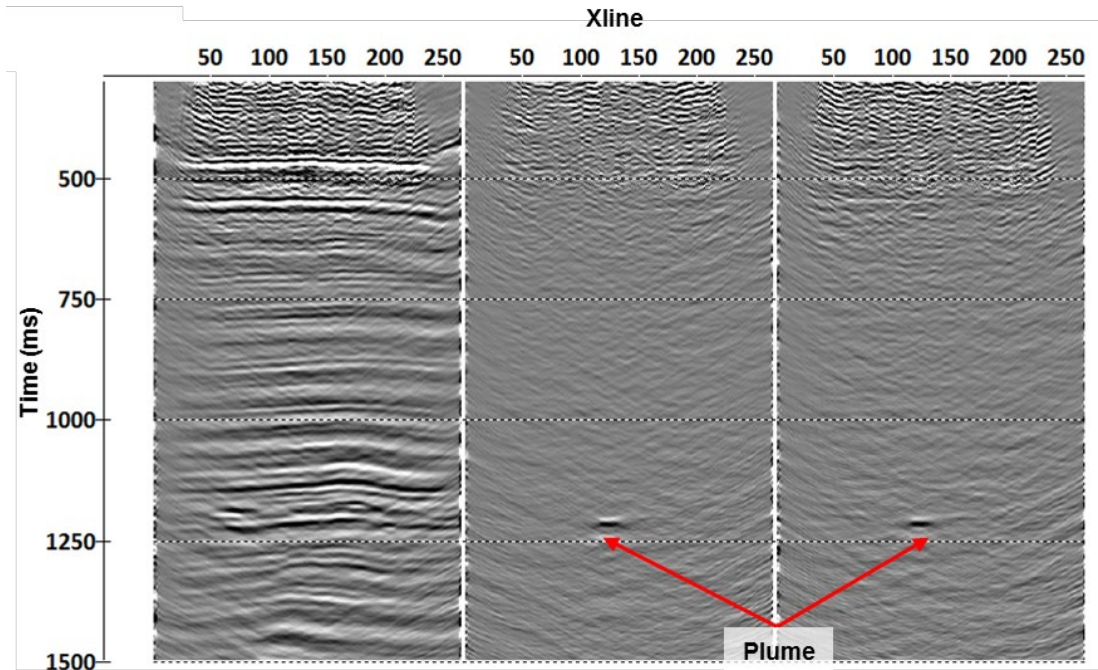
Figure 6-47: Section along Inline 110 through the volume imaged with PSTM. FXY deconvolution is applied after stacking. Left panel – B, middle panel – M3-B, right panel – M4-B.

Figure 6-48 shows a horizontal slice through the plume. The SNR is distributed more uniformly throughout the target interval and the maximum SNR for both vintage pairs has increased. Also, note the change of the plume's shape and its lateral shift compared to the post-stack time migrated image (compare to Figure 6-44). Overall, we observe that the plume looks sharper after PSTM and the bounding fault to the south of the plume is better defined (the fault plane after PSTM is straighter than after PostSTM which is probably correct).
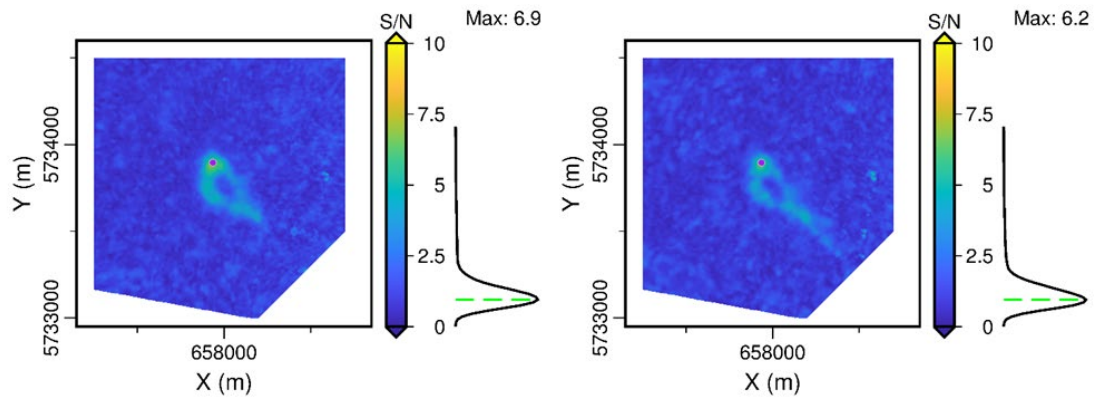
Figure 6-48: Maps of 4D SNR showing plume images on the data stacked after PSTM. Left panel – M3-B, right panel – M4-B.

6.4.6 Pre-stack time images of the plume

In this subsection, we explore the potential impact of the processing on the common image point gathers, which may be required for the QI of the time-lapse data. QI would help to better identify the boundaries and thickness of the plume rather than we could do this just by looking at the seismic images. If sensitive enough it could indicate CO_2 leakage from the reservoir. QI may also show spatial variations of the velocity change related to the spatial variations of the concentration of the injected CO_2.

We could not identify the plume in the pre-stack data because the energy of the plume's reflection is not focused before migration. The PSTM produces a number of common image gathers formed by different offset ranges that contain detectable 4D signal. It turns out that even partial stacking of the seismic signals along coherent travel-time curves reduces the noise level significantly. Figure 6-49 shows a common image gather (inline 110, crossline 123). The left panel corresponds to B, middle – M3-B, right – M4-B. We observe strong correlated noise in the B data that is successfully removed after subtraction. We note that plume reflection is detectable

even in the area covered by ground roll. The quality of the M3-B image is better than that of M4-B.

If one wants to study / interpret an AVO response from the injection, it would be helpful to compare the expected (modelled) 4D AVO response (Caspari et al. 2015) to the actual 4D AVO response in the field data. However, to achieve this we need an improved noise suppression workflow as it is impossible to extract an AVO response from the plume reflection in the middle and right panels of Figure 6-49 due to the low SNR. Also the amplitudes have to be checked for an adequate correction for the amplitude divergence and inelastic attenuation between the near and far offsets.
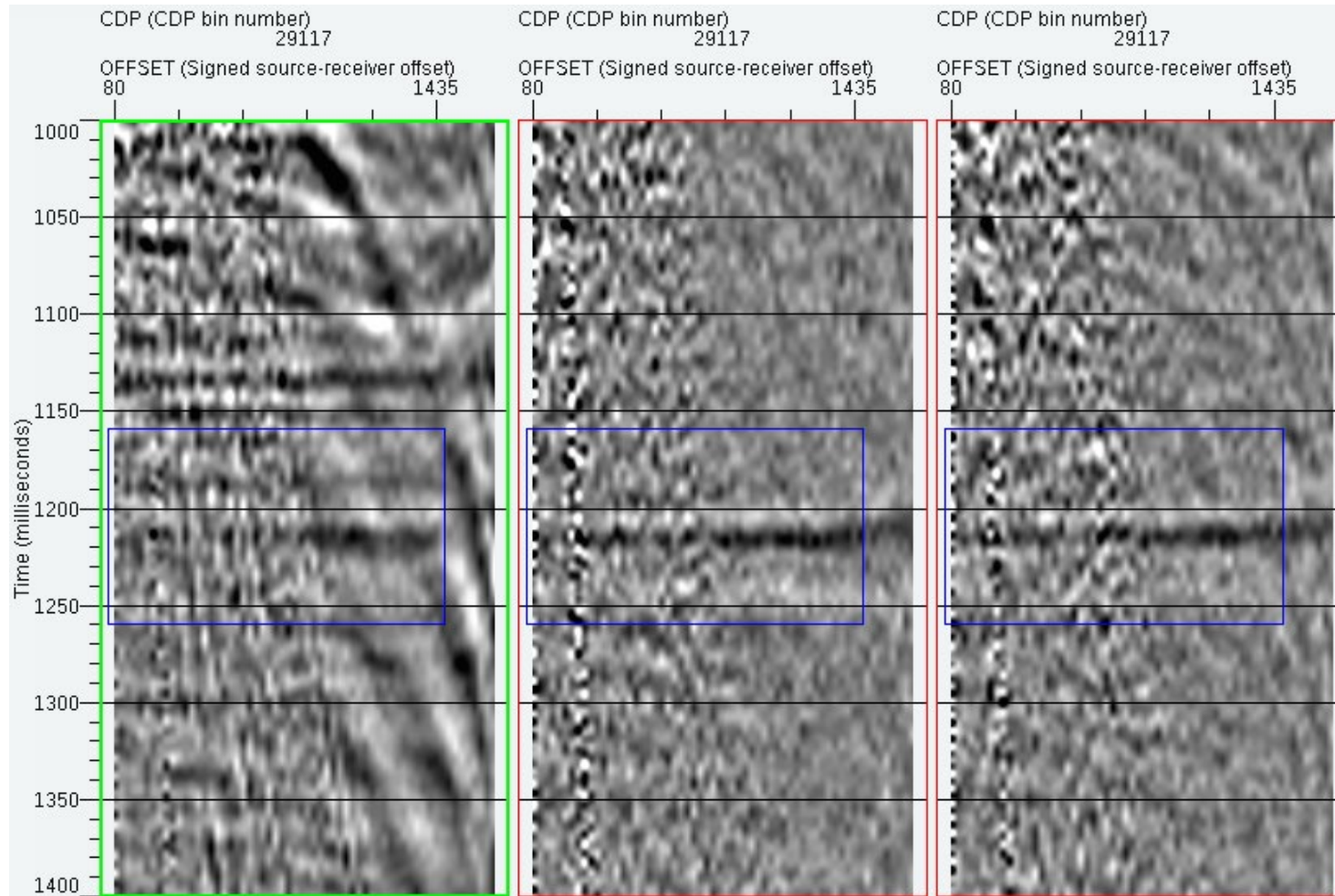
Figure 6-49: Common image gather (inline 110, crossline 123) after PSTM without AGC. B (left), M3-B (middle), M4-B (right).

6.4.7 Introducing automatic gain control into the workflow

Automatic gain control (AGC) in a long window was an important routine that largely controlled the quality of the plume images produced during fast-track processing by Pevzner, Urosevic, Popik, Shulakova, et al. (2017). AGC increased SNR for those images. One of the drawbacks of the application of AGC is that it disturbs vertical and lateral distribution of relative amplitudes. Usually, relative amplitudes along the same trace can be preserved if the window length of AGC is long enough. However, AGC can still corrupt the relationship between the same seismic events for adjacent traces. For example, if relatively strong remnants of ground roll are still present on the near offset traces, then AGC scalars computed for target interval at near offsets will be bigger than the ones at mid and far offsets. This will lead to uneven scaling of a given reflection for a given CDP and as a result to distorted amplitude versus offset (shown further). Thus, we should avoid the use of AGC if common image gathers are the desired output. However, we might use AGC in a long window (e.g., 500 ms) for the post-stack images if the benefit of improving SNR is considerable. We speculate that in such a case, relative amplitudes (including tuning) in the CDP domain can be preserved.

In the following we investigate the effects of AGC application at three different stages. Assessment of the effects is straightforward by comparing images with AGC and without AGC.

AGC applied after SCD and before stacking

In this case we add AGC before stacking into the processing workflow that includes SCD with individual filters and post-stack time migration.

Figure 6-50 shows the maps of NRMS distribution (compare to Figure 6-41). Note that this figure uses unmigrated data. We observe a clear drop in NRMS values

from 0.5 to 0.38 for (B, M3) and from 0.66 to 0.45 for (B, M4) vintage pairs purely due to the application of AGC. The decrease in NRMS values is larger for the poorly repeatable vintage pair. We conclude that that AGC might bring more value when 4D noise between vintages is strong. We note the skew of the distributions of NRMS values towards the low end (black curves in Figure 6-50).

Further QC of the repeatability attributes is shown in Figure 6-51 (compare to Figure 6-42). Note again that this figure uses unmigrated data. The cross-plots indicate decrease of NRMS, increase of SDR, and a slight shrinking of the distribution of TS. Note the similar bias of the extrema of the TS plots relative to the zero of TS axis as was observed after application of PSTM without AGC (Figure 6-46). We speculate that the explanation is the same as given in subsection 6.4.5 for PSTM, namely, AGC ensures the precedence of the 4D noise level induced by the variation of the travel path of seismic energy (traveltime variation) over the 4D noise level induced by random-like noise.

The RMS of amplitude differences are rescaled now due to the application of AGC and, thus, are not directly comparable to the RMS of amplitude differences shown in Figure 6-42. We observe that there is a big change between the look of the right panels of Figure 6-42 and Figure 6-51. AGC shrank the dynamic range of the 4D noise down to 15 dB (noise floor level is about 6 times lower than the noise top level) so that the 4D noise became more homogeneous. As AGC is a non-linear and non-stationary process it is not obvious how to relate the features of the RMSDIF vs NRMS plots before and after AGC.
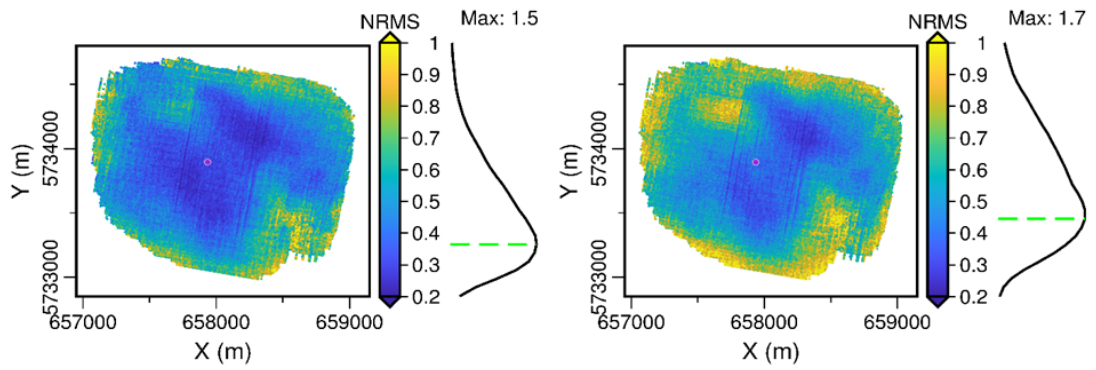
Figure 6-50: NRMS for CDPs computed in the window from 400 to 900 ms on the not-yet-migrated stack after surface-consistent deconvolution with individual sets of filters for each vintage and AGC in 500 ms window applied before stacking. Compare to Figure 6-41. Left panel – B vs M3, right panel – B vs M4.
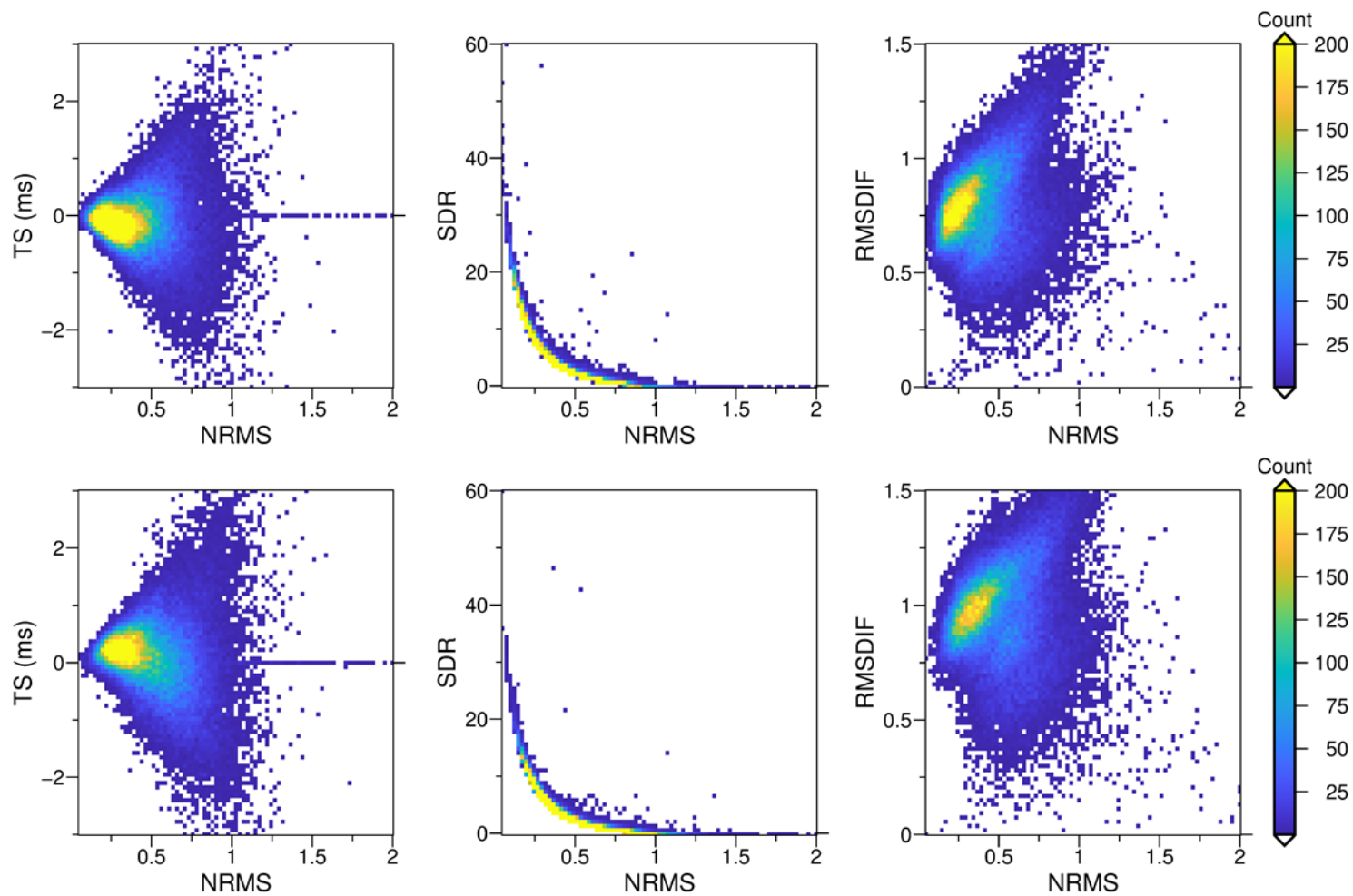
Figure 6-51: 2D histograms of repeatability measures on the not-yet-migrated- stack with surface-consistent deconvolution applied. AGC in 500 ms window is applied before stacking. Compare to Figure 6-42. Plots of TS vs NRMS (left), SDR vs NRMS (middle), RMSDIF vs NRMS (right). Top row– M3 vs B, bottom row – M4 vs B.

We now post-process and migrate the data. The vertical sections along inline 110 are shown in Figure 6-52 (compare to Figure 6-43). The plume with AGC (Figure 6-52) better stands out from the background 4D noise than the plume without AGC (Figure 6-43). AGC suppresses to some extent all types of 4D noise, with the exception of residual reflections. It is clearly seen that residual reflections for the (B, M4) vintage pair stand out from all other background 4D noise types.
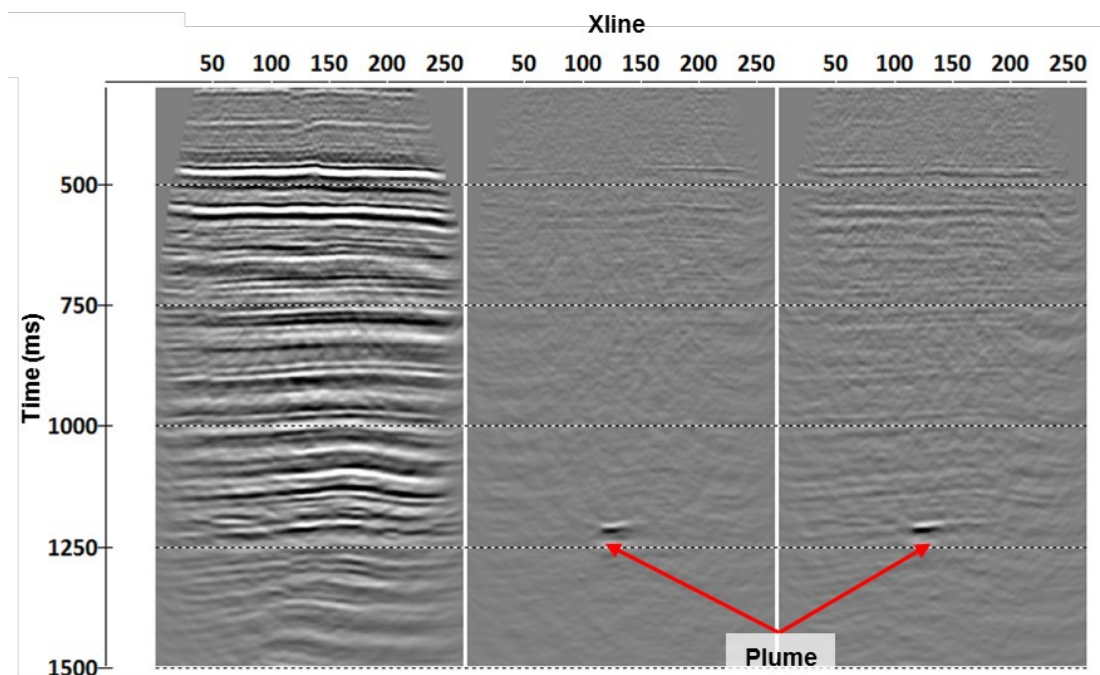
Figure 6-52: Section along Inline 110 through the migrated stack after SCD. AGC in 500 ms window is applied before stacking. FXY deconvolution is applied after stacking. Compare to Figure 6-43. Left panel – B, middle panel – M3-B, right panel – M4-B.

Figure 6-53 shows the plume images after the same processing workflow as was used to obtain Figure 6-44 with the only difference being the application of AGC in 500 ms window right before stacking. We observe an increase in SNR parameter and same values for the maximum SNR for both vintage pairs. AGC also emphasized the difference between (B, M3) and (B, M4) vintage pairs as the level of 4D noise is

now higher for the latter and distributions of 4D noise are different (histograms in Figure 6-53).
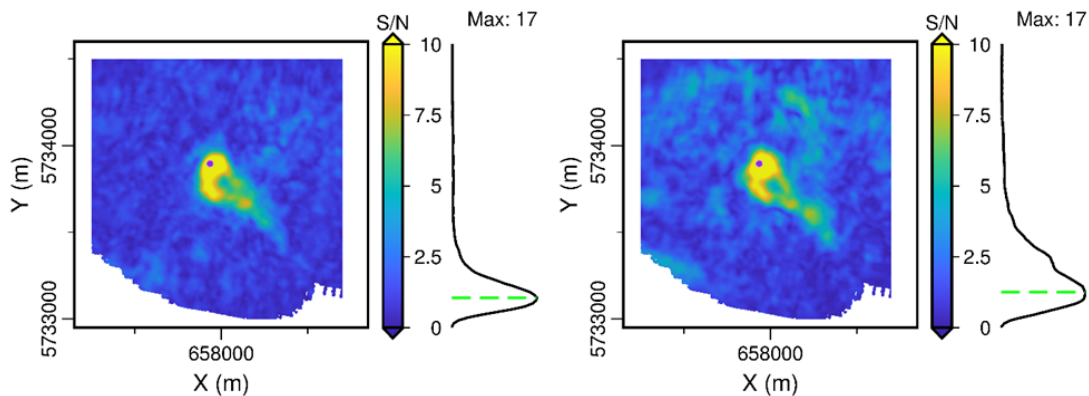
Figure 6-53: Maps of 4D SNR showing plume images on the migrated stack after SCD with individual sets of filters for each vintage. AGC in 500 ms window is applied before stacking. Compare to Figure 6-44. Left panel – M3-B, right panel – M4-B.

AGC applied after PSTM and before stacking

Figure 6-54 shows the plume images after the same processing workflow as was used to obtain Figure 6-48 with the only difference being the application of 500 ms AGC after PSTM and before stacking. We observe virtually no difference between the figures. Maxima and distributions of SNR stay the same as well as the plume definition. We note that 4D noise in the right panel of Figure 6-54 has increased after application of AGC (compared to Figure 6-48). We conclude that there is no benefit of applying AGC after PSTM.
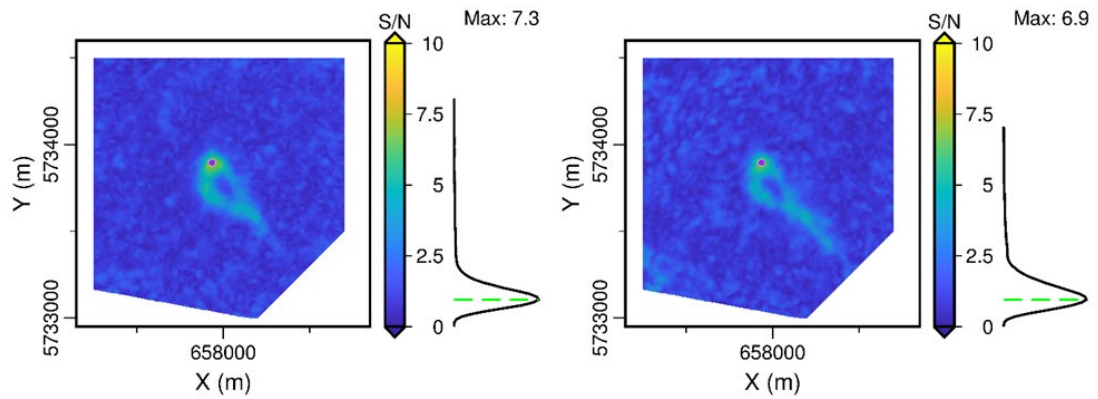
Figure 6-54: Maps of 4D SNR showing plume images on the data stacked after PSTM. AGC in 500 ms window is applied after PSTM and before stacking. Compare to Figure 6-48. Left panel – M3-B, right panel – M4-B.

AGC applied before PSTM

In this case we introduce AGC before PSTM into the processing workflow including SCD with individual filters. We test the application of AGC at this stage to compensate for the relatively strong remnants of the ground roll and other noise types as well as to balance the amplitudes within common offsets prior to PSTM. We apply AGC after SCD and before PSTM.

Figure 6-55 shows the maps of NRMS distribution with CDP number (compare to Figure 6-45). We observe a drop of NRMS values from 0.32 to 0.22 for (B, M3) and from 0.39 to 0.26 for (B, M4) vintage pairs. We note that the asymmetricity of distribution of NRMS values (Figure 6-45) has been emphasized (black curves in Figure 6-55).

Further QC of the repeatability attributes is shown in Figure 6-56 (compare to Figure 6-46). The cross-plots exhibit similar changes to the ones observed between Figure 6-51 and Figure 6-42: decrease of NRMS, increase of SDR, and a slight reduction of variance of the TS. The RMS of amplitude differences are rescaled now

171

due to the application of AGC, and are not directly comparable to the RMS of amplitude differences shown in Figure 6-45.
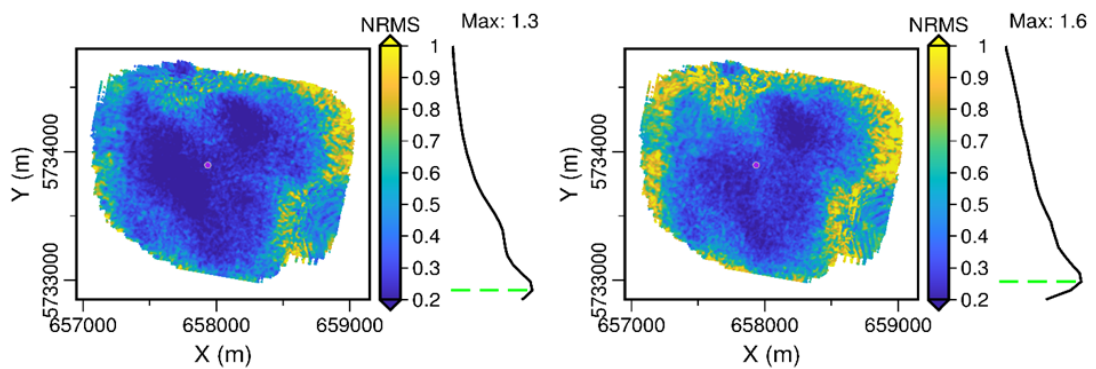
Figure 6-55: NRMS for CDPs computed in a window from 400 to 900 ms on the data stacked after PSTM. AGC in 500 ms window is applied before PSTM. Compare to Figure 6-45. Left panel – B vs M3, right panel – B vs M4.
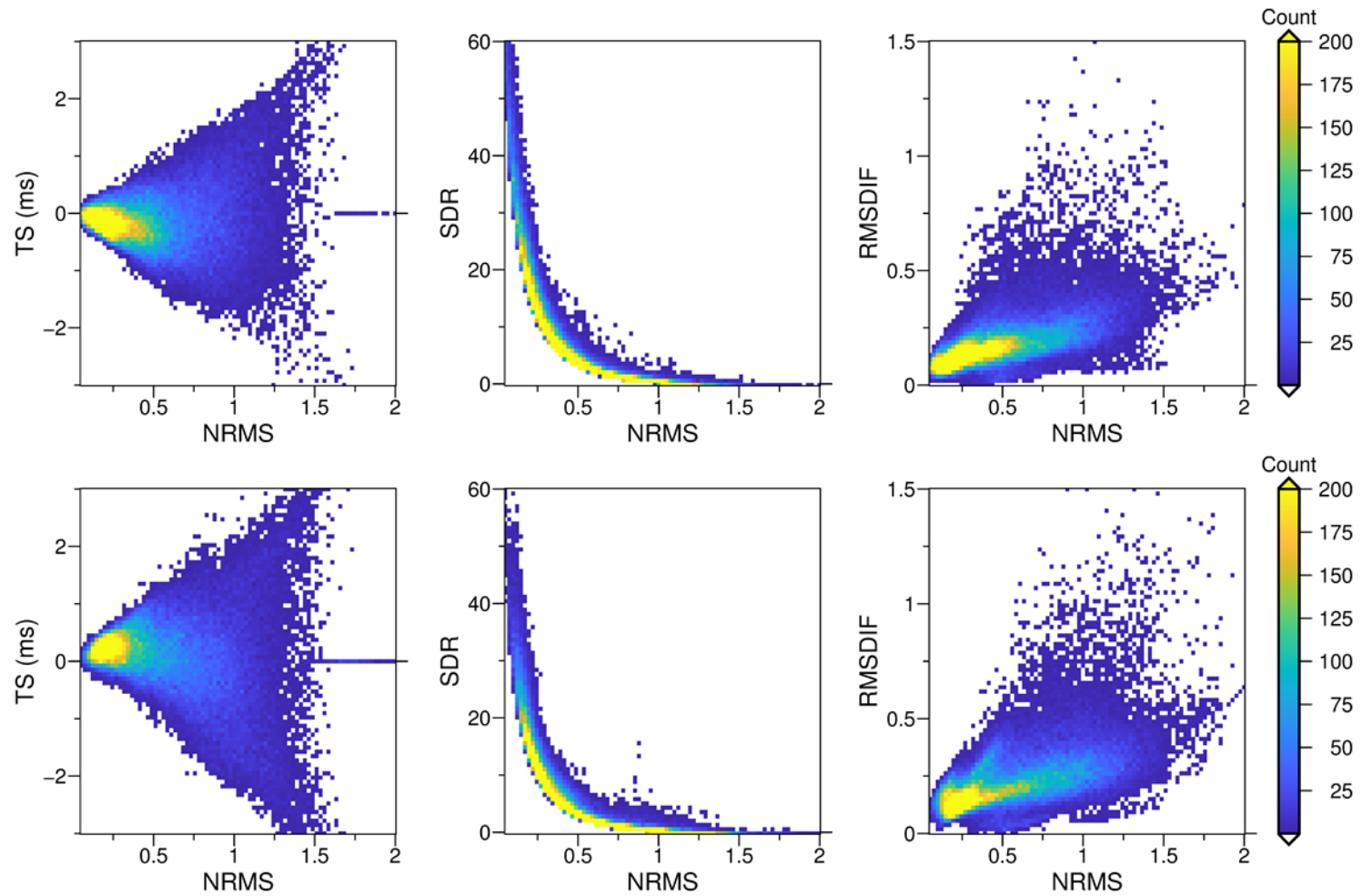
Figure 6-56: 2D histograms of repeatability measures after stacking for the data with PSTM applied before stacking. AGC in 500 ms window is applied before PSTM. Compare to Figure 6-46. Plots of TS vs NRMS (left), SDR vs NRMS (middle), RMSDIF vs NRMS (right). Top row– M3 vs B, bottom row – M4 vs B.

Post-processed and migrated vertical sections along Inline 110 are shown in Figure 6-57 (compare to Figure 6-47). The plume with AGC (Figure 6-57) better stands out from the background 4D noise than the plume without AGC (Figure 6-47). Again, AGC suppressed all types of 4D noise except the residual reflections. It is clearly seen that residual reflections for (B, M4) stand out from all other 4D noises.
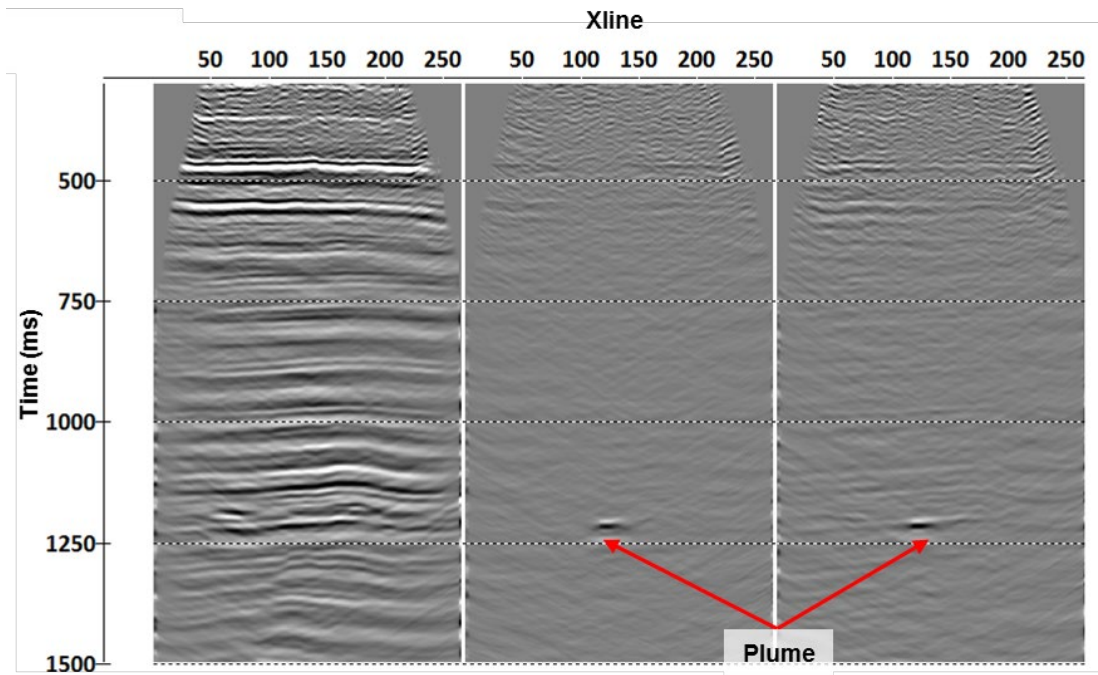
Figure 6-57: Section along Inline 110 through the migrated stack after PSTM. AGC in 500 ms window is applied before PSTM. FXY deconvolution is applied after stacking. Compare to Figure 6-47. Left panel – B, middle panel – M3-B, right panel – M4-B.

Figure 6-58 shows the plume images after the same processing workflow as was used to obtain Figure 6-48 with the only difference being the application of 500 ms AGC before PSTM. We observe improvement in SNR due to the application of AGC for both survey pairs. However, the definition of the (B, M4) plume is less obvious compared to the case presented in Figure 6-53. Workflow with AGC applied before PSTM seems to be more sensitive to the mismatch in the monitor and baseline wavelet as it produces images of lower SNR for the (B, M4) vintage pair compared to

174

(B, M3). It is very important to emphasise that the plume images shown in Figure 6-58 (as well as in all the figures of this kind above) represent an estimate of the 4D SNR (each panel of image scaled individually by its own noise level) rather than just an estimate of the 4D signal (e.g. reflectivity). Thus, we cannot directly compare the change of reflectivity based on the values of these two panels. A simple comparison of the 4D signal strength between the vintages can be done looking at the Figure 6-64 as discussed further in the text.
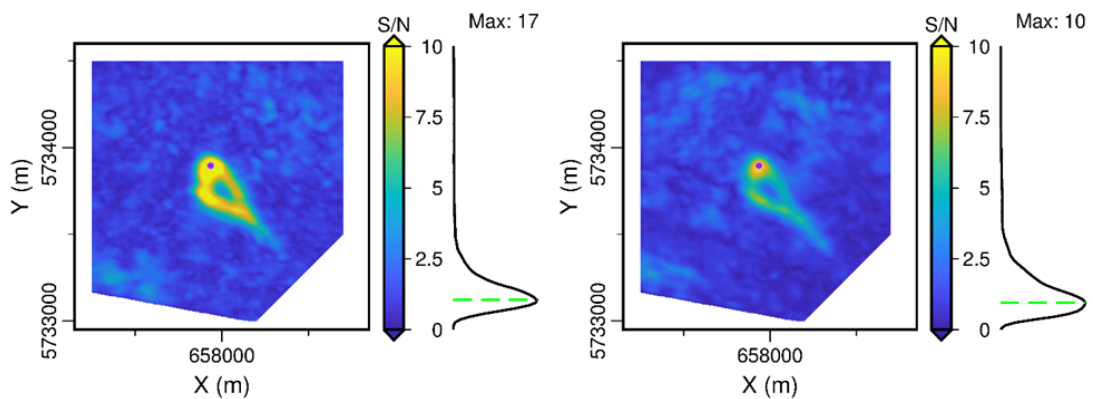
Figure 6-58: Maps of 4D SNR showing plume images after PSTM and stacking. AGC in 500 ms window applied before PSTM. Left panel – M3-B, right panel – M4-B.
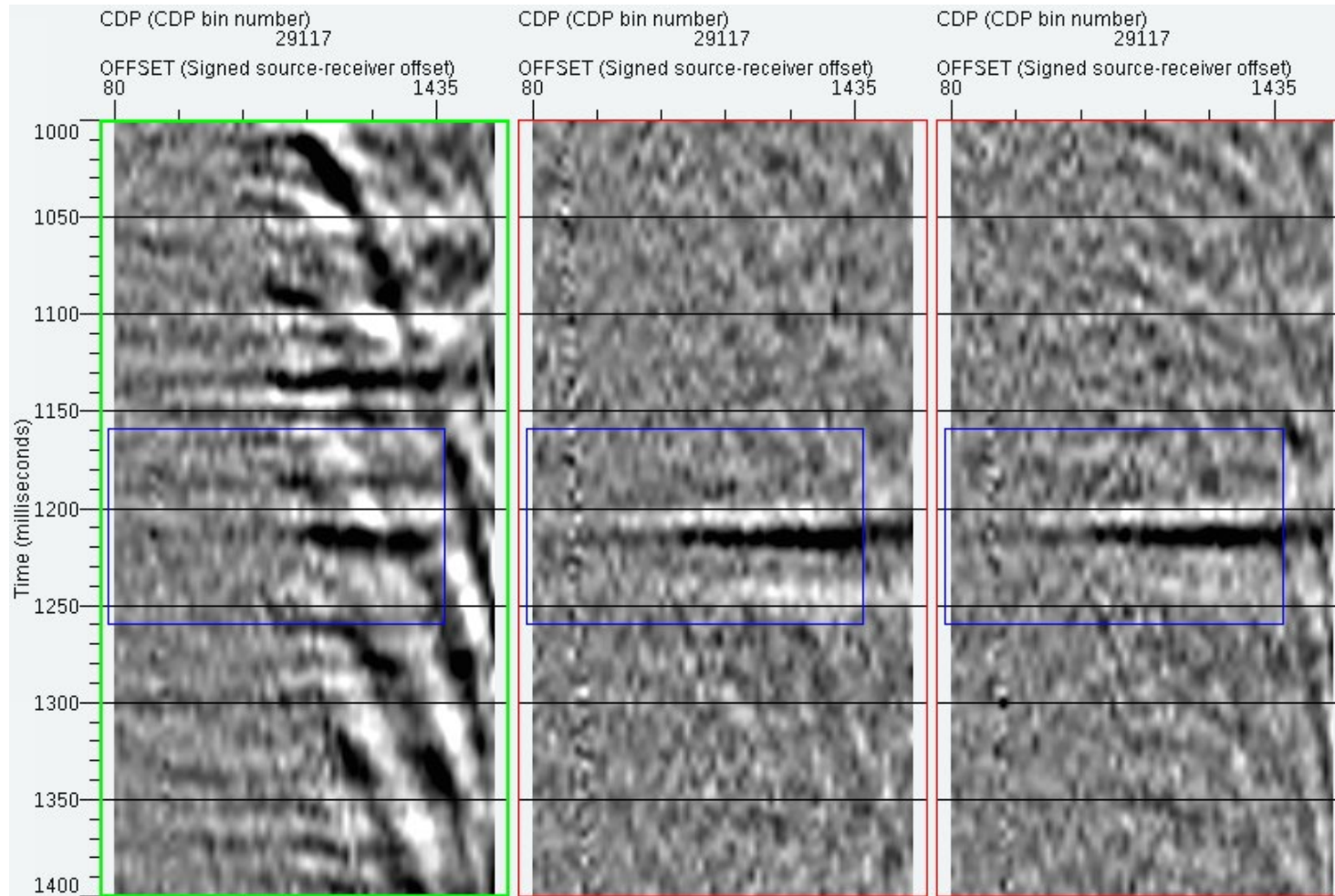
Figure 6-59: Common image gather (inline 110, crossline 123) after PSTM with AGC applied before migration. B (left), M3-B (middle), M4-B (right).

We conclude that the application of AGC allows for better definition of the plume on the post-stack images regardless of the processing workflow used (e.g., pre- or post-stack migration). However, the effect of adding AGC can be different depending on the routines used in the workflow, as can be seen from comparison of the left and right panels in Figure 6-53 and Figure 6-58.

Figure 6-59 shows the same data as Figure 6-49 with the only difference being that 500 ms AGC is applied to the data right before PSTM. We observe amplitude blanking of the near offsets that is caused by the strong remaining energy of ground roll. It is clear that AGC cannot be used in the production of pre-stack images for QI.

6.5   The final workflow

When choosing any step in the workflow we need to consider both the effect of this step on 4D noise and the effect of this step on 4D signal. As we have been measuring both of these quantities throughout processing we can now decide on the final workflow. We have a choose between the workflow with SCD and post-stack time migration and the one with SCD and PSTM.

4D noise measures (Figure 6-50 vs Figure 6-55 and Figure 6-51 vs Figure 6-56) suggest that the PSTM workflow delivers lower NRMS values, higher SDR values, and lower RMS amplitudes of the differences. Only the TS values are similar for the both workflows.

Comparison of post-stack time migration (Figure 6-52) against PSTM (Figure 6-57) favours the PSTM workflow as 4D noise level is lower. The plume (4D signal) representation is quite similar on both figures.

Finally, comparison of the post-stack time migration result in Figure 6-53 and the PSTM result in Figure 6-58 shows that the plume shape, area and definition boundary depend on the imaging algorithm. The edges are clearer in Figure 6-58 than

in Figure 6-53. Interestingly, the difference in 4D noise level between the vintage pairs is less for PSTM (compare the left and right panels of Figure 6-58) than for the post-stack migration case (compare the left and right panels of Figure 6-53). On the other hand, plume images (4D signal) are similar between the left and right panels of Figure 6-53 but not so similar between the left and right panels of Figure 6-58.

If we compare the PSTM image with AGC (Figure 6-57) to the PSTM image without AGC (Figure 6-47), it becomes clear that the weaker 4D signal for (B, M4) is a result of the application of AGC. Otherwise, plume strengths are quite similar between the left and right panels of Figure 6-47 (no AGC). This probably happens due to the higher level of pre-stack time-lapse noise in the (B, M4) difference, which may cause relative suppression of the target signal. The solution to this issue would be application of the same AGC function for a given trace for all the time-lapse vintages.

We now need to decide on the final version of the workflow to be used for processing of all the vintages acquired for Stage 2C. The choice clearly depends on the further use of the processing results and on the time-lapse analysis done so far. We see three main applications for our project. One is structural interpretation which includes determination of the plume's boundary and possibly thickness (e.g. using spectral decomposition), update of the structural model of the injection site and structural history matching. The other two are: QI applied to post-stack images and QI applied to pre-stack images (or common angle stacks). The workflow choices are shown below:

- For the structural interpretation we choose the processing flow that includes PSTM (Figure 6-58, right column of Table 6-1) as it gives a more accurate position of the plume and faults (compared to post-stack time migration) while also providing high SNR values.

- For post-stack QI we have two candidates: either data after SCD, AGC and post-stack time migration (Figure 6-53) or the same data as for the structural interpretation (Figure 6-58). We chose the latter as it provides sufficiently good 4D QC estimates and allows for consistent structural and petrophysical characterisation of the subsurface.

- Development of the workflow for pre-stack QI requires further research. We note that AGC should be avoided in this case.

Our accumulated experience suggests that the processing flow for QI should be gradually optimised through several trials, with QC of each attempt and iterative adjustment of the processing sequence.

Table 6-1: Time-lapse data processing flows.

Express-processing workflow	Workflow for structural interpretation and history matching
CDP binning with bin size 7.5 x 7.5 m	
Elevation statics to final datum of 30 m with replacement velocity of 1800 m/s	
Linear Radon filter and surface wave noise attenuation. AGC in 500 ms window is applied before and removed after ground roll suppression.	Singular value decomposition and adaptive subtraction of ground roll.
Zero-phase spiking deconvolution, 160 ms filter length, 0.1% white noise. AGC in 500 ms window is applied before and removed after deconvolution.	Amplitude correction using $(t*Vrms(t)^2)$ function followed by Surface-consistent spiking deconvolution with individual filters for different vintages, 110 ms filter length, 0.1% white noise.
	Ormsby bandpass zero-phase filter, 5-8-130-145 Hz
Two iterations of residual surface-consistent statics	Two iterations of residual surface-consistent statics
Automatic gain control in 500 ms window	Automatic gain control in 500 ms window
Normal moveout correction with 30 % stretch muting	3D Kirchhoff pre-stack time migration, Two-sided aperture of 1400 m at the target interval of 1200 ms
Ormsby bandpass zero-phase filter, 6-10-110-140 Hz	
	Top mute and FK filtering of common image gathers
Stacking, power for stack normalization – 0.5	Stacking, power for stack normalization – 0.5

FXY deconvolution, spatial size of operator 7 x 7 traces, 600 ms operator length	FXY deconvolution, spatial size of operator 7 x 7 traces, 600 ms operator length
FK filtering to suppress steeply dipping artefacts.	FK filtering to suppress steeply dipping artefacts.
3D explicit finite-difference post-stack time migration – aperture 50 degrees	

6.6 Results of time-lapse processing of 4D surface seismic for Stage 2C

In this section we show the images of the plume produced by the final workflow described in the right column of Table 6-1. At this point all 5 vintages acquired for Stage 2C have gone through the processing flow. The 4D metrics are computed after post-stack post-processed of the pre-stack migrated volumes.

Figure 6-60 shows NRMS in a large window from 400 to 900 ms. Note that the colour scale has been changed for this plot compared with the previous plots of NRMS. We observe generally similar repeatability for all the vintage pairs. The workflow yields mode NRMS of about 0.2. The histograms of NRMS show similar shape for all the vintage pairs.

NRMS depends on the size and location of the window used for calculations. We use a larger window to get an estimate that would characterise the repeatability of the datasets globally.

Figure 6-61 and Figure 6-62 show the 4D QC attributes. We observe low NRMS values and increased SDR values. The time shifts have a systematic bias, which differs slightly for each vintage pair. The minimum bias was obtained for the (B, M3) vintage pair. The B and M3 datasets were acquired at roughly the same time of the year, thus, we expect them to have minimal variation in near-surface velocity. For M1, M2 and M4 the time shifts are biased in the same direction by less than 0.5 ms.
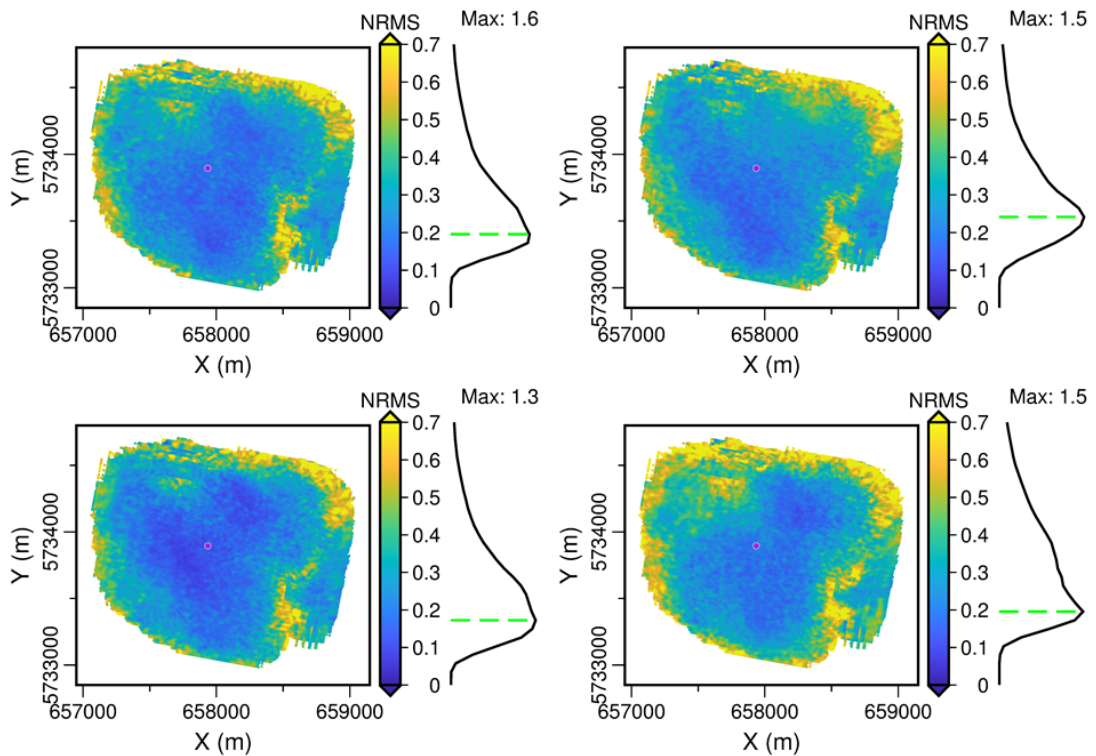
Figure 6-60: NRMS for CDPs computed in a window from 400 to 900 ms on the data stacked after PSTM and post-stack processing. AGC in 500 ms window applied before PSTM. B vs M1 – top left, B vs M2 – top right, B vs M3 – bottom left, B vs M4 – bottom right.

Figure 6-63 shows vertical sections along inline 110. The 4D noise on all the difference images looks quite similar. The (B, M3) pair has the lowest level of energy of residual reflections. The plume has similar representation on all of the images. Finally, Figure 6-64 shows the map view of the plume. At this time, all the plume images are normalized by the same value. Evolution of the plume can be clearly observed as discussed in the following subsection. Again, the vintage pair (B, M3) has the best definition of the plume's boundary and lowest level of 4D noise.
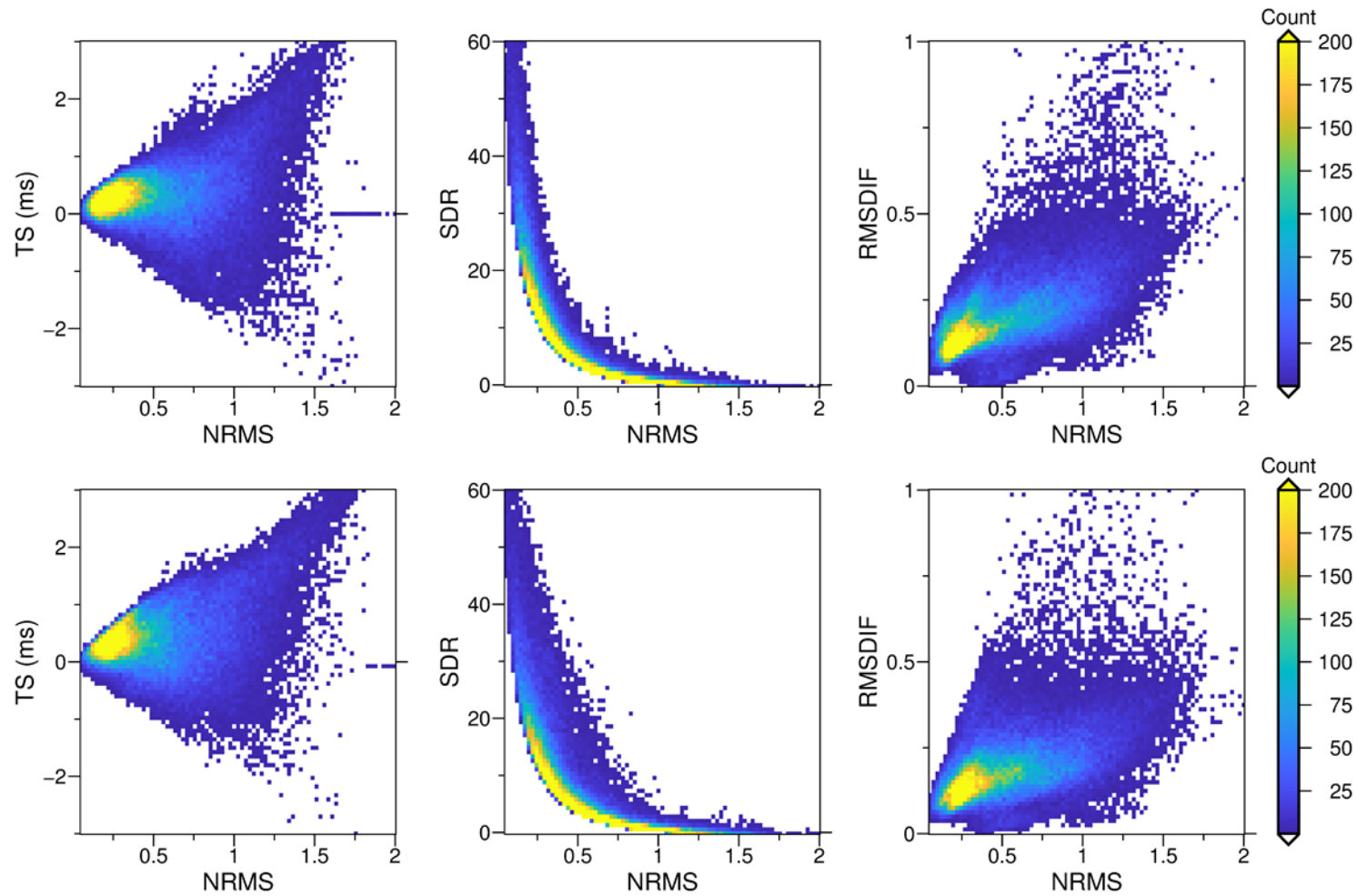
Figure 6-61: 2D histograms of repeatability measures after stacking for the data with PSTM applied before stacking and post-stack processing. AGC in 500 ms window is applied before PSTM. Plots of TS vs NRMS (left), SDR vs NRMS (middle), RMSDIF vs NRMS (right). Top row– M1 vs B, bottom row – M2 vs B.
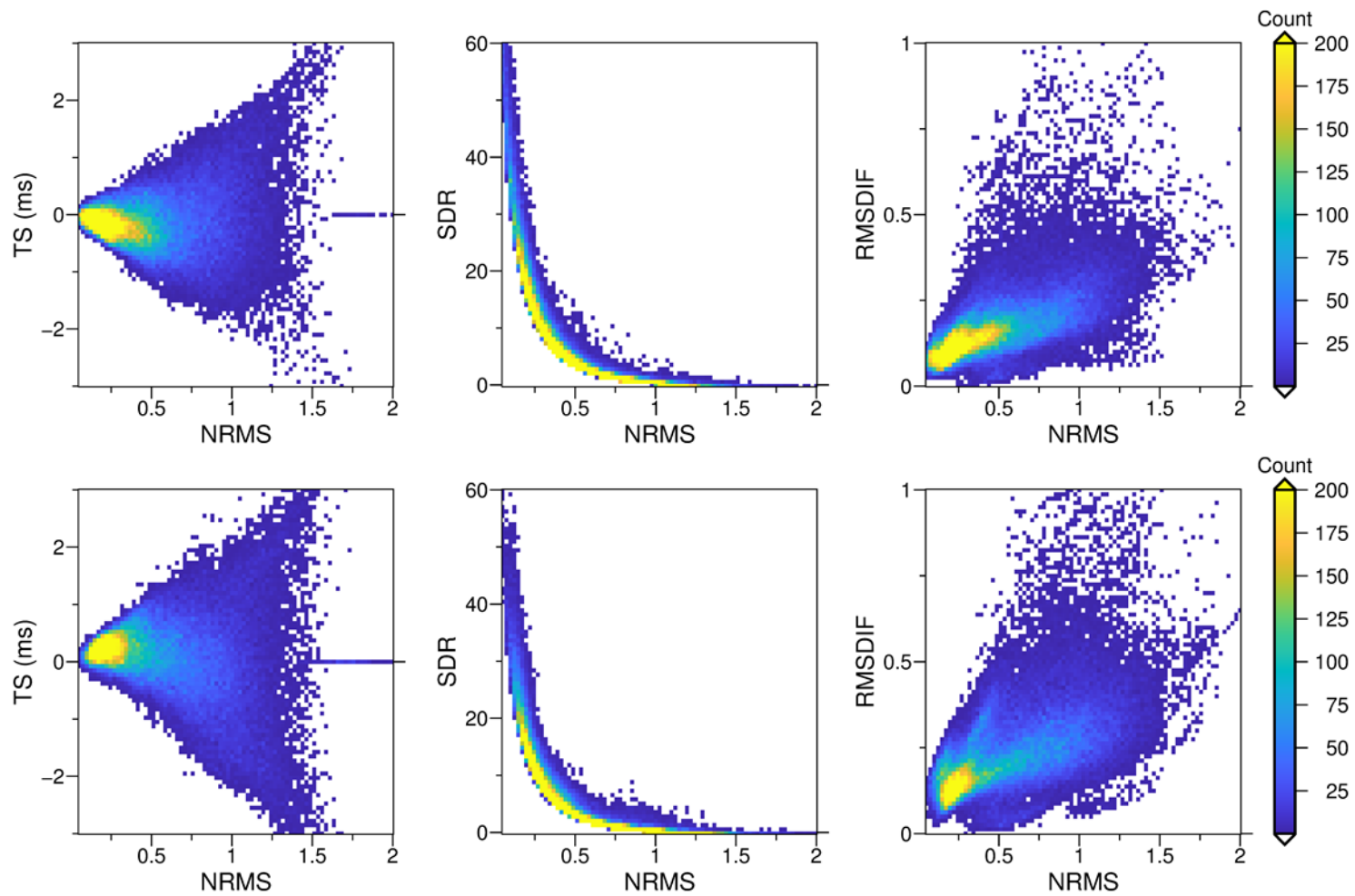
Figure 6-62: 2D histograms of repeatability measures after stacking for the data with PSTM applied before stacking and post-stack processing. AGC in 500 ms window applied before PSTM. Plots of TS vs NRMS (left), SDR vs NRMS (middle), RMSDIF vs NRMS (right). Top row– M3 vs B, bottom row – M4 vs B.
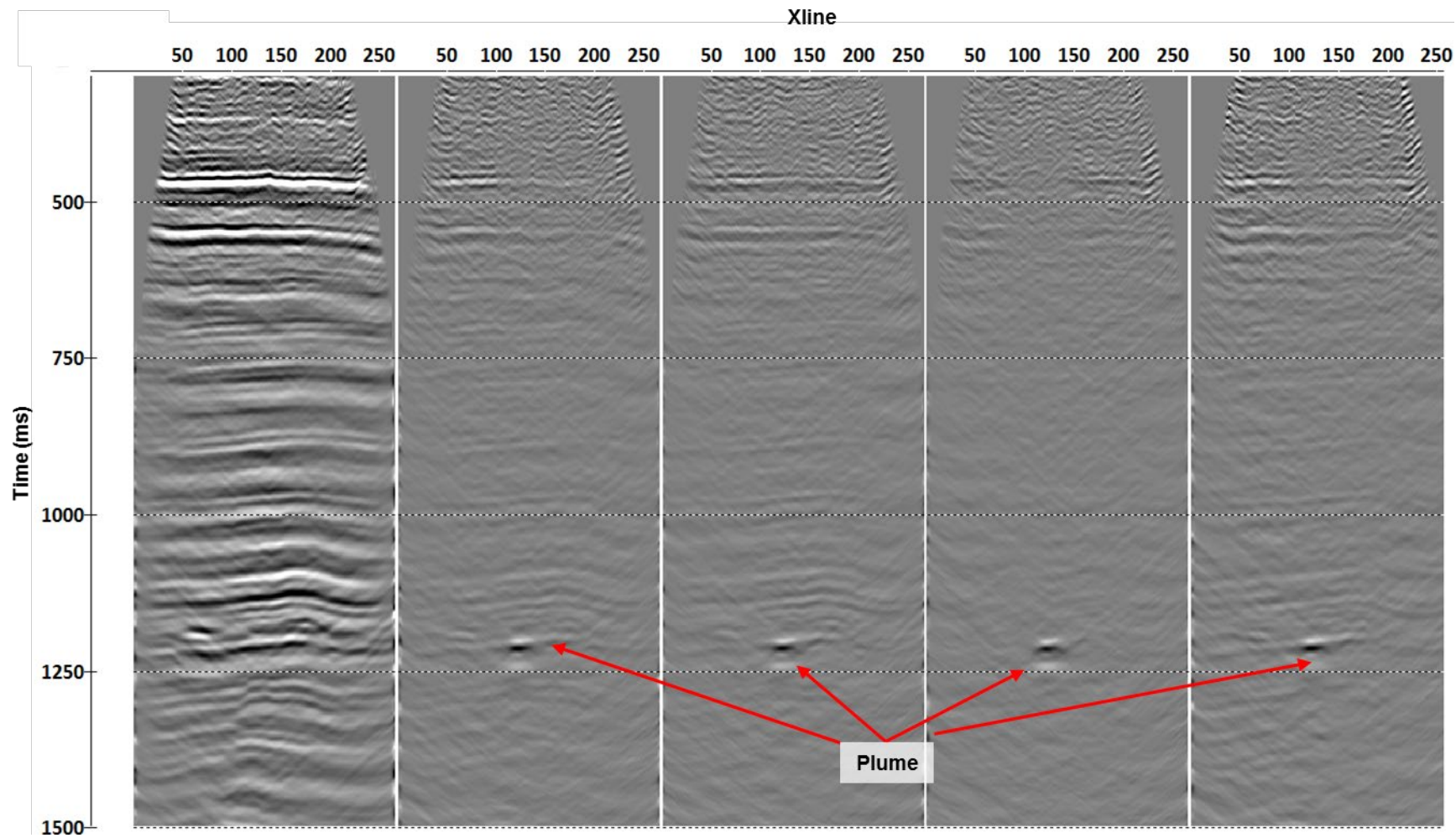
Figure 6-63: Section along Inline 110 through the migrated stack after PSTM. AGC in 500 ms window applied before PSTM. FXY deconvolution is applied after stacking. From left to right – B, M1-B, M2-B, M3-B, M4-B.

185
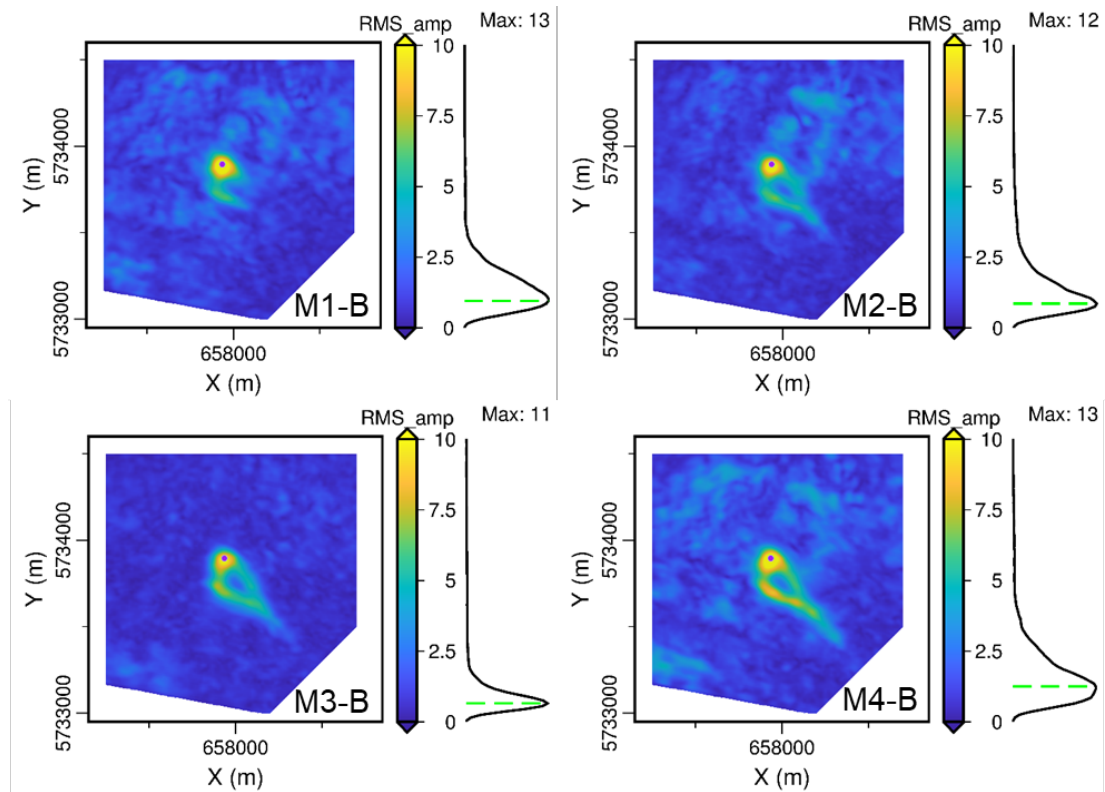
Figure 6-64: Plume image after PSTM and stacking. AGC in 500 ms window is applied before PSTM. RMS amplitude is computed in 24 ms window centred at 1210 ms. All the maps are normalized by the same common value. M1-B – top left, M2-B – top right, M3-B – bottom left, M4-B – bottom right.

As the detailed analysis of the plume's evolution is outside of the scope of this thesis, we provide some simple interpretation of the plume's movement between the injections. The lateral distribution of the RMS amplitude of the differences over the target horizon (Figure 6-64) shows a clear anomaly localized around the injection well. Figure 6-64 shows that initially the anomaly was approximately circular in shape and, as the injection progressed, increased in size and spread in the southern and south-eastern direction. It appears that the plume reached a known sealing fault to the south of the injector and then spread up-dip (in the east-southeastern direction) inside the reservoir alongside the sealing fault (Tenthorey et al. 2014). Heterogeneity of the permeability inside the injection reservoir can be inferred as we clearly observe a "hole" in the plume (blue colour in the middle of the yellow plume in all four panels).

A common interpretation technique in 4D seismic involves estimation of TS right below the injection interval which is indicative of 4D signal (in this thesis we estimate TS above the injection interval to assess 4D noise). These TS can then be related to the presence and properties of the injection. Maps with the estimates of the signal-related TS for the synthetic data are shown in Figure 6 of Pevzner, Caspari, Gurevich, et al. (2015). The maximum TS values barely exceed 1 ms. We attempted estimation of the post-stack TS under the plume for the field data. We could not observe any anomalous behaviour in this time-shift maps. We speculate this is because the plume thickness is too small to cause a noticeable time-shift anomaly as well as all kinds of noise complicate the TS estimation unlike in the synthetic case. As we could not measure any time-shifts below the reservoir in the field data we cannot say whether they meet rock-physics expectations shown in Figure 6 of Pevzner, Caspari, Gurevich, et al. (2015) or not. We speculate that time-shifts induced by the injection may be estimated on the pre-stack images as there is less potential of the error due to wavelet mis-stacking which could have obscured the post-stack measured time shifts.

6.7   Conclusions

In this chapter we described advanced time-lapse processing of the seismic monitoring data acquired for Stage 2C of the CO2CRC Otway Project. This study aimed to increase the accuracy of the plume location and seismic amplitude restoration for QI. In order to do so, we:

- analysed the main causes of poor repeatability of onshore 4D surface seismic from the theoretical standpoint and illustrated some of these noise types. For the Otway site, the most harmful noise is associated with ground roll, source-generated S waves, ambient uncorrelated noise, and instability of the excitation/radiation.

- proposed a methodology to track 4D signal and 4D noise through the processing workflow. We suggested the use of a number of time-lapse attributes that complement each other to represent repeatability:
  - We computed NRMS, TS, SDR and RMSDIF of pre-stack and post-stack data in the signal-free zones to estimate 4D noise. We then suggested ways to display those noise estimates to track repeatability of entire vintages. Also some of the plots (such as source and receiver maps or NRMS vs offset plots) can help to identify domains and traces with poor repeatability. Then the processing workflow can be adjusted to address these problems. We used the plots of these four attributes to see how 4D noise changes as a function of a processing step.
  - 4D signal related to the injection was poorly detectable before seismic migration due to the diffractive character of the plume's unmigrated response. We computed 4D SNR attribute on the final plume images and produced maps that illustrate how SNR in and around the plume changes as a function of each processing step. Even though this approach is very sensitive to the window size, it provides very insightful results.
- explored how certain time-lapse measures represent and react to different sources of 4D noise:
  - NRMS, SDR and TS represent 4D noise or repeatability when the strongest coherent (in the domain of monitoring time) event in a baseline and the corresponding monitor trace is a reflected wave. Only in this case can these measures indicate time-lapse

noise in (repeatability of) reflections and, thus, can properly capture effects associated with ambient noise, instrumentation performance and variability of the acquisition conditions. NRMS, SDR and TS are misleading for traces with strong correlated noise (like ground roll) because they would indicate repeatability of the noise. When this noise is suppressed during processing, the similarity between the remnants of this noise in baseline and monitor traces drops and these measures indicate a degradation of repeatability, while the RMSDIF attribute indicates a drop in the residual noise energy.

- o The RMSDIF attribute is a robust measure of the correlated 4D noise (e.g. ground roll).

- o NRMS, SDR and TS should be used for QC wavelet matching while RMSDIF is useful in QC suppression of high-energy noise events that are coherent between the monitor and baseline traces. Subtle differences in the reaction of NRMS, SDR and TS to time-lapse noise occur only for reflected wavelets with relatively low levels of uncorrelated noise; e.g., in marine seismic.

- developed and justified a seismic processing workflow for 4D surface seismic data of Stage 2C. Table 6-2 summarizes performance of the employed processing routines (please refer to the table's caption for the guidance in interpretation of the table's content). NRMS measures for stacked non-migrated data are generally higher than for migrated data (the blue colour indicates NRMS values for non-migrated data). Table

6-2 can be used not only for tracking repeatability through different processing stages but also for testing different approaches and parametrisations of the routines at the same processing stage (e.g., testing deconvolution or testing different ways of ground roll suppression).

The same seismic images can be used for post-stack QI (e.g., post-stack inversions). The QI would allow updating of the static geological model through history matching. The repeatability of the final images is reasonably good with mode values of NRMS fluctuating around 0.2 for all four monitor vintages (Figure 6-60).

So far we have developed a workflow that provides full-stack images of the plume for structural and QI purposes. A test common image gather clearly shows 4D signal from the plume (Figure 6-49). Further work should focus on improving the 4D AVO response (improve 4D signal in Figure 6-49) required for pre-stack QI.

Table 6-2: Summary of the performance of various repeatability measures for each processing stage. Arrows indicate whether the value of the repeatability measure increased (↑), left unchanged (-) or decreased (↓) after application of this processing step. Colour codes: green – improvement of repeatability measure, yellow – not much change, red – degradation of repeatability measure, blue – indicates that NRMS values were obtained on unmigrated data. All values of 4D SNR are computed on migrated data. Results for (B, M3) and (B, M4) are separated by "/".

	Pre-stack				Post-stack					Mode NRMS (%)	Maximum 4D SNR
	NRMS	SDR	TS	RMSDIF	NRMS	SDR	TS	RMSDIF	4D SNR		
Raw data										38 / 66	8.4 / 5.8
Ground roll removal	↑ / ↑	↑ / ↑	- / -	↓↓ / ↓↓	↑↑ / ↑	↓ / ↓	↓ / ↓	↓↓ / ↓↓	↑ / ↑	53 / 72	11 / 7.7
Surface-consistent deconvolution	↓ / ↓↓	- / -	↓ / ↓	- / -	↓ / ↓	- / -	↓ / ↓	↓ / ↓	- / ↑	50 / 66	11 / 9.2
Pre-stack time migration					↓↓ / ↓↓	↑↑ / ↑↑	↓ / ↓	↓ / ↓	↓ / ↓	32 / 39	6.9 / 6.2
Automatic gain control applied before pre-stack time migration					↓ / ↓	↑ / ↑	↓ / ↓	↓ / ↓	↑↑ / ↑	23 / 25	17 / 10

Chapter 7.

Conclusions and future work

As a part of Stage 2C of the CO2CRC Otway Project, 15,000 tonnes of the supercritical CO_2/CH_4 mixture were injected into the subsurface. In order to monitor the injection, an extensive seismic monitoring program was rolled out, which included 4D seismic conducted using the permanently deployed receiver array. The main objective of this thesis was to develop and justify an approach to producing high quality images from the onshore 4D surface seismic data acquired for monitoring and verification programmes of carbon geosequestration projects. This problem had a number of aspects that we addressed. In essence, we developed and justified a methodology for the acquisition, feasibility study, processing and imaging of 4D surface seismic that yielded the desired high quality images of the injection. In the following I describe the findings of our research.

7.1   Conclusions

Acquisition

High quality of the field data was achieved due to the permanent installation of geophones, the use of differential GPS to reposition vibrator trucks to baseline shot locations and high CDP fold. The buried high-sensitivity geophone array yielded significantly higher SNR than surface geophones, gaining over 20–30 dB in ambient noise reduction and good repeatability. Another benefit of using a permanent receiver array is reduced impact on landowners. The installation of the array took less than 30 days and the total duration of actual acquisition for four 3D surveys (B, M1, M2, M3)

was 30 days. During the installation of the array, only a small portion of the area was affected at any time as the array was deployed on a landowner-by-landowner basis. Acquisition of data was also conducted by sequentially completing the source points located at the land parcels belonging to different landowners with small vibrator trucks and no cables lying in the area. The drastic reduction of acquisition time and minimal crew required to conduct the surveys results in significant cost reduction of seismic monitoring. Further cost reduction can be achieved by using DAS-based receiver arrays and unmanned continuous monitoring (both active and passive).

Synthetic feasibility study

To place the CO_2 plume into realistic seismic imaging conditions we built a full-earth seismic model of the area with the level of detail typical for geomodelling in hydrocarbon reservoir characterisation (2.5 m × 2.5 m × 2 m). The subsurface model was built with geostatistical methods (collocated co-kriging), which provided a convenient approach to create consistent distributions of density and seismic velocities. This proved essential to avoid artefacts in seismic wave simulations.

Simulations of time-lapse elastic wavefield for baseline and monitor models (with the dimensions of 2940 x 3600 x 1860 m each) took about 5 million CPU hours to run and required computations on a supercomputer. We used the results of seismic modelling to verify the detectability of the potential small-scale injection in the presence of bandlimited random and geological noise in a relatively realistic 3D setting.

Model-guided processing

For the synthetic 4D seismic dataset we had relatively good knowledge of the wavefield and we also had the true model of the subsurface. This allowed us to study the effect of different processing procedures on 4D noise and 4D signal and then to

apply these findings to processing of the field data in a model-guided fashion. As our model is still a simplification we did not address some of the issues such as ground roll removal techniques and corrections for surface-consistent variability. Instead, we addressed potential problems of deconvolution, AGC and imaging, and implemented them in the processing of the field data. Table 7-1 shows how we used synthetics to build a model-guided processing workflow for the field data.

Table 7-1: Model-guided processing of the field data.

Findings from the synthetic data processing	Implementation in field data processing
Parts of the shot records affected by ground roll retain a lot of hidden time-lapse signal, hence, ground roll should be carefully removed to avoid damaging 4D signal at near- and mid-offsets.	Applied ground noise removal technique based on singular value decomposition for three frequency bands. Stacked and migrated the removed noise to ensure that 4D signal is preserved.
Long-window AGC to a large extent preserves lateral reflectivity of the plume on full-stack images, hence, it can be applied before stacking if the benefit of noise reduction is considerable.	Applied 500 ms AGC before PSTM which led to an increase in 4D SNR.
Spiking trace-by-trace deconvolution might degrade quality of well-ties and QI.	Avoided use of trace-by-trace deconvolution. Used surface-consistent deconvolution with individual sets of filters instead.
Time migrations introduce lateral shift (few tens of meters) into positions of the faults and plume at the target depth of 1500 m. Pre-stack depth migration is ideally required.	Used PSTM with offset bins of variable sizes to account for uneven distribution of traces for different offset ranges. Detailed velocity model in depth is not available for the field data. Application of time migration to the field data might be justified if actual subsurface does not have strong lateral velocity gradients.

Time-lapse processing of the field data

We have developed a methodology to produce judicious full-stack 4D images of the small-scale injection with good accuracy of the plume location / definition and seismic amplitude restoration for quantitative interpretation. Below, we describe the major findings from the analysis of the field data. We have:

- discussed and demonstrated the types of noise that degrade the repeatability of onshore 4D surface seismic. For our data ground roll, source-generated S waves, ambient uncorrelated noise, and instability of the near-surface and excitation parameters contribute the strongest time-lapse noise;

- proposed a methodology for QC processing workflows from the perspective of 4D noise and 4D signal. We used a combination of time-lapse attributes (NRMS, TS, SDR, RMSDIF and 4D SNR) to assess repeatability after each processing step. We proposed the displays of these attributes for an insightful look at the data.

- investigated how different repeatability metrics respond to different types of time-lapse noise. We found that the measures NRMS, SDR and TS should be used to QC wavelet matching while RMSDIF is useful in QC suppression of high-energy noise events that are coherent between the monitor and baseline traces. Subtle differences in the reaction of NRMS, SDR and TS to time-lapse noise are observed only when we compare reflected wavelets with relatively low levels of uncorrelated noise, which is the case in marine seismic but not onshore.

7.2   Relevance of the findings to other monitoring projects

Even though this thesis is based on a case study for Stage 2C of the Otway Project, we believe that many findings are relevant to other onshore and even offshore monitoring projects. In particular, the methodology that we use to track time-lapse signal and noise through processing can be applied to any kind of time-lapse data. The same time-lapse attributes can be computed and displayed in all the processing domains (pre-stack, post-stack, common source, common receiver, etc). Discussion on

the sources of time-lapse noise is applicable to any land monitoring dataset. The findings about the time-lapse effects of individual processing and imaging routines on repeatability can also be applicable to other projects if caution is taken when using data-driven procedures (e.g. SCD and AGC), as their performance depends on noise.

Of course, the workflow for processing of the field data that we developed in this thesis cannot be transferred as is. An important feature of the Stage 2C experiment is a permanently installed geophone array. This by itself alleviates issues of repeatability on the receiver side and affects the way we build our workflow. Use of the same vibrator trucks with the same sweep parameters improve the repeatability of the raw data on the source side. The use of differential GPS to reposition the trucks for each monitor survey further helps with source repeatability. The initially good repeatability of the data coupled with the surface-consistent deconvolution with individual sets of filters reduce the importance of explicit cross-equalization through application of matching time-shifts, amplitude scalars and filters. Though not shown here, cross-equalization of the pre-stack data after the application of SCD with individual filters did not result in any notable improvement. This is probably due to the fact that the matching corrections required are at the level of the time-lapse noise that stays in the solution even after we solve overdetermined systems for surface-consistent solutions. However, cross-equalization might be an important step in processing of the data where repeatability of the wavelet is worse.

We conclude that even though some of the features of this research are case specific, we still expect the findings from this thesis to be transferrable to other monitoring and verification projects as well as the monitoring of hydrocarbon production.

7.3 Future work

This thesis covers a number of aspects of 4D processing and imaging as summarized above. Nonetheless there are still plenty of things that can be done to extract more value from the data. Below, we outline a few of the things that we consider important.

It gets more and more important to reduce the invasiveness of seismic surveys, particularly if they are repeatedly acquired over the same land patch during the lifetime of a CO_2 storage project. Stage 2C addressed this issue from the receiver side through the permanent installation of the geophones at a depth of 4 m below the surface. The next step would be to reduce the source effort. While not presented here, our testing shows that removal of every second shot record does not alter the full-stack images of the plume. Even though sparser shot locations might degrade the performance of some processing routines (e.g. pre-stack imaging, estimation of residual statics or noise suppression in common receiver gathers) there is a good chance that it will speed up the monitor surveys and reduce the environmental impact. Another way to resolve land access issues is to use permanent sources with surface and borehole recording using traditional geophones, VSP and emerging DAS technology.

Restoration of the 4D AVO response on pre-stack images should first be tried on synthetics and then followed by the field data. This work would require development of an approach for tracking the time-lapse signal in pre-stack configurations. So far we have not seen 4D signal on the field data before PSTM. This means that if we want to track 4D signal through the pre-migration routines (e.g., noise suppression, deconvolution) we either need to run PSTM after every important processing step or perform some sort of illumination analysis to find out which

samples of unstacked traces contribute to the plume image. Only then can 4D signal somehow be quantified and its dependence on angle and azimuth be studied.

To produce pre-stack images of the plume we will also have to regularize our data prior to pre-stack imaging either in offset bins or offset vector tiles. The effects of 3D/4D/5D interpolation and regularisation techniques in the presence of noise on the time-lapse signal are not explored in this thesis at all. We suggest that the behaviour of regularization in relation to 4D SNR should be studied if one wants to further explore the capabilities of time-lapse QI.

Our synthetic study has demonstrated that even in a relatively simple and horizontally layered model time migration (both post-stack and pre-stack) can introduce errors in the lateral plume positioning. As we knew the actual velocity model for the synthetic study we used it to run pre-stack depth migration (RTM) and accurately restore the plume's location. This indicates that pre-stack depth imaging (possibly anisotropic) should be implemented to produce more confident plume images.

In this work we have used these attributes to track the overall quality of processing. However, we did not go into detailed analysis of the crossplots of 4D metrics and plots of NRMS measures for various processing domains (e.g., receiver, source, offset). We believe that a more detailed study of these attributes will help in the fine-tuning of processing workflows that produce pre-stack 4D images.

Bibliography

Al Hosni, M., E. Caspari, R. Pevzner, T. M. Daley, and B. Gurevich. 2016, Case History: Using time-lapse vertical seismic profiling data to constrain velocity–saturation relations: the Frio brine pilot CO2 injection. Geophysical Prospecting, **64**, no. 4,987-1000. doi: 10.1111/1365-2478.12386.

Arts, R., O. Eiken, A. Chadwick, P. Zweigel, B. van der Meer, and G. Kirby. 2004, Seismic monitoring at the Sleipner underground CO_2 storage site (North Sea). Geological Society, London, Special Publications, **233**, no. 1,181-191. doi: 10.1144/gsl.sp.2004.233.01.12.

Arts, R. J., R. A. Chadwick, O. v. Eiken, S. Dortland, M. Trani, and L. G. H. v. d. Meer. 2010, Acoustic and elastic modeling of seismic time-lapse data from the Sleipner CO2 storage operation, in J. C. Pashin M. Grobe, R. L. Dodge, ed., Carbon dioxide sequestration in geological media—State of the science: AAPG Studies in Geology. 391–403.

Avseth, P., T. Mukerji, and G. Mavko. 2005, Quantitative Seismic Interpretation: Applying Rock Physics Tools to Reduce Interpretation Risk.

Bakulin, A., R. Smith, M. Jervis, and R. Burnstad. 2014, Near surface changes and 4D seismic repeatability in desert environment: From days to years, SEG Technical Program Expanded Abstracts 2014. 4843-4847.

Bakulin, A., R. Smith, M. Jervis, and R. Burnstad. 2015, Use of early arrivals for 4D analysis and processing of buried receiver data on land, SEG Technical Program Expanded Abstracts 2015. 5493-5497.

Bakulin, A., R. Smith, M. Jervis, C. Saragiotis, E. Al-Hemyari, and A. Alramadhan. 2016, Processing and repeatability of 4D buried receiver data in a desert environment, SEG Technical Program Expanded Abstracts 2016. 5405-5409.

Bancroft, J. 2007, A practical understanding of pre- and poststack migrations. Edited by L.M. Gochioco. Vol. 13, Course Notes: Society Of Exploration Geophysicists

Batzle, M., and Z. J. Wang. 1992, Seismic Properties of Pore Fluids. Geophysics, **57**, no. 11,1396-1408.

Baysal, E., D. D. Kosloff, and J. W. C. Sherwood. 1983, Reverse time migration. GEOPHYSICS, **48**, no. 11,1514-1524. doi: 10.1190/1.1441434.

Bergmann, P., M. Diersch, J. Götz, M. Ivandic, A. Ivanova, C. Juhlin, J. Kummerow, A. Liebscher, S. Lüth, S. Meekes, B. Norden, C. Schmidt-Hattenberger, F. M. Wagner, and F. Zhang. 2016, Review on geophysical monitoring of CO_2 injection at Ketzin, Germany. Journal of Petroleum Science and Engineering, **139**,112-136. doi: http://dx.doi.org/10.1016/j.petrol.2015.12.007.

Bergmann, P., A. Kashubin, M. Ivandic, S. Lüth, and C. Juhlin. 2014, Time-lapse difference static correction using prestack crosscorrelations: 4D seismic image enhancement case from Ketzin. GEOPHYSICS, **79**, no. 6,B243-B252. doi: 10.1190/geo2013-0422.1.

Bohlen, T. 2002, Parallel 3-D viscoelastic finite difference seismic modelling. Computers & Geosciences, **28**, no. 8,887-899. doi: http://dx.doi.org/10.1016/S0098-3004(02)00006-7.

Bohlen, T., D. De Nil, Kohn D., and J. S. 2015, SOFI 3D: seismic modelling with finite differences 3D - acoustic and viscoelastic version. Users Guide.

Calvert, R. 2005a, 4D technology: where are we, and where are we going? : Geophysical Prospecting, **53**, no. 2,161-171.

Calvert, R. 2005b, Insights and Methods for 4D Reservoir Monitoring and Characterization. Vol. 8, Distinguished Instructor Series: Society of Exploration Geophysicists and European Association of Geoscientists and Engineers.

Cantillo, J. 2011, A quantitative discussion on time-lapse repeatability and its metrics, SEG Technical Program Expanded Abstracts. 4160-4164.

Cantillo, J. 2012, Throwing a new light on time-lapse technology, metrics and 4D repeatability with SDR. The Leading Edge, **31**, no. 4,405-413.

Cantillo, J., J.-L. Boelle, A. Lafram, and D. Lecerf. 2010, Ocean Bottom Nodes (OBN) Repeatability And 4D. Society of Exploration Geophysicists.

Cary, P. W., and G. A. Lorentz. 1993, Four-component surface-consistent deconvolution. GEOPHYSICS, **58**, no. 3,383-392. doi: 10.1190/1.1443421.

Cary, P. W., and C. Zhang. 2009, Ground roll attenuation with singular value decomposition, 11th International Congress of the Brazilian Geophysical Society & EXPOGEF 2009, Salvador, Bahia, Brazil, 24-28 August 2009. 1627-1630.

Caspari, E., R. Pevzner, B. Gurevich, T. Dance, J. Ennis-King, Y. Cinar, and M. Lebedev. 2015, Feasibility of CO2 plume detection using 4D seismic: CO2CRC Otway Project case study — Part 1: Rock-physics modeling. GEOPHYSICS, **80**, no. 4,B95-B104. doi: doi:10.1190/geo2014-0459.1.

Chadwick, A., G. Williams, N. Delepine, V. Clochard, K. Labat, S. Sturton, M.-L. Buddensiek, M. Dillen, M. Nickel, A. L. Lima, R. Arts, F. Neele, and G. Rossi. 2010, Quantitative analysis of time-lapse seismic monitoring data at the Sleipner CO_2 storage operation. The Leading Edge, **29**, no. 2,170-177. doi: doi:10.1190/1.3304820.

Chadwick, R. A., B. P. Marchant, and G. A. Williams. 2014, CO2 storage monitoring: leakage detection and measurement in subsurface volumes from 3D seismic data at Sleipner. Energy Procedia, **63**,4224-4239. doi: http://dx.doi.org/10.1016/j.egypro.2014.11.458.

Chadwick, R. A., D. Noy, R. Arts, and O. Eiken. 2009, Latest time-lapse seismic data from Sleipner yield new insights into CO_2 plume development. Energy Procedia, **1**, no. 1,2103-2110. doi: 10.1016/j.egypro.2009.01.274.

Cook, P. J. E. 2014, Geologically Storing Carbon: Learning from the Otway Project Experience: CSIRO Publishing.

Couëslan, M. L., V. Smith, G. El-Kaseeh, J. Gilbert, N. Preece, L. Zhang, and J. Gulati. 2014, Development and implementation of a seismic characterization and CO2 monitoring program for the Illinois Basin – Decatur Project. Greenhouse Gases: Science and Technology, **4**, no. 5,626-644. doi: 10.1002/ghg.1452.

Daley, T., B. Freifeld, J. Ajo-Franklin, S. Dou, R. Pevzner, V. Shulakova, S. Kashikar, D. Miller, J. Goetz, J. Henninges, and S. Lueth. 2013, Field testing of fiber-optic distributed acoustic sensing (DAS) for subsurface seismic monitoring. The Leading Edge, **32**, no. 6,699-706. doi: doi:10.1190/tle32060699.1.

Daley, T. M., L. R. Myer, J. E. Peterson, E. L. Majer, and G. M. Hoversten. 2008, Time-lapse crosswell seismic and VSP monitoring of injected CO2 in a brine aquifer. Environmental Geology, **54**, no. 8,1657-1665. doi: 10.1007/s00254-007-0943-z.

Dance, T. 2013, Assessment and geological characterisation of the CO2CRC Otway Project CO2 storage demonstration site: From prefeasibility to injection. Marine and Petroleum Geology, **46**,251-269. doi: http://dx.doi.org/10.1016/j.marpetgeo.2013.06.008.

Dance, T., M. Arnot, M. Bunch, R. Daniel, A. Hortle, M. Lawrence, and J. Ennis-King. 2012, Geocharacterisation and static modelling of the lower Paaratte formation. . In CO2CRC Otway project - phase II. Canberra, Australia: Cooperative Research Centre for Greenhouse Gas Technologies.

Davis, T. L., and R. D. Benson. 2004, Weyburn field seismic monitoring project, SEG Technical Program Expanded Abstracts 2004. 2255-2258.

Dou, S., J. Ajo-Franklin, T. Daley, M. Robertson, T. Wood, B. Freifeld, R. Pevzner, J. Correa, K. Tertyshnikov, M. Urosevic, and B. Gurevich. 2016, Surface orbital vibrator (SOV) and fiber-optic DAS: Field demonstration of economical, continuous-land seismic time-lapse monitoring from the Australian CO_2CRC Otway site, SEG Technical Program Expanded Abstracts 2016. 5552-5556.

Doyen, P. 2007, Seismic Reservoir Characterization: An Earth Modelling Perspective: EAGE Publications.

Dvorkin, J., M. A. Gutierrez, and D. Grana. 2013, Seismic Reflections of Rock Properties: Cambridge University Press.

Dvorkin, J., G. Mavko, and B. Gurevich. 2007, Fluid substitution in shaley sediment using effective porosity. GEOPHYSICS, **72**, no. 3,O1-O8. doi: doi:10.1190/1.2565256.

Ennis-King, J., T. Dance, J. Xu, C. Boreham, B. Freifeld, C. Jenkins, L. Paterson, S. Sharma, L. Stalker, and J. Underschultz. 2011, The role of heterogeneity in CO_2 storage in a depleted gas field: History matching of simulation models to field data for the CO2CRC Otway Project, Australia. Energy Procedia, **4**, no. 0,3494-3501. doi: http://dx.doi.org/10.1016/j.egypro.2011.02.276.

Freifeld, B. M., R. Pevzner, S. Dou, T. Daley, M. Robertson, K. Tertyshnikov, T. Wood, J. Ajo-Franklin, M. Urosevic, and B. Gurevich. 2016, The CO2CRC Otway Project deployment of a Distributed Acoustic Sensing Network Coupled with Permanent Rotary Sources. Paper read at 78th EAGE Conference & Exhibition 2016, 30 May - 2 June 2016, at Vienna, Austria.

Gaiser, J. 2016, 3C Seismic and VSP: Converted waves and vector wavefield applications, 3C Seismic and VSP: Converted waves and vector wavefield applications.

Glubokovskikh, S., R. Pevzner, T. Dance, E. Caspari, D. Popik, V. Shulakova, and B. Gurevich. 2016, Seismic monitoring of CO2 geosequestration: CO2CRC Otway case study using full 4D FDTD approach. International Journal of Greenhouse Gas Control, **49**,201-216. doi: http://dx.doi.org/10.1016/j.ijggc.2016.02.022.

Hamarbatan, N., and G. Margrave. 1998, Spectral analysis of a ghost. In CREWES Research Report. Calgary: GREWES.

Hannis, S., A. Chadwick, D. Jones, J. Pearce, J. White, D. Connelly, I. Wright, J. Blackford, S. Widdicombe, T. Leighton, and P. White. 2015, Review of offshore monitoring for CCS projects. IEAGHG.

Hansen, O., D. Gilding, B. Nazarian, B. Osdal, P. Ringrose, J.-B. Kristoffersen, O. Eiken, and H. Hansen. 2013, Snøhvit: The History of Injecting and Storing 1 Mt CO_2 in the Fluvial Tubåen Fm. Energy Procedia, **37**,3565-3573. doi: http://dx.doi.org/10.1016/j.egypro.2013.06.249.

Hatchell, P., R. Kamarudin, J. Lopez, S. Bakku, Z. Yang, K. Wang, V. Gee, J. Mestayer, K. King, A. Kudarova, B. Brookshire, E. Majzlik, J. Gaytan, O. Eriksen, and R. Ha. 2017, Low-cost high-resolution 3D and 4D seismic for deepwater fields, SEG Technical Program Expanded Abstracts 2017. 5782-5786.

Hatton, L., J. Makin, and M. H. Worthington. 1986, Seismic data processing : theory and practice Blackwell Scientific.

Helgerud, M. B., A. C. Miller, D. H. Johnston, M. S. Udoh, B. G. Jardine, C. Harris, and N. Aubuchon. 2011, 4D in the deepwater Gulf of Mexico: Hoover, Madison, and Marshall fields. The Leading Edge, **30**, no. 9,1008-1018. doi: 10.1190/1.3640524.

Huang, F., C. Juhlin, T. Kempka, B. Norden, and F. Zhang. 2015, Modeling 3D time-lapse seismic response induced by CO2 by integrating borehole and 3D seismic data – A case study at the Ketzin pilot site, Germany. International Journal of Greenhouse Gas Control, **36**,66-77. doi: http://dx.doi.org/10.1016/j.ijggc.2015.02.020.

IEA. 2012, Energy Technology Perspectives. Paris: IEA/OECD.

Ivandic, M., C. Juhlin, S. Lüth, P. Bergmann, A. Kashubin, D. Sopher, A. Ivanova, G. Baumann, and J. Henninges. 2015, Geophysical monitoring at the Ketzin pilot site for CO2 storage: New insights into the plume evolution. International Journal of Greenhouse Gas Control, **32**,90-105. doi: http://dx.doi.org/10.1016/j.ijggc.2014.10.015.

Jenkins, C., A. Chadwick, and S. D. Hovorka. 2015, The state of the art in monitoring and verification—Ten years on. International Journal of Greenhouse Gas Control, **40**,312-349. doi: http://dx.doi.org/10.1016/j.ijggc.2015.05.009.

Jenkins, C. R., P. J. Cook, J. Ennis-King, J. Undershultz, C. Boreham, T. Dance, P. de Caritat, D. M. Etheridge, B. M. Freifeld, A. Hortle, D. Kirste, L. Paterson, R. Pevzner, U. Schacht, S. Sharma, L. Stalker, and M. Urosevic. 2012, Safe storage and effective monitoring of CO_2 in depleted gas fields. Proceedings of the National Academy of Sciences, **109**, no. 2,E35-E41. doi: 10.1073/pnas.1107255108.

Jervis, M., A. Bakulin, R. Burnstad, C. Berron, and E. Forgues. 2012, Suitability of vibrators for time-lapse monitoring in the Middle East, SEG Technical Program Expanded Abstracts 2012. 1-5.

Jin, S., R.-S. Wu, and C. Peng. 1999, Seismic depth migration with pseudo-screen propagator. Computational Geosciences, **3**, no. 3,321-335. doi: 10.1023/a:1011587227696.

Johnson, D. L. 2001, Theory of frequency dependent acoustics in patchy-saturated porous media. The Journal of the Acoustical Society of America, **110**, no. 2,682-694. doi: doi:http://dx.doi.org/10.1121/1.1381021.

Johnston, D. H. 2013, Practical Applications of Time-lapse Seismic Data, Distinguished Instructor Seres: SEG Books.

Kharaka, Y., D. Cole, S. Hovorka, W. Gunter, K. Knauss, and B. Freifeld. 2006, Gas-water-rock interactions in Frio Formation following CO_2 injection: Implications for the storage of greenhouse gases in sedimentary basins. Geology, **34**, no. 7,577-580.

Kragh, E., and P. Christie. 2002, Seismic repeatability, normalized rms, and predictability. The Leading Edge, **21**, no. 7,640-647.

Krassay, A. A., D. L. Cathro, and D. J. Ryan. 2004, A regional tectonostratigraphic framework for the Otway Basin., in P.J. Boult, D.R Johns and S.C. Lang, eds., Eastern Australasian Basins Symposium II: Petroleum Exploration Society of Australia.

Kunz, O., Klimeck R., W. Wagner, and M. Jaeschke. 2007, The GERG-2004 wide-range equation of state for natural gases and other mixtures.

Landro, M. 1999, Repeatability issues of 3-D VSP data. Geophysics, **64**, no. 6,1673-1679. doi: 10.1190/1.1444671.

Landrø, M. 2001, Discrimination between pressure and fluid saturation changes from time-lapse seismic data. GEOPHYSICS, **66**, no. 3,836-844. doi: 10.1190/1.1444973.

Lawrence, M. J. F., M. Arnot, G. H. Browne, M. Bunch, S. Menacherry, and T. Dance. 2012, Geological interpretation of Otway Project wells CRC-1 and CRC-2. Canberra, Australia: Cooperative Research Centre for Greenhouse Gas Technologies.

Lumley, D. E. 2001, Time-lapse seismic reservoir monitoring. Geophysics, **66**, no. 1,50-53.

Lüth, S., P. Bergmann, C. Cosma, N. Enescu, R. Giese, J. Götz, A. Ivanova, C. Juhlin, A. Kashubin, C. Yang, and F. Zhang. 2011, Time-lapse seismic surface and down-hole measurements for monitoring CO2 storage in the CO2SINK project (Ketzin, Germany). Energy Procedia, **4**, no. 0,3435-3442. doi: 10.1016/j.egypro.2011.02.268.

Margrave, G. F. 1998, Theory of nonstationary linear filtering in the Fourier domain with application to time-variant filtering. GEOPHYSICS, **63**, no. 1,244-259. doi: 10.1190/1.1444318.

Mavko, G., T. Mukerji, and J. Dvorkin. 2009, The Rock Physics Handbook. 2 ed: Cambridge University Press.

Meadows, M. A., and S. P. Cole. 2013, 4D seismic modeling and CO2 pressure-saturation inversion at the Weyburn Field, Saskatchewan. International Journal of Greenhouse Gas Control, **16**,S103-S117. doi: https://doi.org/10.1016/j.ijggc.2013.01.030.

Misaghi, A., M. Landrø, and S. A. Petersen. 2007, Overburden complexity and repeatability of seismic data: Impacts of positioning errors at the Oseberg field, North Sea. Geophysical Prospecting, **55**, no. 3,365-379. doi: 10.1111/j.1365-2478.2007.00620.x.

Nguyen, P. T., M. Nam, and C. Park. 2015, A review on time-lapse seismic data processing and interpretation. Geosciences Journal, **19**, no. 2,375-392. doi: 10.1007/s12303-014-0054-2.

O'Brien, J., J. Moran, G. Wilburn, S. Morris, J. Andersen, and O. Quezada. 2010, Salt Creek 4-D; Monitoring a CO$_2$ Flood with Fine Time Steps, SEG Technical Program Expanded Abstracts 2010. 4165-4169.

O'Doherty, R. F., and N. A. Anstey. 1971, Reflections On Amplitudes. Geophysical Prospecting, **19**, no. 3,430-458. doi: 10.1111/j.1365-2478.1971.tb00610.x.

Pacala, S., and R. Socolow. 2004, Stabilization Wedges: Solving the Climate Problem for the Next 50 Years with Current Technologies. Science, **305**, no. 5686,968-972. doi: 10.1126/science.1100103.

Partridge, A. D. 2001, Revised stratigraphy of the Sherbrook Group, Otway Basin.: Eastern Australian Basin Symposium,455-464.

Pevzner, R., E. Caspari, B. Gurevich, T. Dance, and Y. Cinar. 2015, Feasibility of CO2 plume detection using 4D seismic: CO2CRC Otway Project case study — Part 2: Detectability analysis. GEOPHYSICS, **80**, no. 4,B105-B114. doi: doi:10.1190/geo2014-0460.1.

Pevzner, R., E. Caspari, M. Urosevic, V. Shulakova, and B. Gurevich. 2015, Carbon Dioxide Capture for Storage in Deep Geological Formations, in K.F. Gerdes, ed.: CPL Press and BPCNAL. 627-650.

Pevzner, R., B. Gurevich, and M. Urosevic. 2011, Estimation of azimuthal anisotropy from VSP data using multicomponent S-wave velocity analysis. Geophysics, **76**, no. 5,D1-D9.

Pevzner, R., V. Shulakova, A. Kepic, and M. Urosevic. 2010, Repeatability analysis of land time-lapse seismic data: CO2CRC Otway pilot project case study. Geophysical Prospecting, **59**, no. 1,66-77. doi: 10.1111/j.1365-2478.2010.00907.x.

Pevzner, R., V. Shulakova, A. Kepic, and M. Urosevic. 2011, Repeatability analysis of land time-lapse seismic data: CO2CRC Otway pilot project case study. Geophysical Prospecting, **59**, no. 1,66-77. doi: 10.1111/j.1365-2478.2010.00907.x.

Pevzner, R., K. Tertyshnikov, V. Shulakova, M. Urosevic, A. Kepic, B. Gurevich*, and R. Singh. 2015, Design and deployment of a buried geophone array for CO_2 geosequestration monitoring: CO2CRC Otway Project, Stage 2C, SEG Technical Program Expanded Abstracts 2015. 266-270.

Pevzner, R., M. Urosevic, and S. Nakanishi. 2010, Applicability of Zero-offset and Offset VSP for Time-lapse monitoring – CO2CRC Otway Project Case Study. Paper read at 72nd EAGE Conference & Exhibition incorporating SPE EUROPEC 2010 14-17 June 2010, at Barcelona, Spain.

Pevzner, R., M. Urosevic, D. Popik, V. Shulakova, K. Tertyshnikov, E. Caspari, J. Correa, T. Dance, A. Kepic, S. Glubokovskikh, S. Ziramov, B. Gurevich, R. Singh, M. Raab, M. Watson, T. Daley, M. Robertson, and B. Freifeld. 2017, 4D surface seismic tracks small supercritical CO2 injection into the subsurface: CO2CRC Otway Project. International Journal of Greenhouse Gas Control, **63**,150-157. doi: https://doi.org/10.1016/j.ijggc.2017.05.008.

Pevzner, R., M. Urosevic, D. Popik, K. Tertyshnikov, J. Correa, A. Kepic, S. Glubokovskikh, S. Ziramov, B. Gurevich, E. Caspari, V. Shulakova, T. Dance, and R. Singh. 2017, Seismic monitoring of CO_2 geosequestration: Preliminary results from Stage 2C of the CO2CRC Otway Project one year post injection, SEG Technical Program Expanded Abstracts 2017. 5895-5900.

Ringrose, P. S., A. S. Mathieson, I. W. Wright, F. Selama, O. Hansen, R. Bissell, N. Saoula, and J. Midgley. 2013, The In Salah CO2 Storage Project: Lessons Learned and Knowledge Transfer. Energy Procedia, **37**,6226-6236. doi: http://dx.doi.org/10.1016/j.egypro.2013.06.551.

Schrag, D. P. 2007, Preparing to Capture Carbon. Science, **315**, no. 5813,812-813. doi: 10.1126/science.1137632.

Shulakova, V., R. Pevzner, J. Christian Dupuis, M. Urosevic, K. Tertyshnikov, D. E. Lumley, and B. Gurevich. 2014, Burying receivers for improved time-lapse seismic repeatability: CO2CRC Otway field experiment. Geophysical Prospecting, **63**, no. 1,55-69. doi: 10.1111/1365-2478.12174.

Sodagar, T. M., and D. C. Lawton. 2014, Time-lapse seismic modelling of CO2 fluid substitution in the Devonian Redwater Reef, Alberta, Canada. Geophysical Prospecting, **62**, no. 3,518-529. doi: 10.1111/1365-2478.12100.

Tenthorey, E., T. Dance, Y. Cinar, J. Ennis-King, and J. Strand. 2014, Fault modelling and geomechanical integrity associated with the CO2CRC Otway 2C injection experiment. Vol. 30.

White, D. 2009, Monitoring CO2 storage during EOR at the Weyburn-Midale Field. The Leading Edge, **28**, no. 7,838-842. doi: doi:10.1190/1.3167786.

White, D. 2011, Geophysical monitoring of the Weyburn CO2 flood: Results during 10 years of injection. Energy Procedia, **4**, no. 0,3628-3635. doi: 10.1016/j.egypro.2011.02.293.

White, D. J., L. A. N. Roach, and B. Roberts. 2015, Time-lapse seismic performance of a sparse permanent array: Experience from the Aquistore CO2 storage site. GEOPHYSICS, **80**, no. 2,WA35-WA48. doi: 10.1190/geo2014-0239.1.

White, D. J., L. A. N. Roach, B. Roberts, and T. M. Daley. 2014, Initial Results from Seismic Monitoring at the Aquistore CO2 Storage Site, Saskatchewan, Canada. Energy Procedia, **63**,4418-4423. doi: http://dx.doi.org/10.1016/j.egypro.2014.11.477.

Xu, W., T. T. Tran, R. M. Srivastava, and A. G. Journel. 1992, Integrating Seismic Data in Reservoir Modeling: The Collocated Cokriging Alternative. Society of Petroleum Engineers.

Yavuz, S., B. M. Freifeld, R. Pevzner, K. Tertyshnikov, A. Dzunic, S. Ziramov, V. Shulakova, M. Robertson, T. Daley, A. Kepic, M. Urosevic, and B. Gurevich. 2016, Subsurface Imaging Using Buried DAS and Geophone Arrays - Preliminary Results from CO2CRC Otway Project. Paper read at 78th EAGE Conference & Exhibition 2016, 30 May - 2 June 2016, at Vienna, Austria.

List of Figures

List of Tables

Appendix A: Copyright consent
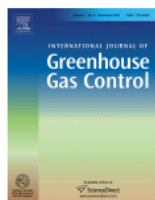
Title: 4D surface seismic tracks small supercritical CO2 injection into the subsurface: CO2CRC Otway Project

Author: Roman Pevzner,Milovan Urosevic,Dmitry Popik,Valeriya Shulakova,Konstantin Tertyshnikov,Eva Caspari,Julia Correa,Tess Dance,Anton Kepic,Stanislav Glubokovskikh,Sasha Ziramov,Boris Gurevich,Rajindar Singh,Matthias Raab,Max Watson,Tom Daley et al.

Publication: International Journal of Greenhouse Gas Control

Publisher: Elsevier

Date: August 2017

© 2017 Elsevier Ltd. All rights reserved.

Quick Price Estimate

I would like to...	reuse in a thesis/dissertation ▼	**This service provides permission for reuse only.** If you do not have a copy of the content, you may be able to purchase a copy using RightsLink as an additional transaction. Simply select 'I would like to.... 'Purchase this content'.
I would like to use...	full article ▼	
My format is...	both print and electronic ▼	
I am the author of this Elsevier article...	Yes ▼	
I will be translating...	No ▼	Unclear about who you are?
My currency is...	AUD - $ ▼	
Quick Price	Click Quick Price	

QUICK PRICE | CONTINUE

Exchange rates under license from XE.com.
To request permission for a type of use not listed, please contact Elsevier Global Rights Department.

Are you the author of this Elsevier journal article?

Title: 4D surface seismic tracks small supercritical CO2 injection into the subsurface: CO2CRC Otway Project

Author: Roman Pevzner,Milovan Urosevic,Dmitry Popik,Valeriya Shulakova,Konstantin Tertyshnikov,Eva Caspari,Julia Correa,Tess Dance,Anton Kepic,Stanislav Glubokovskikh,Sasha Ziramov,Boris Gurevich,Rajindar Singh,Matthias Raab,Max Watson,Tom Daley et al.

Publication: International Journal of Greenhouse Gas Control

Publisher: Elsevier

Date: August 2017

© 2017 Elsevier Ltd. All rights reserved.

Please note that, as the author of this Elsevier article, you retain the right to include it in a thesis or dissertation, provided it is not published commercially. Permission is not required, but please ensure that you reference the journal as the original source. For more information on this and on your other retained rights, please visit: https://www.elsevier.com/about/our-business/policies/copyright#Author-rights

BACK | CLOSE WINDOW

217

Copyright

Describes the rights related to the publication and distribution of research. It governs how authors (as well as their employers or funders), publishers and the wider general public can use, publish and distribute articles or books.

Journal author rights   Government employees   Elsevier's rights   Protecting author rights   Open access

Journal author rights

In order for Elsevier to publish and disseminate research articles, we need publishing rights. This is determined by a publishing agreement between the author and Elsevier. This agreement deals with the transfer or license of the copyright to Elsevier and authors retain significant rights to use and share their own published articles. Elsevier supports the need for authors to share, disseminate and maximize the impact of their research and these rights, in Elsevier proprietary journals* are defined below:

For subscription articles	For open access articles
Authors transfer copyright to the publisher as part of a journal publishing agreement, but have the right to: • Share their article for Personal Use, Internal Institutional Use and Scholarly Sharing purposes, with a DOI link to the version of record on ScienceDirect (and with the Creative Commons CC-BY-NC- ND license for author manuscript versions) • Retain patent, trademark and other intellectual property rights (including research data). • Proper attribution and credit for the published work.	Authors sign an exclusive license agreement, where authors have copyright but license exclusive rights in their article to the publisher**. In this case authors have the right to: • Share their article in the same ways permitted to third parties under the relevant user license (together with Personal Use rights) so long as it contains a CrossMark logo, the end user license, and a DOI link to the version of record on ScienceDirect. • Retain patent, trademark and other intellectual property rights (including research data). • Proper attribution and credit for the published work.

Appendix B: Relevant publications

Journal Articles

R. Pevzner, M. Urosevic, D. Popik, V. Shulakova, K. Tertyshnikov, E. Caspari, J. Correa, T. Dance, A. Kepic, S. Glubokovskikh, S. Ziramov, B. Gurevich, *4D surface seismic tracks small supercritical CO2 injection into the subsurface: CO2CRC Otway Project.* International Journal of Greenhouse Gas Control 63, 150-157.

S. Glubokovskikh, R. Pevzner, T. Dance, E. Caspari, D. Popik, V. Shulakova and B. Gurevich, 2016. *Seismic monitoring of CO2 geosequestration: CO2CRC Otway case study using full 4D FDTD approach.* International Journal of Greenhouse Gas Control 49, 201-216.

Conference Proceedings

D. Popik, V. Shulakova, K. Tertyshnikov, S. Ziramov, M. Urosevic, R. Pevzner, 2018. *Time-lapse surface seismic processing for Stage 2C of CO2CRC Otway Project.* ASEG Extended Abstracts 2018.

D. Popik, V. Shulakova, K. Tertyshnikov, S. Ziramov, M. Urosevic, R. Pevzner, 2017. *Model-guided processing of time-lapse seismic for real-time monitoring of CO_2 geosequestration – CO2CRC Otway Project case study.* Extended Abstract at 79th EAGE Conference and Exhibition 2017.

D. Popik, R. Pevzner, S. Glubokovskikh, V. Shulakova, S. Ziramov, 2018. *Optimising Time-Lapse Seismic Data Processing: Stage 2c of the Co2crc Otway Project Case Study.* 14th Greenhouse Gas Control Technologies Conference Melbourne.

R. Pevzner, M. Urosevic, D. Popik, K. Tertyshnikov, J. Correa, A. Kepic, S. Glubokovskikh, S. Ziramov, B. Gurevich, E. Caspari, V. Shulakova, T. Dance, R. Singh, 2017. *Seismic monitoring of CO2 geosequestration: Preliminary results from Stage 2C of the CO2CRC Otway Project one year post injection.* Expanded Abstract at SEG Technical Program 2017.

S. Glubokovskikh, R. Pevzner, D. Popik, T. Dance, E. Caspari, V. Shulakova and B. Gurevich, 2016. *Seismic Monitoring of CO2 Geosequestration-CO2CRC Otway Case Study Using Full 4D Elastic Modelling.* 78th EAGE Conference and Exhibition 2016.

M. Urosevic, B. Gurevich, R. Pevzner, K. Tertyshnikov, V. Shulakova, S. Glubokovskikh, D. Popik, A. Kepic, M. Robertson, B.M. Freifeld, T.M. Daley, R. Singh, 2015. *Monitoring CO2 injection with a buried geophone array: Stage 2C of CO2CRC Otway Project.* AGU Fall Meeting Abstracts.